How water, ice, and sediment deform the Earth: Novel developments and applications of models of glacial isostatic adjustment

by

Joseph Kuchar

Submitted to the Department of Physics
in partial fulfillment of the requirements for the degree of

Doctor of Philosophy

at the

UNIVERSITY OF OTTAWA

November 2018

How water, ice, and sediment deform the Earth: Novel developments and applications of models of glacial isostatic adjustment

by

Joseph Kuchar

Submitted to the Department of Physics
on November 22, 2018, in partial fulfillment of the
requirements for the degree of
Doctor of Philosophy

Abstract

Sea-level change in response to the growth and melt of ice sheets and glaciers is a process called glacial isostatic adjustment (GIA). This includes deformation of the surface of the Earth itself in response to the extreme mass exchanges between the oceans and continents, as well as changes to the gravitational potential that describe the sea surface in response to the redistribution of surface mass as well as mass within the Earth. This thesis describes four research projects I've conducted in the field of GIA modelling.

Most GIA models represent the lithosphere, the outermost layer of the Earth, as functionally elastic. However, there is a large temperature gradient within the lithosphere that would lead to a reduction in viscosity with depth. Therefore, in Chapter 2, I developed and incorporated more realistic lithosphere structure into the GIA model, and demonstrate that this added structure results in a time-dependence to the response of the lithosphere.

While the usual inputs to a GIA model are the ice load and Earth description, there are regions where other processes need to be accounted for. In the Mississippi Delta region, processes associated with the deposition of sediment carried by the Mississippi River are strong drivers of local sea-level change, and include isostatic adjustment as well as compaction of the sediment layers over time. Therefore, in Chapter 3, I incorporated a treatment of sediment isostatic adjustment into the GIA model and applied it to the Mississippi Delta region. Our results indicate that the sediment isostatic adjustment signal is important in the vicinity of the delta, but small otherwise. By comparing model projections to GPS measurements, we demonstrate that most subsidence in the region is due to non-isostatic processes (such as sediment compaction).

Data used to constrain GIA models are generally sensitive to both ice and Earth structure. Therefore data parametrizations that are insensitive to one input or the other are valuable constraints. One such commonly used parametrization is the post-

glacial decay time. Previous research has shown that the decay times are relatively insensitive to the ice history, and therefore provide a more robust constraint on Earth structure. In Chapter 4 I tested the extent of the ice insensitivity of decay times by considering a suite of ice reconstructions. I found that decay times are sensitive to ice history, and that the sensitivity depends on the location of the data relative to the geometry of the ice sheet. In particular, my results suggest that James Bay (in Hudson Bay) is a location that should not be used in a decay time analysis.

The GIA model applied in the projects described above is a 1-D, spherically symmetric model. However, it is known that the Earth's viscous structure is likely to feature significant lateral variation. This is evident in the differences in viscosities found in this thesis between what satisfies the RSL data in Hudson Bay (in Chapter 4) and the Gulf coast of the US (Chapter 3), as well as various previous studies. Therefore, in Chapter 5, I applied a 3-D model with lateral viscous structure determined by seismic shear wave velocity models, to determine whether incorporating this more realistic structure could resolve this apparent discrepancy. I demonstrated that the fit to relative sea level data on the Atlantic and Gulf coasts of the US can be significantly improved by incorporating lateral viscous structure, but also that there is significant uncertainty associated with the more complex viscous structure.

Acknowledgments

First of all, I need to acknowledge my supervisor, Professor Glenn Milne. I have known Glenn since I was a student in his Physics of the Earth course nearly a decade ago, and it was Glenn at that time who heard that I was looking for a position as an undergraduate research assistant, and who offered me a job I never applied for. In retrospect, it was this opportunity more than any other that propelled me to becoming the researcher I am today, and I feel lucky to have had Glenn as a supervisor.

I would be remiss not to acknowledge the group members and co-authors who have helped me over the years. Discussions with all group members over the years have been valuable, but in particular, Ryan Love's Linux expertise was frequently invaluable when I encountered various compiler or package installation issues on the group's clusters. Professor Lev Tarasov of Memorial University, while not an official co-supervisor, was very gracious with his time and knowledge (even meeting me at his home in Guelph while I was still wrapping up my MSc to give me advice before starting my PhD). Similarly, Professor Torbjörn Törnqvist of Tulane University was very generous with his time, and his knowledge of the sediment distribution of the Mississippi Delta region was an invaluable help for the second manuscript in this thesis.

I would also like to thank my examination committee, Professors Natalya Gomez, Ivan L'Heureux, Liam Kieser, Pascal Audet, and Laurel Sinclair, for volunteering to read and evaluate this thesis.

Finally, all of my love and gratitude goes to my wife, Hilary Paulin. Hilary's love and support is everything to me, and this thesis could not exist without her.

Contents

List of Figures

Glossary

Here we provide a short list of frequently used terms and abbreviations in this thesis.

Glacial Isostatic Adjustment (GIA) Glacial isostatic adjustment is the process of Earth deformation and sea level change in response to changes in ice volume.

Last Glacial Maximum (LGM) The last glacial maximum is the point in time during the previous glaciation when global ice volume was at its maximum, and occurred approximately twenty thousand years ago.

Lower Mantle Viscosity (LMV) The viscosity in the lower mantle, defined in our model as a constant viscosity layer from 670 km depth to the core-mantle boundary. See 'Viscosity'.

Relative Sea Level (RSL) Relative sea level is sea level at some time in the past with respect to present-day sea level.

Sea Level (SL) By sea level we mean the height of the ocean surface with respect to the solid surface of the Earth below.

Sediment Isostatic Adjustment (SIA) This is similar to glacial isostatic adjustment, except that the Earth deformation and sea level change occurs in response to the erosion and deposition of sediment.

Upper Mantle Viscosity (UMV) The viscosity in the upper mantle, defined in our model as a constant viscosity layer from the base of the lithosphere to a depth of 670 km. See 'Viscosity'.

Viscosity (η) Viscosity is a scalar quantity that relates stress and strain rate, and is a key model parameter.

1
Introduction

1.1 Glacial Isostatic Adjustment

Contemporary global mean sea-level rise is estimated to be about 3mm/yr (Watson et al., 2015). Dangers associated with rising sea levels have been identified as a key concern for this century by the International Panel on Climate Change (IPCC), with the most recent assessment report predicting the rate of sea-level rise around 2100 to be greater than 8 mm/yr (Church et al., 2013). However, while we often speak of global average sea level, in reality regional and local sea-level change can deviate strongly from the global mean. The main contributions to contemporary sea-level rise are thermal expansion and the addition of meltwater from the retreat of glaciers and ice sheets. However, there is also a component to sea-level change that is due to the influence of ice sheets and glaciers that have not existed for thousands of years.

This process, called glacial isostatic adjustment (GIA), is a major component to sea-level change over millennial time scales, and to contemporary sea level in previously glaciated regions such as Canada, which was nearly entirely ice-covered during the last glacial maximum (LGM).

Over the past several million years, continental ice sheets have undergone a cycle of slow growth and relatively rapid retreat with a period of approximately 100 thousand years. In fact, we happen to exist in a global ice volume minimum within the current glacial cycle, which was at its peak approximately 25 thousand years ago. At maximum ice volume, not only were the Greenland and Antarctic ice sheets significantly expanded relative to present, there were also major ice sheets covering nearly all of present-day Canada (the Laurentide ice sheet), a significant portion of Northern Europe (the Fennoscandian ice sheet), and the British Isles (the British-Irish ice sheet). At the LGM eustatic sea level (*eustatic* sea-level change is the volume of meltwater divided by the area of the oceans, and is more of a concept related to mass conservation than it is a reflection of actual sea-level change) was approximately 130 m lower than present (Lambeck et al., 2014). For a sense of scale, we can use the eustatic shift $h = 130$ m, the density of water at 1000 kg m^{-3}, and the area of the oceans of approximately 360 million square kilometres to estimate the mass transported between the continents and oceans during the most recent glacial cycle. With the numbers above, a glacial episode represents a transfer of surface water mass on the order of 10^{19} kg or approximately 0.001% of the total mass of the Earth. This large transfer of mass represents an equivalently large forcing on the surface of the Earth, which deforms in response. Moreover, the static sea surface is determined by the Earth's gravitational potential. The net effect is that during deglaciation sea level rises substantially and non-uniformly as the gravitational potential surface changes in response to both the surface mass transport and also to the (deformational) mass transfer within the Earth in response to the loading. GIA is this process of Earth deformation and sea level change in response to changes in the global ice distribution. The pattern of sea level change during the transition from LGM to present is recorded in relative sea level (RSL) records such as coral, fossilized shells and driftwood, and sediment cores (e.g., Mitrovica et al., 2000; Peltier and Fairbanks, 2006; Engelhart and Horton, 2012). While sea level is defined as the height of the sea surface relative to the solid Earth, RSL is sea level at some time in the past with respect to present-day sea level.

In this thesis I describe several research projects related to modelling the GIA process. The GIA model itself is a forward model that takes as inputs a description of the material properties of the Earth and a prescribed ice loading history, and computes deformation of the surface of the Earth, the gravitational potential, and the surface that describes sea level. The primary constraint data are RSL records, which are indicators of the elevation of the sea surface relative to the sea floor at some time in the past. By running these models and varying either the Earth description or the ice loading history, an optimal solution is determined by minimizing the misfit with the RSL records.

At this point it might be reasonable to ask why we should focus on a process with a timescale of thousands of years, that is at present contributing less to ongoing global sea-level change than either thermal expansion or meltwater associated with the warming climate. While thermal and meltwater effects dominate changes in ocean volume and therefore global mean sea level, there is significant variability in regional and local sea level changes due to regional processes such as sediment erosion and deposition, GIA, and ocean dynamics, and in some regions GIA is a dominant signal (Love et al., 2016). Moreover, while there is always the "Because it's there!" response to "Why climb the mountain?", there are also practical reasons that make GIA an important field of research.

One consideration is that to determine the relative impact of the different processes that govern present-day sea-level change, we need to have an independent estimate of the GIA signal. This is especially important to make corrections to sea-level records such as tide gauges, so that what they measure is related to the height of the ocean surface and not to the motion of the solid Earth surface itself (Church et al., 2004; King et al., 2012b). Another reason is that estimates of meltwater from Greenland and Antarctica are typically derived from gravity data such as from the GRACE (Gravity

Recovery and Climate Experiment) satellite, and because changes in ice mass lead to GIA-driven mass transfer in the solid Earth, the resulting gravity changes need to be corrected for GIA effects as well (King et al., 2012a; van der Wal et al., 2015). GIA observables also allow us to determine how past ice sheets have responded to climactic changes (e.g. Lambeck et al., 2014). Finally, while thermal expansion and meltwater make up the majority of global mean sea-level change, GIA can very strongly affect local sea level. For example, Love et al., 2016, estimate GIA driven sea level changes over the coming century of only a few centimetres in the Southern United States, but tens of centimetres in Atlantic Canada. Therefore it is a process that needs to be taken into account to provide accurate sea level projections for certain coastal populations.

A final motivation for modelling the GIA process is that the Earth's response to an external forcing is among the only ways we have to infer its physical properties. A fundamental limitation of the Earth sciences is that there is only one Earth, and that it does not fit in a laboratory. The bulk properties of the Earth can not generally be directly measured, only indirectly inferred, and the best experiments available to infer these properties are the Earth's natural response to forcings. Estimates of the Earth's viscosity structure obtained through GIA studies are useful to the broader Earth science community. For example, mantle viscosity is a key parameter when modelling mantle convection, and a model of the Earth's viscous response is essential to glaciological modellers interested in the dynamics of glaciers on glacial-cycle time scales. Moreover, there is evidence that the GIA process is a key stabilizing feedback on the stability of marine ice sheets (Gomez et al., 2012).

As an additional tidbit to provide a sense of scale of the Earth and the problems we face, the deepest borehole that has been drilled to date is the Kola Superdeep Borehole in Russia, and it is approximately 12 km deep. At this depth it measures properties of the shallow crust - as a fraction of the earth's radius, this is only about 0.2%, and yet the temperature at this depth is already 600 °C and the pressure is 150 MPa (Zharikov et al., 2003). Thus, given the difficulties of making direct measurements at high pressure and temperature, if we wish to determine the material properties of the earth's deeper lithosphere or mantle, we need to use indirect methods.

1.2 Outline of Thesis

The bulk of this thesis describes four research projects I've conducted over the course of my PhD. Three of these projects have culminated in manuscripts that have either been published (as in Chapters 2 and 3) or else have been submitted and are currently in peer-review (Chapter 4). The results of Chapter 5 are currently being prepared in a manuscript to be submitted for publication, and therefore that chapter describes a work in progress.

Most numerical GIA studies make several simplifying assumptions about the rheology and structure of the Earth. In particular, it is usually assumed that the Earth can be modelled as a one-dimensional Maxwell body with a fairly simple viscosity structure, including an elastic lithosphere layer and viscoelastic upper and lower mantle. However, laboratory experiments indicate that, while the lithosphere's deformation response may be elastic for shallow depths and low stresses, its large temperature gradient leads to a significant reduction in viscosity with depth. In Chapter 2 I provide an overview of how the lithosphere has been treated in previous GIA studies, as well as what structure may be inferred from the microphysics of rocks and laboratory experiments. I then describe how we incorporated a more realistic lithosphere structure into a GIA model, and compare resulting Earth deformation and sea level with results from models featuring elastic lithosphere layers. The results are presented in the manuscript at the end of Chapter 2.

An interesting result we found from incorporating ductile lithosphere structure was a sensitivity of the response to loads of different sizes and timescales. This motivated the next problem, which is modelling the isostatic adjustment in response to sediment loading alongside ice loading. In particular, our interest was in modelling the sea level and Earth response to sediment loading in the Mississippi Delta region, where tens of thousands of years of sediment transport has resulted in a load that is small relative to the major ice sheets, but large enough to be an important contributor to local deformation and sea level change. A theory to self-consistently treat sediment loading alongside ice and ocean loading was developed by Dalca et al., 2013, and I modified a sea level code to incorporate this theory, and applied it to the Mississippi Delta region along with a realistic history of the sediment load. Sediment transport into the Mississippi Delta has lead to significant ongoing subsidence in the region, which is partly a result of the isostatic response to the sediment and ice loading, and partly caused by the compaction of the sediment through time. The relative contributions of sediment isostasy versus sediment compaction has been a subject of ongoing debate that we have been able to make a significant contribution to. In Chapter 3 I provide background on the particular geography of the region that makes it an interesting and important study area, as well as describe the implementation of the theory of Dalca et al., 2013. The resulting manuscript is then presented at the end of Chapter 3. (Unfortunately, incorporating the ductile lithosphere models of Chapter 2 ended up being outside the scope of this project, but there are plans for this in a future study.)

Generally, relative sea level data, and the model predictions compared with them, are sensitive to both the assumed viscosity structure of the Earth, and to the assumed ice loading history. Because there are significant uncertainties in both inputs, it's very useful to find data parametrizations that are insensitive to either input. One such parametrization is the *postglacial decay time*, which is the characteristic decay time of the exponential sea level response observed in some previously glaciated regions. Previous studies have shown that postglacial decay times are relatively insensitive to details in the assumed ice history, and instead are determined by the Earth's viscosity structure. However, in recent years numerical modelling of glacial systems has lead to a significant increase in the number and variety of ice histories available to GIA modellers. In Chapter 4 I describe the use of postglacial decay times, and discuss the studies that have concluded that they are relatively insensitive to the input ice history. We investigated the extent of this insensitivity by computing RSL for a set of ice history inputs, and developed necessary corrections to the RSL data to ensure that the assumptions inherent in the postglacial decay time theory are satisfied as well as they can be. The results of this investigation are presented in the manuscript (currently in peer review) at the end of Chapter 4, and we demonstrate that the previously reported insensitivity of decay times to ice history is not universally valid, and depends on location.

An interesting result of Chapter 3, modelling RSL changes including sediment loading in the Mississippi Delta, was that the Earth viscosity parameters that satisfied the data best are of surprisingly large magnitude. The same result has been found in a recent study by Love et al., 2016 who considered data along both the Atlantic and Gulf coasts of North America (but did not include sediment loading). These are in contrast to what has been found to satisfy the Hudson Bay data, as well as various global inversions. This motivates the final study, which is an investigation into exactly why the RSL data require such high viscosities, and what this implies about Earth structure. In particular, and in contrast to the other studies in this thesis, in Chapter 5 we apply a 3-D GIA model with laterally varying viscosity. Our goal is to determine whether the apparent large viscosity values required by the RSL data are in some respects a result of the limitations of the 1-D model, and whether a 3-D model with a more reasonable global average viscosity may be able to capture the same fundamental behaviour. In particular, we show that the RSL data do not support a large peripheral bulge, and that the peripheral bulge may be suppressed either by a uniformly high (1-D) viscosity mantle, or by a mantle with lower average viscosity but with structure that varies laterally. Moreover, we demonstrate that by including lateral viscous structure, it's possible to greatly improve the fit to the Gulf coast RSL data with an average viscosity structure consistent with the decay time analysis found in Chapter 4, relative to the 1-D reference model.

However, before we get to the meat of Chapters 2-5, we need to eat our metaphorical vegetables. In the next section I provide an overview of the current state of GIA research in order to put my own work into a broader context. I will then give a brief overview of the GIA model, considering separately the approach for computing the Maxwell response of a spherically symmetric Earth, and then the sea level equation, which describes how to calculate sea-level changes in response to a surface load.

1.2.1 Research in Context

The key components to the study of GIA are models of Earth deformation in response to a surface load, and a model of sea level change in response to the surface load and mass redistribution in the Earth.

Early work in the study of the deformation of the solid Earth in response to surface loading caused by ice sheets goes back as far as Haskell, 1935, who considered the problem of a large cylindrical surface load on a viscoelastic half space to determine the mantle's viscosity from measurements of Earth deformation. From this simple model, he derived a value for the viscosity of the mantle of around 3×10^{20} Pa s, which still holds up as a reasonable estimate nearly a century later. Similarly, it has been known since the 1800s that local sea level is defined by a gravitational equipotential and will be perturbed by the presence of large surface masses such as continents or ice sheets (Woodward, 1888).

The fundamental works for determining sea level and Earth deformation for a spherical viscous Earth were developed in the 1970s, by Peltier, 1974 and Farrell and Clark, 1976. An impulse response formalism was developed by Peltier, who assumed a Maxwell viscoelastic structure for the Earth. By computing Green's functions describing the Earth's deformational and gravitational response to a delta function mass load, the response to an arbitrary surface load is obtained by a convolving the impulse response Green's functions with the general load history. A method for exactly computing changes in sea level in response to changing surface masses was developed by Farrell and Clark, 1976, who developed an integral equation to determine sea level change in response to Heaviside-type ice loading for a non-rotating Earth with fixed shorelines. It is in some respects similar to the approach of Peltier, where Green's functions representing the sea level change for a point ice mass are first found, and the general solution is obtained by performing a convolution with with more generalised ice loads. The impulse response formalism of Peltier and the sea level equation of Farrell and Clark make up the foundation of modern GIA modelling, and will be discussed in more detail in the next section.

Significant advances to GIA research since the pioneering works mentioned above have been numerous, and include improvements in the sea level algorithms to include higher order processes that impact sea level, improvements to the ice histories that serve as model inputs, and a general increase in the availability and quality of data with which to test the models.

The original sea level equation of Farrell and Clark, 1976 applies to a non-rotating Earth with fixed shorelines. A treatment for rotation and GIA-induced perturbations to the Earth's rotation vector was developed by Milne and Mitrovica, 1998. Treatments for time-varying shorelines (caused by both direct sea-level changes and by treating grounded marine ice) were developed by Peltier (Peltier, 1994; Peltier, 1998) and Milne and Mitrovica (Milne, 1998; Milne and Mitrovica, 1998; Mitrovica and Milne, 2003). All studies I present in this thesis use the 'generalised' sea-level equation of Milne and Mitrovica that accounts for rotation and time-varying shorelines. A relatively recent refinement to the sea-level equation was developed by Dalca et al., 2013, to account for the isostatic effects of sediment loading. This realistic treatment of sediment loading affects sea level through the sediment load's effect on the gravitational potential and on the solid Earth, and also by displacing water in areas of marine sediment. This more complete theory was applied to the Indus River basin in Pakistan by Ferrier et al., 2015, and to Fennoscandia and the Barents Sea by van der Wal and IJpelaar, 2017. It was found in these studies that the isostatic effects of sediment loading are small but measurable, and so neglecting them may bias inferences based on RSL observations.

The nature of the deformational response of the solid Earth is also a long outstanding research question. The most commonly assumed rheology for the Earth is that of a Maxwell solid, which is a linear combination of a Hookean elastic and Newtonian viscous element. The Maxwell Earth is the simplest rheology that can be assumed that features both elastic and viscous responses, but it is by no means the only possible rheology. For example, an alternative linear rheology is the Burgers rheology, which features both transient and longer term viscous relaxation. Both the Maxwell and Burgers rheologies were recently employed in a study by Caron et al., 2017, who performed an inversion of a global database of RSL records to determine an optimal average Earth viscosity structure in each case (and who found that, in the case of the more complicated Burgers rheology, unique solutions could not always be found).

The alternative to a linear rheology is a non-linear rheology, and laboratory deformation experiments indicate that some mantle rocks deform with power-law rheologies under certain environmental conditions (stress, temperature, etc) (Bürgmann and Dresen, 2008), which is something I will discuss more in Chapter 2 in the context of the ductile structure of the lithosphere. Power-law rheologies have been used in GIA studies, notably by Patrick Wu and collaborators (Wu, 1995; Wu, 2002), as well as composite models featuring both linear and non-linear rheologies depending on the stress state (van der Wal et al., 2010). Moreover, even within the context of a Maxwell rheology, there are many approaches to modelling the viscous structure of the Earth. The most common method is to assume spherical symmetry, so that the viscous structure varies only with depth, and parametrizing viscosity with depth with a number of layers of constant viscosity. In such cases the outermost layer, representing the lithosphere, typically has a viscosity many orders of magnitude greater than that of the underlying mantle to enforce elastic behaviour in this layer. Several Maxwell models with laterally varying viscosity (so that spherical symmetry is no longer assumed) have also been developed (e.g., Latychev et al., 2005; Paulson et al., 2005). Three-dimensional Earth models are more realistic, but come with an increase in complexity and computation time. These models are particularly important in regions that are known to feature significant lateral variation in viscosity structure. For example, the West Antarctic Ice Sheet is supported by a relatively thin lithosphere and relatively hot and low viscosity mantle beneath the lithosphere, while the East Antarctic Ice Sheet is supported by a thicker lithosphere and colder, more viscous upper mantle (Morelli and Denesi, 2004). Comparisons of 1D and 3D Maxwell GIA models in Antarctica by van der Wal et al., 2015 indicate that models with lateral structure can better satisfy GPS data, and significantly affect estimates of mass loss when used to correct GRACE gravity data. An analysis by A et al., 2013 demonstrated that, with the Canadian RSL data used to constrain global average 1D viscosity models such as VM2 (Peltier, 2004), the resulting viscosity profile is more representative of a Canadian average viscosity profile than an accurate global average viscosity profile. Finally, in a 3D model such as that of Latychev et al., 2005, the lateral structure is obtained by converting a global seismic velocity model to a global temperature distribution, and then using that temperature distribution to compute viscosity variations with respect to a background 1D viscosity structure. This therefore makes the assumption that viscosity variations are related only to temperature variations (and not, for example, changes in bulk composition), and also makes the 3D model results sensitive to the choice of seismic velocity model.

A fundamental issue in GIA modelling is that RSL records are the key observational constraints of GIA models, and they are sensitive to both the viscosity structure of the Earth and to the ice history. This means that when a GIA study finds a certain Earth viscosity structure that best fits the data, it is generally understood there is a caveat that it assumes a given ice history.

There are three general approaches to constrain Earth and ice components of GIA models. The first is to use a data source or parametrization that is insensitive to either the ice load or the Earth viscosity structure to constrain one input independently of the other. One example is the postglacial decay time mentioned in Section 1.2 and discussed further in Chapter 4, which are generally less sensitive to the assumed ice history than they are to the Earth's viscosity structure (Mitrovica et al., 2000). For example, the widely used ice and viscosity models of Peltier, such as ICE5G and VM2 (Peltier, 2004) are developed by first determining the viscosity structure, partially by constraining with the decay times in Hudson Bay and Fennoscandia. Once the Earth viscosity structure is determined, then the ice history can be iterated on to satisfy global RSL constraints. For example, Peltier's ICE4G ice history was further refined to the ICE5G history largely in order to satisfy updated far-field sea level data that constrained total ice volume (Peltier, 2004). Another method to minimize sensitivity to uncertainties in the ice history are differential sea-level highstands. In locations far-removed from formerly glaciated areas (far-field sites), the largest sensitivity is to the local ocean load. By taking the difference in RSL from nearby far-field sites the sensitivity to the ice load is reduced (Nakada and Lambeck, 1989). These methods allow for the regional Earth viscosity structure to be estimated semi-independently of the ice history.

A second approach to determining ice or Earth model components is by a joint inversion for both model components simultaneously (e.g. Lambeck et al., 2014, Caron et al., 2017). In this type of approach, an initial global ice configuration and Earth viscosity are assumed, and then scaling parameters are assigned to components of the ice history (for example, to each individual ice sheet). The RSL data can be separated into far-field data used to constrain Earth rheology and ice volume, and near-field data used to constrain the individual ice sheets (and therefore refine the scaling parameters). Combinations of scaling parameters and Earth viscosity are found that minimize the misfit with RSL data. This is the approach used to develop the Australian National University (ANU) ice history (Lambeck et al., 2014).

The two methods described above are fairly similar, and a potential flaw in both is that they are generally not constrained to satisfy ice physics, beyond being forced to satisfy ice extent data (and in the case of the ANU history, that the ice profiles be parabolic). The ICE-NG models are essentially hand-tuned to minimize misfits with global RSL data, and the ANU model is scaled to do the same thing, and as a result there is no guarantee that the final ice models would be consistent with the behaviour of actual physical ice sheets in a realistic climate scenario. The third method to obtain ice histories for GIA models, then, is to use output from glaciological models. A glaciological model computes ice dynamics, growth, and ablation, in response to an applied climate forcing. Glaciological modelling can be computationally expensive, particularly over a full glacial cycle, but in recent years more glacial cycle reconstructions have become available to GIA modelers. For example, during my undergraduate studies I had the opportunity to evaluate reconstructions of the British-Irish Ice Sheet developed by Hubbard et al., 2009 by using them as input into a GIA model and comparing resultant RSL predictions with available data (Kuchar et al., 2012). A large ensemble of reconstructions of the North American Ice Sheet has been developed by Tarasov et al., 2012, many of which have since been used as inputs in GIA studies (e.g. Love et al., 2016, and Chapters 3 and 4 of this thesis). Even with glaciological model output, the feedback between Earth viscosity models and ice models remains an important issue, because a glaciological model requires an assumed model of Earth deformation, as ice dynamics are sensitive to basal geometry and sea level. The reconstructions of Tarasov et al., 2012 assumed the VM5 (Peltier and Drummond, 2008) viscosity model, and Earth viscosity was identified by the authors as a key model uncertainty in their conclusions. There has also been a push within the last decade to couple glaciological and GIA models to model marine ice sheets on long time scales (e.g. Gomez et al., 2012, Pollard et al., 2017). The interface between the ice sheet and the floating ice shelves, and in particular the behaviour of the grounding line (the edge of the grounded portion of the ice sheet) is an important control for the mass-balance of an ice sheet, as most mass is lost as ice flow through this boundary (Schoof, 2007). The amount of ice flux at the grounding line increases with ice depth, which results in the marine ice-sheet instability: a marine ice sheet on a reverse sloping bed is naturally unstable because as the ice sheet loses mass and recedes at the grounding line, the depth to the grounding line, and therefore the flux, increases, triggering a still more rapid mass loss. Results of coupled GIA-glaciological models, however, indicate that the GIA response may act to counter the instability. This is because, as the ice sheet loses mass at the margins, the local sea level falls by a combination of a weakening of the direct gravitational potential and uplift of the solid surface of the Earth (Gomez et al., 2012). While glaciological models typically feature simple Earth deformation subroutines, they generally do not include a treatment of local sea-level in response to global ice changes, which, through its impact on the grounding line depth, may be important for modelling ice sheets in the transition from LGM to present-day.

1.3 The Maxwell Rheology and the Correspondence Principle

Before we can compute Earth deformation we need a constitutive equation to describe how a model Earth would respond to stress. The simplest model of deformation is that of a Hookean elastic, where the strain is proportional to the applied stress:

$$\sigma_{ij} = \lambda \epsilon_{kk} \delta_{ij} + 2\mu \epsilon_{ij}. \tag{1.1}$$

In the above equation strain ϵ_{ij} and stress σ_{ij} are directly related through the material constants λ and μ. An elastic material is deformed immediately in the presence of an applied stress, and recovers totally immediately upon the removal of that stress. This makes the Hooke model insufficient to describe the Earth, which exhibits viscous relaxation over long timescales (approximately 100 years).

The simplest model of viscous deformation is that of a Newtonian fluid, which behaves hydrostatically when the body is at rest, but that has a linear relationship between applied stress and strain rate. If we consider only the deviatoric component of the stress and strain rate, then a Newtonian fluid is described by

$$\sigma'_{ij} = 2\eta \dot{\epsilon_{ij}}', \tag{1.2}$$

where η is the Newtonian viscosity and the primes denote this is the deviatoric component (which is what is left over when you remove the hydrostatic component). Unlike an elastic material, a viscous material will not experience recovery after the removal of a load. In fact, it is easy to see that when a constant stress is applied, the strain will increase linearly, and upon removal of the stress the strain will remain at its maximum obtained value.

The simplest model of viscoelasticity is a linear combination of a Hooke elastic and a Newtonian viscous element, and this is what is called a *Maxwell* material. A

Maxwell solid is described mathematically by

$$\dot{\epsilon_{ij}'} = \frac{\sigma_{ij}'}{2\eta} + \frac{\dot{\sigma_{ij}}'}{2\mu} \tag{1.3}$$

A Maxwell material exhibits the instant elastic deformation of a Hookean material and the linear stress-strain rate relationship of a Newtonian viscous material. After unloading, it will entirely recover the elastic component of the deformation, but not the viscous component. If the strain is held constant, then the solution to the Maxwell rheological equation is

$$\sigma'(t) = \sigma_0' e^{-\frac{\mu}{\eta}t} \tag{1.4}$$

which defines the Maxwell time, $t_M = \frac{\eta}{\mu}$. The Maxwell time describes the time above which a material will behave primarily viscously, and below which primarily elastically. Using reasonable values for the viscosity and rigidity of mantle rocks, we obtain a Maxwell time on the order of thousands of years, which is the same as the characteristic time scale of GIA.

A key feature of a Maxwell material is its application in the Correspondence Principle (Peltier, 1974). This states that the Laplace transform of the constitutive equation for a Maxwell material results in that for an elastic material in the domain of the Laplace transform variable. To see that this is true, consider a Maxwell material described by

$$\dot{\sigma_{ij}} + \frac{\mu}{\eta}\left(\sigma_{ij} - \frac{1}{3}\sigma_{kk}\delta_{ij}\right) = 2\mu\dot{\epsilon_{ij}} + \lambda\dot{\epsilon_{kk}}\delta_{ij}, \tag{1.5}$$

which (unlike equation 1.3) accounts for both deviatoric and hydrostatic stress. The Laplace transformed version of equation 1.5 is

$$\tilde{\sigma_{ij}}(s + \mu/\eta) - \frac{\mu}{3\eta}\tilde{\sigma_{kk}}\delta_{ij} = 2\mu s\tilde{\epsilon_{ij}} + \lambda s\tilde{\epsilon_{kk}}\delta_{ij}. \tag{1.6}$$

We can take the trace of equation 1.6 to get an expression for $\tilde{\sigma_{kk}}$, which gives us

$$\tilde{\sigma_{kk}} = (2\mu + 3\lambda)\tilde{\epsilon_{kk}}. \tag{1.7}$$

Now we can substitute equation 1.7 into equation 1.6, and rearrange, giving us

$$\tilde{\sigma_{ij}} = \frac{2\mu s}{s+\mu/\eta}\tilde{\epsilon_{ij}} + \frac{\left[\lambda s + \frac{\mu}{3\eta}(2\mu+3\lambda)\right]}{s+\mu/\eta}\tilde{\epsilon_{kk}}\delta_{ij}, \tag{1.8}$$

which is equivalent to the description of an elastic material (1.1), with the material parameters μ and λ now functions of the transform variable s:

$$\begin{aligned}\mu(s) &= \frac{\mu s}{s+\mu/\eta} \\ \lambda(s) &= \frac{\left[\lambda s + \frac{\mu}{3\eta}(2\mu+3\lambda)\right]}{s+\mu/\eta}.\end{aligned}$$

Therefore to solve a given Maxwell problem, we can instead transform to the Laplace domain and solve the elastic problem for many values of s, and then transform back.

1.4 Deformation of a Maxwell Earth

The details of the impulse response formalism can be found in numerous sources (e.g. Peltier, 1974; Wu and Peltier, 1983), and so here I review only the fundamental aspects of the theory necessary for context.

For a spherical, self-gravitating Earth, the field equations describing the conservation of momentum and the gravitational field are:

$$0 = \nabla\cdot\sigma - \nabla(\vec{u}\cdot\rho_0 g_0\vec{e_r}) - \rho_0\nabla\phi_1 - \rho_1\nabla\phi_0 \tag{1.9}$$

$$\nabla^2\phi_1 = 4\pi G\rho_1 \tag{1.10}$$

$$\nabla^2\phi_0 = 4\pi G\rho_0 \tag{1.11}$$

$$\rho_1 = -\nabla\cdot(\rho_0\vec{u}). \tag{1.12}$$

In equations 1.9 - 1.12, σ is the stress, ρ is the density, $\vec{u}$ is the displacement, ϕ is the gravitational field, g is the gravitational acceleration, and subscript zero denotes the equilibrium fields and subscript one denotes the perturbations to those fields, and $\vec{e_r}$ denotes the unit vector in the radial direction. The density perturbation ρ_1 is obtained through the linearized continuity equation (1.12), and is then used to determine the perturbation to the gravitational field by the Poisson equation (1.10). In equation 1.9, the first term is the gradient of the stress field, the second term is known as the advection of the pre-stress, and represents perturbations to the equilibrium state caused by initial elastic displacements through the background hydrostatic stress field, and the third and fourth terms are the perturbed gravity field acting on the equilibrium density field and the background gravity field acting on the perturbed density field. The stress in equation 1.9 can be converted to strain using the Maxwell constitutive equation, and the density perturbation ρ_1 can be expressed in terms of displacements via equation 1.12. Then Laplace transformed versions of equations 1.9 and 1.10 are solved for many values of the Laplace transform variable s, and transformed back. The problem to be solved is for a point mass placed on the surface. Because the load is a point load, it is reasonable to look for solutions with spherical symmetry. We therefore look for solutions of the form

$$U^G(a, \theta, t) = \sum_{l=0}^{\infty} u_l(a, t) P_l(\cos\theta) \tag{1.13}$$

$$V^G(a, \theta, t) = \sum_{l=0}^{\infty} v_l(a, t) P_l(\cos\theta) \tag{1.14}$$

$$\phi_1^G(a, \theta, t) = \sum_{l=0}^{\infty} \phi_{1,l}(a, t) P_l(\cos\theta) \tag{1.15}$$

where U^G and V^G are the impulse responses of the radial and tangential components of the displacement (and are therefore Green's functions of these quantities for the generalized load case, which we highlight by labelling with the superscript G), a is the radius of the Earth (as the measurable displacements we are interested in are those of the Earth's surface), P_l are the Legendre polynomials, and θ is the angle between the load and observation point. For a Maxwell Earth, the amplitudes are defined in terms of an immediate elastic response and a time-dependent viscous response:

$$u_l = u_l^E \delta(t) + \sum_{k=1}^{N} \delta u_k^l e^{-s_k^l t} \tag{1.16}$$

$$v_l = v_l^E \delta(t) + \sum_{k=1}^{N} \delta v_k^l e^{-s_k^l t} \tag{1.17}$$

$$\phi_{1,l} = \phi_{1,l}^E \delta(t) + \sum_{k=1}^{N} \delta \phi_{1,k}^l e^{-s_k^l t} \tag{1.18}$$

The response to an arbitrary load can be obtained by convolving the expressions above with the general load description. Instead of calculating directly the surface variable Green's functions above, what are generally computed are the related surface load Love numbers, defined as

$$h_l(a,t) = \frac{g_0}{\phi_{2,l}} u_l(a,t) \tag{1.19}$$

$$l_l(a,t) = \frac{g_0}{\phi_{2,l}} v_l(a,t) \tag{1.20}$$

$$k_l(a,t) = -\frac{1}{\phi_{2,l}} \phi_{3,l}. \tag{1.21}$$

The Love numbers h_l, l_l, and k_l are associated with the radial and tangential deformation, and gravitational potential, respectively. The perturbation to the gravitational field, ϕ_1, is decomposed into a component due to the surface load, ϕ_2, and a component due to the redistribution of mass within the Earth, ϕ_3. Analogously to the expressions for u_l, v_l, and $\phi_{1,l}$, the Love numbers are expressed as a combination of an elastic component and a sum of exponentially decaying viscous components:

$$h_l = h_l^E \delta(t) + \sum_{k=1}^{N} r_k^l e^{-s_k^l t} \tag{1.22}$$

$$l_l = l_l^E \delta(t) + \sum_{k=1}^{N} q_k^l e^{-s_k^l t} \tag{1.23}$$

$$k_l = k_l^E \delta(t) + \sum_{k=1}^{N} p_k^l e^{-s_k^l t}. \tag{1.24}$$

It should be pointed out here that there are actually two sets of Love numbers computed in this process. The first are the Love numbers in the domain of the Laplace transform variable s (and for example, h_l^E would be one such quantity). The Love numbers in the physical space of the viscoelastic problem are obtained by means of an inverse Laplace transform. While the Laplace domain Love numbers are dimensionless, the transformed Love numbers have the dimension of inverse time (reflecting that the viscoelastic problem is time-dependent). The l component of the Green's function for the load-induced potential perturbation, $\phi_{2,l}$, at the surface of the Earth, is given by $\phi_{2,l} = \frac{ag}{m_E}$ (Longman, 1963). This lets us compute the Green's function for the radial deformation of the Earth's surface, U^G, as

$$U^G(a,t,\theta) = \sum_{l=0}^{\infty} u_l P_l(\cos\theta) = \frac{a}{m_E} \sum_{l=0}^{\infty} h_l P_l(\cos\theta). \tag{1.25}$$

The radial deformation in response to a generalised load $L = L(t, \gamma, \psi)$ (which includes both ice and ocean load components, and has dimensions of mass per area), is then determined by a convolution integral with the point-load response function as

$$U(t,\gamma,\psi) = \int_{-\infty}^{t} \int\int_{\Omega} U^G(t,\theta) L(t-t', \gamma', \psi') a^2 d\Omega' dt'. \tag{1.26}$$

Here we have dropped the superscript G, as once the convolution integral has been performed, we obtain the actual computed radial deformation. The angles γ and ψ are the spherical polar angles, and $d\Omega'$ is the usual spherical polar differential element, $\sin(\gamma')d\gamma'd\psi'$. Once the Love numbers describing the deformation of the Earth and gravitational potential have been found, then in principle we can determine sea level for any arbitrary load history. The issue remaining is that the oceans are self-gravitating, and so the load history L is a function of itself, as well as a function of the response of the Earth. Therefore we will now describe the sea level equation, which describes how to iteratively determine the sea level change in response to a prescribed surface load (such as an ice load) and Earth model.

1.5 The Sea Level Equation

In GIA studies, the particular sea level surface we're interested in is 'static' sea level, which is a time averaged surface such that it approximates an equipotential of the gravity field (i.e. the effects of atmosphere-ocean interaction, ocean circulation and tides are averaged out), and we define the sea level as the height difference between the gravitational potential surface describing the upper surface of the ocean (known as the geoid) and the solid surface of the Earth,

$$SL(t, \gamma, \psi) = G(t, \gamma, \psi) - R(t, \gamma, \psi). \tag{1.27}$$

In the above, G is the height of the gravitational potential surface that defines the geoid, and R the solid surface of the Earth. With this definition, sea level, SL, is defined globally, and ocean depth is the projection of sea level over the oceans,

$$S(t, \gamma, \psi) = C(t, \gamma, \psi) SL(t, \gamma, \psi), \tag{1.28}$$

where C is the ocean function, defined to be unity over the oceans and zero otherwise.

Changes to the height of the solid surface, R, and to the gravitational potential surface G, in response to a surface load L, can be found using the impulse response formalism described in the previous section. Specifically, if we denote the radial deformation and gravitational potential Green's functions in response to a point load as U^G and Γ^G, then the perturbed height of the gravitational potential relative to the solid surface is

$$SL^*(t, \gamma, \psi) = \int_{-\infty}^{t} \int \int_{\Omega} L(t', \gamma', \psi') \left(\frac{\Gamma^G(t - t', \gamma', \psi')}{g} - U^G(t - t', \gamma', \psi') \right) a^2 d\Omega' dt'. \tag{1.29}$$

However, while this describes the change in the equipotential due to the surface loading, it is not the particular equipotential surface describing sea level because it does not account for the volume changes of the ocean in response to the mass transfer between the ice-sheets and oceans, or for deformations in the sea floor that change the volume of the ocean basin. For any equipotential surface G^*, $G = G^* + c$ is also an equipotential for any constant c. This constant c is determined by accounting for the volume change described above. The correction for the volume change associated with the mass transfer (which may be called the eustatic meltwater component) is simply

$$c_{mw} = -\frac{M_I}{\rho_w A_o}, \tag{1.30}$$

where M_I is the mass change of the ice sheets at that time step, ρ_w is the density of water, and A_o is the area of the ocean at that time step. This change is negative because a positive change in ice mass represents a decrease in the height of the ocean surface. The height change associated with the volume change of the ocean basins due to deformation (which may be called the eustatic deformation component) is simply the average over the oceans of SL^*. If we use $*$ to denote convolution, then the full expression to determine the change in ocean depth at a time t is

$$S(t,\gamma,\psi) = C(t,\gamma,\psi)\left(L * (\frac{1}{g}\Gamma^G - U^G) - \frac{M_I}{\rho_w A_o} - \left\langle L * (\frac{1}{g}\Gamma^G - U^G)\right\rangle_o\right) \tag{1.31}$$

where the angled brackets denote a spatial average and the subscript o indicates that the average is over the oceans. This is the full sea-level equation of Farrell and Clark, 1976, which exactly describes sea level change in response to ice growth or melting episodes for a viscoelastic Earth with fixed shorelines. The final complication we may observe is that this is in fact an integral, or implicit, equation. This is because the surface load L is a combination of ice and ocean loads, and may be written more explicitly as

$$L(t,\gamma,\psi) = \rho_w S(t,\gamma,\psi) + \rho_i I(t,\gamma,\psi), \tag{1.32}$$

where $I(t,\gamma,\psi)$ is the height of the ice at a given location and time, and ρ_i is the density of ice. Therefore the quantity we're interested in is explicitly a function of itself. In practice, the sea level equation is solved iteratively, where the first guess is the eustatic sea level, and this is used in equation 1.31 to obtain a refined estimate. The process is then repeated until the computed sea level converges.

The rheology of the mantle in the long time range can be studied by analysing geodynamic processes in which steady-state flow is thought to play an important role (i.e., mainly, but not exclusively, postglacial rebound), or by extrapolating to mantle conditions theoretically established and when possible experimentally controlled, creep equations for relevant mantle materials...
In an ideal situation, their results should be identical. Such an ideal state of affairs, however, does not apply. The fact that both approaches involve unverified assumptions and considerable uncertainties, already worrisome per se, is made more disturbing by the divergence of their results.

Ranalli and Fischer, 1984

2

Incorporating Ductile Structure in the Lithosphere

So far we have developed the framework necessary for computing RSL and Earth deformation on a spherically symmetric Maxwell Earth. The assumption of spherical symmetry means that the viscosity structure we assume for the Earth can vary with depth only. These are essentially one dimensional spherical Earth models. However, even with the constraint of a single dimension, there is a lot of potential variation and uncertainty in defining the depth-dependent viscous structure of the Earth. The quote that opens this chapter, by Ranalli and Fischer, refers to the divergence of predictions of mantle rheology according to either a macro-scale geodynamics approach such as GIA modelling or a micro-scale physical approach based on solid state physics and laboratory-derived stress-strain relationships of polycrystals and rocks. In this chapter our concern is primarily the behaviour of the lithosphere rather than the mantle, but we will see that the same issue applies.

The most commonly assumed Earth viscosity structure in studies of GIA is one where the viscosity of the Earth is parameterised by discrete layers with a very high viscosity lithosphere (Peltier, 1974, suggests a lithosphere 20 orders of magnitude more viscous than the mantle), and the mantle broken into an upper and lower mantle component, with the upper mantle extending from the base of the lithosphere to the 670km seismic discontinuity, and a lower mantle extending from 670km to the core mantle boundary. This way the Earth viscosity structure is parametrised by the triplet $(LT, \eta_{\mathrm{UM}}, \eta_{\mathrm{LM}})$, with lithospheric thickness LT, and upper and lower mantle viscosities η_{UM} and η_{LM}. This sort of parametrisation is used in the vast majority of numerical GIA studies, e.g., Peltier and Tushingham, 1991; Fleming et al., 1998; Shennan et al., 2006; Milne and Mitrovica, 2008; Caron et al., 2017 (along with all the material presented in this thesis aside from the present chapter). We might therefore ask how reasonable a parametrisation it is, and what might be the consequences of assuming its validity? In particular, if a model-data comparison suggests that the data are satisfied by an effectively elastic lithosphere of a given thickness, what does this imply for the actual physical lithosphere of the Earth?

In these sorts of models, by incorporating a lithosphere of such high viscosity ($\approx 10^{42}$ Pa s), the Maxwell time (introduced in Section 1.2.1) of the lithosphere will be such that it never experiences ductile behaviour on typical GIA timescales. While the rheology is visco-elastic, by choosing such a large viscosity for the lithosphere, the lithosphere simulates an effectively elastic plate resting on top of a viscoelastic mantle. The primary value in this parametrisation is in its simplicity, characterising the Earth by only three values. However, the drawback, as we will illustrate, is that the lithosphere is not well represented by an elastic plate.

In this chapter I describe incorporating more realistic viscous structure into the lithosphere component of 1-D Maxwell Earth models than has typically been used in the past. In Section 2.1 we will motivate our search for a better viscosity model by first discussing the rheology of the lithosphere, and then considering how it has been treated in GIA studies. In Section 2.2 I will present the physics of the deformation of lithosphere rock as described by creep equations with temperature dependence, and in Section 2.3 I will describe how it is then implemented into our GIA model. Finally, in Section 2.4 I will summarise the research we carried out with the more realistic lithosphere models we developed, and in Section 2.5 I present the published manuscript.

2.1 The Rheology and Strength of the Lithosphere

Recall the Kola Superdeep Borehole discussed in the Introduction. It is only approximately 12 km deep, and yet its max temperature may exceed 600 °C and the pressure 150 MPa. This large vertical temperature gradient within the lithosphere leads to a fundamental behaviour change from cold and brittle near the surface of the Earth to hot and ductile (Bürgmann and Dresen, 2008), with a zone of transition (the aptly-named Brittle-Ductile Transition Zone) between them. In the brittle regime, the dominant response to stress is to fail by fracture, and the strength of the rock is governed by the friction and stress state. In the ductile regime, creep (slow flow) becomes the dominant response to stress, and is primarily a function of temperature and physical characteristics and composition of the rock. The constitutive equations describing ductile flow by creep can be either linear (and therefore compatible with a Maxwell rheology) or non-linear, and in general depend on stress, temperature, pressure, and various material and state variables such as elastic parameters, grain size, and number of lattice dislocations (Ranalli, 1995).

The criterion for brittle fracture along a fault can be expressed by (Ranalli, 1995)

$$\sigma_D = \alpha \rho g z (1 - \lambda), \tag{2.1}$$

where σ_D is the differential stress, α is a parameter related to fault geometry, ρ is average density, g is the gravitational acceleration, z is the depth, and λ is a pore fluid factor. This describes the necessary differential stress for brittle failure. Note that it's an increasing linear function of depth, but that it is also not a constitutive equation. It does not relate stress and strain, it merely tells you at what stress fracture will occur. It also has no dependency on temperature or other properties of the crustal rock, only on the lithostatic pressure $\rho g z$.

Rocks in the lithosphere may also deform through ductile flow, which is governed by creep. In general, steady-state creep in experimental conditions is generally well described by a function of the form (Bürgmann and Dresen, 2008):

$$\dot{\epsilon} = A\sigma^n d^{-m} f_{H_2O}^r e^{-\frac{Q+pV}{RT}}, \tag{2.2}$$

where Q is the activation energy, p and V are pressure and volume, R is the gas constant, T is temperature, d is grain size, f_{H_2O} is the water fugacity, A is a material constant, and n, m, and r are the stress, grain size, and fugacity exponents, respectively. It is a strong function of both stress and temperature. We can define the strength of the lithosphere at a given depth to be the stress at which it will deform either by fracture or ductile flow, which will be the minimum of the brittle fracture criteria or the ductile flow criteria. This allows us to compute lithosphere strength profiles, with an example shown in Figure 2-1.

The dominant creep mechanisms in the lithosphere and mantle are dislocation creep and diffusion creep. Diffusion creep is the diffusion of atoms and vacancies either within a lattice or across grain-boundaries. Dislocation creep is the movement of dislocations (which are defects or irregularities) through a lattice. With reference to equation 2.2, diffusion creep is linear in the stress dependence ($n = 1$), and exhibits a strong grain-size dependence ($m = 2$ for lattice diffusion and $m = 3$ for grain-boundary diffusion). Dislocation creep, on the other hand, is a non-linear ($n = 2 - 6$) function of stress that depends weakly on grain size ($m = 0$) (Bürgmann and Dresen, 2008). While it is not typically framed that way, the assumption that the Earth has a Maxwell rheology is equivalent to assuming that diffusion creep is the dominant flow mechanism throughout the Earth (Wu and Wang, 2008). However, the dominant creep mechanism may be either diffusion or dislocation creep depending on material,

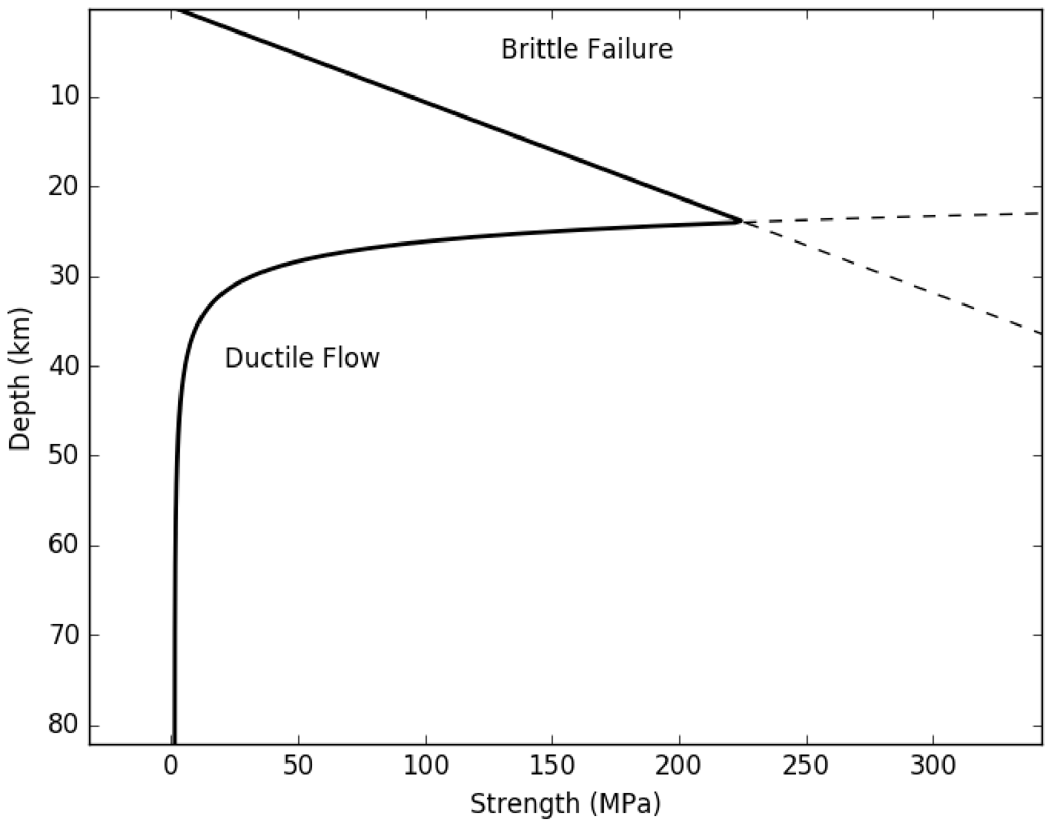

Figure 2-1: An example of a computed strength envelope for oceanic lithosphere. The brittle and ductile stresses are defined for the entire depth range, and the envelope is defined as the lower stress. The Brittle-Ductile transition is the intersection of the curves (though in reality the brittle-ductile transition is a depth range over which both brittle and ductile failure may occur, and not a single depth value.

temperature, and physical characteristics such as grain size. For example, Bürgmann and Dresen, 2008, show that, assuming a density of 2800 kg m^{-3}, a surface heat flow of 80 mW m^{-2}, and a constant strain rate of 10^{-15} s^{-1}, that dislocation creep is the dominant creep mechanism for wet quartz (a major component of the crust) for the majority of the temperature range of the lithosphere, and for wet feldspar dislocation creep is dominant for grain sizes larger than approximately 100 μm (with diffusion being the dominant mechanism for smaller grain sizes). This suggests that, contrary to most GIA models that employ Maxwell rheologies, a non-linear rheology is best-suited to modelling the deformation of the lithosphere. However, the fact is that determining what creep mechanism is dominant in different depth and temperature regimes in the Earth is an ongoing question. A review by Karato and Wu, 1993, that synthesised laboratory and postglacial rebound data concluded that the shallow mantle may flow by dislocation creep, with the deep mantle flowing by diffusion creep. However, these conclusions were criticised by Fei et al., 2016 on the basis that they overestimated the effects of water and pressure on creep rates, and instead concluded from silicon grain-boundary diffusion rates that in fact the opposite scenario is true, namely that diffusion creep dominates at low pressures and low temperatures, and dislocation creep at higher pressures and higher temperatures.

We have been discussing the strength of the lithosphere, which is given by the differential stress at failure, but the relevant quantity in GIA studies is the viscosity. The viscosity of a Newtonian or Maxwell material at a constant strain rate is defined by the ratio $\eta = \frac{\sigma}{2\dot{\epsilon}}$, and because for a linear rheology the stress and strain rate are proportional, this results in a constant viscosity. However, for a power law rheology this is no longer the case, and the effective viscosity becomes dependent on the stress state. These are two fundamentally different ways to consider viscosity (i.e., as a constant parameter that describes Earth deformation to a function of the forces causing that deformation). The scale of the differential stress in the lithosphere is typically hundreds of MPa, which when assuming a strain rate of $\dot{\epsilon} = 10^{-15}$ s^{-1} leads to viscosities on the order of 10^{23} Pa s, which is a far cry from the 10^{40} Pa s or greater viscosities often assumed in elastic plate lithosphere models in many GIA studies.

Examples of the sorts of viscosity structures that have been prescribed to the lithosphere in GIA studies are shown in Figure 2-2. The most common way to model the lithosphere is as a single very high (essentially elastic) viscosity layer, such as VM2 (Peltier, 2004) in Figure 2-2. However, because the VM2 model could not satisfy vertical and horizontal land motion rates recorded by VLBI (very long baseline interferometry) and GPS measurements, Peltier and Drummond, 2008 introduced VM5, which has a 60 km thick elastic layer overlying a 40 km thick layer of 10^{22} Pa s, which they note is justified as the strong temperature gradient in the lithosphere should lead to lower viscosities with depth. Perhaps a better treatment is that of

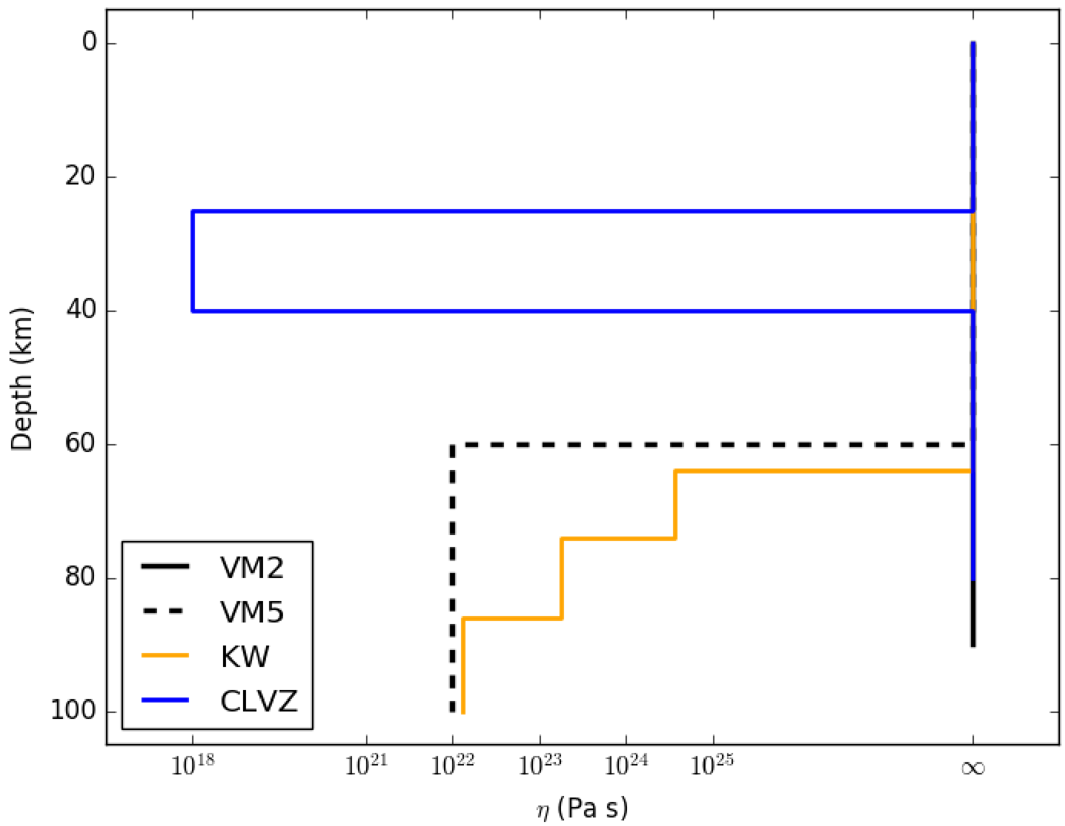

Figure 2-2: Examples of viscosities prescribed to the lithosphere from the literature. The VM2 model (Peltier, 2004) has a lithosphere of thickness $h = 90$ km with an 'infinite' viscosity (η on the order of 10^{40} Pa s). The VM2 type of lithosphere with a single very high viscosity layer is the simplest and commonly used. The VM5 model was introduced by Peltier and Drummond, 2008, which is essentially VM2 with the lower 40 km reduced to 10^{22} Pa s. An example of a more complex lithosphere model is that of Klemann and Wolf, 1998, denoted KW, which features progressively lower viscosities in the lithosphere with depth. The CLVZ model (DiDonato et al., 2000; Kendall et al., 2003) is one where a 15 km thick crustal low viscosity zone is inserted into an otherwise elastic lithosphere.

Klemann and Wolf, 1998 (denoted KW in Figure 2-2), who consider a model described by a 64 km thick elastic layer overtop several layers with progressively lower viscosity, from 5.7×10^{24} Pa s to 1.2×10^{22} Pa s, to a depth of 100 km (though in contrast to the other models mentioned, Klemann and Wolf, 1998 used a linear viscous half-space model, and not a full spherical treatment of the Earth). The more complex lithosphere model employed by Klemann and Wolf compared to that of Peltier and Drummond largely reflects the goals of each - VM5 is a global model meant to approximate the average viscosity structure of the entire Earth, whereas the KW model was used to investigate stresses in the lithosphere in Fennoscandia in response to postglacial loading. The final lithosphere model shown in Figure 2-2 is the model featuring a crustal low viscosity zone (CLVZ in Figure 2-2), a thin layer of very low viscosity embedded in an otherwise elastic lithosphere. The example shown in Figure 2-2 is that of DiDonato et al., 2000 and Kendall et al., 2003, but similar models were also considered by Wu, 1997 and Klemann and Wolf, 1999. In such models the lithosphere may exhibit ductile behaviour on GIA time scales, but only within a narrow region. Such models are justified physically on the basis that, depending on the composition of the lithosphere, there may be one brittle-ductile transition (as shown in the strength envelope in Figure 2-1), or else several layers, which would result in a ductile layer sandwiched between two brittle layers (Rannalli and Murphy, 1987, Bürgmann and Dresen, 2008).

A common characteristic of both the models featuring lower viscosity zones underneath an elastic lithosphere, such as the KW model, and those featuring a CLVZ, are that the effective elastic thickness is significantly reduced. Additionally, for the KW model it was observed that the impact of the ductile layers was greater over cycles of repeated glaciation, whereas a purely elastic layer will reach equilibrium between load cycles. This indicates a time dependence to the load history in the models featuring lithosphere ductile structure that is otherwise absent.

In the next section I develop my own model of lithosphere viscosity with structure informed by the creep equation (equation 2.2) and realistic temperature profiles.

2.2 Developing a Ductile Lithosphere Model

Our goal is to develop a lithosphere strength profile that has more in common with the strength envelope shown in Figure 2-1 than most of the viscosity profiles used in previous GIA studies shown in 2-2. To do this, our starting point is a creep equation (such as equation 2.2). The particular equation we use is

$$\dot{\epsilon} = A_D \sigma^n e^{-\frac{E_D}{RT}}, \tag{2.3}$$

which is similar to equation 2.2 with the key difference that we have dropped the dependence on grain size as we assume primarily dislocation creep in the lithosphere. Dislocation creep is a power law rheology, which means that the effective viscosity, if defined the same way as the Newtonian viscosity as $\eta = \frac{\sigma}{2\dot{\epsilon}}$, is actually a function of the stress. This leads to an inconsistency that we should note in our modelling approach, which is that we are applying a (linear) Maxwell model of Earth deformation, but using a power-law rheology to obtain our initial viscosity profile.

By using the Newtonian viscosity definition, we can obtain an expression for the viscosity as

$$\eta = \frac{1}{2}\left(\frac{\dot{\epsilon}^{1-n}}{A_D}\right)^{1/n} \exp\left(\frac{E_D}{nRT}\right), \tag{2.4}$$

which is a function only of material parameters such as the creep constant A_D and the creep exponent n, and the temperature, assuming a constant strain rate. The constant strain rate we assume is $\dot{\epsilon} = 10^{-15}$ s^{-1}, which may stand out as a very small number. To see that it is appropriate for the GIA process, we will do a quick order of magnitude calculation. Considering Earth deformation in Canada within the last 10 thousand years, deformation on the order of 10^2 metres over a time scale of 10^4 years is about right for Hudson Bay. The depth of the deformation is expected to reach the lower mantle, which is a depth of order 10^3 km. This deformation over this depth gives a strain of around 10^{-4}. This strain occurs over 10^4 years, which is approximately 10^{11} seconds, which finally gives us a strain rate on the order of 10^{-15} s^{-1}.

To obtain a lithosphere viscosity profile with depth, we first need a temperature profile. For lithosphere temperature, we assume radiogenic heat production within the lithosphere that is an exponential decreasing function of depth (Furlong and Chapman, 2013)

$$A(z) = A_0 e^{-z/h}, \tag{2.5}$$

where A is the radiogenic heat production per unit volume, A_0 is the value at $z = 0$, and h is a scaling parameter (usually around 10 m). To determine the temperature throughout the lithosphere, we apply Fourier's law,

$$q = -k\frac{\mathrm{d}T}{\mathrm{d}z}, \tag{2.6}$$

where q is the material's heat flux and k is the conductivity. If we consider a thin slab of thickness δz, then the net flux through the slab is

$$q(z) - q(z - \delta z) = \delta z\frac{\mathrm{d}q}{\mathrm{d}z} = -k\frac{\mathrm{d}^2T}{\mathrm{d}z^2}\delta z, \tag{2.7}$$

where we have used equation 2.6 to express q in terms of the temperature. The net flux must be equal to the net production inside the slab, which is $A(z)\delta z$. We therefore have the differential equation governing the temperature in the lithosphere is

$$k\frac{\mathrm{d}^2T}{\mathrm{d}z^2} + A(z) = 0. \tag{2.8}$$

This can be integrated twice to give a temperature profile. The first integration is

$$-A_0he^{-z/h} + k\frac{\mathrm{d}T}{\mathrm{d}z} = c_1, \tag{2.9}$$

where the constant of integration c_1 is determined by setting $z = 0$, so that $c_1 = -A_0h + kT_0'$, where T_0' is the surface temperature gradient. The second integration is

$$A_0h^2e^{-z/h} + kT - (-A_0h + kT_0')z = c_2. \tag{2.10}$$

The second constant of integration is once again obtained by setting $z = 0$, so that $c_2 = A_0h^2 + kT_0$, where T_0 is the surface temperature. Our final temperature profile for the lithosphere then is

$$T(z) = \frac{A_0h^2}{k}(1 - e^{-z/h}) + (T_0' - \frac{A_0h}{k})z + T_0. \tag{2.11}$$

In applying this temperature profile, and assuming a surface temperature of zero degrees Celsius and surface temperature gradients of $14-20$ K/km, we obtain the profiles shown in Figure 2-3 (reproduced from Kuchar and Milne, 2015).

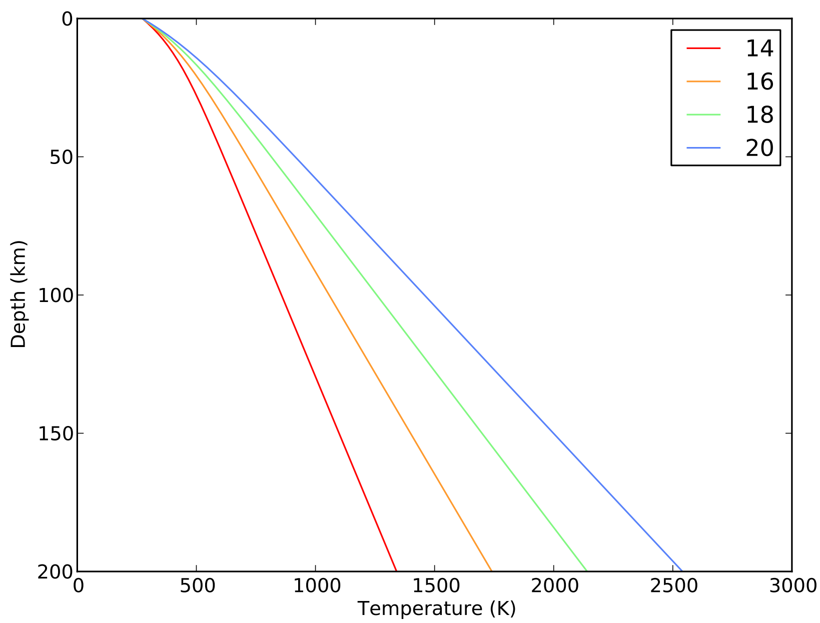

Figure 2-3: Temperature profiles computed using equation 2.11, reproduced from Kuchar and Milne, 2015, computed assuming a surface temperature $T_0 = 273$ K and surface temperature gradient T_0' of $14, 16, 18$, and 20 K/km.

Using these temperature profiles we can calculate viscosity profiles using equation 2.4. To do so we need appropriate material parameters. We divide the lithosphere into two layers, a top quartzite layer and a bottom mafic granulite layer (separated at the Moho, which is a discontinuity in the density and elastic structure of PREM (Dziewonski and Anderson, 1981), the Preliminary Reference Earth Model, which is the global elastic/density model we use) with values taken from the temperature and rheological model of the European lithosphere of Tesauro et al., 2009. The resulting viscosity profiles are shown in Figure 2-4.

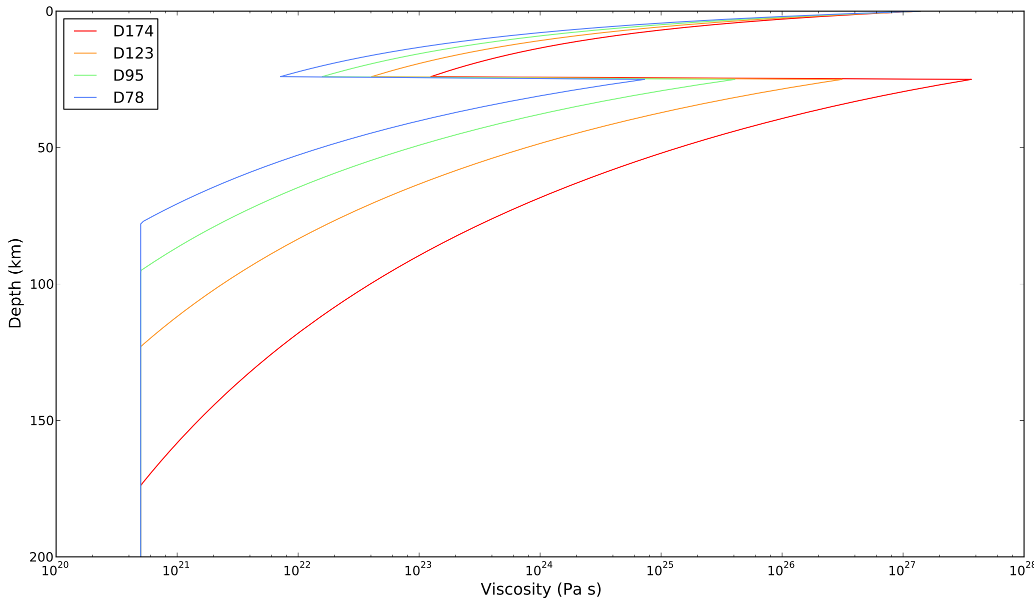

Figure 2-4: Viscosity profiles, corresponding to the temperature profiles shown in Figure 2-3, computed using equation 2.3 and parameters described in Kuchar and Milne, 2015, reproduced from Kuchar and Milne, 2015. The curves are labelled according to their thickness, so for example D123 is a 123 km thick ductile lithosphere model.

The viscosity profiles shown in Figure 2-4 are an improvement over those shown in Figure 2-2, in the sense that they better represent the structure we would expect from lithosphere strength envelopes (as in Figure 2-1). A key difference between the strength envelope and the profiles we have just constructed, however, is that our profiles do not exhibit brittle failure. The reason for this is practical: our model does not have any treatment of faulting or brittle failure, and so it wouldn't make sense to incorporate it into our viscosity structure. An alternative would be to use an infinite viscosity approximation for the cold and brittle regions, as is done for the uppermost layer of the models shown in Figure 2-2. The deformation of the uppermost lithosphere is well described by an elastic model at stresses below those that cause brittle failure (Bürgmann and Dresen, 2008). Our viscous deformation profile at these depths is at a relatively high viscosity, but may still exhibit ductile failure. We decided that ultimately, in the absence of a treatment of brittle failure, ductile failure in the upper lithosphere is preferable to no failure at all, but this decision does lead to complications that will be discussed in the next section.

2.3 Implementation

2.3.1 The Earth Generator Code

In the previous section we developed the viscosity profiles for the lithosphere, however they need to be constructed in a format that we can use to compute the viscoelastic Love numbers. Therefore the first step was to develop a Python code ("Earth Generator", or *EarthGen.py*) where the inputs are a maximum lithosphere thickness L_{Max}, a depth resolution within the lithosphere, the surface temperature gradient T_0', and the upper and lower mantle viscosities η_{UM}, η_{LM}, and the output is a text file with 6 columns: radius r, density ρ, P and S-wave velocities v_p and v_s, gravitational acceleration g, and viscosity η.

Given the input maximum lithosphere thickness and resolution, a list is created of lithosphere depth. The input temperature gradient is used to compute a second list containing a temperature profile throughout the lithosphere using equation 2.11. Lithosphere viscosity is then computed using equation 2.4, with parameters for an assumed quartzite composition above the Moho (24.4 km depth) and mafic granulite below. The code performs a check to see if at any point the viscosity of the granulite layer becomes less than the input viscosity of the upper mantle - if so, the viscosity at that depth is set to the upper mantle viscosity, and this depth is considered the lithosphere thickness (That is, $L = \min(L_{\text{Max}}, L_{\eta_{UM}})$).

Because the lithosphere viscosity is much more quickly changing than is the case in the rest of the Earth in our model, we typically use a high resolution (1 km) for the lithosphere. Within the rest of the Earth model, the resolution is approximately 10 km. The density and seismic wave velocities are computed from the piece-wise functions defining the PREM model (Dziewonski and Anderson, 1981), and the gravity computed by first integrating the density to obtain the mass for each shell, and then computing $g = \frac{GM}{r^2}$.

The lists containing r, ρ, v_p, v_s, g, and η are then written to an output file in a format that can be read by the existing programs that compute Love numbers. A particular feature of the ductile lithosphere models makes the Love number calculation important to discuss before we move on to the next section.

2.3.2 Love Number Complications

As discussed in the Introduction, the Maxwell response is determined by computing solutions to the momentum, continuity, and Poisson equation in the Laplace transform domain, and assuming the solution radial and tangential displacements and gravitational potential have spherical symmetry and so can be written as spherical harmonic decompositions. Assuming this form of the solution reduces the system of PDE's to a set of coupled ODE's, and so we can write the system of equations as a matrix equation,

$$\frac{\mathrm{d}Y}{\mathrm{d}r} = \mathbf{A}Y \tag{2.12}$$

with solution Y. The general solution that satisfies it is a linear combination of three linearly independent solutions (Peltier, 1974; Peltier, 1985):

$$Y(r, s) = c_1(s)T_1(r, s) + c_2(s)T_2(r, s) + c_3(s)T_3(r, s). \tag{2.13}$$

If a vector C is constructed out of the coefficients c_i, and a matrix $\mathbf{M}$ is constructed with the vectors T_i as columns, then this can be written as

$$Y = \mathbf{M}C. \tag{2.14}$$

Strictly speaking, the general solution Y is a 6 vector, but only three components are independent (Peltier, 1985), and so we apply boundary conditions to only those three elements. We also consider only those components in the vectors T_i, which makes the matrix $\mathbf{M}$ a 3x3 matrix. Representing the three boundary conditions at $r = a$ by the vector B with elements b_i, we have

$$B = \mathbf{M}C, \tag{2.15}$$

and so the coefficients determining the general solution are given by

$$C = \mathbf{M}^{-1}B. \tag{2.16}$$

The inverse of $\mathbf{M}$ can be determined by dividing its adjugate by its determinant, $\mathbf{M}^{-1} = \frac{\mathrm{adj}(\mathbf{M})}{\det(\mathbf{M})}$. The general solution is then determined by (Peltier, 1985)

$$Y(r,s) = \frac{Q(r,s)}{\det(\mathbf{M})} = \frac{\sum_{i,j} \mathrm{adj}(\mathbf{M})_{ij} b_j T_i}{\det(\mathbf{M})}. \tag{2.17}$$

This can then be separated into an elastic component (which is $Y^E = \lim_{s\to\infty} Y$ and a viscous component $Y^V = Y - Y^E$. Then we can write the solution as

$$Y(r,s) = \frac{Q^V(r,s)}{\det(\mathbf{M})} + Y^E. \tag{2.18}$$

Equation 2.18 gives the general solution in the Laplace transform domain, and so we will need to perform the inverse Laplace transform to get the time-dependent solution. Up to this point we've been considering the general solution vector Y, but what are usually computed are the Love numbers h_n, l_l, k_l, which can be written with the same form of expression (Mitrovica and Peltier, 1992), i.e.

$$h_n(s) = \frac{Q_n}{\det(\mathbf{M})} + h_n^E. \tag{2.19}$$

It is equation 2.19 that needs to be inverted to the time domain. We can apply the inverse Laplace transform directly to obtain

$$h_n(t) = \frac{1}{2\pi i}\int_L \frac{Q_n(s)}{\det(\mathbf{M})} e^{st} ds + h_n^E \delta(t). \tag{2.20}$$

If the determinant of $\mathbf{M_n}$ has zeroes s_i^n, then the integral in equation 2.20 can be solved by applying the Residue theorem, giving

$$h_n(t) = \sum_{k=1}^{N} r_k^n e^{s_k^n t} + h_n^E \delta(t), \tag{2.21}$$

where r_k^n are the residues, given by (Mitrovica and Peltier, 1992)

$$r_k^n = \frac{Q_n(s_k^n)}{\frac{\mathrm{d}}{\mathrm{d}s}\det(\mathbf{M})|_{s=s_k^n}}. \tag{2.22}$$

This illustrates the first common method to invert the Love Numbers, which is called the *normal mode* method. The roots of the determinant are found numerically by searching s-space, and the derivative of the determinant numerically estimated by finite difference. A drawback of this method is that, as we do not know in advance where the roots of the determinant may be found (though they are restricted to the negative real axis, Mitrovica and Peltier, 1992), we do not know where to search or when we will have found all (or most) of the roots. In fact, there is a standard check to determine whether enough of the normal modes have been found to perform an accurate inversion, but we will see that it does not actually apply to the viscosity profiles we have constructed.

Regardless of the mantle viscosity profile, if a point mass load is applied and held indefinitely, in the infinite time limit the Earth's response is the same as an Earth with a similar elastic structure but inviscid mantle. Equation 2.21 applies for an instantaneous load, and to obtain the response to a load applied and held indefinitely, we convolve equation 2.21 with a Heaviside function. The result of this convolution is

$$h_n^*(t) = \sum \frac{r_k^n}{s_k^n}(1 - e^{-s_k^n t}) + h_n^E, \tag{2.23}$$

and therefore the long time viscous response is

$$h_n^*(t \to \infty) - h_n^E = \sum \frac{r_k^n}{s_k^n}, \tag{2.24}$$

and so the viscous response in the limit that $t \to \infty$ for each spherical harmonic degree n is simply the sum of the ratios of residues r_k^n to normal modes s_k^n. The same final state can be found without invoking the correspondence principle by solving the equations describing the deformation of an inviscid sphere with the same elastic structure (Wu and Peltier, 1982), and so it is generally possible to compare the Love numbers obtained from the normal mode approach for each spherical harmonic degree to those of an inviscid sphere to determine whether all the normal modes have been found successfully, and such a test is recommended by Mitrovica and Peltier, 1992. However, these tests are valid only for Earth models that feature elastic lithospheres. This is because the test relies on the longtime scale response of a delta function mass, which has effectively infinite density. This infinite density point mass must sink to the center of an inviscid planet (Wu and Peltier, 1982), and it is in fact precisely the elastic layer of the lithosphere that supports this load so that this does not happen. Our own models do not feature anything resembling an elastic uppermost layer, and so we found (unsurprisingly in hindsight) that this test fails for these models. We therefore needed an alternative method to verify our models. To do this, we decided to compute the Love number inversion using an alternative method, and would be satisfied in the inversion if the two methods agreed. There is a second common method to perform the inversion, which is the *collocation* method (Mitrovica and Peltier, 1992) (in fact, there are two collocation methods, *mixed* collocation and *full* collocation, but we will only consider full collocation).

In the collocation method of inversion, the time domain Love numbers are approximated rather than computed, by (Mitrovica and Peltier, 1992)

$$\tilde{h}_n(t) = \sum_{p=1}^{P} R_p^n e^{-\alpha_p t} + h_n^E \delta(t), \tag{2.25}$$

where the Love number spectra is sampled at P points, α_p, in the s-domain. These points have no relationship to the matrix M, and instead are prescribed in advance to typically be equidistantly spaced in $\log(s)$ space. It is shown in Peltier, 1974 that, if the approximation $\tilde{h}_n$ is to minimize the mean square error with the actual Love numbers h_n, then in particular the Laplace transform of the approximation should agree with the true values at least at the collocation points α_q,

$$h_n(s)|_{s=\alpha_q} = \tilde{h}_n(s)|_{s=\alpha_q}. \tag{2.26}$$

Considering only the non-elastic component, the Laplace transform of the approximation, $\tilde{h}_n(t)$ is given by

$$\tilde{h}_n(s) = \sum_{p=1}^{P} \frac{R_p^n}{s+\alpha_p}. \tag{2.27}$$

Using the above expression, then the condition that the Laplace transform of the approximation agree with the true values at the collocation points is expressed as

$$h_n(\alpha_q) = \sum_{p=1}^{P} \frac{R_p^n}{\alpha_q+\alpha_p}. \tag{2.28}$$

Therefore, the misfit between h_n and $\tilde{h}_n$ is minimized by solving (Mitrovica and Peltier, 1992; Peltier, 1974)

$$h_q = \mathbf{X}_{pq} R_p, \tag{2.29}$$

with $h_q = h_n(\alpha_q) - h_n^E$, and $\mathbf{X}_{pq} = \frac{1}{\alpha_p+\alpha_q}$. As there is no need to perform a search through s-space for the appropriate α values and instead they can be prescribed in advance, the collocation method is computationally much faster than the normal mode method. In practice, we generated Love numbers using both methods and compared output RSL to determine whether our results were robust. Typically results agreed to within 5%, which was decided to be an acceptable level of agreement.

2.4 Research Summary and Conclusions

After developing Earth models with ductile structure in the lithosphere, we were interested in determining what impact incorporating such structure would have on inferences of lithosphere thickness. Our modelling approach was to compute Earth deformation for a simple loading scenario where an ice sheet with a parabolic height profile was placed and left for a period of time. We then compared the resulting deformation for several models with ductile lithospheres and for traditional models with elastic plate lithospheres and identical mantle viscosity structures. Additionally, we computed RSL in response to a realistic loading history (given by ICE5G) for the ductile lithosphere models shown in Figure 2-4 as well as for the elastic plate models, at a selection of sites in the near, intermediate, and far field (relative to major glaciation centers).

There were two major results of the analysis. The first, which is perhaps unsurprising, is that the RSL predicted with an elastic lithosphere model of a given thickness is in general similar to that of a significantly thicker ductile lithosphere model. This means that estimates of lithosphere thickness made with elastic lithosphere models likely underpredict the actual lithosphere thickness. The second major result is that when the lithosphere is given ductile structure, its effective elastic thickness (which has various meanings in the literature but here we mean in the sense of the elastic model its results are most similar to) depends on the size of the load as well as the timescale of the response.

2.5 Article 1: The influence of viscosity structure in the lithosphere on predictions from models of glacial isostatic adjustment

Statement of Contribution

The following manuscript is my own written work, detailing research that I carried out under the supervision of Dr. Milne. I developed the ductile lithosphere models by computing the temperature and viscosity profiles, as described in Sections 2.2 and 2.3.1. I then computed all Love numbers and RSL results using programs previously developed in the group of Dr. Milne, and produced all figures.

Journal of Geodynamics 86 (2015) 1–9

Contents lists available at ScienceDirect

Journal of Geodynamics

journal homepage: http://www.elsevier.com/locate/jog

Technical note

The influence of viscosity structure in the lithosphere on predictions from models of glacial isostatic adjustment

Joseph Kuchar[a,*], Glenn A. Milne[b]

[a] Department of Physics, University of Ottawa, Ottawa, Ontario, Canada K1N 6N5
[b] Department of Earth Sciences, University of Ottawa, Ontario, Canada K1N 6N5

ARTICLE INFO

Article history:
Received 21 July 2014
Received in revised form
22 December 2014
Accepted 7 January 2015
Available online 3 February 2015

Keywords:
Glacial isostatic adjustment
Lithosphere structure
Rheology

ABSTRACT

The thickness of the lithosphere inferred in most glacial isostatic adjustment (GIA) modelling studies tends to be significantly thinner than when found through seismic or thermal modelling studies. In those GIA studies, the lithosphere tends to be modelled as a plate of uniform and very high viscosity. We develop and test Earth models that include depth-dependent viscosity in the lithosphere to consider the implications for inferring lithospheric thickness from observed relative sea-level (RSL) changes. We find that when comparing predictions of RSL between the traditional plate lithosphere models and those with viscous structure, the latter produce RSL predictions that most closely resemble those from traditional models that are 10 s of km thinner. The greatest sensitivity to this change in the Earth model is most evident in regions loaded by relatively small ice sheets such as the British Isles. We also find that the effective elastic thickness of the lithosphere models with viscous structure is time-dependent, with thinning by tens of kilometres over a timescale of ~10 kyr.

1. Introduction

The lithosphere's response to stresses associated with various processes on a range of time scales helps shape the form of the Earth around us. The rheological structure of the lithosphere is not well determined in many regions but is essential to understand dynamical processes such as seismic and post-seismic deformation, flexure and isostatic adjustment due to surface loads (such as ice sheets and volcanos), sedimentary basin formation, and inter and intra plate deformation (e.g., Watts et al., 2013; Turcotte and Schubert, 2002). The particular property of the lithosphere that we are concerned with in this study is its thickness.

The thickness of the lithosphere has been estimated through a number of methods, including inversions of gravity and seismic observations (Audet and Mareschal, 2004) and through thermal (Tesauro et al., 2009) and geodynamic modelling – which includes glacial isostatic adjustment (GIA) modelling (Lambeck et al., 1998). The values obtained through these different methods vary widely for a given region as the thicknesses inferred relate to different properties. For example, a recent study inferred lithospheric thicknesses in Europe through seismic constraints on mantle temperatures (Tesauro et al., 2009) and by choosing the 1200 °C isotherm as defining the lithosphere-asthenosphere boundary. In the British Isles region, their inferred depth to this isotherm ranged from less than 100 km off the northwest coast of Scotland to almost 200 km in the North Sea, with an average value around 150 km. In contrast, GIA studies have inferred lithosphere thickness values of 60–90 km (Lambeck et al., 1996; Peltier et al., 2002; Bradley et al., 2009; Kuchar et al., 2012). As another example, a thermal study of the Canadian Shield (Levy et al., 2010) used surface heat flux measurements to infer the thickness of the lithosphere, and they found it varied from 200 km to 300 km. In contrast, GIA studies of the region typically adopt Earth models with lithosphere components around 120 km thick (e.g., Davis and Mitrovica, 1996; Sella et al., 2007). Finally, the effective elastic thickness (EET) of the Canadian Shield lithosphere was estimated to be 30 km to 130 km from Bouguer gravity anomaly data (Audet and Mareschal, 2004). A more detailed summary of lithosphere definitions and thickness estimates is given by Martinec and Wolf (2005), in the context of the Fennoscandian lithosphere.

The differences noted above are a reflection of the fact that the lithosphere thicknesses inferred relate to different properties or timescales. For example, the consistently low thicknesses estimated via GIA modelling are related to how the lithosphere tends to be defined in these models, which is as a region of very high and constant viscosity (often of order 10^{30} Pa s or higher), such that the lithosphere acts essentially as an elastic layer over typical GIA timescales (1–10 kyr). In this way, the inferences made via GIA

* Corresponding author. Tel.: +1 6135525728.
E-mail address: joseph.kuchar@gmail.com (J. Kuchar).

http://dx.doi.org/10.1016/j.jog.2015.01.002

studies are more compatible with the EET estimates from gravity data. We note, however, that the latter tends to result in even lower thickness estimates due to the longer timescales involved when considering this approach (and consequently more time for extensive stress relaxation through ductile failure; e.g., Ranalli, 1995).

The primary goal of this study is to consider how GIA model output is affected when the lithosphere is defined with viscous structure in order to gauge how inferences of lithospheric thickness, based on the typical elastic layer approach, might be affected. More specifically, we consider whether incorporating viscous structure in the lithosphere can result in estimates of this parameter that are more in line with those made using other methods, such as the thermal modelling approach outlined above. For convenience, we refer to the high viscosity lithospheres typical in GIA studies as "elastic lithospheres," with the understanding that they are generally not modelled as being elastic, but rather as having Maxwell rheologies with very high viscosities. In this study we let the strength profile of the lithosphere be determined by temperature and composition, as described by the Dorn equation (see next section).

Previous GIA modelling studies have included lithosphere components with more structure by investigating the influence of a low viscosity region within an otherwise high viscosity lithosphere (DiDonato et al., 2000; Kendall et al., 2003; Klemann and Wolf, 1999), which resulted in a thinning of the lithosphere's EET to approximately the thickness of the lithosphere above the low viscosity zone. This differs from our own approach, which does not limit the ductile behaviour in the lithosphere to a small zone within it. Our approach is more closely aligned with that of Klemann and Wolf (1998) who estimated continuous changes in viscosity with depth associated with temperature-activated creep processes. Some recent studies have considered sub-crustal viscosity structure in the lithosphere within the context of non-linear, power-law deformation (van der Wal et al., 2013).

Additionally, it is known that the EET of the lithosphere depends on factors like the size and age of the load inducing the deformations (Watts et al., 2013), and so by incorporating more realistic viscous structure into the lithosphere we are effectively making the strength of the lithosphere time and load-size dependent. This may be an important consideration in GIA studies, where the time scales can range from thousands to tens of thousands of years and the load size from (typically) hundreds to thousands of kilometres.

2. Methodology

2.1. GIA model

In general, a GIA model has three key components: an ice history, provided in this study by ICE5G (Peltier, 2004; version 1.2); an Earth model to calculate solid Earth deformation and perturbation to the geopotential in response to the ice-ocean loading; and a sea level model that solves the sea level equation to determine how sea level changes in response to the ice loading and Earth deformation. We discuss the Earth model component in detail below. The sea level model we apply solves the generalised sea level equation (Kendall et al., 2005; Mitrovica and Milne, 2003), and therefore includes a treatment of time varying shorelines and sea level change in regions of ablating marine based ice. The influence of GIA-induced perturbations to the Earth's rotation vector on sea level is also included (Milne and Mitrovica, 1998; Mitrovica et al., 2005).

All the Earth models in this study are spherically symmetric Maxwell bodies with an elastic and density structure given by PREM (Dziewonski and Anderson, 1981). The sub-lithosphere viscous structure is defined in two regions: the upper mantle (base of lithosphere to 660 km seismic discontinuity) and the lower mantle (660 km to the core-mantle boundary); we adopt values for these respective regions of 5×10^{20} Pa s and 10^{22} Pa s. As described above, the lithosphere is commonly defined as a shell of uniform and very high viscosity – several orders of magnitude higher than that of the upper mantle. We improve upon these simplistic lithosphere models by considering variations in lithosphere strength due to changes in composition and temperature. Specifically, we assume a quartzite composition to the Mohorovicic discontinuity ("Moho") at 24.4 km depth, and a mafic granulite composition for the mantle component, with parameters given in Tesauro et al., 2009; see Table 1. We adopt a power law flow model for the lithosphere as defined by the Dorn equation,

Table 1
Parameters adopted in defining the lithosphere viscosity profiles shown in Fig. 1.

Parameter	Upper crust	Lower crust
$\dot{\varepsilon}$ (s^{-1})	10^{-15}	10^{-15}
A_D ($Pa^{-n}\,s^{-1}$)	6.03×10^{-24}	8.83×10^{-22}
n	2.72	4.2
E_D ($J\,mol^{-1}$)	134×10^3	445×10^3

$$\dot{\varepsilon} = A_D \sigma^n e^{-E_D/RT} \tag{1}$$

where $\dot{\varepsilon}$ is the strain rate and is set to $10^{-15}\,s^{-1}$, E_D is the activation enthalpy, R is the gas constant, T is temperature, and A_D and n are experimentally determined parameters that depend on the type of rock, pressure and other environmental parameters that we will neglect in this preliminary analysis. Eq. (1) can be inverted to produce an expression for stress, σ (Table 1).

It is important to note an inconsistency in our approach: the Earth component of the GIA model we are applying assumes a Maxwell rheology, which has a linear stress–strain relationship, but we are defining the viscosity-depth structure in the lithosphere derived from a non-linear relationship (Eq. (1)). In a non-linear rheology the viscosity is stress dependent, with regions of higher stress being characterised by lower (effective) viscosities. In a Maxwell model, the viscosity values are constant and stress independent. We obtain the initial viscosity profile assuming a non-linear stress–strain relationship, but it is treated in our model linearly. We chose to follow this approach for two reasons: (1) there is growing evidence that non-linear (as opposed to linear) deformation is dominant in the lithosphere (e.g., Bürgmann and Dresen, 2008) and so application of Eq. (1), as opposed to a linear relation ($n = 1$), leads to a more accurate estimate of the viscosity structure; (2) while the application of a non-linear Earth model within our GIA model would be consistent with the application of Eq. (1), this adds a second advance compared to most previous GIA modelling studies and so interpretation of the results would be less straightforward. Our aim in this study is not to investigate the effects of non-linear versus linear rheology on postglacial rebound (e.g., Wu and Wang, 2008), rather, we adopt the Dorn equation to compute a viscosity profile for the lithosphere that should more closely resemble reality than does the traditional elastic layer model adopted in most previous GIA studies.

The lithosphere viscosity profile is modelled as two ductile zones separated by a discontinuity at the Moho. The Dorn Eq. (1) requires a temperature profile, for which we assume radiogenic heat production within the lithosphere. The analytic expression for temperature that we adopt within the lithosphere is (e.g., Turcotte and Schubert, 2002),

$$T(Z) = \frac{A_0 h^2}{K}(1 - e^{-Z/h}) + \left(T_0' - \frac{A_0 h}{K}\right) Z + T_0, \tag{2}$$

where A_0 is the radiogenic heat production rate at the surface, h is a scaling parameter set to 11 km, K is the conductivity, set to a constant 3 W/mK, T_0' is the surface temperature gradient, and T_0

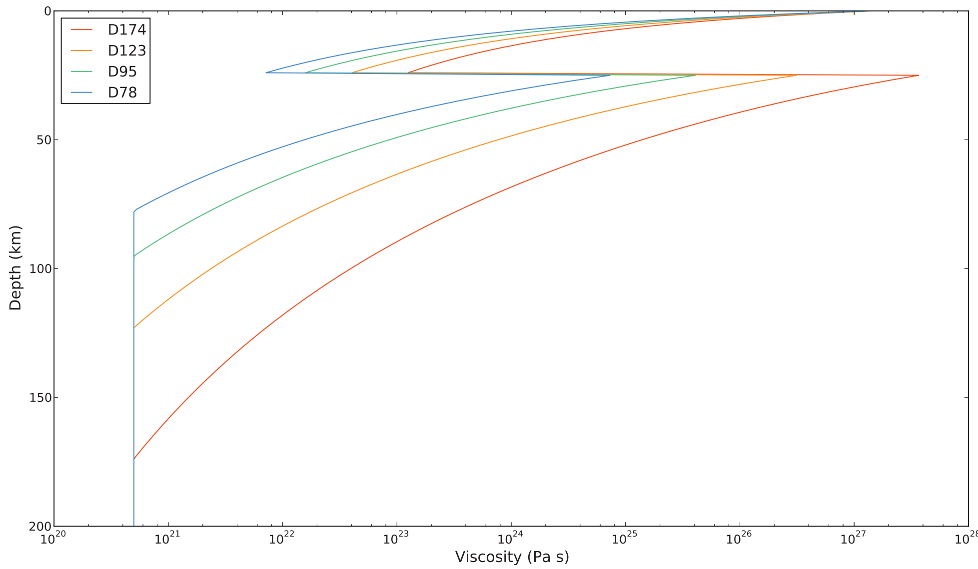

Fig. 1. Lithosphere viscosity profiles for the four Earth models described in the text. Labels in the key denote the lithospheric thickness of each model in kilometres. Note that the *x*-axis (viscosity) is plotted logarithmically.

is the temperature at the Earth's surface, assumed to be 0 °C. Our temperature profiles and thus our strength profiles are dependent on the surface temperature gradient. Note that, by applying Eq. (2), we ignore the effect of heat transfer via convection on the Earth's temperature profile. This would lead to greater temperatures and therefore lower viscosities at depth in the lithosphere. We convert our strength profiles to viscosity profiles through

$$\eta = \frac{\sigma}{2\dot{\varepsilon}} \tag{3}$$

which, when combined with Eq. (1), gives

$$\eta = \frac{1}{2}\left(\frac{\dot{\varepsilon}^{1-n}}{A_D}\right)^{1/n} \exp\left(\frac{E_D}{nRT}\right) \tag{4}$$

Eq. (4) indicates that the viscosity (for $n > 1$) will depend on stress such that regions of higher stress will exhibit lower (effective) viscosity.

We test four Earth models, with surface temperature gradients $T_0' = 14,\ 16,\ 18,$ and 20 K/km, corresponding to a range of surface heat flow values of 42–60 mW/m^2. The four models are shown in Fig. 1 and their associated temperature profiles in Fig. 2. Because we

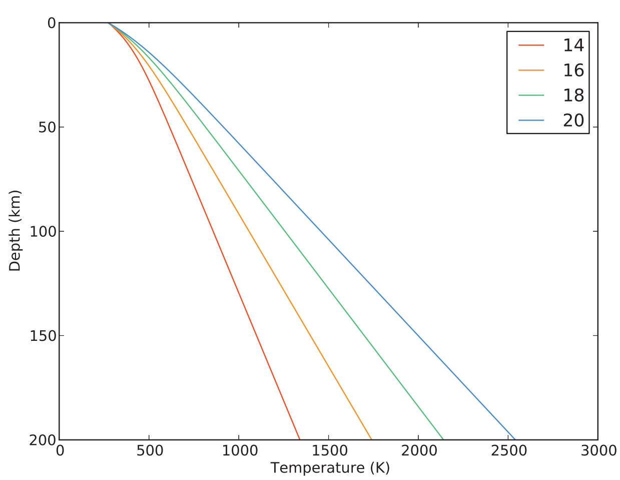

Fig. 2. Temperature profiles corresponding to the viscosity profiles shown in Fig. 1.

assume different compositions above and below the Moho (taken to be at 24.4 km based on PREM; Dziewonski and Anderson (1981)), the calculated viscosity profile has a discontinuity at this depth.

In traditional GIA studies, the lithosphere viscosity is much greater than that of the upper mantle and so the thickness of this region corresponds to that of an (effectively) elastic layer. Our more realistic model results in a lithosphere with a viscosity that is not, in general, many orders of magnitude greater than that of the upper mantle, and so defining an EET is less straightforward, as it will depend on the spatial and temporal scale of the loading (see Fig. 4 and related discussion). Therefore, to simplify the comparison between these two lithosphere models and more directly address the aim of this study, we chose to define a thickness of our viscosity-varying lithosphere models as the depth at which the viscosity in the component of the lithosphere between the Moho and the upper mantle drops down to the viscosity of the upper mantle (5×10^{20} Pa s). Applying this approach results in values of 174, 123, 95 and 78 km. In the following, these are referred to as D174, D123, D95 and D78 to indicate that these models can exhibit ductile failure on GIA timescales (see Fig. 4 and related discussion). The continuous viscosity profiles shown in Fig. 1 are discretized with a depth resolution of ~1 km for the purpose of computing viscoelastic Love numbers (Peltier, 1974).

Barnhoorn et al. (2011) suggest ~10^{25} Pa s as a good minimum viscosity value in the lithosphere to ensure elastic deformation on GIA timescales. We note that only very small sections of our ductile models have values above this minimum and so we expect that our models (Fig. 1) have an effective elastic thickness that is much thinner than their defined thickness would suggest.

2.2. Modelling approach

Changes in RSL have provided the most robust constraints on Earth viscosity structure in previous GIA modelling studies (e.g., Lambeck et al., 1996; Paulson et al., 2007). We therefore consider predictions of RSL at a small suite of sites around the globe where data have been obtained and used to infer lithospheric thickness. Six of the eight localities were chosen (sites 1–6 in Fig. 3a) due to their location relative to ancient ice sheets of a given size; from largest to smallest considered: Laurentian (1 & 2); Fennoscandian (5 & 6) and British-Irish (3 & 4). In each of these site pairs, one

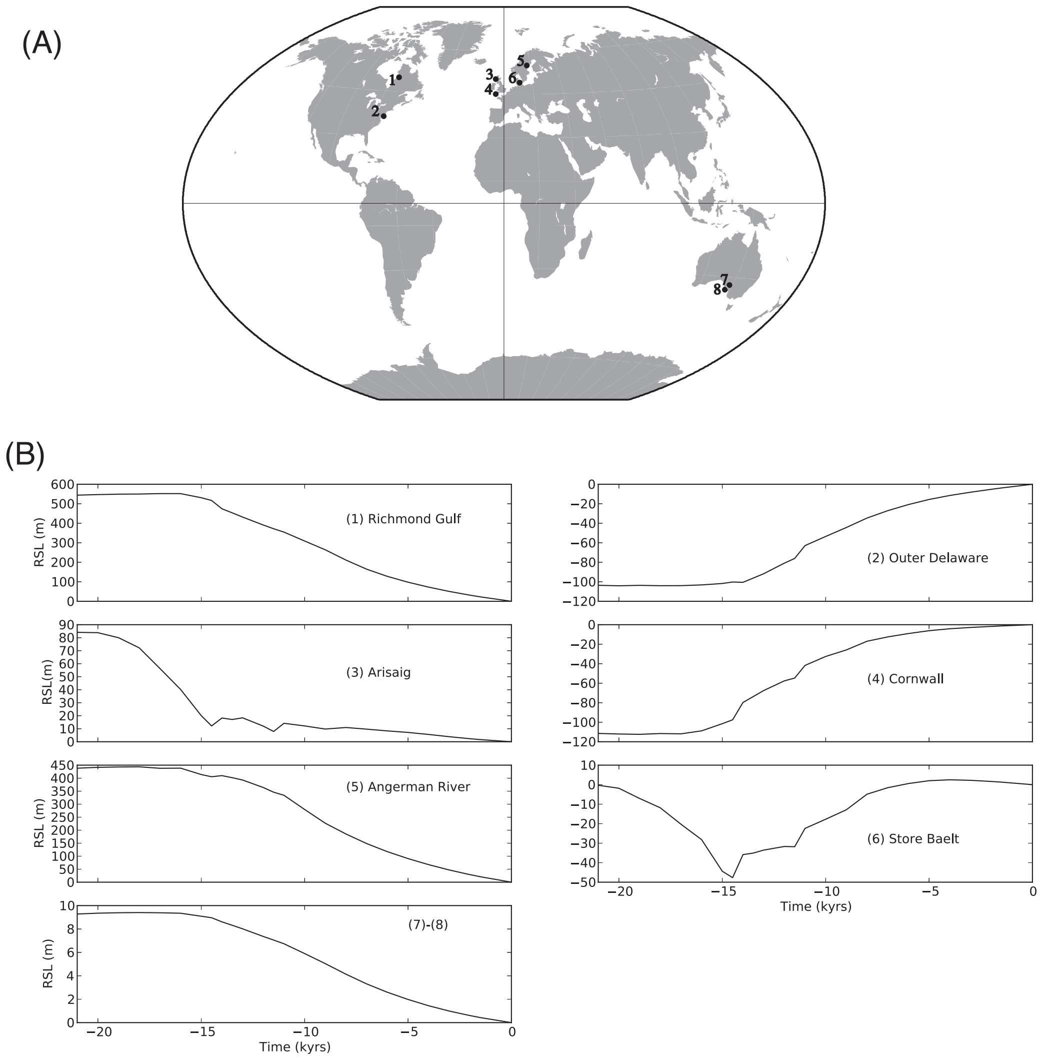

Fig. 3. (A) The sites considered in this study, from 1 to 8, are Richmond Gulf, Outer Delaware, Arisaig, Cornwall, Angerman River, Store Baelt, Port Pirie, and Cape Spencer (see Section 3). (B) An example of RSL curves for each of the sites, along with the difference in RSL between Port Pirie and Cape Spencer (see Section 3) for a 96 km elastic plate lithosphere model.

site is located near the centre of the, now melted, ice sheet and the other close to the margin. By considering a range of ice sheet size as well as locality of the sites with respect to the ice sheet, different depth sensitivities to viscosity structure are sampled. In this analysis, sensitivity to shallow (lithosphere) structure is the primary focus. The other two sites (7 & 8) are located distant from major glaciation centres, where the RSL signal is driven primarily by ocean loading (hydro-isostasy). These sites, and particularly the RSL difference between the two sites, have provided powerful constraints on viscosity structure (e.g., Nakada and Lambeck, 1989).

To complement the RSL predictions outlined above, we also generated model output of land height change produced by a simple parabolic load that is placed on the model Earth and does not vary in time. These model results, shown at the beginning of the following section, enable a more straightforward interpretation of the difference in output between the two lithosphere models (with and without viscous structure).

3. Results and discussion

In Fig. 4 we show the modelled deformation of the Earth under a time invariant parabolic ice load. We compare the deformation of D123 and D95 with the deformation of the suite of high viscosity lithosphere models by plotting the vertical deformation radially from the centre of the ice load, and we consider small (radius 1°, maximum thickness 100 m) and large (radius 15°, maximum thickness 3000 m) loads. We denote the high and uniform viscosity lithosphere models by their thickness with a prefix E (i.e., E71, E96, and E120) since the thickness reflects the EET in this case.

When we compare the deformation of D123 and D95 with the elastic models it is evident that any conclusion we may make about the effective thickness of the lithosphere for the ductile models is dependent on both the size and age of the load. Examining the vertical displacement near the loading centre for the larger ice load, when the ice load has been left for 2 kyr, the deformation of D123 is similar to that of E120; while for the smaller ice load the deformation of D123 at this time step is slightly less than that of E96. After the load has been left for 20 ka, comparison between the two sets of models indicates that the EET of the ductile models has thinned considerably relative to the elastic lithosphere models. For example, in the larger load test, the deformation near the centre of the load for D123 is similar to that for E96, whereas, for the smaller load, the result for E71 is about midway between D123 and D96. This is a result of viscous flow in the lower viscosity ductile models.

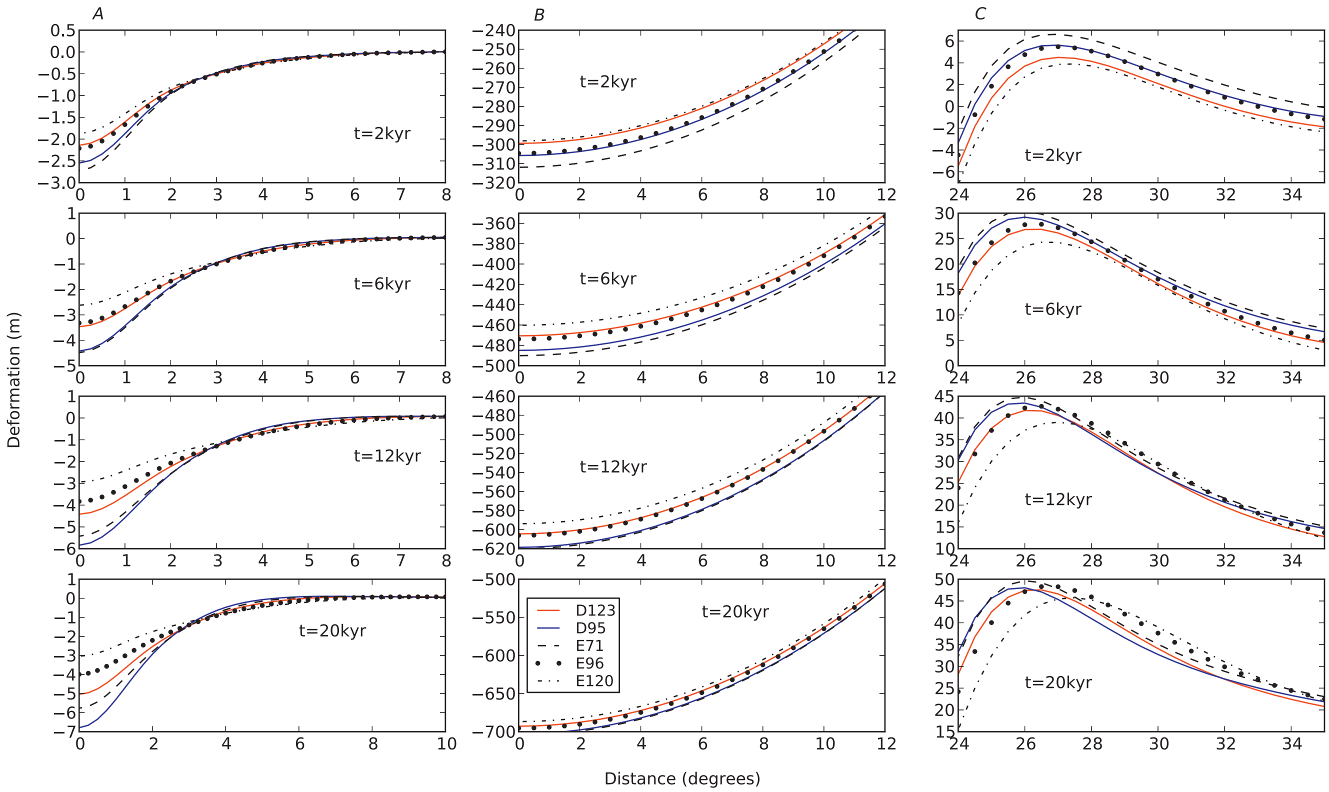

Fig. 4. Vertical displacement of the model Earth surface for a parabolic ice load along a radial transect from the centre of the ice sheet. In column A we show the vertical displacement for a small ice load (radius 1°, maximum thickness 100 m), while columns B and C show the deformation at the load centre (B), and peripheral bulge (C), for a relatively large (radius 15°, maximum thickness 3000 m) ice load.

The enhanced thinning in the case of the smaller load reflects its shallower depth sensitivity.

Towards the edge of the load and beyond, there are also some interesting differences between the two types of lithosphere model. However, the comparison is complicated by lateral migration of the peripheral bulge. This is most evident in the results for the smaller load as the bulge is completely captured in Fig. 4 (left column). For a given lithospheric thickness, the lateral movement of the bulge becomes more pronounced with time in the 'D' models compared to the 'E' models as the EET thins leading to some interesting differences. For example, the vertical deflection profiles in Fig. 4 for the 15° radius load demonstrate that directly at the bulge, D123 closely matches E96 at 20 kyr, as it does under the load. However, further away from the load D123 no longer tracks E96, and instead seems to suggest its behaviour there would be analogous to a lithosphere even thinner than E71. Indeed, there is no overlap between E123/96/71 and D123/95 moving away from the load centre beyond the peripheral bulge.

The above comparison demonstrates increasing amounts of viscous flow in the lithosphere with time and therefore a reduction in the EET in the ductile models. However, it is important to note that since we assume a linear Maxwell rheology in the numerical computations, the influence of changing stress with time is not modelled.

The results in Fig. 4 show the response of an idealised ice load. We will now consider RSL predictions from a more realistic loading history (provided by ICE5G, version 1.2; Peltier, 2004). By RSL we mean the height between the bedrock and the geopotential surface that defines sea level. In order to determine how the RSL predictions based on the more realistic lithosphere models differ from those of the elastic models for a more realistic ice history, we generated results for the 8 locations described in Section 2. Before going on to examine the difference in output for the two types of lithosphere model, it is useful to first look at the predicted RSL curves for each location. Relative sea level curves at these sites for a traditional 96 km elastic lithosphere model are displayed in Fig. 3b. For the sites in Australia we have shown the difference between the two sites, which is more sensitive to lithosphere variation than the RSL curves for individual sites on their own (Nakada and Lambeck, 1989).

Richmond Gulf and Angerman River (sites 1 and 5) show the largest responses, as they are located at the centre of where the Laurentide and Fennoscandian ice sheets were, respectively. The sea level fall shown for these sites is primarily caused by uplift. The Arisaig RSL curve is similarly dominated by land uplift, but the magnitude of the sea level fall is less than at Richmond Gulf and Angerman River because the British-Irish ice sheet was significantly smaller than the Laurentide and Fennoscandian ice sheets. We note also that Arisaig is located on the peripheral bulge of the Fennoscandian ice sheet, which contributes subsidence during the postglacial period. Sites like Outer Delaware in North America and Cornwall in southern UK are located outside the ice margin position during the last glacial maximum, on the peripheral bulge regions of, respectively, the North American and Eurasian ice complexes. The prediction for Store Baelt is the most complicated because the site is located near the hingeline of the Fennoscandian ice sheet and so the RSL curve displays an initial fall due to land uplift followed by a rise as the peripheral bulge migrates towards the location of the primary load centre. Finally, Port Pirie and Cape Spencer, in

Australia, are far from past centres of glaciation and so are more sensitive to ocean loading than ice loading. Due to their respective locations in Spencer Gulf, the RSL change at each site reflects a different response to the ocean loading: being further inland, Port Pirie is more strongly affected by continental levering (e.g., Clark et al., 1978) and thus exhibits a smaller RSL rise (due to enhanced land uplift) through the deglaciation. Hence, the difference between these sites is a monotonically decreasing signal with time that is dominated by the ocean loading signal.

Predicted RSL curves were generated for a suite of lithosphere models with and without viscous structure. To highlight differences between the results of these two models, we show in Fig. 5(A–D) predictions for D78, D95, D123, D174 minus those for E46 (A), E71 (B), E96 (C) and E120 (D). While the results from the simple parabolic loading models provide useful insight to the differences in the nature of the isostatic response between the two different types of lithosphere model, those in Fig. 5 provide a more accurate reflection of the implications for inferring lithospheric thickness from reconstructions of RSL. However, given the greater complexity of the load model (in terms of both time history and spatial extent), interpretation of the results in Fig. 5 is more difficult, particularly for sites significantly affected by peripheral bulge dynamics (as

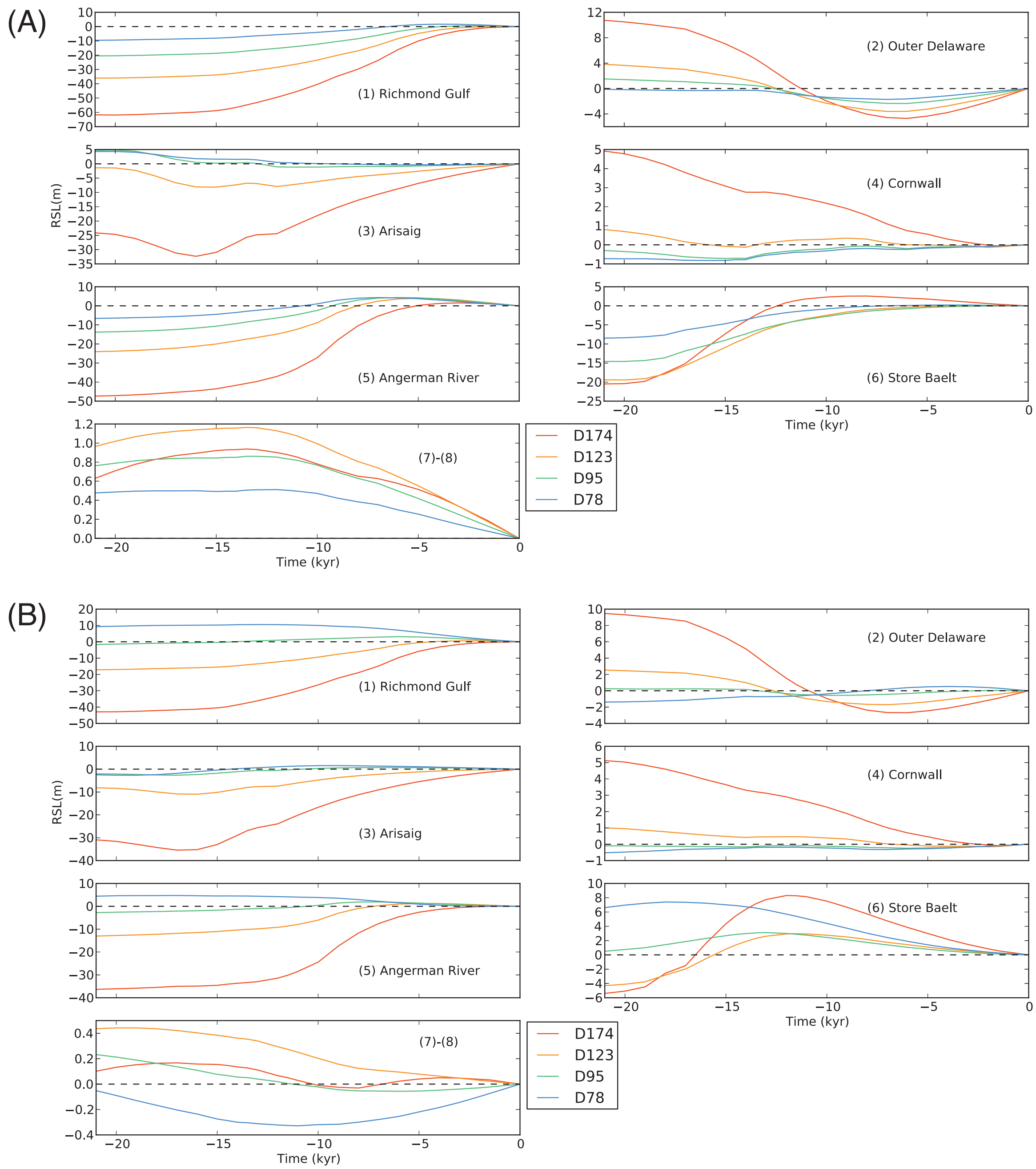

Fig. 5. Differences in RSL predictions between each of the more realistic lithosphere models (see colour key) and those of the (A) 46 km, (B) 71 km, (C) 96 km, and (D) 120 km elastic models. (For interpretation of the references to color in figure legend, the reader is referred to the web version of the article.)

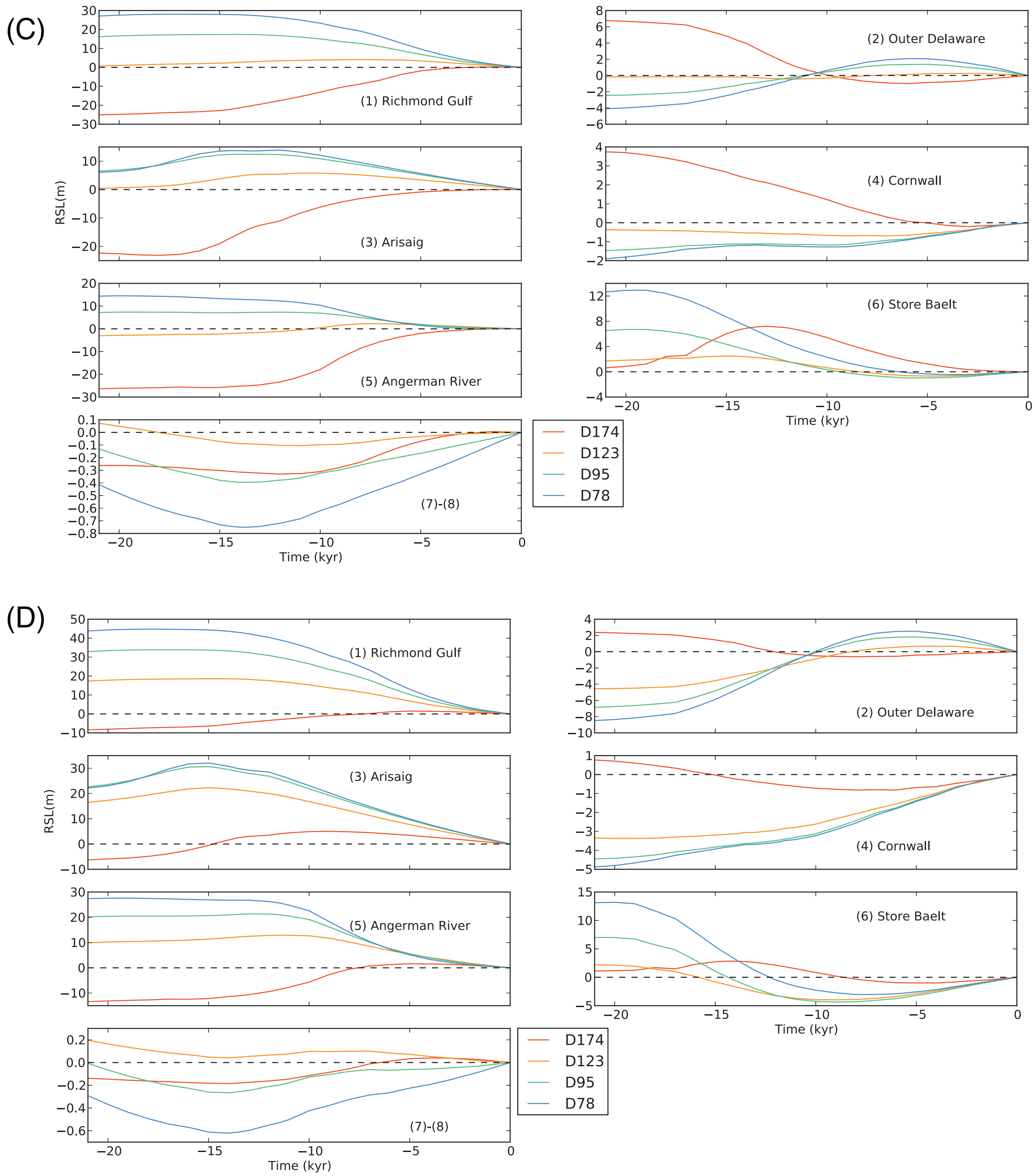

Fig. 5. (*Continued*).

indicated in Fig. 4). In particular, the tendency of the RSL differences to actually change sign and cross the zero-line at Outer Delaware, Cornwall and Store Baelt in Fig. 5(A–D) seems to be a reflection of this behaviour. This increased complexity is particularly true for Store Baelt and Cornwall; the former due to its proximity to the LGM margin of the Fennoscandian ice sheet and the latter because of the significant influence of both the British-Irish and Fennoscandian ice sheets (each with very different depth sensitivities and chronologies).

We found it to be often (but not exclusively) true that the predictions of any given elastic model were closest to the ductile model that was 20–30 km thicker. This is true in all cases for Richmond Gulf, Outer Delaware, and Angerman River, and it is frequently true for Store Baelt. This is consistent with the results from the parabolic ice load tests. However, we can see that for the sites in the British Isles, the predicted behaviours of D78 and D95 are very close to each other, often within a metre or less, and so it is not possible to say without ambiguity whether one ductile model would be preferable to another at this locality. Another interesting feature evident in the British Isles is that when comparing the ductile models to E96 (Fig. 5C), we can see that D123 provides the closest match to E96 early in the deglaciation up to about 10 ka BP, but nearer to the present it is D174 that tracks E96 the most closely. A possible explanation for this is that, as a relatively small ice sheet, the deformation associated with the BIIS is more sensitive to shallower Earth structure than that caused by either the Laurentian or Fennoscandian ice sheets. The results for the Australian sites generally show the same overall behaviour of the closest match to a given elastic lithosphere model being the ductile lithosphere model 10–20 km thicker, with the exception of E120, which tends to be most similar to D123. In no cases (except Store Baelt, to an extent) do the results indicate that the best match for an elastic plate model is a significantly thinner ductile model.

The differences shown in Fig. 5 – those between the two model types and those between the different ductile models – reflect the ability of RSL data to infer lithospheric thickness. The precision of sea-level reconstructions ranges from sub-metre to several metres depending on the indicator(s) available at a given location and time (e.g., Elias, 2013; see contributions to section titled "Sea Level Studies"). Since the majority of data span the Holocene (past ~12 kyr) only, our results indicate that existing data are capable of resolving between several but not all (e.g., D95 and D71 at some sites) of the models considered in Fig. 5. However, this statement does not consider the issue of parameter trade-off which will limit the ability of RSL data to constrain lithospheric thickness given uncertainty in the loading history and sub-lithosphere viscosity.

4. Conclusion

We incorporated realistic viscosity structure in the lithosphere in the Earth component of a GIA model. We find that the RSL predictions of a given lithosphere model with viscous structure are, in general, most similar to those of an elastic model with a significantly thinner lithosphere. We conclude that the application of elastic lithosphere models in previous GIA analyses generally results in an underestimation of lithosphere thickness by tens of kilometres compared to models with viscous structure in the lithosphere. The greatest sensitivity to the imposed changes in lithosphere viscosity structure is evident in the British Isles, where there was a relatively small ice sheet and in Store Baelt which is located near the hingeline of the Fennoscandian ice sheet. We also investigated the time dependence of vertical deformation and found that for short time scales (~2 kyr), the response of a model with lithosphere structure is similar to that of an elastic plate of similar thickness, but that it effectively thins by tens of kilometres over a time scale of ~10 kyr.

While this work does not fully bridge the gap between lithosphere thickness estimates derived through GIA modelling as opposed to through other means, it does close the gap and thus provides a part explanation for the difference. For example, while seismic studies of the British Isles have determined a distance to the lithosphere-asthenosphere boundary of 110–150 km, GIA studies tend to find best fitting Earth models with ~70 km thick lithospheres. Comparing predictions of a 71 km elastic plate lithosphere model to our more realistic models, the predictions in Arisaig and Cornwall are comparable to either the 78 km or 95 km ductile models for time up to about 10 kyr BP, or the 123 km ductile model after 10 kyr BP and approaching the present.

An important avenue for future work is to incorporate non-linear (power law) flow into the type of analysis presented above. Allowing non-linear flow would cause the (effective) viscosity in the model to change in time. This process could act in an opposite sense to the EET thinning indicated in our results as stresses are maximum at the onset of loading and progressively relax as deformation proceeds.

Acknowledgements

JK would like to acknowledge funding from the University of Ottawa and through the Ontario Graduate Scholarship program. GAM acknowledges funding from the Natural Science and Engineering Research Council of Canada, the Canada Research Chairs program, the Canadian Foundation for Innovation and the University of Ottawa. We thank Jerry Mitrovica for discussions that contributed to the results presented in this paper.

References

Audet, P., Mareschal, J.C., 2004. Variations in elastic thickness in the Canadian Shield. Earth Planet. Sci. Lett. 226, 17–31.
Barnhoorn, A., van der Wal, W., Vermeersen, B.L.A., Drury, M.R., 2011. Lateral, radial, and temporal variations in upper mantle viscosity and rheology under Scandinavia. Geochem. Geophys. Geosyst. 12.
Bradley, S.L., Milne, G.A., Teferle, F.N., Bingley, R.M., Orliac, E.J., 2009. Glacial isostatic adjustment of the British Isles: new constraints from GPS measurements of crustal motion. Geophys. J. Int. 178, 14–22.
Bürgmann, R., Dresen, G., 2008. Rheology of the lower crust and upper mantle: evidence from rock mechanics, geodesy, and field observations. Annu. Rev. Earth Planet. Sci. 36, 531–567.
Clark, J.A., Ferrel, W.E., Peltier, W.R., 1978. Global changes in postglacial sea level: a numerical calculation. Quat. Res. 9, 265–287.
Davis, J.L., Mitrovica, J.X., 1996. Glacial isostatic adjustment and the anomalous tide gauge record of eastern North America. Nature 379, 331–333.
DiDonato, G., Mitrovica, J.X., Sabadini, R., Vermeersen, L.L.A., 2000. The influence of a ductile crustal zone on glacial isostatic adjustment: geodetic observables along the U.S. East Coast. Geophys. Res. Lett. 27, 3017–3020.
Dziewonski, A.M., Anderson, D.L., 1981. Preliminary reference earth model. Phys. Earth Planet. Inter. 25 (4), 297–356.
Elias, S. (Ed.), 2013. Encyclopedia of Quaternary Science. , 2nd ed. Elsevier, London, UK.
Kendall, R.A., Mitrovica, J.X., Sabadini, R., 2003. Lithospheric thickness inferred from Australian post-glacial sea-level change: the influence of a ductile crustal zone. Geophys. Res. Lett. 30, 14.1–14.4, http://dx.doi.org/10.1029/2003GL017022.
Kendall, R.A., Mitrovica, J.X., Milne, G.A., 2005. On post-glacial sea level-II. Numerical formulation and comparative results on spherically symmetric models. Geophys. J. Int. 161 (3), 679–706.
Klemann, V., Wolf, D., 1998. Modelling of stresses in the Fennoscandian lithosphere induced by Pleistocene glaciations. Tectonophysics 294, 291–303.
Klemann, V., Wolf, D., 1999. Implications of a ductile crustal layer for the deformation of the Fennoscandian ice sheet. Geophys. J. Int. 139, 216–226.
Kuchar, J., Milne, G., Hubbard, A., Patton, H., Bradley, S., Shennan, I., Edwards, R., 2012. Evaluation of a numerical model of the British-Irish ice sheet using relative sea-level data: implications for the interpretation of trimline observations. J. Quat. Sci. 27, 597–605.
Lambeck, K., Smither, C., Johnston, P., 1998. Sea-level change, glacial rebound and mantle viscosity for northern Europe. Geophys. J. Int. 134, 102–144.
Lambeck, K., Johnston, P., Smither, C., Nakada, M., 1996. Glacial rebound of the British Isles 2. Constraints on mantle viscosity. Geophys. J. Int. 125 (2), 340–354.
Levy, F., Jaupart, C., Mareschal, J.C., Bienfait, G., Limare, A., 2010. Low heat flux and large variations of lithospheric thickness in the Canadian Shield. J. Geophys. Res. 115.
Martinec, Z., Wolf, D., 2005. Inverting the Fennoscandian relaxation-time spectrum in terms of an axisymmetric viscosity distribution with a lithospheric root. J. Geodyn. 39, 143–163.
Milne, G.A., Mitrovica, J.X., 1998. Postglacial sea-level change on a rotating Earth. Geophys. J. Int. 133 (1), 1–19.
Mitrovica, J.X., Milne, G.A., 2003. On post-glacial sea level: I. General theory. Geophys. J. Int. 154 (2), 253–267.
Mitrovica, J.X., Wahr, J., Matsuyama, I., Paulson, A., 2005. The rotational stability of an ice-age Earth. Geophys. J. Int. 161, 491–506.
Nakada, M., Lambeck, K., 1989. Late Pleistocene and Holocene sea-level change in the Australian region and mantle rheology. Geophys. J. Int. 96 (3), 497–517.
Paulson, A., Zhong, S., Wahr, J., 2007. Inference of mantle viscosity from GRACE and relative sea level data. Geophys. J. Int. 171, 497–508.
Peltier, W.R., 1974. The impulse response of a Maxwell Earth. Rev. Geophys. 12, 649–669.
Peltier, W.R., Shennan, I., Drummond, R., Horton, B., 2002. On the postglacial isostatic adjustment of the British Isles and the shallow viscoelastic structure of the Earth. Geophys. J. Int. 148, 443–475.
Peltier, W.R., 2004. Global glacial isostasy and the surface of the ice-age Earth: the ICE5G (VM2) model and GRACE. Ann. Rev. Earth Planet. Sci. 32, 111–149.
Ranalli, G., 1995. Rheology of the Earth, 2nd ed. Chapman and Hall, pp. 230.
Sella, G.F., Stein, S., Dixon, T.H., Craymer, M., James, T.S., Mazzotti, S., Dokka, R.K., 2007. Observation of glacial isostatic adjustment in stable North America with GPS. Geophys. Res. Lett. 34, L02306.

Tesauro, M., Kaban, M.K., Cloetingh, S.A.P.L., 2009. A new thermal and rheological model of the European lithosphere. Tectonophysics 476, 478–495.
Turcotte, D.L., Schubert, G., 2002. Geodynamics, 2nd ed. Cambridge University Press.
van der Wal, W., Barnhoorn, A., Stocchi, P., Gradmann, S., Wu, P., Drury, M., Vermeersen, L.L.A., 2013. Glacial isostatic adjustment model with composite 3D earth rheology for Fennoscandia. Geophys. J. Int., http://dx.doi.org/10.1093/gji/ggt099.
Watts, A.B., Zhong, S.J., Hunter, J., 2013. The behaviour of the lithosphere on seismic to geologic timescales. Annu. Rev. Earth Planet. Sci. 41, 443–468.
Wu, P., Wang, H., 2008. Postglacial isostatic adjustment in a self-gravitating spherical earth with power-law rheology. J. Geodyn. 46, 118–130.

The primary response to an increasing flood threat is investment in infrastructure and restoration activities to protect human populations and areas of high economic value... However, at the most basic level, improving resiliency requires understanding the underlying processes driving subsidence.

Jones et al., 2016

3

Incorporating Alternate Loading Sources: Subsidence in the Mississippi Delta

Contemporary sea level is rising at a global average rate of approximately 3 mm/year (Watson et al., 2015), but the local sea level change observed in any particular region may differ substantially from the mean. For instance, contemporary RSL rates in the Mississippi Delta region of Louisiana have been measured to be as high as 12 ± 8 mm/year (Jankowski et al., 2017). These very high RSL rates lead to a significant loss of wetlands along the Louisiana coast: while Louisiana is home to approximately 40% of the wetlands of the continental United States, it experiences up to 90% of the wetland loss (Couvillion et al., 2017). Since 1932, Louisiana has lost 5000 km^2 of its coastal wetlands, with the United States Geological Survey noting "if this loss were to occur at a constant rate, it would equate to Louisiana losing an area the size of one football field per hour" (Couvillion et al., 2017).

These rising sea levels present danger to public safety and strong economic risk. The Mississippi Delta region contains infrastructure for approximately 25% of the petroleum production of the United States, and the Delta's marine ecosystem supports approximately 30% of the commercial fisheries of the United States (Blum and Roberts, 2012). Rising sea level and wetland loss also contribute to an increased likelihood of major storm damage (Day et al., 2007), as wetlands provide a natural buffer against storm surges. This is particularly important as the region that has already been devastated by Hurricane Katrina, which resulted in a death toll of over 1800 and caused 125 billion dollars in damage.

To mitigate problems related with ongoing sea-level rise in the region, it is imperative to determine the key mechanisms responsible. In the next section I will describe what it is about the geography of the Mississippi Delta region that leads to such high rates of RSL rise compared to the global average. In particular I will consider the influence of the sediment transported through the Mississippi catchment and deposited in the delta. Following this, I will describe the necessary changes to the sea level theory and algorithm to account for sediment loading.

3.1 Background: Understanding Subsidence in the Mississippi Delta Region

The Mississippi Delta region is the last stop for the sediment transported through the Mississippi drainage basin and down the Mississippi River (Figure 3-1). This drainage baisin is the fourth largest in the world by area (about 3.2 million square kilometres), and 7th largest in transported sediment (Blum and Roberts, 2012). The sediment flow to the delta, in modern times (1987-2006), is estimated at 145 million metric tons per year, and is estimated to have been 400 million metric tons per year before 1900 (Meade and Moody, 2010), greatly reduced in the present-day largely because of the construction of dams in the major rivers composing the drainage basin.

Figure 3-1: The Mississippi drainage basin (Public domain image reproduced from the National Park Service of the United States).

In general, sea level at a given location is determined by global processes with regional variability, such as GIA or thermal expansion (steric sea-level rise), or local processes, which would include the effects of sediment loading. As an example, in Figure 3-2 (reproduced from Love et al., 2016), sea level projections for the Gulf and Atlantic coasts of North America are presented for three climate scenarios, with the totals broken into components (see caption). What is clearly evident from the figure is that each major component of sea level exhibits significant spatial variability. Note that while Figure 3-2 includes projections for New Orleans, the authors state that their estimate is biased low, as it does not account for the effects of sediment loading or compaction.

The flux of sediment into the Gulf affects RSL in two key ways, the first is through isostasy, and the second is through sediment compaction. Sediment isostatic adjustment, or SIA, is similar to GIA - a mass transfer on the surface of the Earth leads to a deformation of the Earth's surface and changes to the gravitational potential surface that defines sea level. Sediment compaction is the process of sediment becoming more densely packed through time, which leads to a subsidence of the upper surface. These processes are considered to be the most important controls on subsidence and sea level in the Mississippi Delta region (Blum and Roberts, 2012), though

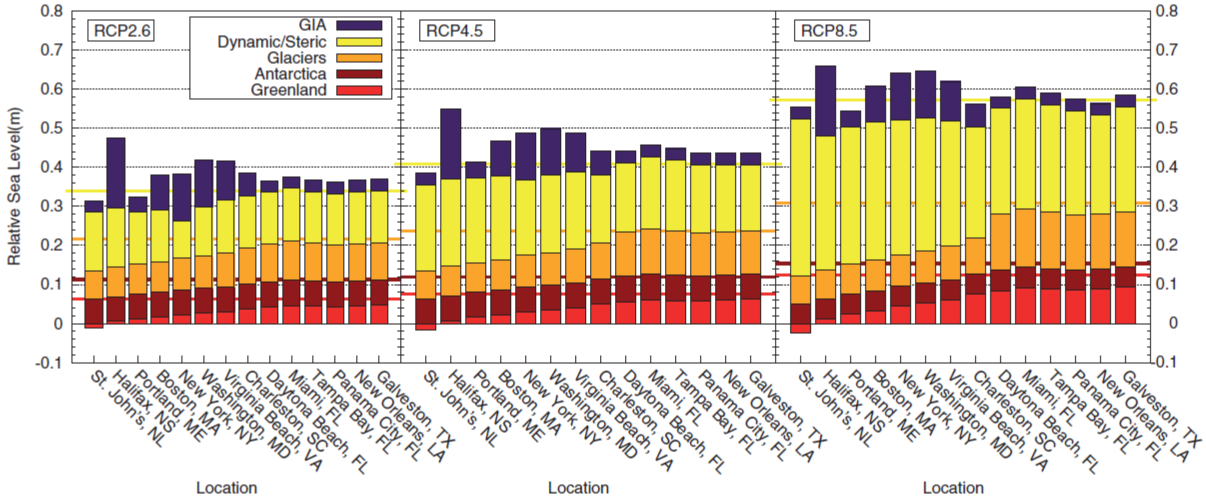

Figure 3-2: Relative sea level at 2100 relative to present for three climate scenarios, for select cities on the Atlantic and Gulf coast of North America, reproduced from Love et al., 2016 under a Creative Commons CC BY-NC-ND 4.0 license. The total is broken into components from the melting of the Antarctic and Greenland ice sheets, as well as smaller glaciers, ocean dynamic/thermal effects, and ongoing GIA.

of course other processes can be very important. For example, the relative proximity of the Mississippi Delta to the North American Ice Sheet makes the glacial isostatic adjustment signal (corresponding primarily to a collapse of the peripheral bulge) important. Another important component to land subsidence is fluid extraction. I have mentioned that the Louisiana coast is home to a large petroleum industry, and the extraction of petroleum (and groundwater in residential areas) also leads to significant land subsidence (Morton et al., 2006; Jones et al., 2016).

The extent to which SIA is responsible for subsidence in the Mississippi Delta has been debated for some time. It was first proposed to be a dominant mechanism in Fisk, 1939. Attempts to model land motion in the Mississippi Delta have been carried out that have recreated the observed high subsidence rates in the Mississippi Delta. For example, both Jurkowski et al., 1984 and Ivins et al., 2007 modelled Earth deformation in response to sediment loading in the Delta, and obtained subsidence rates on the order of millimetres per year. However, these attempts were later criticized by Wolstencroft et al., 2014, as either requiring unrealistically large sediment loads in the case of Ivins et al. or else unrealistically low mantle viscosities in the case of

Jurkowski et al. It was shown by Wolstencroft et al., 2014, by modelling both GIA and Earth deformation in response to sediment loading in the Mississippi Delta, that the GIA component to sea level in the region is likely as large or larger than the SIA signal, and that the combination of the two would not be large enough to match the observed subsidence rates. Another important study to estimate the size of the SIA contribution was that of Yu et al., 2012, who took a difference of sea level curves at sites within the delta and peripheral to it, in order to determine a differential sea level rate that reflected the SIA rate (assuming that both sites recorded a similar GIA signal, and ignoring non-isostatic effects). They found that the differential RSL rate was only 0.15 ± 0.07 mm/year, which would make SIA far from the dominant contributor to land subsidence. Typical GIA and SIA timescales are thousands of years, and on these timescales Törnqvist et al., 2008 estimated that sediment compaction can result in subsidence rates of 5 mm/year, and up to twice as much on decadal timescales.

Measurements from GPS stations in the Delta have recorded rates of up to nearly 7 mm/year (Karegar et al., 2015), and it's noteworthy that these rates are a minimum estimate of the total subsidence at the land surface. This is because the GPS antennas are typically on the rooftops of buildings with foundation depths of five to tens of metres. The GPS stations record the motion of the foundations, and therefore are insensitive to processes in the layers of subsidence above this depth, including shallow compaction.

An interesting feature of the study of Wolstencroft et al., 2014 was that different data sets (RSL data and a record of vertical land motion along the Mississippi River) required different Earth viscosity models to satisfy. A possible explanation put forth by the authors was that this suggests different behaviours of the Earth over different timescales and in response to different loads, which was a feature of the ductile structure Earth models that we investigated in the previous chapter. In fact, this was my original motivation for investigating the Mississippi Delta sediment loading problem. However, the study I present here does not address the application of these models in the Mississippi Delta, because there is a clear step to be made in extending the analysis of Wolstencroft et al., 2014 before incorporating possible unnecessary complexity into the model.

In the study of Wolstencroft et al., 2014, the sea level was calculated in response to an input ice history, and then separately the Earth's deformation response to a sediment loading scenario was calculated, and then these two responses were combined. This is not gravitationally self-consistent, as it ignores the effects of the sediment load both on the gravity field and on the height of the water column when marine sediment displaces water. It was essentially a sensitivity test to estimate the size of the SIA signal relative to the GIA signal. Therefore, before investigating any effects of ductile viscosity structure, we chose to compute sea level and Earth deformation using a gravitationally self-consistent theory and standard layered viscous Earth models. A self-consistent theory for computing GIA and SIA together was developed by Dalca et al., 2013, and in the next section I describe this theory as well as how I implemented it into existing sea level codes. A recently compiled RSL database including sea-level indicators in the Delta region considered to be free from compaction (Love et al., 2016) allow us to refine estimates of Earth viscosity structure in the region. Finally, Wolstencroft et al., 2014 considered a relatively small class of Earth viscosity structures, and so by broadening our parameter space and using the updated RSL database, we more rigorously determine the relative impacts of SIA and GIA than was done in Wolstencroft et al., 2014.

3.2 A Self-Consistent Sea Level Theory

The original sea level theory of Farrell and Clark, 1976, described in the Introduction, is one for which static sea level is computed for a non-rotating Earth with fixed shorelines. The original sea level equation has been improved upon in the years since it was introduced, with the effects of Earth rotation (Milne and Mitrovica, 1998) and the effects of time varying shorelines (Peltier, 1994; Mitrovica and Milne, 2003, Kendall et al., 2005). A gravitationally self-consistent treatment for sea-level change that includes sediment loading was introduced relatively recently by Dalca et al., 2013. While the general response of the Earth-ocean system to a sediment load is not fundamentally different from the response to an ice load (in both cases a large mass deforms the Earth and gravitational potential surface describing sea level), there is one subtle difference between them. In particular, because ice is less dense than water, it is impossible to have grounded ice and ocean at the same position. This is not true for sediment, as a sediment load can exist equally on land or below sea level. This means that, when including sediment loading, care must be taken to accurately compute the ocean function (that describes the ocean and its boundary) as well as the thickness of the water column in areas where there is marine sediment. In the following we closely follow Dalca et al., 2013 to describe how the sea level equation must be modified to include sediment loading. For a simple visual reference, see Figure 3-3. We denote the height of the solid bedrock of the Earth as R, the thickness of the sediment as H, the thickness of the ice I, and the height of the gravitational potential surface coinciding with the top of the ocean surface as G. All these fields are functions of geographic position and time, i.e. $H = H(t, \theta, \phi)$, but for simplicity we will drop the geographic position dependency (understanding that it still exists) and express a field's value at time step i with a subscript, such as $H(t = t_i, \theta, \phi) = H_i$.

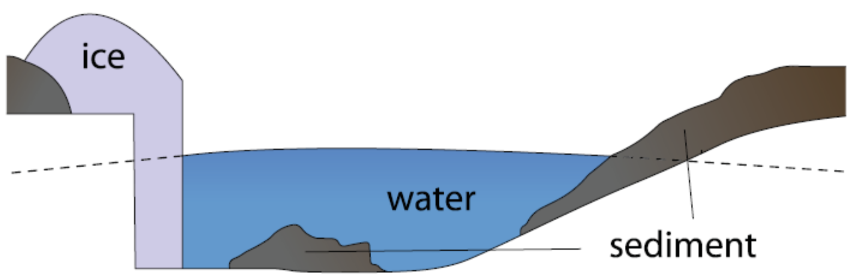

Figure 3-3: This figure (reproduced from Figure 1 a) of Dalca et al., 2013) illustrates the relevant quantities for a revised sea level equation that includes sediment redistribution. Sea level depends on the height of the gravitational potential surface describing the ocean surface (shown by the dashed line), the sediment thickness, ice thickness, and position of the solid bedrock underneath.

This gives us sea level (SL) at any given geographic position as

$$SL = G - (R + I + H). \tag{3.1}$$

Defined this way, sea level is the negative of the topography T,

$$T = (R + I + H) - G. \tag{3.2}$$

While sea level is defined globally, the thickness of the ocean is of course non-zero only where the ocean actually exists. We denote the ocean thickness S and define it as

$$S = C \times SL, \tag{3.3}$$

where C is the ocean function, $C = 1$ over the oceans (when $SL > 0$) and $C = 0$ otherwise. The total surface mass load, L, on the Earth can be written as a sum of the sediment, ice, and ocean loads as

$$L = \rho_w S + \rho_i I + \rho_s H, \tag{3.4}$$

where ρ_w, ρ_i, and ρ_s are the densities of ocean water, ice, and sediment, respectively. As the loading history is described by a series of Heaviside episodes, we consider discrete time steps, and changes between these discrete time steps. We denote a change in a quantity Z between time steps i and $i+1$ as $\delta Z_i = Z_i - Z_{i-1}$. A change in sea level between subsequent time steps is then

$$\delta SL_i = \delta G_i - (\delta R_i + \delta I_i + \delta H_i). \tag{3.5}$$

We may also write the total change from the initial time step to the current time step as $\Delta X_i = X_i - X_0$. Using this we can write the total change in the ocean thickness over time as

$$\Delta S_i = C_i SL_i - C_0 SL_0. \tag{3.6}$$

Now, using the fact that $SL_i = SL_0 + \Delta SL_i$, we can rewrite equation 3.6 as

$$\Delta S_i = C_i \Delta SL_i + SL_0 (C_i - C_0). \tag{3.7}$$

We can use this to obtain an expression for the incremental change in the ocean load at time i, δS_i, by using the fact that $\delta S_i = \Delta S_i - \Delta S_{i-1}$. We therefore have

$$\delta S_i = -\Delta S_{i-1} + C_i \Delta SL_i - T_0(C_i - C_0), \tag{3.8}$$

where we've used the fact that the sea level at $t = 0$ is the negative of the initial topography, T_0. Equation 3.8 can be considered the generalised form of the sea level equation. Equation 3.7 relates a total change in ocean thickness as the total change in sea level projected on to the area of the oceans, plus an additional term that accounts for migrating shorelines. We can write equation 3.8 more clearly in terms of previously defined physical quantities if we first consider the change in total sea level ΔSL to be a combination of a spatially uniform and spatially variable component,

$$\Delta SL_i = \Delta \mathcal{SL}_i + \frac{\Phi_i}{g}, \tag{3.9}$$

where Φ_i is a uniform shift to the gravitational potential, g is gravitational acceleration, and

$$\Delta \mathcal{SL}_i = \Delta \mathcal{G}_i - (\Delta R_i + \Delta H_i + \Delta I_i), \tag{3.10}$$

with $\Delta \mathcal{G}_i$ the spatially variable change in the gravitational potential (which will depend on changes in the total load, equation 3.4). We can then rewrite equation 3.8 as

$$\delta S_i = -\Delta S_{i-1} + C_i(\Delta \mathcal{SL}_i + \frac{\Phi_i}{g}) - T_0(C_i - C_0). \tag{3.11}$$

The uniform shift in the gravitational potential can be written as

$$\frac{\Phi_i}{g} = -\frac{1}{A_i}\frac{\rho_i}{\rho_w}\iint_\Omega \Delta I_i \; d\Omega - \frac{1}{A_i}\iint_\Omega C_i \Delta \mathcal{SL}_i \; d\Omega + \frac{1}{A_i}\iint_\Omega T_0(C_i - C_0) \; d\Omega \tag{3.12}$$

where Ω represents the surface of the Earth, and $A_i = \iint_\Omega C_i \; d\Omega$ is the area of the oceans at time i. In equation 3.12, the first term represents a uniform transfer of mass between the ice sheets and the ocean. The second term is a global surface integral of the spatially variable component of sea level, and represents changes in the volume of the ocean due to spatially variable processes, such as changes in the height of the bedrock or the addition of marine sediment. The final term represents changes in volume corresponding to changes in coastlines from the initial time step to time i. Equations 3.11 and 3.12 describe the generalised sea level equation. In the next section I will describe how I modified our existing sea level solver to accommodate sediment loading.

3.3 Implementation

Before making any changes to the sea level code it is necessary to enforce conservation of mass by making sure that any sediment load incorporated into the model has a corresponding erosion of mass. In our particular case, the sediment load is composed of five component loads with their own individual chronologies and densities (see Figure 3-4). Therefore the first step is to combine the individual sediment load histories into combined total sediment height and total sediment mass histories.

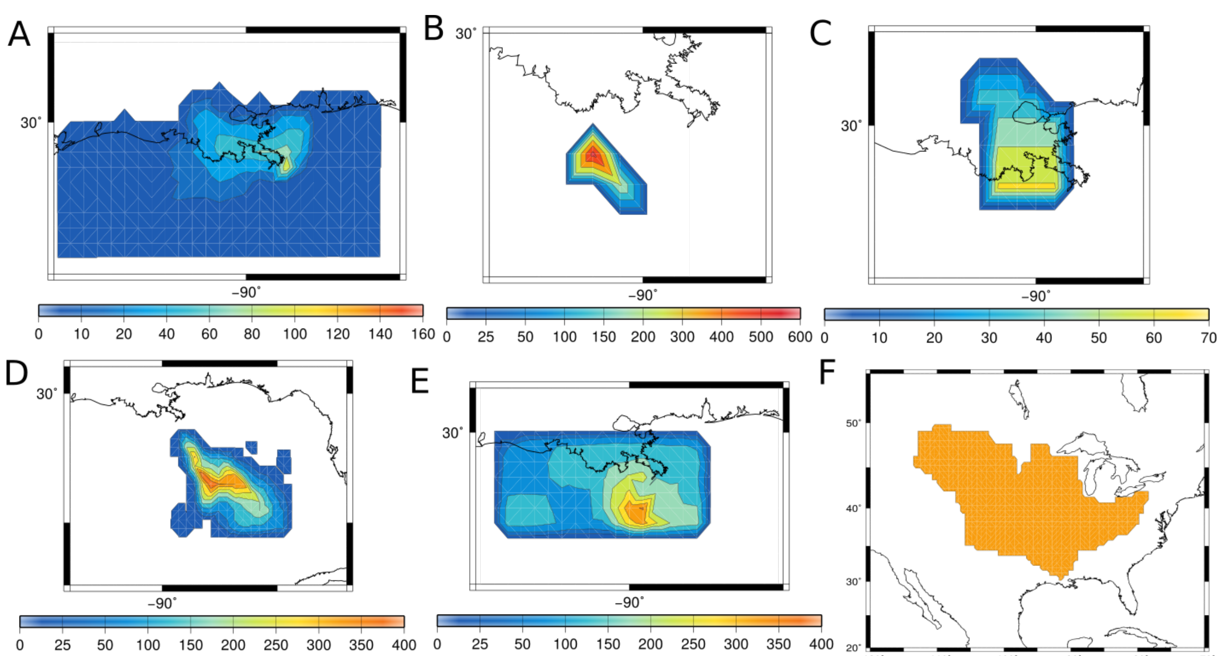

Figure 3-4: This figure (reproduced from Kuchar et al., 2018a) shows the geometry of the individual components of the sediment load (A-E), as well as the geometry of the Mississippi Catchment (F) used as an erosion zone for conservation of mass.

The total sediment mass m_i deposited in the delta at a time i is computed as

$$m_i = \sum_n \rho_n V_{n,i}, \tag{3.13}$$

where ρ_n is the density of the nth component of the sediment load and $V_{n,i}$ is its volume. The height shift then applied to the erosion zone at that time step is computed as

$$h_i = \frac{m_i}{A_{ez}\rho_{avg}}, \tag{3.14}$$

where A_{ez} is the area of the erosion zone and ρ_{avg} is the average sediment density.

A key difference in our algorithm from that of Kendall et al., 2005, is in our definition of topography and sea level. While Kendall et al., 2005 define the topography as the height of the solid upper boundary of the Earth, which may be composed of ice or sediment or the solid surface of the Earth itself, the sea level code developed by Dr. Milne defines the topography only by the solid Earth surface (that is, $T = R - G$ and $SL = G - R$). This leads to several subtle differences in the implementation of the sea level algorithm. In particular, in our implementation we have the sea level defined only as the difference between the gravitational potential surface G and the solid Earth surface R without any consideration of the sediment load. However, when we compute the actual ocean depth, which is the thickness of the water column, then it is necessary to correct for the sediment thickness:

$$SL_i = G_i - R_i \tag{3.15}$$

$$S_i = C_i \left(SL_i - H_i\right). \tag{3.16}$$

This is a little less elegant than than the definitions used in Kendall et al., 2005, but is motivated by practical considerations. In particular, when comparing sea level predictions to historical data, it is this definition of sea level that is recorded by the data (for more on this point, see section 2.1 in Kuchar et al., 2018a).

As described in Kendall et al., 2005, the sea level algorithm consists of several loops. There is a loop through the time steps over the entire deglacial cycle to determine the change in ocean load depth (equation 3.11) at each time step. There is also an iterative loop at each time step that solves equation 3.11 for the ocean depth at a given time step until convergence is reached. Finally, there is an iteration loop that repeats the calculations over the entire deglacial history until the calculated initial topography converges. Because the algorithm is described in detail in Kendall et al., 2005, I'll limit the discussion here to the changes that need to be made in order to include the sediment load in our framework.

The sea level code has two stages, which we will refer to as Stage 1 and Stage 2. The first stage determines the initial topography (recall from equations 3.8 and 3.11 that we need to determine the topography at the initial time step), as well as the ocean function for each time step, and the second computes Earth deformation and solves the sea level equation. Denoting the present-day topography as T_p, the paleotopography at some time T_i can then be computed as

$$T_i = T_p - RSL_i + (H_i - H_p), \tag{3.17}$$

where $RSL_i = SL_i - SL_p$ is the relative sea level at time i, and where H is the height of the sediment load. On the first iteration loop over the glacial cycle, the sea level has not been computed and is set to zero, so $RSL_i = 0$, and therefore the first guess for paleotopographyy is the present-day topography (plus a sediment correction). The present-day topography we use is ETOPO1 (Amante and Eakins, 2009) which is a 1 arc-minute resolution map of the Earth's solid surface. Because the sediment load we are including (which is hundreds of meters thick in the present-day) must already be present in the topography map, this necessitates the third term in equation 3.17, which removes the present-day sediment height from the topography, and adds the sediment height of the appropriate time step. The ocean depth is defined as the negative of the topography, and the ocean function is $C_i = 1$ when $T_i \leq 0$, and $C_i = 0$ otherwise. Additionally, at this stage there is a check for floating ice, where if the mass of the ocean load at a given location is greater than that of the ice, then the ocean function is set to 1.

In stage 2, the deformation of the Earth's surface in response to the ice, ocean, and sediment loads is computed by convolving these loads with the appropriate Love numbers, and thus solving equation 3.11. At a given time step, the deformation of the Earth includes an elastic component that depends on the full mass load at that time step (equation 3.4), and a viscous component that depends on the full load history up to that time step. We will reproduce equation 3.11 here for convenience as we discuss how it must be modified in our algorithm:

$$\delta S_i = -\Delta S_{i-1} + C_i(\Delta\mathcal{SL}_i + \frac{\Phi_i}{g}) - T_0(C_i - C_0).$$

The first term in the above expression is known because for a given time step i the ΔS_{i-1} have already been computed. The second and third terms are modified to account for the sediment height:

$$\delta S_i = -\Delta S_{i-1} + C_i(\Delta\mathcal{SL}_i - H_i + \frac{\Phi_i}{g}) - (T_0 + H_0)(C_i - C_0). \tag{3.18}$$

At a given time step, the ocean load increment δS_i depends on the calculated sea level $\Delta\mathcal{SL}_i + \frac{\Phi_i}{g}$, which is itself a function of the ocean load. This is therefore solved for iteratively, where the first guess for sea level is the eustatic sea level (a uniform shift of $\delta SL = \frac{\rho_I \delta I_i}{\rho_w A_i}$), where A_i is the area of the ocean at that time step.

Steps 1 and 2 are repeated three times for convergence of the initial topography.

3.4 Research Summary and Conclusions

After modifying the sea level code with the theory of Dalca et al., 2013, and with access to a realistic sediment load history for the Mississippi Delta (Wolstencroft et al., 2014), we set out to determine the following:

1. How much does the SIA signal impact computed estimates of past sea-level change?

2. What are the implications of (1) for estimating Earth viscosity structure from the RSL data in this region?

3. Can we better quantify the contribution of SIA and GIA to present-day land motion in the region, and also estimate the compaction contribution?

A recent study by Love et al., 2016 determined sea level projections for the Atlantic and Gulf Coasts of North America using a high quality database of sea-level index points, including data for the Gulf coast region in particular that was determined to be free from the effects of compaction. We used this same compaction-free data in our study, and explored a large parameter space of Earth viscosity models as well as several ice histories (with choices of ice histories informed by the study of Love et al., 2016, who considered more ice histories but at a lower resolution). We found that our optimal parameters (that is, the ones that produce a sea level history with the lowest data-misfit) were nearly the same as those of Love et al., 2016, with the same preferred ice history and mantle viscosity, but a thinner lithosphere. The mantle viscosity profile of the optimal model is fairly stiff, which has the effect of suppressing the influence of the relatively small sediment load. This close agreement indicates that the data correction applied by Love et al., 2016 is a good substitute for a full SIA treatment as we performed here. For our optimal model, the SIA contribution to future sea level projections was found to be at most only a few centimetres on a centennial time scale, and is therefore much less important than other processes such as compaction. We calculated present-day vertical land motion rates from GIA and SIA at the geographic positions of GPS stations, and by removing these signals from the GPS data we calculated estimates of the deep compaction signal, which ranged from 1.4 to 5.5 mm/year. We therefore conclude that the subsidence rates in the Mississippi Delta can not be caused primarily by isostatic motion, and other processes (most notably compaction, but also fluid extraction and faulting) must be the primary drivers of subsidence in this region. I note there is a typo in the proceeding manuscript, where Equation 7, defining the data-model misfit, contains a negative separating the two terms under the square root, instead of the proper plus. This has been brought to the attention of the Journal, but as of yet not updated.

3.5 Article 2: The Influence of Sediment Isostatic Adjustment on Sea Level Change and Land Motion Along the U.S. Gulf Coast

Statement of Contribution

The following manuscript is my own written work, carried out under the supervision of Dr. Milne. I modified the sea-level code of Dr. Milne to incorporate the sediment load theory of Dalca et al., 2013, and produced all model output and figures. Martin Wolstencroft developed the sediment load history for the Mississippi Delta region for his own study (Wolstencroft et al., 2014), which we used here. We computed misfits using scripts written by Ryan Love. Lev Tarasov developed the ice histories, and had valuable insight into uncertainty estimations. The sea level data was compiled by Mark Hijma.

AGU PUBLICATIONS

JGR

Journal of Geophysical Research: Solid Earth

RESEARCH ARTICLE

10.1002/2017JB014695

Key Points:

- Along the Gulf Coast, sediment isostatic adjustment needs to be considered, though it is not a dominant contributor to sea level change
- Model results show that sediment loading can influence sea level by up to several meters in the Holocene
- By removing modeled isostatic subsidence from GPS records we estimate the deep compaction signal

Supporting Information:

- Supporting Information S1
- Table S1
- Table S2

Correspondence to:
J. Kuchar,
jkuch083@uottawa.ca

Citation:
Kuchar, J., Milne, G., Wolstencroft, M., Love, R., Tarasov, L., & Hijma, M. (2017). The influence of sediment isostatic adjustment on sea level change and land motion along the U.S. Gulf Coast. *Journal of Geophysical Research: Solid Earth*, *122*. https://doi.org/10.1002/2017JB014695

Received 11 JUL 2017
Accepted 15 NOV 2017
Accepted article online 20 NOV 2017

The Influence of Sediment Isostatic Adjustment on Sea Level Change and Land Motion Along the U.S. Gulf Coast

Joseph Kuchar[1], Glenn Milne[2], Martin Wolstencroft[3], Ryan Love[4], Lev Tarasov[4], and Marc Hijma[5]

[1]Department of Physics, University of Ottawa, Ottawa, Ontario, Canada, [2]Department of Earth and Environmental Science, University of Ottawa, Ottawa, Ontario, Canada, [3]JBA Risk Management Limited, Skipton, UK, [4]Department of Physics and Physical Oceanography, Memorial University of Newfoundland, St. John's, Newfoundland and Labrador, Canada, [5]Department of Applied Geology and Geophysics, Deltares, Utrecht, Netherlands

Abstract Sea level rise presents a hazard for coastal populations, and the Mississippi Delta (MD) is a region particularly at risk due to the high rates of land subsidence. We apply a gravitationally self-consistent model of glacial and sediment isostatic adjustment (SIA) along with a realistic sediment load reconstruction in this region for the first time to determine isostatic contributions to relative sea level (RSL) and land motion. We determine optimal model parameters (Earth rheology and ice history) using a new high-quality compaction-free sea level indicator database. Using the optimal model parameters, we show that SIA can lower predicted RSL in the MD area by several meters over the Holocene and so should be taken into account when modeling these data. We compare modeled contemporary rates of vertical land motion with those inferred using GPS. This comparison indicates that isostatic processes can explain the majority of the observed vertical land motion north of latitude 30.7°N, where subsidence rates average about 1 mm/yr; however, subsidence south of this latitude shows large data-model discrepancies of greater than 3 mm/yr, indicating the importance of nonisostatic processes. This discrepancy extends to contemporary RSL change, where we find that the SIA contribution in the Delta is on the order of 10^{-1} mm/yr. We provide estimates of the isostatic contributions to 20th and 21st century sea level rates at Gulf Coast Permanent Service for Mean Sea Level tide gauge locations as well as vertical and horizontal land motion at GPS station locations near the MD.

Plain Language Summary We have modeled solid Earth deformation and sea level change in response to past ice-ocean and ocean loading as well as sediment loading in the Mississippi Delta region. We find that sea level change and Earth deformation related to sediment loading is nonnegligible, but that it is a small signal when compared to other processes contributing to land subsidence (e.g., sediment compaction). We estimate part of the compaction signal by comparing our modeled results to GPS records and find that the Earth deformation component of the vertical motion recorded at GPS stations is roughly a tenth that of compaction.

1. Introduction

The average annual global sea level rise since 1993 is on the order of 3 mm/yr (Watson et al., 2015). The Mississippi Delta (MD) region, on the other hand, is experiencing contemporary relative sea level (RSL) rise as high as 13 mm/yr (Jankowski et al., 2017), making it an acutely vulnerable area. Rising sea level increases risk of extreme weather events and coastal flooding and contributes to wetland loss, which is an important natural feature that mitigates damage done by regular hurricanes and storm surges in the area (Day et al., 2007).

Predicting relative sea level rise is complicated because there are many contributing factors that operate on different time and spatial scales (Church et al., 2013). Processes driving contemporary sea level change include thermal expansion, contemporary land ice melt, ocean dynamics, and long timescale processes such as isostatic motion associated with both past ice changes (glacial isostatic adjustment or GIA) and the erosion and deposition of sediment (sediment isostatic adjustment or SIA). Global contemporary sea level change is dominated in most coastal areas by ocean steric/dynamic and land ice meltwater contributions, but other processes can be equally or more important in some locations; for example, sea level rise in the MD region of the Gulf coast has a large land subsidence component. This is partly due to the proximity of the MD to the former Laurentide ice sheet, which makes it susceptible to GIA related subsidence (Clark et al., 1978; Potter & Lambeck, 2003; Wolstencroft et al., 2014). Additionally, the MD is the depocenter of the Mississippi River drainage basin, the fourth largest drainage basin in the world. The sediment accumulated in the MD contributes to crust and mantle deformation related subsidence as well as sediment compaction-related subsidence (Blum et al., 2008). All of these processes need to be understood to make accurate projections of regional sea level for the MD and adjacent coastline. Regional sea level rise is distinct from global RSL rise as even in the absence of local subsidence sea level is typically not equal to global mean sea level (Love et al., 2016; Slangen et al., 2014).

SIA, which is the ongoing deformation of the solid Earth in response to loading of sedimentary deposits, has been proposed as a primary mechanism for subsidence in the MD region as far back as Fisk (1939). However, when the subsidence rate is modeled as a result of SIA alone, it is typically found that either the sediment loads required are very large (e.g., Ivins et al., 2007) or else the required mantle viscosity or lithosphere thickness needed to reproduce the measured uplift rates is unrealistically low (e.g., Jurkowski et al., 1984). Indeed, a study that compared subsidence rates in the MD with those in the nearby Chenier Plain (where effects of SIA are expected to be minimal) found a differential SIA-driven subsidence rate of only 0.15 ± 0.07 mm/yr (Yu et al., 2012), leaving a large part of the subsidence rate budget to be filled by other processes like GIA and sediment compaction. The MD is sufficiently close to the formerly glaciated region of North America to also experience ongoing deformation as a result of GIA, which results in contemporary subsidence on the order of 1 mm/yr (Wolstencroft et al., 2014). Additionally, it is known that nonisostatic processes such as sediment compaction are a dominant contributor to subsidence and sea level rise in the MD, along with subsidence related to fluid extraction and faulting. Sediment compaction can lead to rates of subsidence of up to 5 mm/yr on millennial timescales, and up to 10 mm/yr on decadal timescales (Törnqvist et al., 2008.) Extraction of groundwater led to subsidence rates in heavily developed areas, such as New Orleans, of tens of mm/yr (Jones et al., 2016), and extraction of hydrocarbons in Southern Louisiana and Texas led to subsidence rates of tens of mm/yr, 3 orders of magnitude higher than the "background" geologic subsidence rate (Morton et al., 2006).

Wolstencroft et al. (2014) modeled deformation and uplift rates in the MD and accounted for both GIA and deformation caused by sediment loading; they concluded that SIA alone could not account for the high rates of observed subsidence in the MD, with a maximum estimated rate of subsidence from SIA of about 0.5 mm/yr. The total subsidence rate from GIA and SIA was estimated to be at most 2 mm/yr, from which they concluded that while it was clear GIA needed to be considered alongside SIA, neither of these processes (nor their sum) could explain the high subsidence rates observed in the area. The work presented here can be considered an extension of the Wolstencroft et al. study (hereafter referred to as W2014), who computed GIA and sediment-driven Earth deformation separately and summed the results, whereas we have incorporated the sediment load history (along with the inclusion of an erosion zone for mass conservation) into our GIA model for self-consistency and greater model accuracy (Dalca et al., 2013). A primary motivation for doing this is to make use of a recently compiled and quality-assessed RSL data base (Hijma et al., 2015; Love et al., 2016) for constraining model parameters. An important quality of these data is that they are not significantly affected by compaction (Love et al., 2016) and so represent one of the few data sets in the region that can provide accurate constraints on vertical motion of the underlying consolidated strata. We also consider a much larger parameter space of ice loading histories and Earth viscosity models compared to W2014: the number of Earth rheologies has increased from 8 to 400, and the number of ice histories has increased from 1 to 4.

The importance of SIA effects on RSL modeling in the Indus River basin and Arabian Sea has been demonstrated by Ferrier et al. (2015), who found that the perturbation to current rates of change of RSL in the region caused by sediment fluxes is nonnegligible. A recent study (Van der Wal & IJpelaar, 2017) applied the sea level theory of Dalca et al. (2013) to examine the influence of glacially induced sediment redistribution to modeled observables in Fennoscandia for the last glacial cycle. They found that while the effects on RSL and uplift rates were relatively small (few meters for Holocene RSL; order of a tenth of a mm/yr for present-day uplift rates), they represent a significant bias to the modeled signal. One aim of this work is to quantify the influence of SIA on RSL in the MD region to determine if the application of RSL models that simulate SIA is necessary. A recent study considered RSL observations from the U.S. Gulf Coast to constrain GIA model parameters and place bounds on the contribution of this process to future RSL change (Love et al., 2016). The model they applied did not include the influence of SIA and so they removed the contribution of this process using estimates of this signal from geological observations (Yu et al., 2012). By explicitly modeling the SIA process, we can assess the accuracy of the RSL data "correction" applied by Love et al. (2016) and consider the relative contribution of GIA and SIA to future RSL changes along the U.S. Gulf coast. We find the correction applied by Love et al. to be reasonable, albeit slightly conservative.

Measurements of vertical land motion using the Global Positioning System (GPS) (Dokka et al., 2006; Karegar et al., 2015; Yu & Wang, 2016) and interferometric synthetic aperture radar (InSAR) (Dixon et al., 2006; Jones et al., 2016) provide important observational control on the processes responsible for subsidence in the MD region. The InSAR rates record the sum of all processes (e.g., compaction and isostasy) on the inferred vertical motion. The interpretation of the GPS-inferred rates is less straightforward because of variations of the depth to which receiver monuments are anchored in the surface sediment and the contribution of compaction below this depth. As tabulated in Karegar et al. (2015) (see their Table DR1), the foundation depth (where known) ranges from 1 m to 36.5 m for the GPS sites they considered and so the contribution from compaction to the inferred vertical rates will likely vary from sites to site. Our model parameters are estimated without the use of GPS data, and using only RSL data that are not significantly affected by compaction. Our model results can therefore be used to estimate the isostatic contribution to present-day subsidence rates, allowing us to estimate the contribution of nonisostatic processes (such as compaction) to the GPS rates.

2. Methodology

2.1. The Model

The GIA model has three components: a loading history (that is partitioned into ice, ocean, and sediment components) to provide a forcing for the model, an Earth model to calculate deformational response of the solid Earth, and a sea level equation to compute changes in sea level in response to changes in surface loads and Earth deformation.

The framework for computing sea level on a spherical Earth was developed by Farrell and Clark (1976), who used a Green's function approach to determine sea level changes in response to changes in ice loads on a nonrotating Earth with fixed shorelines. The equilibrium sea level lies on a surface of constant gravitational potential, and because changes to the distribution of mass of the ocean change the gravitational field and deform the Earth, the result is an integral equation where the ocean load is solved for iteratively. The sea level equation as presented in Farrell and Clark (1976) can be written as

$$\Delta SL = \Delta G - \Delta R - \Delta I. \tag{1}$$

where G is the height of the equipotential defining the ocean surface, R is the height of the solid surface, and I is the height of the ice surface. The sea level equation has since been generalized to include the effects of rotation (Milne & Mitrovica, 1998), shoreline migration (Kendall et al., 2005; Mitrovica & Milne, 2003), and sediment transfer (Dalca et al., 2013), all of which are incorporated here. When computing changes in sea level that include sediment transfer, we also have to consider the height of the sediment field, so the sea level equation is modified:

$$\Delta SL = \Delta G - \Delta R - \Delta I - \Delta H, \tag{2}$$

where H is the height of the sediment load. In general, a surface load change (including ice, sediment, and ocean) will deform the Earth and the gravitational potential field. The total load forcing the model can be written as

$$L = \rho_I I + \rho_w S + \rho_H H, \tag{3}$$

where ρ_I, ρ_S, and ρ_H are the densities of ice, water, and sediment, respectively, and S is the ocean load (obtained from the product $SL \cdot \beta$, where β is unity over the oceans and zero otherwise). The ocean will change to conform to its new equipotential surface, which changes the surface load of the Earth and induces further deformation.

It is the above definition of sea level (equation (2)) that is solved for in the sea level equation to compute the redistribution of ocean water and therefore the ocean load.

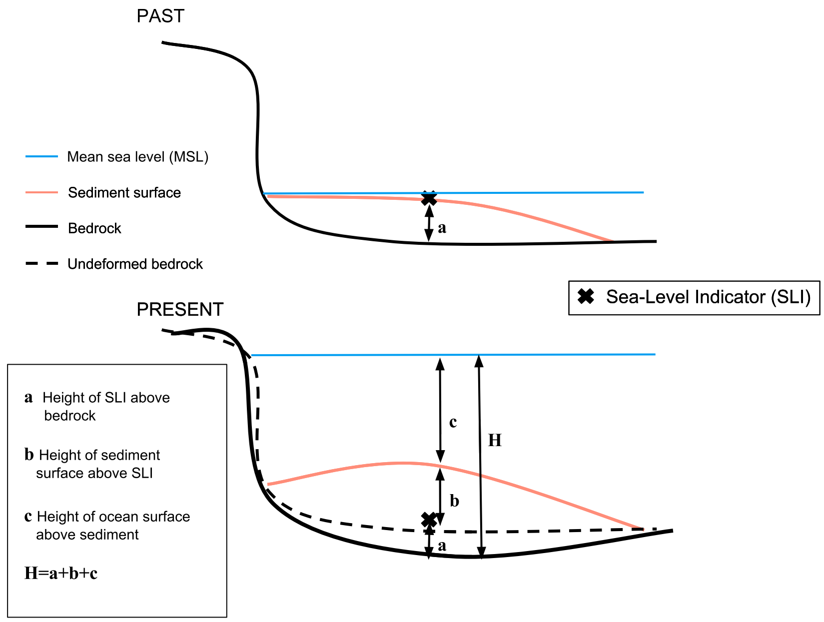

Figure 1. Diagram illustrating that the RSL recorded by a sea level indicator is the same as the RSL measured with respect to the solid Earth surface, not with respect to the changing sediment surface.

Relative sea level at some historic time t_i is defined with respect to sea level at present time (t_p) as

$$\mathrm{RSL}(t_i) = \mathrm{SL}(t_i) - \mathrm{SL}(t_p). \tag{4}$$

Following Ferrier et al. (2015), we also define sea level and relative sea level that does not include the direct effect of sediment and ice as

$$\mathrm{SL}_{\mathrm{GR}} = G - R, \tag{5}$$

$$\mathrm{RSL}_{\mathrm{GR}}(t_i) = \mathrm{SL}_{\mathrm{GR}}(t_i) - \mathrm{SL}_{\mathrm{GR}}(t_p). \tag{6}$$

This is a field that includes the gravitational and deformational effects of all surface loads (with the ocean load determined as in equation (2) with a total load given by equation (3)), but not the direct height contribution of the sediment load. As discussed by Ferrier et al. (2015), this is a useful field to consider because it allows us to analyze the isostatic effects of the load history without complications arising from uncertainties in the sediment height history.

An important aspect of this study is the comparison of predicted and reconstructed RSL to constrain Earth model parameters. As described in the following, it is the modified sea level $\mathrm{SL}_{\mathrm{GR}}$ that more closely represents the sea level as measured by sea level indicators (see Figure 1). Typically, relative sea level is defined as the height from the solid surface (ocean floor) to the time-averaged height of the ocean surface. Paleo-RSL is the difference in this measurement between a given time in the past and the present. Because the top of the sediment pile defines the ocean floor in many locations, a change in height of the ocean floor can be caused by changes in marine sediment thickness, changes in the height of the solid Earth surface, or a combination of these. In Figure 1 we show a sample loading scenario involving changes of sediment and ocean loading at two time steps. The RSL measured with respect to the ocean floor height when including sediment change in this scenario would be $-\mathbf{c}$, while ignoring sediment height change ($\mathrm{RSL}_{\mathrm{GR}}$) would give $-(\mathbf{c}+\mathbf{b})$. As illustrated in Figure 1, the latter is the height change that would be estimated via a reconstruction of RSL based on the indicator shown. This is true so long as the distance between the indicator and the solid Earth surface (**a** in Figure 1) does not change in time, or equivalently, so long as we can neglect compaction in the sediment column underneath the indicator. Essentially, the isostatic uplift or subsidence of the sea level indicator is the same as that of the solid Earth beneath it, and for this reason changes in sea level with respect to the indicator are the same as those with respect to the bedrock below it. We will therefore be considering SL_{GR} and RSL_{GR} exclusively in the following sections.

The Earth models used in this study are spherically symmetric Maxwell bodies (e.g., Peltier, 1974) with elastic and density structures given by the preliminary reference Earth model (Dziewonski & Anderson, 1981). They are parameterized by their lithosphere thickness and upper and lower mantle viscosities. The lithosphere is characterized by a high viscosity to simulate an elastic response on millennial timescales. The upper mantle extends from the base of the lithosphere to the 660 km seismic discontinuity, and the lower mantle extends from 670 km to the core-mantle boundary. The upper mantle viscosity (UMV) ranges from 0.05×10^{21} Pa s to 5×10^{21} Pa s, and the lower mantle viscosity (LMV) ranges from 1×10^{21} Pa s to 90×10^{21} Pa s. We consider four lithosphere thicknesses of 46 km, 71 km, 96 km, and 120 km. In all we compute the GIA response for 400 Earth rheologies for every loading history.

For the ice load component of the model, we have incorporated four reconstructions of the North American ice complex from Tarasov et al. (2012) into a background ice history supplied by ICE-5G (Peltier, 2004). The MD region is close enough to the former Laurentide Ice Sheet that present-day subsidence in the region is associated both with ongoing collapse of the peripheral bulge of the ice sheet as well as SIA effects. The Tarasov et al. reconstructions are glaciological model output calibrated against RSL, marine limit, and geodetic data using a Bayesian statistical analysis and are more realistic than the North American component of ICE-5G. Because these models were calibrated against RSL and geodetic data using a specific Earth viscosity structure, there is an inconsistency in using these regional ice histories (as well as the ICE-5G history as a background model) and varying the Earth rheology as we do here. Given that our region of interest is a considerable distance from the locations of the data used to constrain the adopted ice models, we believe that this inconsistency does not impact our primary conclusions. Love et al. (2016) incorporated 35 model reconstructions of the North American ice complex, and three of the reconstructions we chose (1087, 1243, and 1287) were found by Love et al. to fit the Gulf coast RSL data reasonably well, while the fourth model (7042) was chosen for contrast. We consider only four ice reconstructions because the RSL data are relatively insensitive to this aspect of the GIA model (e.g., see Love et al., 2016, Figure S12). Additionally, to capture the sediment load accurately, we need to run our model at a relatively high spherical harmonic truncation (degree and order 512). These runs take approximately 4 times longer than the more standard truncation of degree and order 256 and so time constraints become an issue.

The sediment load component was originally published in W2014 and is itself a combination of results from Kulp et al. (2002), Stelting et al. (1986), Blum et al. (2008), and Coleman and Roberts (1988). The complicated structure of the load makes it advantageous to decompose it into five components referred to as *canyon*, *delta*, *fan*, *shelf*, and *valley*, each with their own density and chronology. Each load is applied linearly over its loading period. The load geometries are shown in Figure 2, and their corresponding densities and chronologies are given in Table 1. The sediment load also includes an erosion zone, for which we have taken the same Mississippi catchment area as in Dalca et al. (2013) (Figure 2f). The model requires conservation of mass, and therefore, any addition of mass to the sedimentation zone is balanced as a constant height decrease from the erosion zone.

Significant uncertainty exists in the sediment component of the loading model, as the precise chronologies can be difficult to constrain and assigning reasonable densities to sediment load components is not an easy task (Wolstencroft et al., 2014). A limitation of this study is that we only have one reconstruction of the sediment load, and no associated uncertainty. To explore the impact of uncertainty in the sediment load component, we have performed sensitivity tests with variations in sediment density (±15% density variations) as well as chronology (the onset of the delta load was shifted to 8 kyr from 6 kyr, resulting in a slower rate of deposition for this component of the load). The effect these changes had on computed RSL for our choice of parameters was very small (Figure S1 in the supporting information), and so for the remainder of this analysis we consider only the published reconstruction of W2014. We note also that our densities are generally greater than those recorded in W2014 because for marine sediment they used the relative density of the sediment to account for the displaced ocean water, which was necessary because their sediment loading was not self-consistently integrated into their sea level model. Using the full sea level theory outlined in Dalca et al. (2013), we do not need to distinguish between marine and terrestrial densities.

For every ice history, we compute the GIA response both with and without the effects of the sediment load, which results in 3,200 model runs.

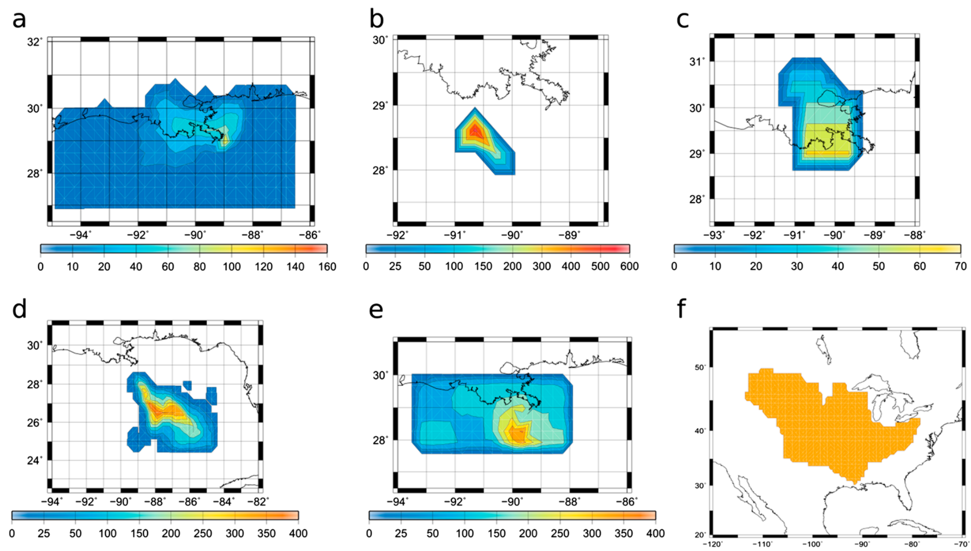

Figure 2. Sediment load geometries. (a) delta, (b) canyon, (c) valley, (d) fan, (e) shelf, and (f) the erosion zone. In Figures 2a–2e the scalebars represent height in meters. The sediment load component was originally published in W2014 and is a combination of results from Kulp et al. (2002), Stelting et al. (1986), Blum et al. (2008), and Coleman and Roberts (1988). The erosion zone is as in Dalca et al. (2013).

2.2. The Data

The full U.S. Gulf Coast RSL data set we use in this study was presented in Love et al. (2016) and consists of 291 sea level index points (SLIPs). For the statistical analysis of our model results we consider only a subset of index points that are minimally affected by compaction, which reduces our number of SLIPs to 134. We consider a sample to be compaction-free when: (1) they were taken at or less than 0.2 m above the consolidated substrate or (2) the sampled peat layer starts at the modern surface, rests directly on top of the consolidated substrate, and the sample was taken from a continuous core. In this case the depth of the sample to the consolidated substrate is irrelevant or (3) the depth to the consolidated substrate is more than 0.2 m, but less than 3% of the total depth. Love et al. applied a correction to data in the MD region to account for SIA of 0.25 mm/yr for data in the range (−92, −89) degrees longitude, and a correction of 0.1 mm/yr for data in the ranges of (−89, −87.5) and (−93.5, −92) degrees longitude. We use the uncorrected data, as we are directly calculating the SIA response. A contribution of this research will be to evaluate the accuracy of these corrections.

In our RSL figures showing model results compared to RSL data (Figures 6 and 7 and the supporting information) we use the full selection of SLIPs, but highlight those that are compaction-free. In our statistical analysis, each SLIP is considered individually, and at the location it was measured, but for visual analysis of RSL curves we define aggregate sites at data cluster locations. We show the spatial RSL data distribution, along with our aggregate sites for RSL curve visualization, in Figure 3.

Table 1
Sediment Load Chronologies and Densities

Load component	Chronology (kyr BP)	Density (kg/m^3)
Canyon	29–22, 22–12	1,800
Delta	6–0	1,500
Fan	55–10	1,500
Shelf	80–24	1,800
Valley	30–11.5, 11.5–6	1,500

Note. The canyon and valley load chronologies are for erosion followed by deposition. These densities are different from those of W2014 because they considered density relative to water rather than air given the limitations of their ocean load model.

We also compare present-day subsidence rates for our optimal parameter set with published GPS data (Karegar et al., 2015; Yu & Wang, 2016). We note that the model is calibrated only with compaction-free RSL data, and so model results are independent of GPS data, which are used only for model-data comparison. The Karegar et al. data set (Karegar et al., 2015, Table DR1) comprises 36 GPS stations with a spatial coverage extending from the delta shoreline to a latitude of 33.5°. Our model parameters are determined by comparison with RSL data, and so we limit our selection of GPS data to 31 GPS stations by considering only data extending up to 32°, to remain near the coast. These data also include depth to station anchor (where known), ranging from 1 m depth to over 30 m depth. We also include a selection of five stations from Yu and Wang (2016), chosen to extend our GPS

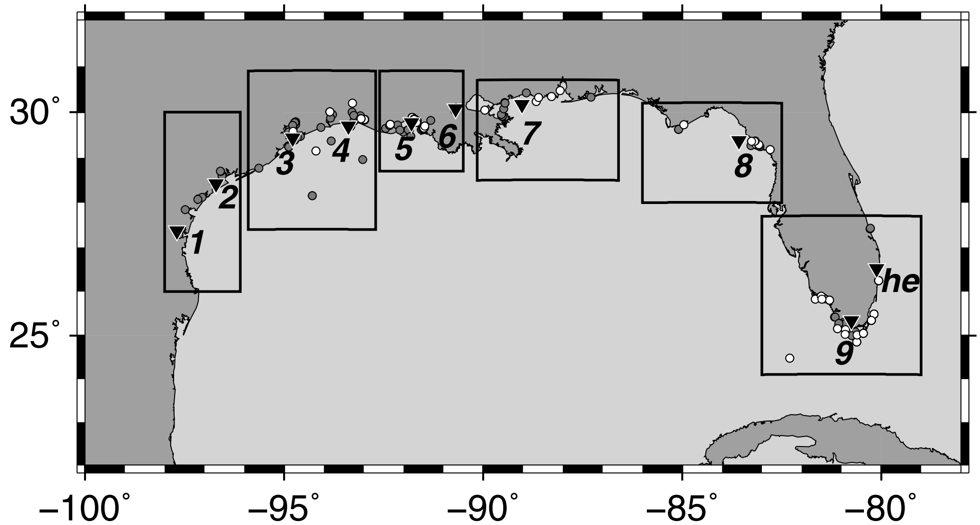

Figure 3. RSL data distribution with compaction-free data shown by white circles, other data shown by gray circles, and with aggregate sites for visualization by black triangles. The aggregate sites are (1) South Texas, (2) Central Texas, (3) East Texas, (4) West Louisiana, (5) West Mississippi Delta, (6) East Mississippi Delta, (7) Mississippi, (8) North West Florida, (9) South Florida, and (10) South East Florida. The six regions shown by rectangular boxes are used for spatial data weighting (see section 2.3). The RSL data were originally published in Love et al. (2016).

comparison farther east than if we were to consider the Karegar et al. data alone, while remaining in or near the Delta (Yu & Wang, 2016, Table A1).

We separate the GPS stations into two groups; those we believe to be grounded in consolidated Pleistocene sediment, and those grounded in Holocene sediment. The stations grounded in Pleistocene sediment should not be affected by compaction, and therefore should be reliable records of isostatic motion. The stations anchored in Holocene sediment record isostatic motion, as well as compaction that occurs at or below their anchoring depth. As we are only modeling GIA and SIA, model-data misfits can help us evaluate the magnitude of the deep compaction signal at these stations. These can be considered lower bound estimates for compaction, as the GPS stations do not record shallow compaction occurring above their anchoring depth (Jankowski et al., 2017). We note that the reference frame implicit in our modeled uplift rates (center of mass that includes deformation of the solid Earth as well as mass redistribution in the ice, ocean, and sediment loads) is different to that used to determine the rates via GPS (Blewitt, 2003). However, this issue likely produces data-model uplift rate differences that are uniform across our study region with amplitude at the sub-mm/yr level (Argus, 2012) and so is a relatively minor contribution to the rate differences evident in Figures 9, 10, S11, and S12 and Table 3.

2.3. Optimal Parameter Estimation and Uncertainty Bounds

We follow the procedure outlined in Love et al. (2016), where for each SLIP location, an RSL curve is computed and the minimum distance between each SLIP and the RSL curve is found. The misfit parameter is computed by

$$\delta = \frac{\sqrt{\sum_{n=1}^{N} \frac{\left(\mathrm{RSL}_{\mathrm{data},n} - \mathrm{RSL}_{\mathrm{model},n}\right)^2}{\Delta_{\mathrm{RSL},n}{}^2} - \frac{\left(t_{\mathrm{data},n} - t_{\mathrm{model},n}\right)^2}{\Delta_{t,n}{}^2}}}{N} \tag{7}$$

where $\Delta_{\mathrm{RSL};n}$ and $\Delta_{\mathrm{t};n}$ are the estimated 2σ uncertainties in the reconstructed RSL and age of the nth SLIP.

The optimal parameter set (that is, combination of load history and Earth rheology) is the one that minimizes this misfit parameter δ.

Equation (7) assumes that the data are independent, which is not necessarily a valid assumption for RSL index points. To minimize biases incurred by this assumption, we applied a data-weighting scheme where uncertainties were scaled by a weight factor of $w_i = \sqrt{\frac{n_i}{N}}$, where n_i is the number of index points in a subregion and N is the total number of index points (Briggs & Tarasov, 2013). We also incorporate a normalization

Table 2
Minimum Misfit Parameters for Each Ice History and Sediment Load Combination

Load model	Lithosphere Thickness (km)	UMV (10^{21} Pa s)	LMV (10^{21} Pa s)	δ
1087	120	1.0	20	8.30
1087+SIA	46	3.0	70	7.39
1243	120	2.0	30	8.13
1243+SIA	96	5.0	50	6.89[a]
1287	96	2.0	30	8.52
1287+SIA	46	5.0	50	7.01[b]
7042	96	3.0	30	9.36
7042+SIA	46	5.0	50	7.73

Note. The numbers 1087, 1243, 1287, and 7042 refer to the ice histories, while +SIA indicates that it also includes the SIA contribution.
[a]An equivalent fit for the 1243+SIA scenario was found for the 71, 5, 50 parameter set. [b]An equivalent fit in the 1287+SIA scenario was found with the 71, 5, 50 parameter set.

factor for the weighting scheme, which is given by $c = \sqrt{\frac{1}{N}\sum_{i=1}^{N}\frac{1}{w_i^2}}$. This weighting was done spatially with the six regions shown in Figure 3, as well as temporally, with data arranged into bins of (0–1) kyr, (1–3) kyr, (3–6) kyr, (6–10) kyr, and 10+ kyr. Without this sort of weighting scheme all SLIPs would be treated equally in equation (4), which is not desirable when there is an uneven data distribution.

Determining appropriate uncertainties for such a complex model is nontrivial. To be done rigorously, it would involve quantifying the uncertainty of the inputs (such as ice histories and the sediment load), as well as systematic uncertainty associated with limitations of the forward model, such as ignoring the effects of lateral Earth structure and departures from a Maxwell rheology. We therefore follow Love et al. in estimating the uncertainty in our optimal model predictions by determining upper and lower bounding model runs such that a specific portion of the RSL data is contained in the region between the bounding model runs. In particular, the bounding models ensure that $(P + (100 - P)/2)$% of the compaction-free SLIP uncertainty boxes for the entire region are captured at the P confidence level for one-way bounding. This allows us to define so-called *heuristic error bounds* for our RSL curves and present-day uplift rates. We use a 1-σ ($P = 68.27$%) confidence level to determine our bounding models. As in Love et al., we also provide so-called *nominally Bayesian* (NB) uncertainty estimates, in which the misfit parameter δ is used to construct a relative probability distribution. As discussed by Love et al., the NB bounds are not defined as rigorously as the heuristic ones (in particular, the assumption of uniform priors used to construct the probabilities is invalid in our case), but these bounds are more in line with the traditional χ^2 bounds employed in past RSL studies (e.g., Bradley et al., 2011; Kuchar et al., 2012). The NB bounds are determined by constructing a normalized probability distribution proportional to $\exp(-\delta)$ (so that lower misfits are considered more probable) and defining the 1-σ envelope as the combination of "most probable" models up to a cutoff of 68%. The choice of $\exp(-\delta)$ for the probability distribution, rather than a standard Gaussian $\exp(-\delta^2)$, is to account for the general lack of independence of RSL data and is consistent with what was done in Love et al. It also has the effect of increasing the number of models in the uncertainty envelope; our NB envelope contains 36 models, while an envelope constructed from an $\exp(-\delta^2)$ approach would only result in two models in the envelope before reaching the 1-σ cutoff. A drawback of the NB bounds is that while the heuristic bounds are defined by individual model runs, the NB bounds are defined by an entire envelope of model runs such that a curve defining a lower bound of RSL at a given site may contain predictions from multiple model runs.

3. Results and Discussion

The parameter set that yields the lowest data misfit δ is defined by the 1243 ice history with sediment loading, a lithosphere thickness of 96 km, an upper mantle viscosity of 5×10^{21}Pa s, and a lower mantle viscosity of 50×10^{21}Pa s. We show the minimum misfit for each loading model in Table 2, and we can see that for each ice history, the minimum misfit is lower when the sediment load is accounted for. We show examples of the misfit distribution in Figures 4 and 5 for the 1243 ice history with and without the sediment load. The misfit figures show that the lowest δ values are obtained when the sediment load is included and that when SIA is

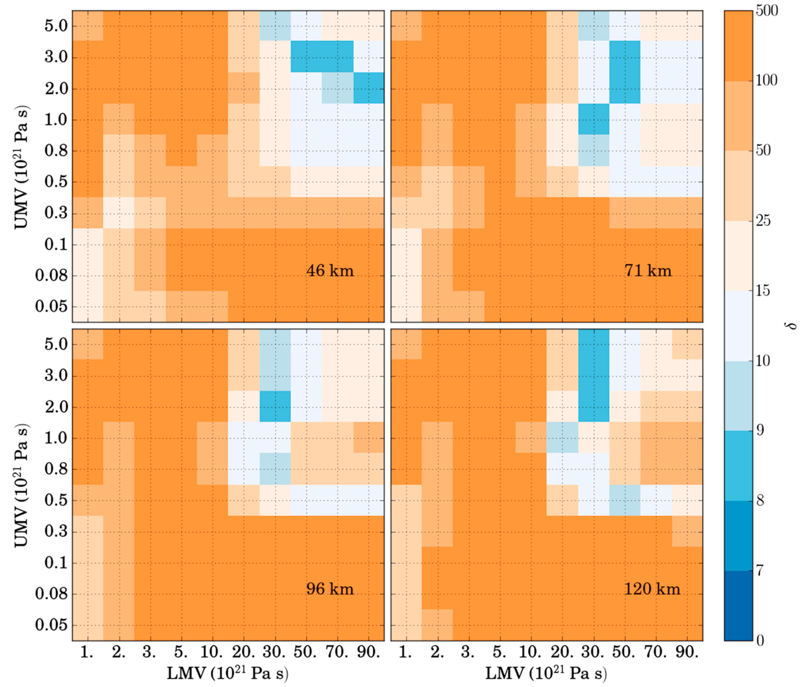

Figure 4. Data-model misfit as a function of upper and lower mantle viscosities at a given lithosphere thickness (46, 71, 96, and 120 km) for the 1243 ice history with no SIA effects.

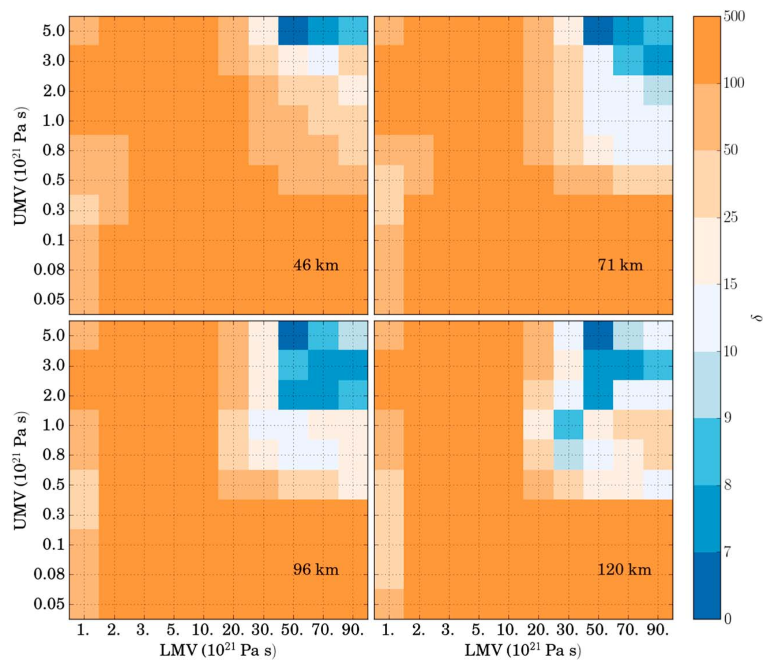

Figure 5. As in Figure 4 but including SIA effects.

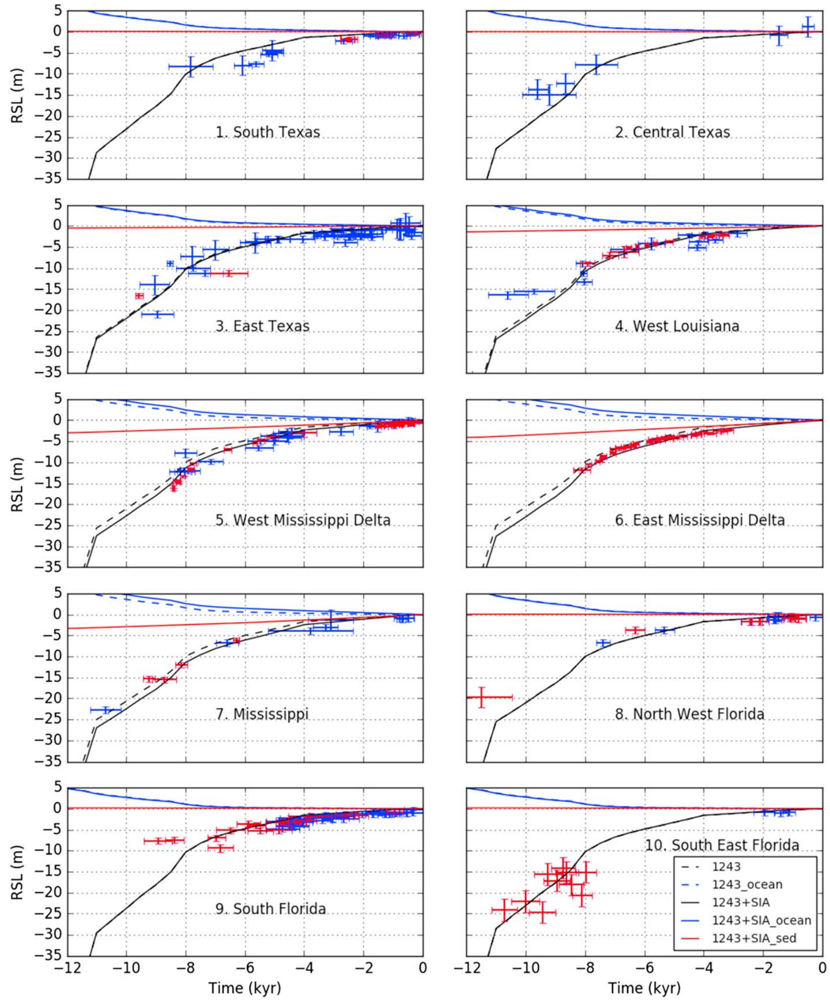

Figure 6. RSL curves for the optimal parameter set (the 1243 ice history, Earth model with 96 km lithosphere, 5×10^{21} Pa s UMV, and 50×10^{21} Pa s LMV). The solid curves are the results of the model run with SIA effects, while the dashed curves are the model run without sediment loading. The black curves show the full RSL signal, while the blue curves show just the ocean loading component. The red curve is the sediment loading contribution to RSL. Observations of RSL are shown with 2-σ time and height uncertainty. The red SLIPs are considered to be compaction free; our parameter estimates are based on these data only.

accounted for the acceptable region of parameter space is larger for thick lithosphere models (96 km and 120 km). Inclusion of SIA also pushes the best fitting parameter values to higher mantle viscosities, which will lead to relatively low deformation rates. Misfit figures for the other three ice histories are shown in Figures S2–S7 in the supporting information, which show similar structure to those in Figures 4 and 5. While these figures show the misfits for the weighted data, we have also computed the misfits with unweighted data, and the best fitting model is the same in both cases demonstrating that our assumption of independent index points does not strongly influence the parameter estimates. We include Figure S8 in the supporting information to show an example misfit where the data are unweighted. In general, the effect of data weighing is to broaden the region of parameter space that fits the data.

The preference for high mantle viscosities is similar to the results of Love et al. (2016), who found that the Gulf Coast data preferred a lithosphere of 120 km, an upper mantle viscosity of 5×10^{21} Pa s, and a lower mantle viscosity of 90×10^{21} Pa s. Relatively high mantle viscosities (0.8×10^{21} Pa s upper mantle viscosity and

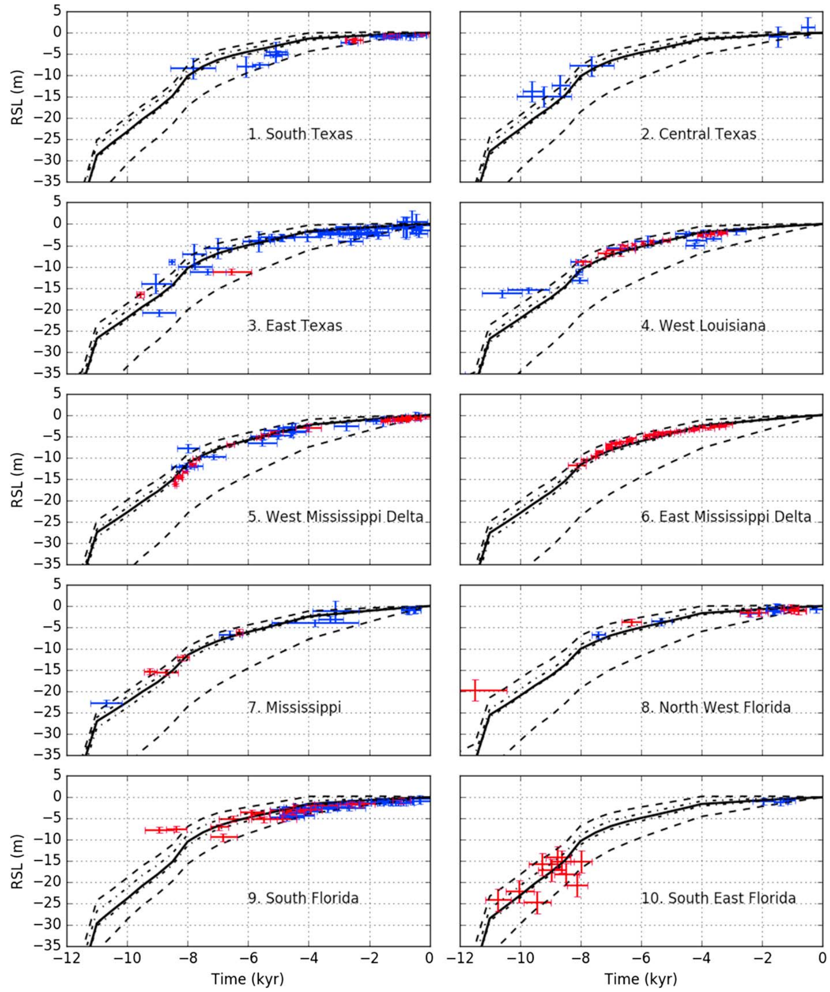

Figure 7. RSL curves with solid black curve as in Figure 6, also including heuristic (dashed) and NB (dash-dotted) uncertainty bounds. Locations of model output are indicated by black triangles in Figure 3.

$>3 \times 10^{21}$ Pa s lower mantle viscosity) were found to be preferred in the Caribbean by Milne and Peros (2013), along with thick lithospheres. There are a number of viscosity estimates using data from Canada and the northern U.S. (e.g., Lambeck et al., 2017; Mitrovica & Forte, 2004), and these typically find lower viscosities in the mantle. It is also noteworthy that while our best fitting model has a lithosphere thickness of 96 km, we also have well-fitting models with thinner (46 km) lithospheres compared to the values found by both Love et al. and Milne and Peros.

In Figure 6 we show modeled RSL curves for the optimal parameter set when sediment effects were included and compare it to model output for the same Earth and ice parameters but without sediment loading. The general effect (if any) of the sediment loading is to shift the total RSL curve to slightly lower values. We also show the components of the RSL signal due to the ocean load and sediment load, and we can see that these signals partly compensate each other, thus diminishing the net influence of SIA on past RSL change. This is because an increase in the height of a column of marine sediment will lead to a corresponding lowering of the thickness of the ocean load above it. The sites outside of the MD show no discernible SIA response in RSL during the time interval illustrated.

In Figure 7 we show the heuristic and NB uncertainty bounds (as defined in section 2.3). The heuristic upper bound is defined by the model having the 1087 ice history, a 120 km lithosphere thickness, an upper mantle

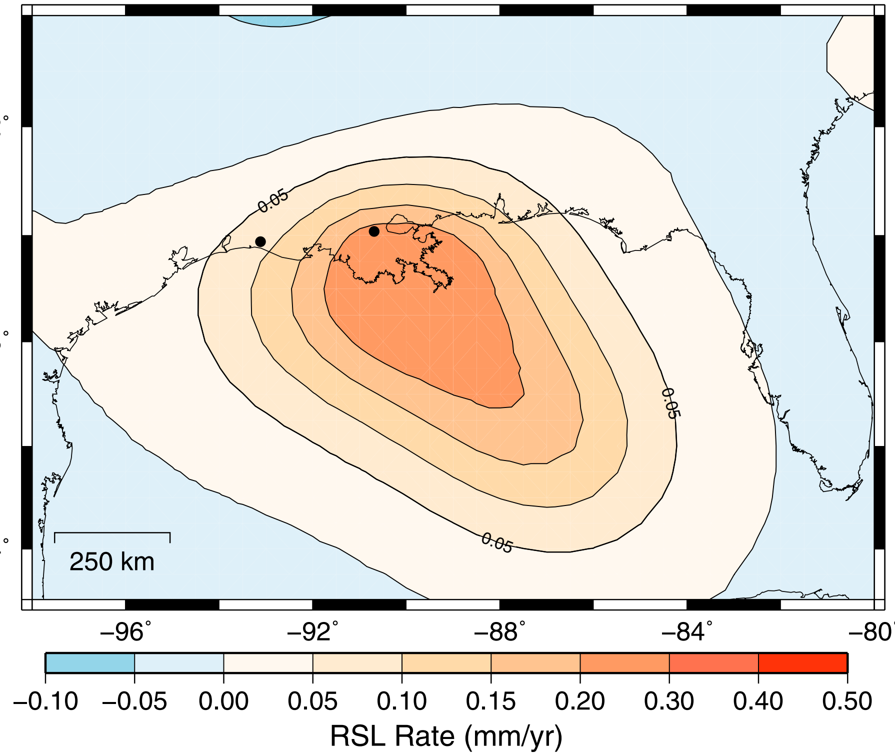

Figure 8. Modeled RSL rate due to sediment loading only at present day. The black circles show sites used by Yu et al. (2012) to estimate the average SIA rate over the last 7 kyr in the delta area. The modeled rates are consistent with the differential RSL rate determined by Yu et al. We highlight the 0.05 mm/yr contour as a cutoff to illustrate the spatial scale of the SIA effect. Figures S9 and S10 in the supporting information show the same output for the heuristic bounding models.

viscosity of 1×10^{21} Pa s and a lower mantle viscosity of 90×10^{21} Pa s. The heuristic lower bound is defined by the model having the 7042 ice history, a 120 km thick lithosphere, an upper mantle viscosity of 0.3×10^{21} Pa s, and a lower mantle viscosity of 10×10^{21} Pa s. The optimal model results lie very near to the upper bound, as both models are characterized by high mantle viscosities, and both with ice histories that were found to fit the Gulf Coast RSL data by Love et al. (2016). As discussed in Love et al. (2016), we note that the lower bound can be strongly influenced if there is a large density of index points within the last few thousand years (e.g., sites 5 and 8), which we have addressed by temporally weighting the data. The NB bounds are defined by an envelope of models with lithosphere thicknesses ranging from 46 to 120 km, upper mantle viscosity ranging from 1×10^{21} Pa s to 5×10^{21} Pa s, and lower mantle viscosity ranging from 30×10^{21} Pa s to 90×10^{21} Pa s. All four ice histories are also included in the uncertainty envelope. The heuristic lower bound is very low, and likely overestimates the true model uncertainty, while the NB bounds are likely an underestimate.

The bounding model parameters, like those for the optimal model, were estimated using the totality of compaction free observations from the Gulf coast. The bounding run parameter sets will be used to define model uncertainty ranges for the data-model comparisons discussed below.

In Figure 8 we show present-day RSL rates due to SIA in the Gulf. We note that these rates are representative for past ~6 kyr. Love et al. applied a correction to the RSL data to account for the effects of SIA of 0.25 mm/yr in the longitude range of (−92, −89) degrees east and 0.1 mm/yr in the longitude ranges of (−89, −87.5) and (−93.5, −92) degrees east. Referring to Figure 8, we can conclude that these are reasonable corrections. In the (−93.5, −92) degree range the SIA contribution to RSL is in the range of about 0.05–0.15 mm/yr, making 0.1 mm/yr a reasonable choice. The estimate on the other side of the delta of 0.1 mm/yr between (−89, −87.5) is a bit low, as we can see that the SIA RSL rate in that area is between around 0.1 and 0.25 mm/yr.

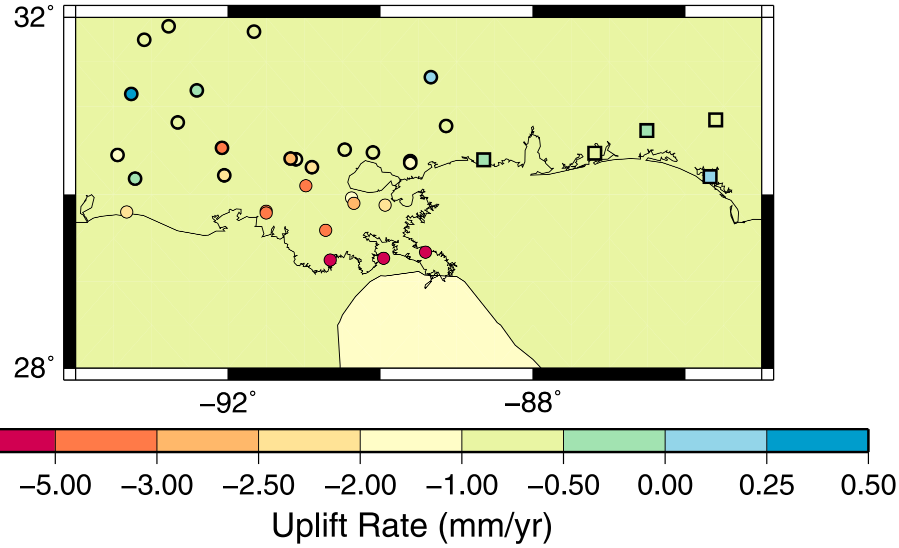

Figure 9. Present-day uplift rates for our optimal parameter set (96 km lithosphere, 5×10^{21} Pa s UMV, and 50×10^{21} Pa s LMV) and inferred from GPS data (colored circles: Karegar et al., 2015; squares: Yu & Wang, 2016). We use thicker outlines to isolate GPS stations that we believe are grounded in Pleistocene sediments, and therefore less likely to be affected by compaction. Figures S11 and S12 in the supporting information show the same output for the heuristic bounding models.

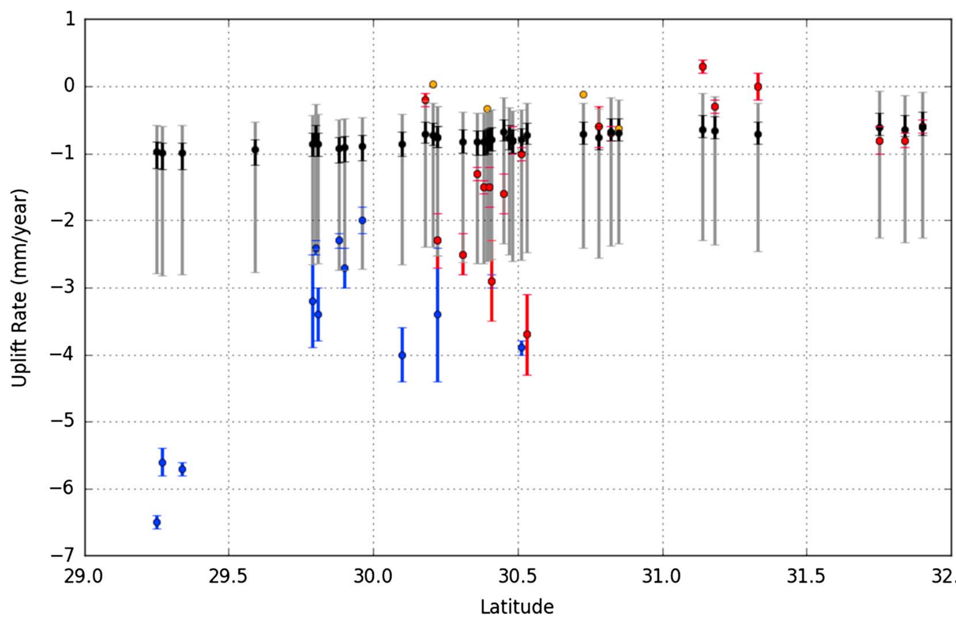

Figure 10. Modeled uplift rates (black) and those inferred from GPS data (red, orange, and blue). The red circles indicate the results for stations considered by Karegar et al. (2015) that are not significantly affected by compaction (corresponding to the circles with bolder outlines in Figure 9); the blue circles indicate rates for other stations. The orange circles correspond to data from Yu and Wang (2016); stations indicated as squares in Figure 9). The modeled results include grey error bars for the heuristic bounds and black error bars for the NB bounds.

Table 3
GPS Stations From Karegar et al. (2015) Likely Anchored in Holocene Sediment, and South of 32° North

Station	Longitude	Latitude	GPS	GIA + SIA	Residual
AWES	−90.98	30.1	−4.00	−0.85	−3.15
BVHS	−89.41	29.34	−5.70	−0.99	−4.71
CAMR	−93.33	29.8	−2.40	−0.74	−1.66
DSTR	−90.38	29.96	−2.00	−0.90	−1.10
ENG1	−89.94	29.88	−2.30	−0.92	−1.38
FSHS	−91.5	29.81	−3.40	−0.85	−2.55
GRIS	−89.96	29.27	−5.60	−0.99	−4.61
HOUM	−90.72	29.59	−3.90	−0.94	−2.96
LALA	−92.05	30.22	−3.40	−0.76	−2.64
LAFR	−91.5	29.79	−3.20	−0.85	−2.35
LMCN	−90.66	29.25	−6.50	−0.97	−5.53
LWES	−90.35	29.9	−2.70	−0.91	−1.79

Note. By removing the isostatic rate (GIA + SIA) from the GPS rate, we obtain an estimate of deep compaction (the residual). All rates in mm/yr.

The choice of 0.25 mm/yr between (−92, −89) is also representative of the range we see there, though we note that near the coast the rates can be as high as 0.3 mm/yr.

Yu et al. (2012) estimated an SIA contribution to subsidence in the MD region of 0.15 ± 0.07 mm/yr by differencing RSL rates within the central delta from those at a site on the periphery of this region (the locations are shown in Figure 8). This approach is based on the reasoning that the ongoing GIA response at these sites should be similar, and thus, the difference between them would be largely due to SIA. Our model results agree with their estimated differential SIA rate. The peripheral region in the west is located in a region of 0.05–0.1 mm/yr, while the delta site is experiencing a rate of 0.2–0.25 mm/yr, and we have calculated the differential SIA rate between these locations to be 0.14 mm/yr for our optimal parameter set. However, we note that this is the differential rate and should not be taken as a representative SIA rate for the entire MD region.

We also highlight the 0.05 mm/yr contour in Figure 8 to show the approximate scale of the SIA effect. It was estimated by Blum et al. (2008) that the SIA effect would dissipate within ~100 km of the loading center; however, we see that the SIA effect is present up to several hundred kilometers from the loading center. This length scale is consistent when the heuristic upper and lower bounding models are considered as well (Figures S9 and S10 in the supporting information).

In Figure 9 we show present-day uplift rates in the delta region as predicted by our optimal model, as well as the values as determined via GPS observations (Karegar et al., 2015; Yu & Wang, 2016). The equivalent figures for our bounding heuristic models are given by Figures S11 and S12 in the supporting information, where the upper bounding model has rates very similar to those of the optimal model, and the lower bounding model has significantly higher rates of subsidence (as seen also in Figure 10 as higher rates of sea level rise). As the NB bounds are defined by a large envelope of model runs we do not include those figures in the supporting information.

The largest subsidence value obtained by our optimal model is 0.99 mm/yr on the coast of the Delta. This value increases to 1.24 mm/yr with NB uncertainty bounds, and 2.82 mm/yr when considering predictions from the model parameters that define the heuristic lower bounding run (the lower bounding run gives the greatest subsidence rates). Even considering model uncertainty, the GPS-inferred rates are substantially greater, giving values as much as 7 mm/yr subsidence. It is true, in general, that the GPS stations record significantly more subsidence than our model can predict (with the exception of two stations that record uplift, as we do not predict any uplift in this region). This is clearly shown in Figure 10 where we plot both model predicted uplift with uncertainty and GPS data with uncertainty, as a function of latitude. Our selected sites from Yu and Wang (2016) allow us to extend our GPS comparison to the east; however, these records have no published uncertainty. As these records are all recorded over a minimum of 5 years, standard error is estimated to be approximately 0.02 mm/yr (G. Wang, private communication). At high latitudes there is reasonable agreement between modeled and inferred rates. However, at low latitudes, there are large

Table 4
RSL Projections at 2100 for Selected Cities on the Gulf Coast, Followed by Heuristic and NB Bounds

Site	RSL (m) (GIA + SIA)	RSL (m) (SIA)
Panama City, Florida	0.04 (0.00–0.16) (0.03–0.05)	0.002
New Orleans, Louisiana	0.05 (0.02–0.18) (0.04–0.06)	0.02
Galveston, Texas	0.04 (0.00–0.15) (0.03–0.05)	0.003

discrepancies. This was also found by Wolstencroft et al. (2014), who posited that the disagreement at low latitudes was likely due to sediment compaction. We have used red and orange symbols to identify the stations that we believe are anchored in Pleistocene sediment (the bold outlined sites in Figure 9). Our model agreement with these sites is good, with the exception of one particular site recording uplift, and four sites between latitudes 30.2 and 30.6 with subsidence values well below our model output. If our assumption that compaction is minimal at these sites is correct, then the misfit may be due to fluid extraction or faulting related subsidence. Two of these four stations (GVMS and 1LSU) are in the Baton Rouge area, which experiences significant fluid extraction related subsidence (Davis & Rollo, 1969).

In Table 3 we estimate the compaction occurring at the GPS stations anchored in Holocene sediment. The GPS stations record land motion due to all processes, including isostasy, as well as compaction occurring in sediment below their anchoring depths. By removing our modeled isostatic motion from the GPS records we obtain an estimate of compaction beneath the anchor depth of each receiver. The deep compaction ranges from ~1.4 to ~5.5 mm/yr, and so is substantial. The total compaction at a GPS station must also include compaction occurring above the anchoring depth. Shallow compaction in the MD has been estimated to be 7.1 ± 8.6 mm/yr (Jankowski et al., 2017), which would bring total compaction to 12 mm/yr or more. In the above, we are assuming that all of the vertical motion is either induced by GIA or SIA, or else related to sediment compaction. We are therefore assuming that faulting-related motion can be neglected, which is not necessarily the case. Shen et al. (2017) found that throw rates in the Tepetate-Baton Rouge fault zone in Southern Louisiana are on the order of 10^{-1} mm/yr during the Holocene, which is small compared to compaction, but the same order as the SIA signal. We are also neglecting fluid extraction, which can be a large cause of subsidence, with shallow subsidence for groundwater extraction and deep subsidence for hydrocarbon extraction for petroleum production. Around New Orleans subsidence rates as high as 30 mm/yr or more have been measured by Jones et al. (2016), largely due to local groundwater extraction.

Love et al. (2016) provided RSL projections for the Eastern seaboard of North America, including several sites within the Gulf of Mexico. We can update their projections for these sites to explicitly account for SIA effects. The sites are Panama City, Florida; New Orleans, Louisiana; and Galveston, Texas, and their projected GIA contributions to local RSL 100 years in the future were 0.03 (0.01–0.13) m, 0.03 (0.01–0.12) m, and 0.03 (0.00–0.11) m respectively, with the bounds estimated by the heuristic method described previously, and using the compaction free subset of the RSL data. Our estimates for these sites including both GIA and SIA are given in Table 4. The SIA contributions for our optimal model at these sites are 0.002 m, 0.02 m, and 0.003 m, respectively. The contribution of GIA and SIA to sea level rise on the Gulf coast in the next hundred years will be small compared to other processes. For example, our corrections push the estimated RSL at 2100 to be 0.45 m for all three sites mentioned, based on the RCP 4.5 climate scenario and considering future ice melt and ocean dynamic and steric effects (Love et al., 2016). We stress, however, that these projections do not account for nonisostatic effects like sediment compaction or fluid extraction, which will be a dominant contributors to future sea level rise in many parts of the delta.

4. Conclusions

We have used a gravitationally self-consistent sea level theory (Dalca et al., 2013) and a realistic sediment load history (Wolstencroft et al., 2014) to compute RSL associated with GIA and SIA along the U.S. Gulf coast. Comparing model rates to those in a recently compiled regional RSL database that are known to be compaction free, we determined optimal model parameters (from a suite of four different ice histories and several hundred Earth viscosity models). We find that a model with a high viscosity upper and lower mantle best fits the available RSL data. Using the optimal parameter set we show that SIA lowers the predicted RSL values by up to ~3 m during the Holocene in the vicinity of the MD where recent sediment accumulation was concentrated. The influence of SIA reduces to sub meter levels at locations outside of the delta (see Figure S13 in the supporting information). The significant influence of SIA in the MD region impacts the inferred model parameters, with the data preferring higher upper and lower mantle viscosities when SIA was included in the model. The spatial extent of the SIA signal is estimated to be several hundred kilometers measured from the loading center.

Using 1-σ bounding and our optimal parameter set, we applied our model to consider the contribution of GIA and SIA to contemporary rates of vertical land motion as inferred using GPS. This comparison indicates that isostatic deformation can explain the majority of the observed vertical land motion north of latitude 30.7°N. The comparison of observed and modeled vertical rates south of this latitude shows large discrepancies of greater than 3 mm/yr, indicating the importance of other processes controlling the observed subsidence. We have shown that SIA is not a primary driver of land subsidence and therefore sea level rise in the MD, and we have combined our model results with GPS records to estimate the deep compaction signal present in Holocene sediment in the MD. Our model provides an estimate of the isostatic contribution (GIA and SIA) that can be used to better isolate the amplitude of other contributing processes and thus improve the accuracy of sea level projections in this area. We provide modeled contemporary vertical and horizontal land motion rates at the GPS station locations of Karegar et al. (2015) in Table S1 in the supporting information and RSL rates at Permanent Service for Mean Sea Level tide gauge locations around the Gulf of Mexico coast in Table S2 in the supporting information.

Acknowledgments
We thank Torbjörn Törnqvist for comments and insights that have improved this manuscript, as well as Ken Ferrier for providing the boundary of the erosion zone. Joseph Kuchar, Glenn Milne, and Lev Tarasov acknowledge the National Science and Engineering Research Council for funding that aided this research. Joseph Kuchar and Glenn Milne additionally acknowledge support from the University of Ottawa. Modeled present-day RSL rates for select tide gauge station locations and land motion rates at select GPS station locations are available in the supporting information, and data used to generate all figures in the paper are available from the corresponding author upon request. This paper is a contribution to the PAGES/INQUA funded PALSEA2 working group.

References

Argus, D. F. (2012). Uncertainty in the velocity between the mass center and surface of Earth. *Journal of Geophysical Research*, *117*, B10405. https://doi.org/10.1029/2012JB009196.

Blewitt, G. (2003). Self-consistency in reference frames, geocenter definition, and surface loading of the solid Earth. *Journal of Geophysical Research*, *108*(B2), 2103. https://doi.org/10.1029/2002JB002082

Blum, M. D., Tomkin, J. H., Purcell, A., & Lancaster, R. R. (2008). Ups and downs of the Mississippi Delta. *Geology*, *36*, 675–678. https://doi.org/10.1130/G24728A.1

Bradley, S., Milne, G., Shennan, I., & Edwards, R. (2011). An improved glacial isostatic adjustment model for the British Isles. *Journal of Quaternary Science*, *26*, 541–552. https://doi.org/10.1002/jqs.1481

Briggs, R. D., & Tarasov, L. (2013). How to evaluate model-derived deglaciation chronologies: A case study using Antarctica. *Quaternary Science Reviews*, *63*, 109–127. https://doi.org/10.1016/j.quascirev.2012.11.021

Church, J. A., Clark, P. U., Cazenave, A., Gregory, J. M., Jevrejeva, S., Levermann, A., … Unnikrishnan, A. S. (2013). Sea level change. In T. F. Stocker, et al. (Eds.), *Climate change 2013: The physical science basis. Contribution of working Group I to the Fifth Assessment Report of the Intergovernmental Panel on Climate Change*. Cambridge, United Kingdom and New York, NY: Cambridge University Press.

Clark, J. A., Farrell, W. E., & Peltier, W. R. (1978). Global changes in postglacial rebound: A numerical calculation. *Quaternary Research*, *9*(03), 265–287. https://doi.org/10.1016/0033-5894(78)90033-9

Coleman, J. M., & Roberts, H. H. (1988). Sedimentary development of the Louisiana continental shelf related to sea level cycles: Part I—Sedimentary sequences. *Geo-Marine Letters*, *8*(2), 63–108. https://doi.org/10.1007/BF02330967

Dalca, A. V., Ferrier, K. L., Mitrovica, J. X., Perron, J. T., Milne, G. A., & Creveling, J. R. (2013). On postglacial sea level—III. Incorporating sediment redistribution. *Geophysical Journal International*, *194*(1), 45–60. https://doi.org/10.1093/gji/ggt089

Davis, G. H., & Rollo, J. R. (1969). *Land Subsidence Related to Decline of Artesian Head at Baton Rouge, Lower Mississippi Valley*, *Proc. Tokyo Symp. On Land Subsidence*, USA: IASH-UNESCO.

Day, J. W. Jr., Day, J. W., Boesch, D. F., Clairain, E. J., Kemp, G. P., Laska, S. B., … Whigham, F. (2007). Restoration of the Mississippi Delta: Lessons from Hurricanes Katrina and Rita. *Science*, *315*, 1679–1684. https://doi.org/10.1126/science.1137030

Dixon, T. H., Amelung, F., Ferretti, A., Novali, F., Rocca, F., Dokka, R., … Whitman, D. (2006). Space geodesy: Subsidence and flooding in New Orleans. *Nature*, *441*, 587–588. https://doi.org/10.1038/441587a

Dokka, R. K., Sella, G. F., & Dixon, T. H. (2006). Tectonic control of subsidence and southward displacement of southeast Louisiana with respect to stable North America. *Geophysical Research Letters*, *33*, L23308. https://doi.org/10.1029/2006GL027250

Dziewonski, A., & Anderson, D. (1981). Preliminary reference Earth model. *Physics of the Earth and Planetary Interiors*, *25*(4), 297–356. https://doi.org/10.1016/0031-9201(81)90046-7

Farrell, W. E., & Clark, J. A. (1976). On Postglacial Sea Level. *Geophysical of Journal of the Royal Astronomical Society*, *46*, 647–667.

Ferrier, K. L., Mitrovica, J. X., Giosan, L., & Clift, P. D. (2015). Sea-level responses to erosion and deposition of sediment in the Indus River basin and the Arabian Sea. *Earth and Planetary Science Letters*, *416*, 12–20. https://doi.org/10.1016/j.epsl.2015.01.026

Fisk, H. N. (1939). Depositional terrace slopes in Louisiana. *Journal of Geomorphology*, *2*, 181–200.

Hijma, M. P., Engelhart, S. E., Horton, B. P., Törnqvist, T. E., Hu, P., & Hill, D. F. (2015). A protocol for a geological sea-level database. In I. Shennan, A. J. Long, & B. P. Horton (Eds.), *Handbook of sea-level research* (pp. 536–553). Chichester, UK: John Wiley.

Ivins, E. R., Dokka, R. K., & Blom, R. G. (2007). Post-glacial sediment load and subsidence in coastal Louisiana. *Geophysical Research Letters*, *34*, L16303. https://doi.org/10.1029/2007GL030003

Jankowski, K. L., Törnqvist, T. E., & Fernandes, A. M. (2017). Vulnerability of Louisiana's coastland wetlands to present-day rates of relative sea-level rise. *Nature Communications*, *8*. https://doi.org/10.1038/ncomms14792

Jones, C. E., An, K., Blom, R. G., Kent, J. D., Ivins, E. R., & Bekaert, D. (2016). Anthropogenic and geologic influences on subsidence in the vicinity of New Orleans, Louisiana. *Journal of Geophysical Research: Solid Earth*, *121*(5), 3867–3887. https://doi.org/10.1002/2015JB012636

Jurkowski, G., Ni, J., & Brown, L. (1984). Modern uparching of the Gulf coastal plain. *Journal of Geophysical Research*, *89*(B7), 6247–6255. https://doi.org/10.1029/JB089iB07p06247

Karegar, M. A., Dixon, T. H., & Malservisi, R. (2015). A three-dimensional surface velocity field for the Mississippi delta: Implications for coastal restoration and flood potential. *Geology*, *43*(6), 519–522. https://doi.org/10.1130/G36598.1

Kendall, R., Mitrovica, J., & Milne, G. (2005). On post-glacial sea level—II. Numerical formulation and comparative results on spherically symmetric models. *Geophysical Journal International*, *161*(3), 679–706. https://doi.org/10.1111/j.1365-246X.2005.02553.x

Kuchar, J., Milne, G., Hubbard, A., Patton, H., Bradley, S., Shennan, I., & Edwards, R. (2012). Evaluation of a numerical model of the British-Irish ice sheet using relative sea-level data: Implications for the interpretation of trimline observations. *Journal of Quaternary Science*, *27*, 597–605. https://doi.org/10.1002/jqs.2552

Kulp, M., Howell, P., Adiau, S., Penland, S., Kindinger, J., & Williams, S. J. (2002). Latest Quaternary stratigraphic framework of the Mississippi River delta region. *Gulf Coast Association of Geological Societies*, *52*, 573–582.

Lambeck, K., Purcell, A., & Zhao, S. (2017). The North American Late Wisconsin ice sheet and mantle viscosity from glacial rebound analyses. *Quaternary Science Reviews*, *158*, 172–210.

Love, R., Milne, G. A., Tarasov, L., Engelhart, S. E., Hijma, M. P., Latychev, K., … Törnqvist, T. E. (2016). The contribution of glacial isostatic adjustment to projections of sea-level change along the Atlantic and gulf coasts of North America. *Earth's Future*, *4*(10), 440–464. https://doi.org/10.1002/2016EF000363

Milne, G. A., & Mitrovica, J. X. (1998). Postglacial sea-level change on a rotating Earth. *Geophysical Journal International*, *133*(1), 1–19. https://doi.org/10.1046/j.1365-246X.1998.1331455.x

Milne, G. A., & Peros, M. (2013). Data–model comparison of Holocene sea-level change in the circum-Caribbean region. *Global and Planetary Change*, *107*, 119–131. https://doi.org/10.1016/j.gloplacha.2013.04.014

Mitrovica, J., & Milne, G. (2003). On post-glacial sea level: I. General theory. *Geophysical Journal International*, *154*(2), 253–267. https://doi.org/10.1046/j.1365-246X.2003.01942.x

Mitrovica, J. X., & Forte, A. M. (2004). A new inference of mantle viscosity based upon a joint inversion of convection and glacial isostatic adjustment data. *Earth and Planetary Science Letters*, *225*, 177–189. https://doi.org/10.1016/j.epsl.2004.06.005

Morton, R. A., Bernier, J. C., & Barras, J. A. (2006). Evidence of regional subsidence and associated interior wetland loss induced by hydrocarbon production, Gulf Coast region, USA. *Environmental Geology*, *50*, 261–274. https://doi.org/10.1007/s00254-006-0207-3

Peltier, W. R. (1974). The impulse response of a Maxwell Earth. *Reviews of Geophysics*, *12*(4), 649–669. https://doi.org/10.1029/RG012i004p00649

Peltier, W. R. (2004). Global glacial isostasy and the surface of the ICE-age Earth: The ICE-5G (VM2) model and GRACE. *Annual Review of Earth and Planetary Sciences*, *32*, 111–149. https://doi.org/10.1146/annurev.earth.32.082503.144359

Potter, E.-K., & Lambeck, K. (2003). Reconciliation of sea-level observations in the western north Atlantic during the last glacial cycle. *Earth and Planetary Science Letters*, *217*, 171–181.

Shen, Z., Dawers, N. H., Törnqvist, T. E., Gasparini, N. M., Hijma, M. P., & Mauz, B. (2017). Mechanisms of late Quaternary fault throw-rate variability along the north central Gulf of Mexico coast: Implications for coastal subsidence. *Basin Research*, *29*(5), 557–570. https://doi.org/10.1111/bre.12184

Slangen, A. B. A., Carson, M., Katsman, C. A., van de Wal, R. S. W., Köhl, A., Vermeersen, L. L. A., & Stammer, D. (2014). Projecting twenty-first century regional sea-level changes. *Climactic Change*, *124*(1-2), 317–332. https://doi.org/10.1007/s10584-014-1080-9

Stelting, C. E., Droz, L., Bouma, A. H., Coleman, J. M., Cremer, M., Meyer, A. W., … Stow, D. A. V. (1986). Late Pleistocene seismic stratigraphy of the Mississippi fan. In A. H. Bouma, et al. (Eds.), *Initial Reports of the Deep Sea Drilling Project 96* (pp. 437–456). Washington, DC: U.S. Government Printing Office. https://doi.org/10.2973/dsdp.proc.96.119.1986

Tarasov, L., Dyke, A., Neal, R., & Peltier, W. R. (2012). A data-calibrated distribution of deglacial chronologies for the North American ice complex from glaciological modeling. *Earth and Planetary Science Letters*, *315–316*, 30–40.

Törnqvist, T. E., Wallace, D. J., Storms, J. E. A., Wallinga, J., van Dam, R. L., Blaauw, M., … Snijders, E. (2008). Mississippi Delta subsidence primarily caused by compaction of Holocene strata. *Nature Geoscience*, *1*, 173–176. https://doi.org/10.1038/ngeo129

Van der Wal, W., & IJpelaar, T. (2017). The effect of sediment loading in Fennoscandia and the Barents Sea during the last glacial cycle on glacial isostatic adjustment observations. *Solid Earth*, *8*, 955–968.

Watson, C. S., White, N. J., Church, J. A., King, M. A., Burgette, R. J., & Legresy, B. (2015). Unabated global mean sea-level rise over the satellite altimeter era. *Nature Climate Change*, *5*(6), 565–568. https://doi.org/10.1038/nclimate2635

Wolstencroft, M., Shen, Z., Törnqvist, T. E., Milne, G. A., & Kulp, M. (2014). Understanding subsidence in the Mississippi Delta region due to sediment, ice, and ocean loading: Insights from geophysical modeling. *Journal of Geophysical Research: Solid Earth*, *119*, 3838–3856. https://doi.org/10.1002/2013JB010928

Yu, J., & Wang, G. (2016). GPS-derived ground deformation (2005-2014) within the Gulf of Mexico region referred to a stable Gulf of Mexico reference frame. *Natural Hazards and Earth System Sciences*, *16*(7), 1583–1602. https://doi.org/10.5194/nhess-16-1583-2016

Yu, S.-Y., Törnqvist, T. E., & Hu, P. (2012). Quantifying Holocene lithospheric subsidence rates underneath the Mississippi Delta. *Earth and Planetary Science Letters*, *331–332*, 21–30.

Journal of Geophysical Research: Solid Earth

Supporting Information for

The Influence of Sediment Isostatic Adjustment on Sea-Level Change and Land Motion along the US Gulf Coast

Joseph Kuchar[1], Glenn Milne[2], Martin Wolstencroft[3], Ryan Love[4], Lev Tarasov[4], Marc Hijma[5]

1. Department of Physics, University of Ottawa, Ottawa, Ontario, Canada
2. Department of Earth and Environmental Science, University of Ottawa, Ottawa, Ontario, Canada
3. JBA Risk Management Limited, Broughton Hall, Skipton, BD23 3AE, UK
4. Department of Physics and Physical Oceanography, Memorial University of Newfoundland, St. John's, Newfoundland and Labrador, Canada
5. Department of Applied Geology and Geophysics, Deltares, Utrecht, The Netherlands

Contents of this file

Figures S1 to S16

Additional Supporting Information (Files uploaded separately)

Captions for Tables S1 to S2

Introduction

This supplemental section contains additional figures to complement discussion and figures presented in the main text. All of the figures below are referred to in the main text. See captions for further details.

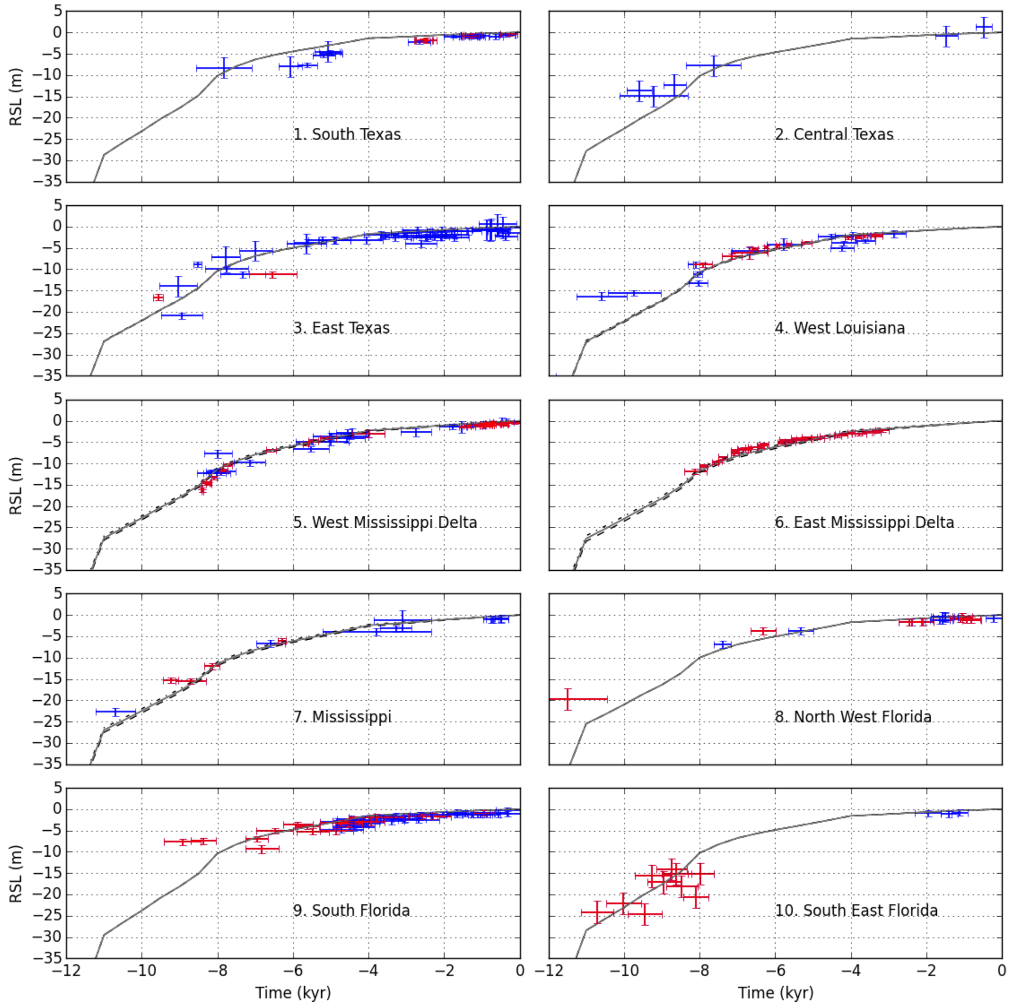

Figure S1. RSL for optimal parameter set (black) with sediment load as described in Section 2.1), as well as with a 15% sediment density increase (black dashed), a 15% sediment density decrease (black dash-dotted), and an earlier onset delta loading component (grey).

2

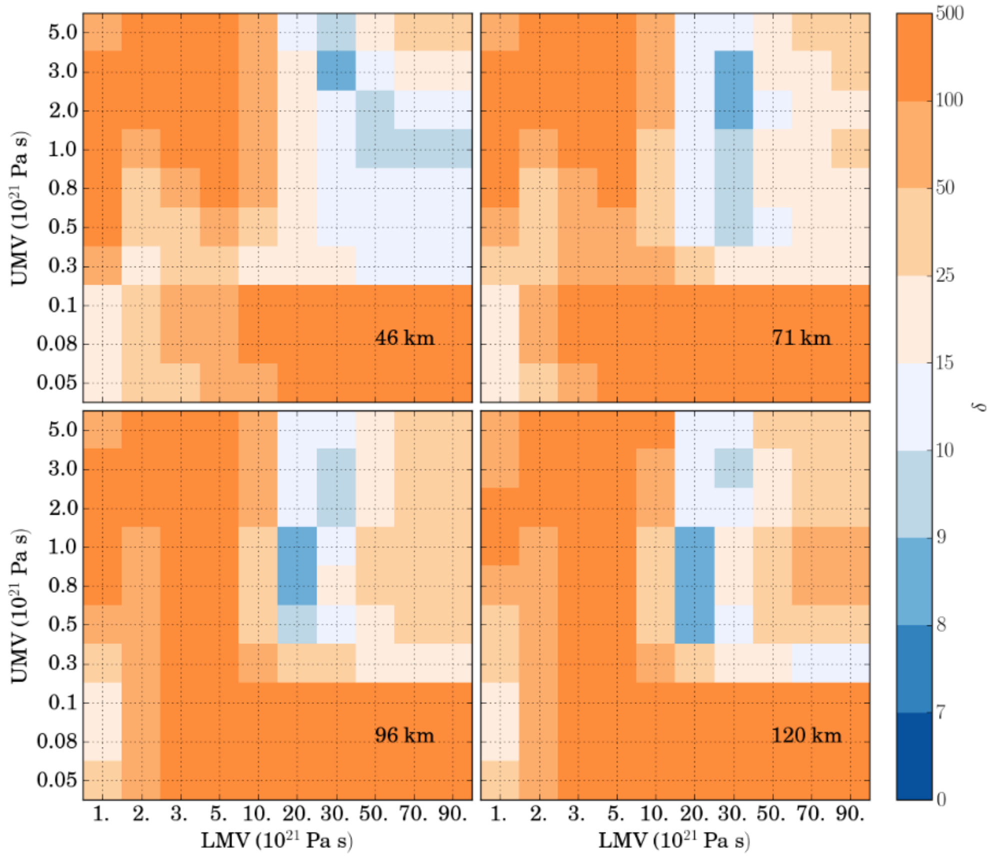

Figure S2. As in Figure 4, except for the 1087 ice history and no sediment loading effects.

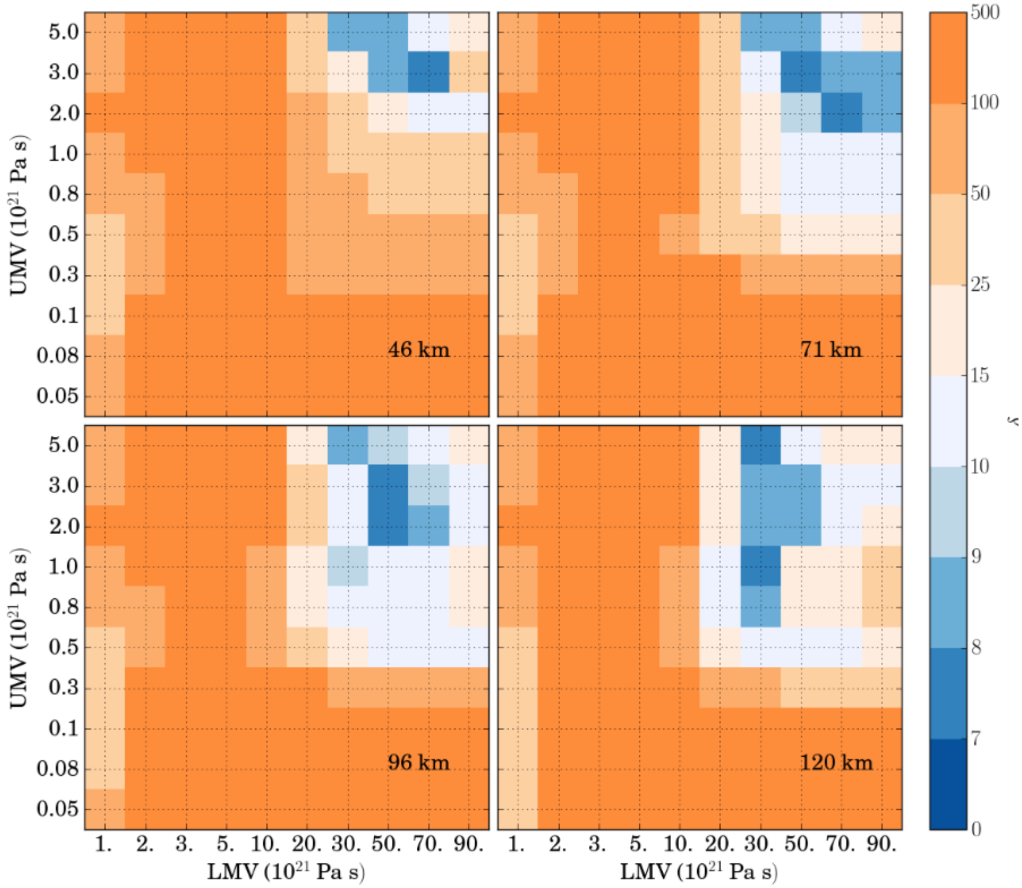

Figure S3. As in Figure 4, except for the 1087 ice history and including sediment loading effects.

4

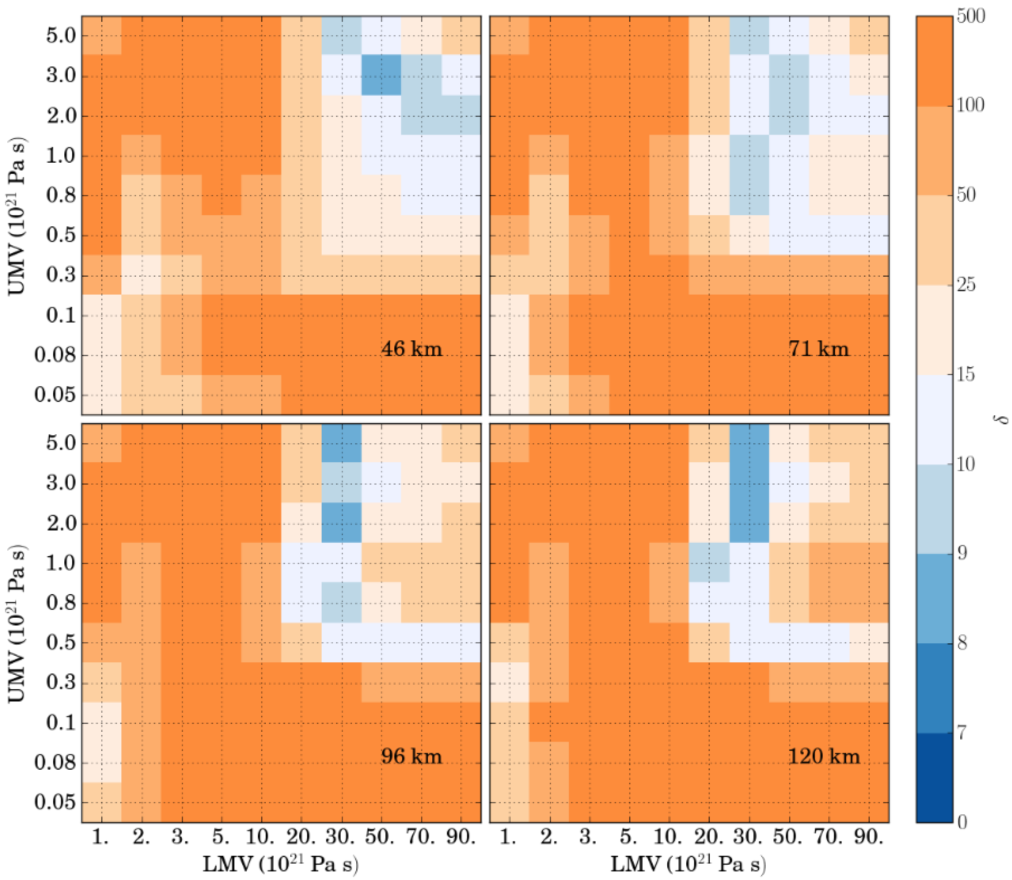

Figure S4. As in Figure 4, except for the 1287 ice history and no sediment loading effects.

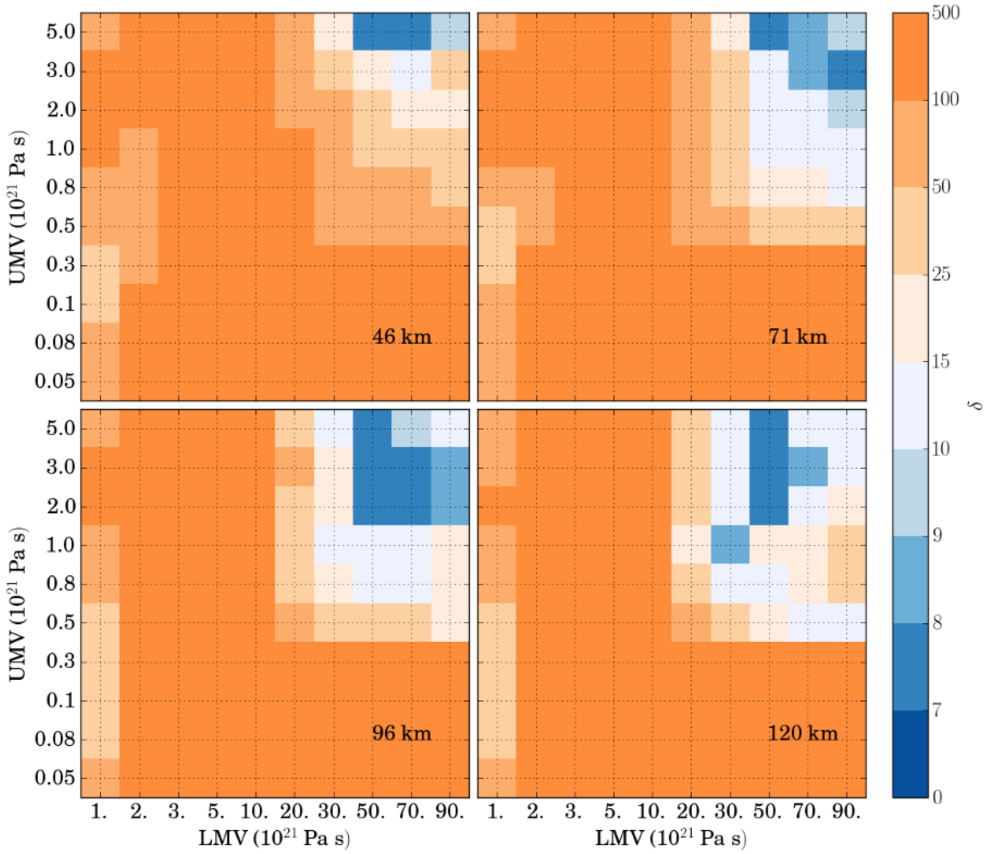

Figure S5. As in Figure 4, except for the 1287 ice history and including sediment loading effects.

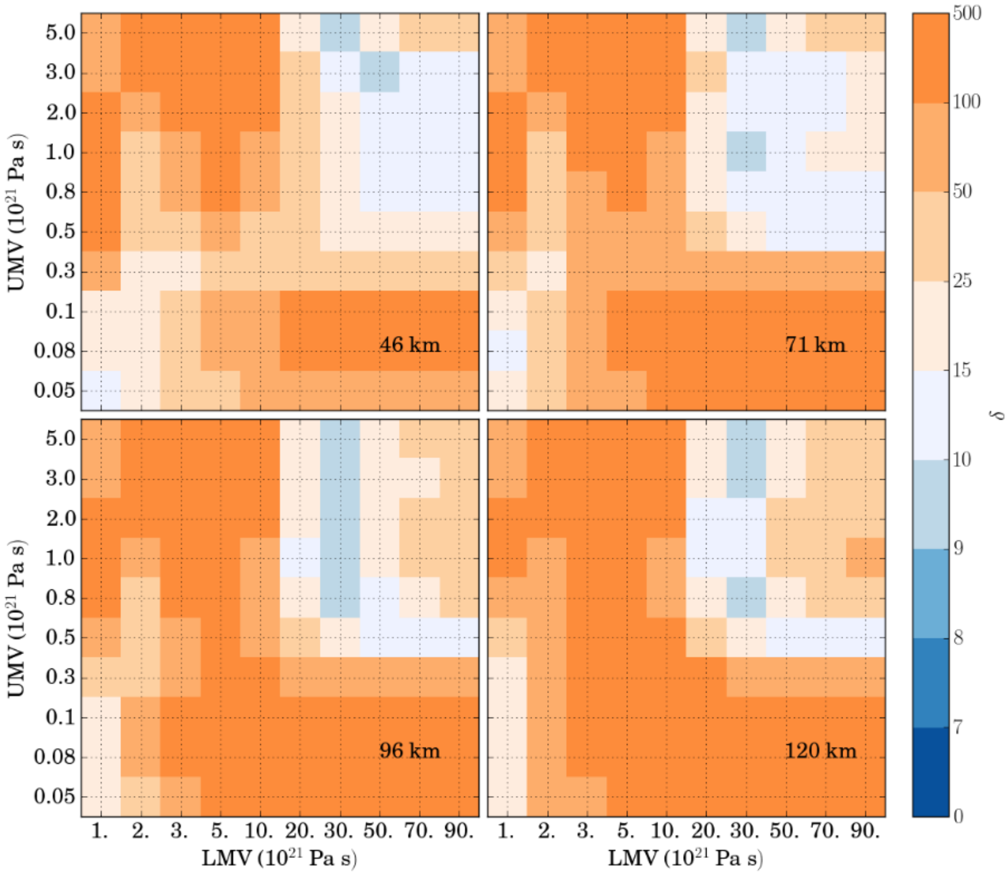

Figure S6. As in Figure 4, except for the 7042 ice history and no sediment loading effects.

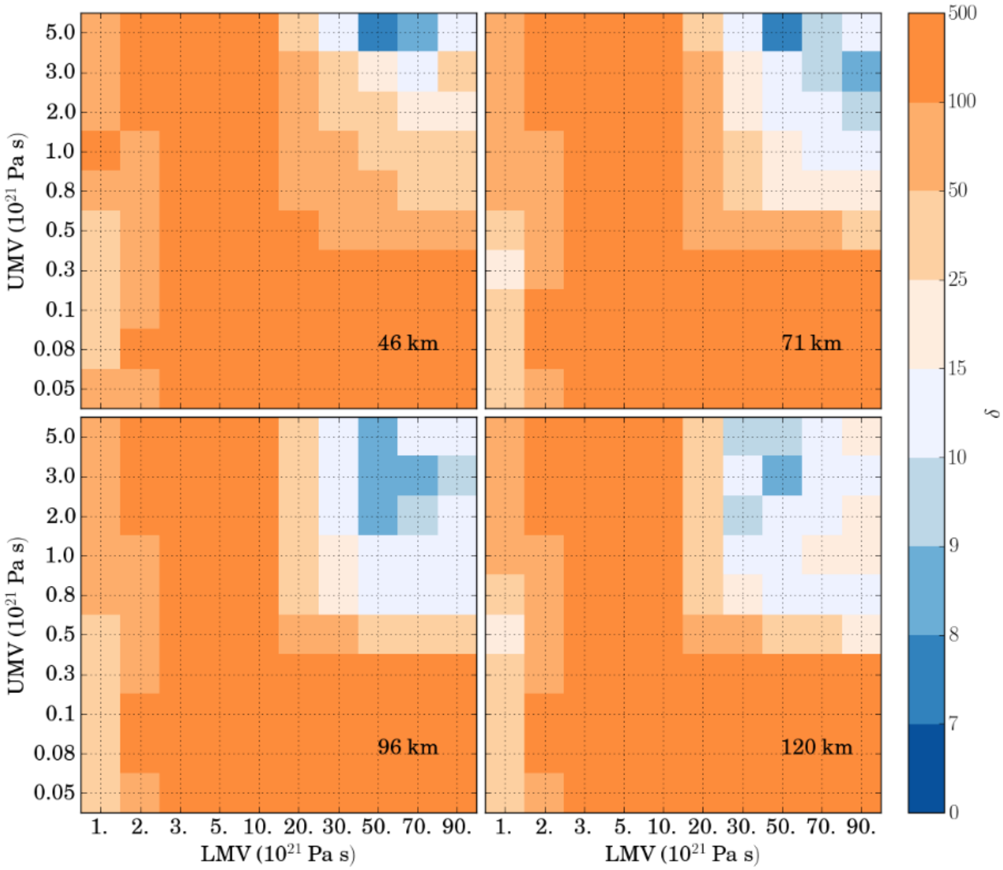

Figure S7. As in Figure 4, except for the 7042 ice history and including sediment loading effects.

8

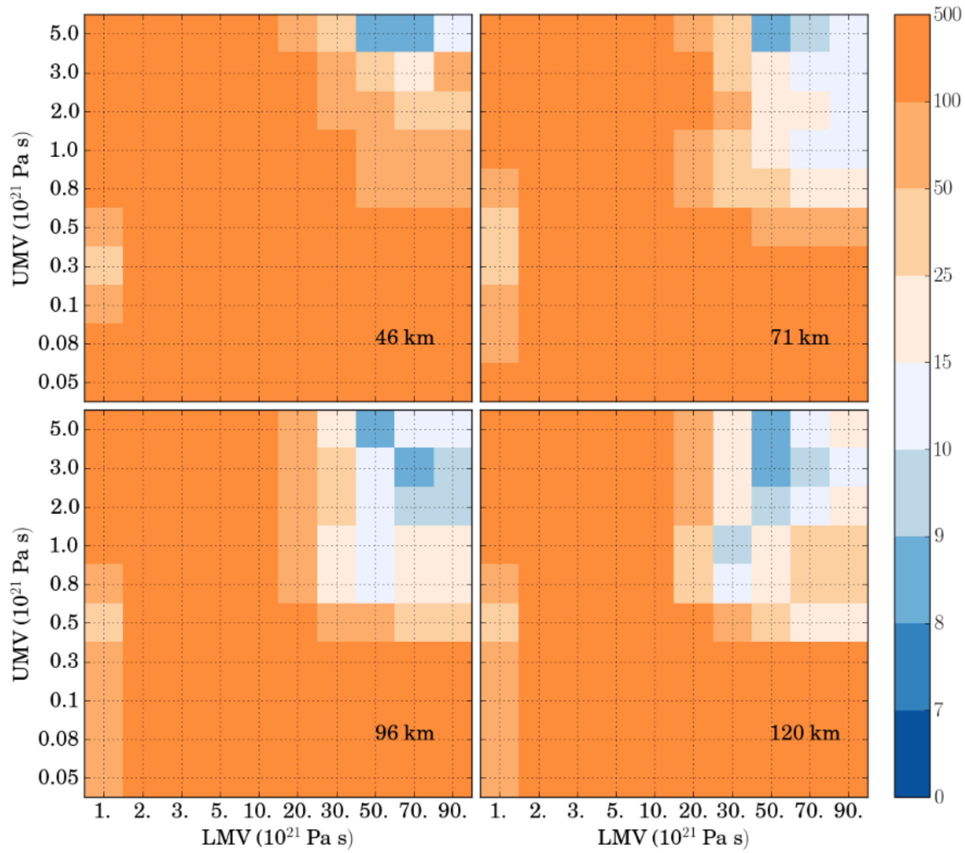

Figure S8. As in Figure 4, except including sediment loading effects and without data weighting.

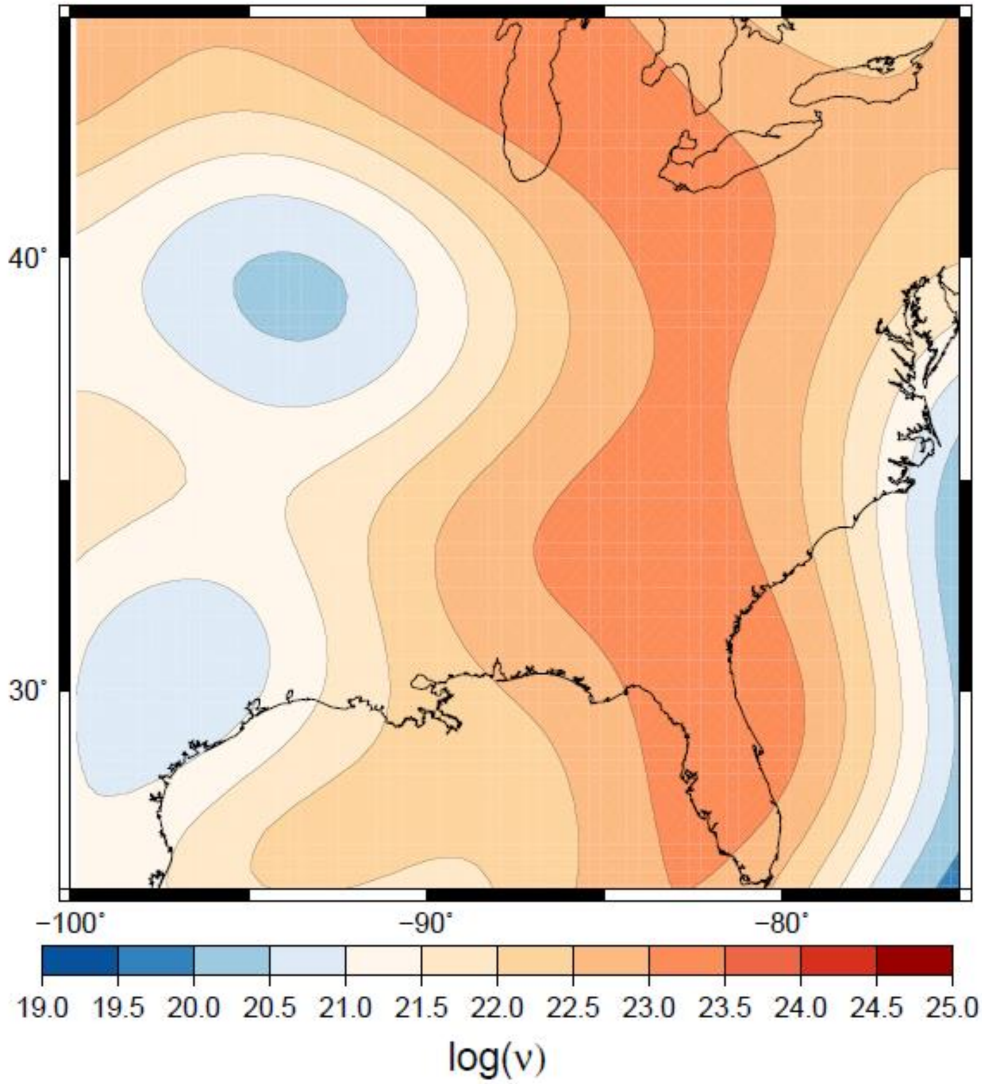

Figure S9. Mantle viscosity layer at 1000m depth according to the S40RTS tomographic velocity model (Ritsema *et al.*, 2011) and the procedure described in Latychev *et al.* (2005) for converting lateral velocity perturbations to lateral viscosity variations.

10

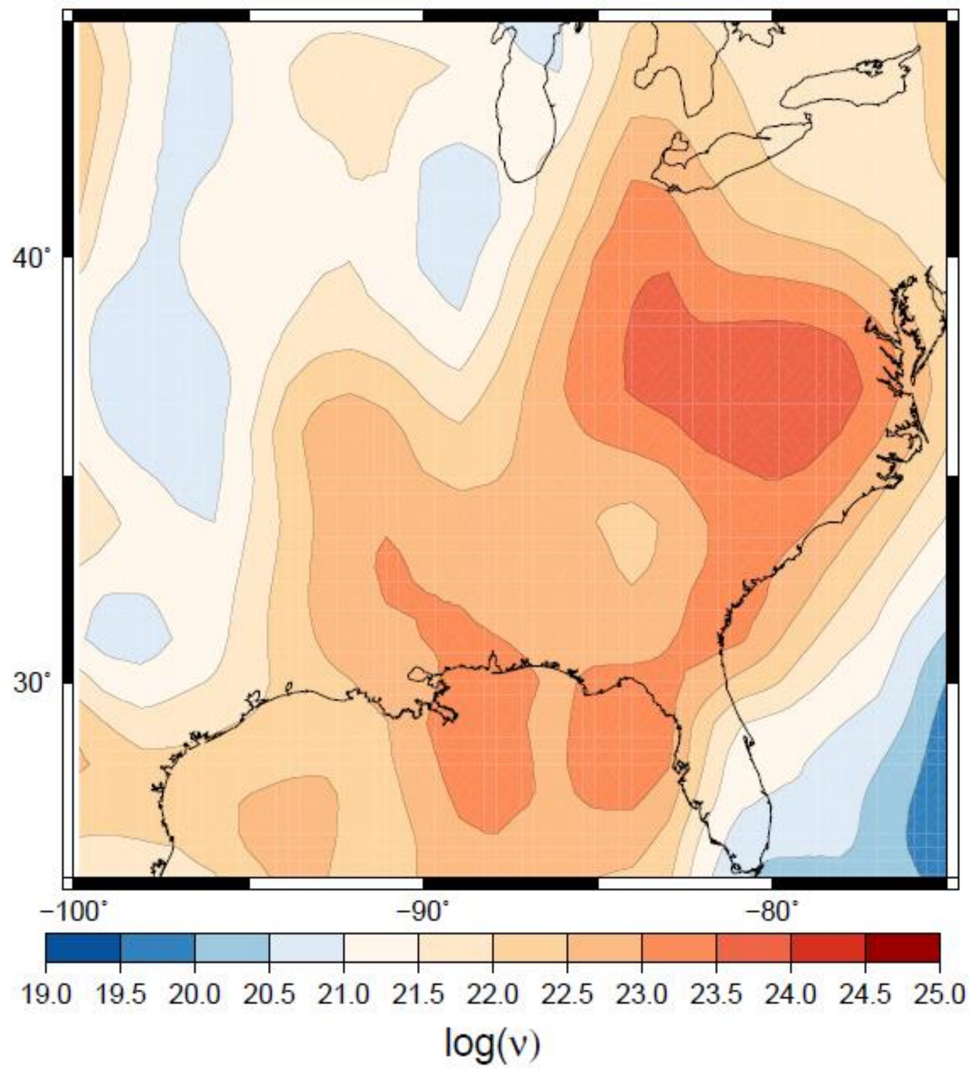

Figure S10. As in Figure S9, but for the Savani tomographic model (Auer *et al.*,2014).

11

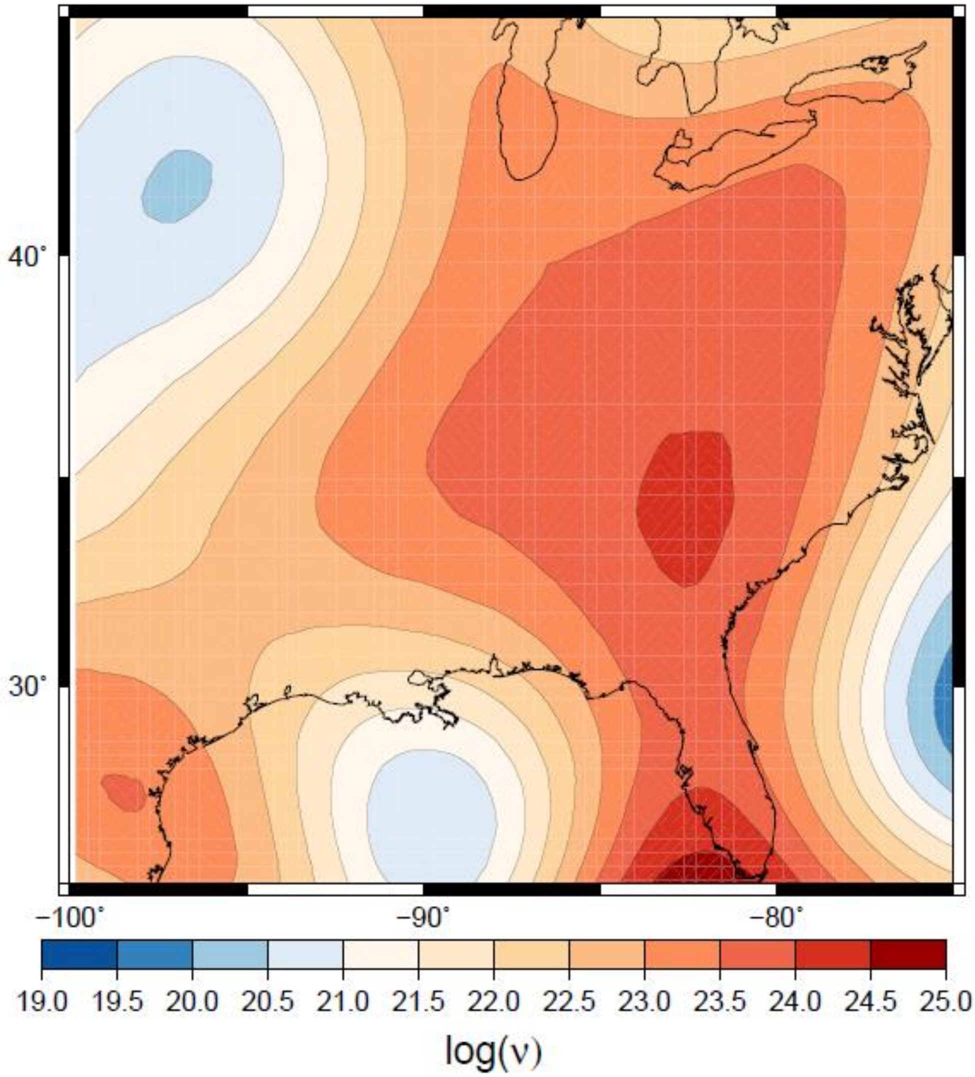

Figure S11. As in Figure S9 but for the SEMUCB-WM1 tomographic model (French and Romanowicz, 2014).

12

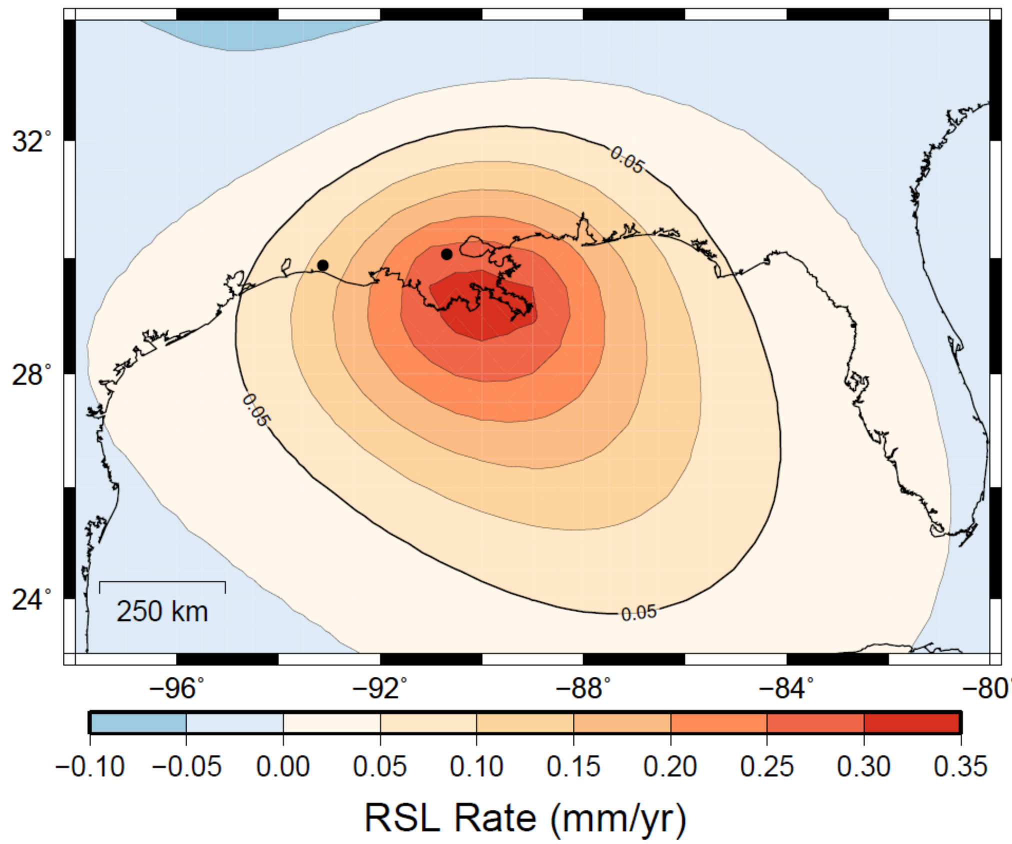

Figure S12. As in Figure 8, but for our heuristic upper bounding model.

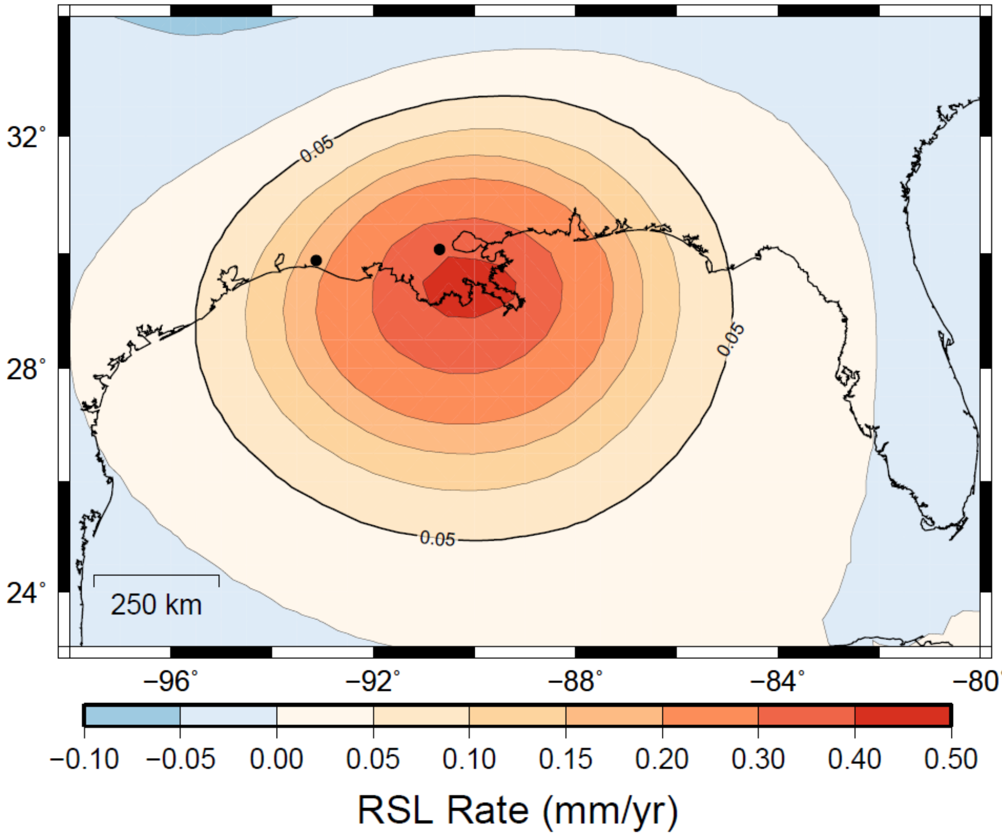

Figure S13. As in Figure 8, but for our heuristic lower bounding model. Note the scale bar has changed.

14

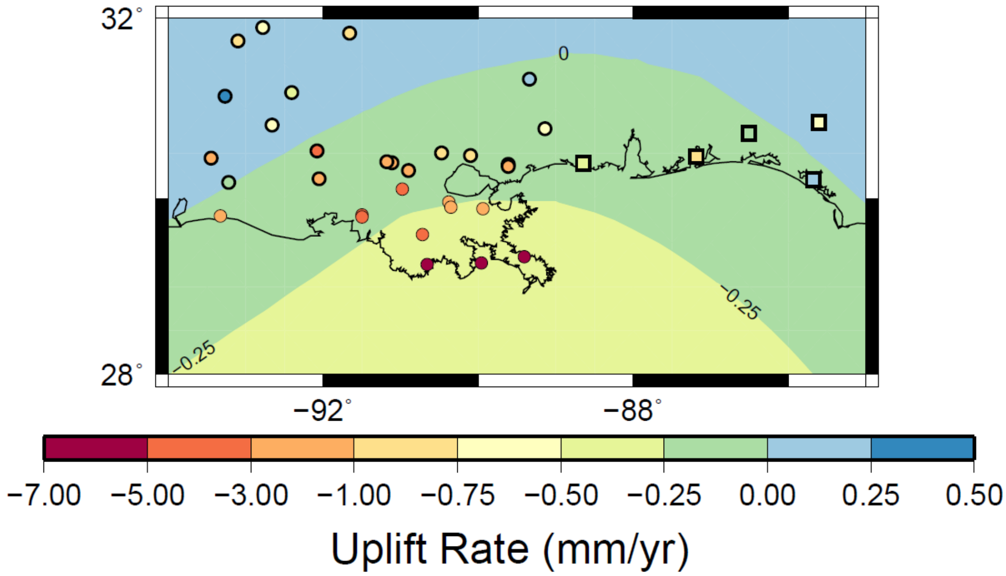

Figure S14. As in Figure 9, but for our heuristic upper bounding model.

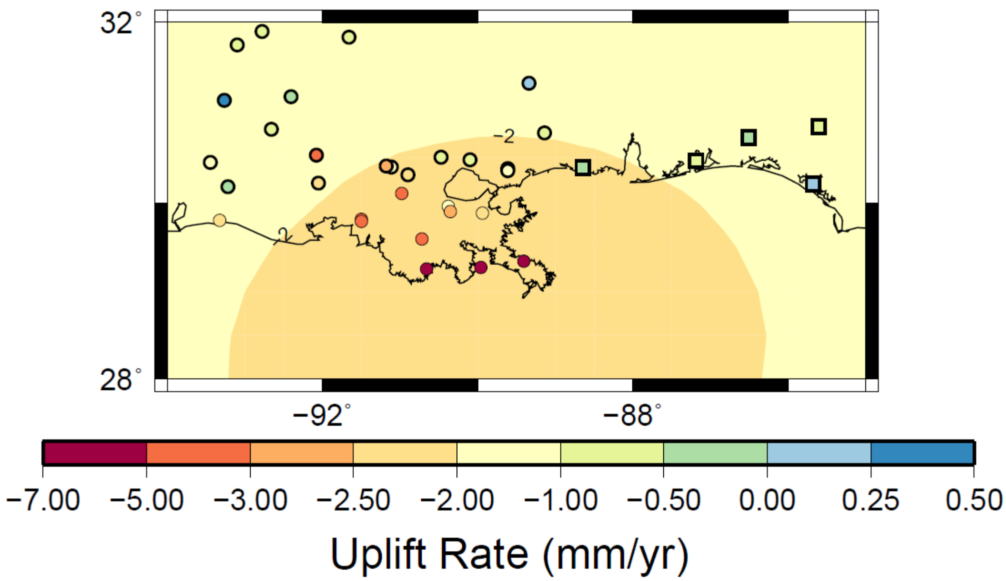

Figure S15. As in Figure 9, but for heuristic lower bounding model (note that the scale has also changed).

15

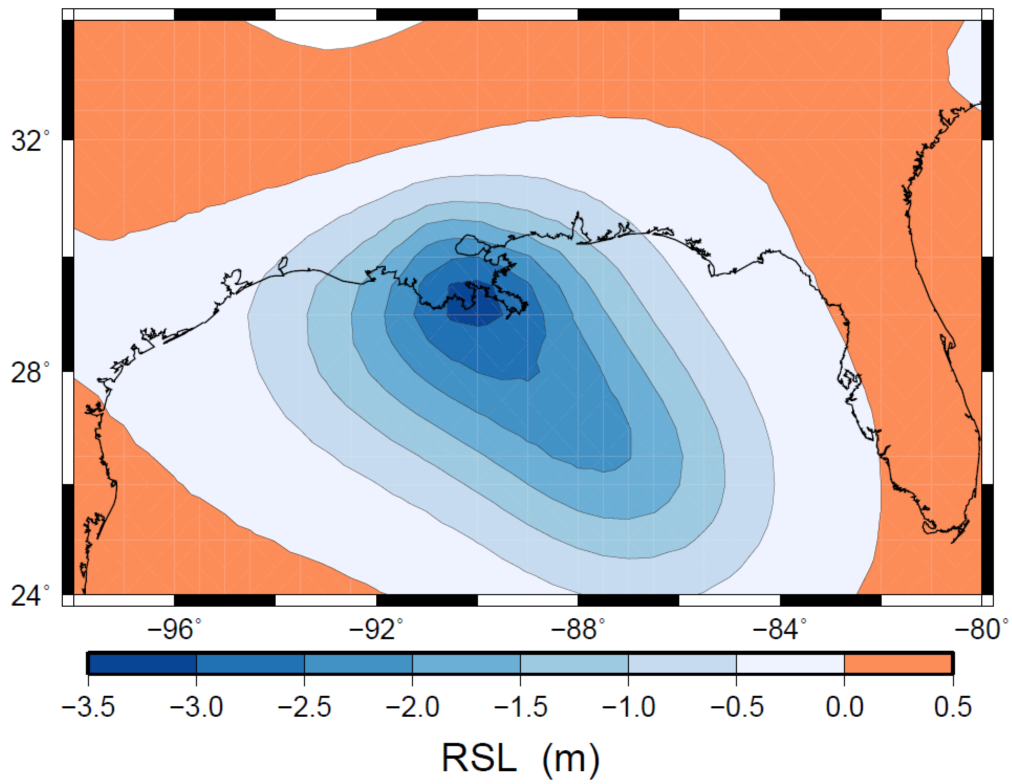

Figure S16. Pattern of SIA driven RSL at 10ky BP for optimal parameter set.

Table S1. Modelled vertical and horizontal land motion rates at locations of GPS stations provided in Karegar *et al.* (2015). We provide contributions from both GIA and SIA independently for the optimal parameter set. As the nominally Bayesian bounds are defined by an envelope of model runs, the bounds are defined by the minimum and maximum rates for each GPS site location from all the models within the envelope. Our rates are computed relative to the center of mass of the solid Earth.

Table S2. Modelled RSL rates for optimal and bounding parameter sets for PSMSL tide gauge locations along the Gulf coast, with contributions from GIA and SIA available separately for the optimal parameter set.

Inferring mantle viscosity from the analysis of data associated with the glacial isostatic adjustment (GIA) of the planet is a classic problem in geophysics. Unfortunately, in spite of a large body of published work spanning at least 60 years, little, if any, consensus has emerged.

Mitrovica, 1996

4

Postglacial Decay Times and Mantle Viscosity

When records of sea-level change since the last glacial maximum are examined, very different patterns are observed depending on where the records are collected. The patterns of sea level rise or fall over this time period are indicative of the processes that govern sea level change in those regions. As an example, records of RSL for Barbados, Ångerman River, Sweden and East Maine, USA are shown in Figure 4-1. Barbados, being far from any ice sheets, mainly records the addition of meltwater to the oceans and so records a sea level rise that is in some respects a measure of eustatic (ice-equivalent) sea level (Peltier and Fairbanks, 2006; Whitehouse and Bradley, 2013). I say *in some respects* because even far-field sites such as the Barbados are still influenced by isostatic effects and need to be corrected if one would like to determine an actual measure of ice volume (Milne and Mitrovica, 2008). Ångerman River, in Sweden, is in a formerly glaciated area and shows a steep sea level fall, which is largely a function of the uplift of the solid Earth following the unloading of the ice. The proximity of East Maine to the Laurentide ice sheet makes those records sensitive to the addition of water to the oceans, but also of the deformation of the surface of the Earth in response to the removal of the nearby ice sheet.

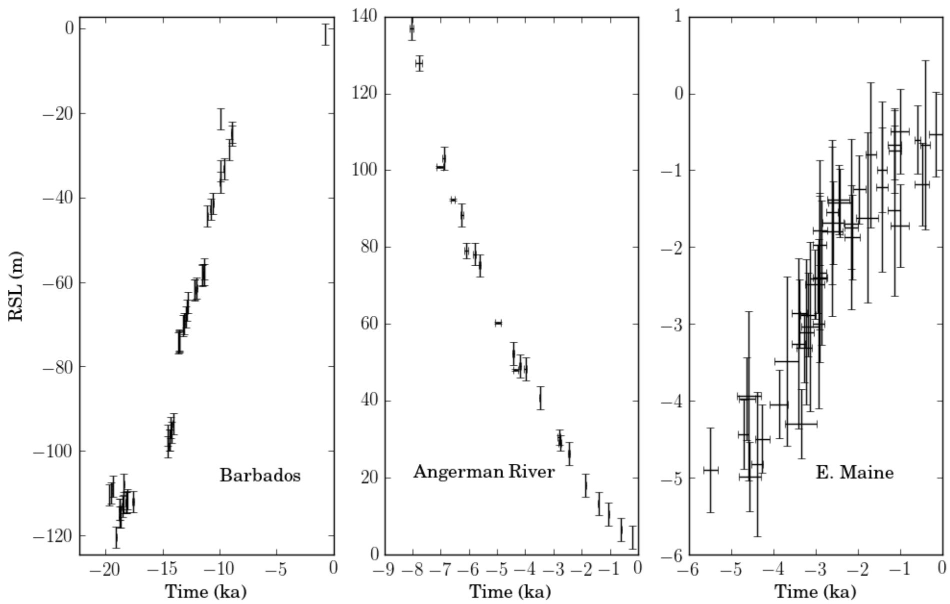

Figure 4-1: RSL data for Barbados, Angerman River, and East Maine. The Barbados record is based on samples of the coral species *Acropora palmata*, published in Peltier and Fairbanks, 2006. The Ångerman River data consists of both varve (layered clay and sediment) and carbon dated organic material, and was published in Nordman et al., 2015. The East Maine data are salt marsh microfossils published in Engelhart and Horton, 2012.

What is evident from the Ångerman River sea level record is that the sea level fall is in the form of an exponential decay. Such an exponential sea level fall is also observed in other previously glaciated areas such as Richmond Gulf and James Bay in Hudson Bay (Mitrovica and Peltier, 1995; Mitrovica et al., 2000). Moreover, it has previously been shown that for these curves the exponential decay constant is relatively insensitive to changes in the ice history (Mitrovica and Peltier, 1995; Mitrovica, 1996; Nordman et al., 2015), making decay times obtained from the sea level records relatively robust constraints on Earth viscosity. As it is typically the case that RSL data are sensitive to both Earth viscosity structure and details of the ice history, this makes these so-called *postglacial decay times* particularly valuable for constraining the Earth's viscosity, and as a result they have been used to constrain widely-used Earth viscosity models such as VM2 and VM5 (Peltier, 2004; Peltier and Drummond, 2008), and their associated ice histories. However, in the manuscript included at the end of this section (Kuchar et al., 2018b) we show that postglacial decay times are not as insensitive to ice history as has been previously thought. In the next section I provide context by discussing the studies and arguments that suggest the RSL decay times are relatively insensitive to the ice history (some of which is also discussed in the manuscript). I will then briefly summarise the approach and results of my research, and what the ultimate consequences are for constraining Earth viscosity.

4.1 Background: The Exponential Form of Relative Sea Level

The exponential form of sea level records in Hudson Bay was first applied by Andrews, 1970, who modelled future sea level change remaining at some time t with

$$SL(t) = Ae^{-t/\tau}, \tag{4.1}$$

where τ is the decay time and A the amplitude. Later studies (e.g. Mitrovica et al., 2000) would use such a form to determine RSL, where $RSL(t) = SL(t) - SL(t_p)$:

$$RSL(t) = A(e^{-t/\tau} - 1). \tag{4.2}$$

A vertical shift c was introduced to equation 4.2 by Walcott, 1980, on the basis that the sea level data are a better constraint of relative altitude differences than they are on absolute historical sea level. Moreover, uncertainties associated with real sea level data may result in the best-fitting curve through RSL data being one that doesn't pass through the origin. Therefore, RSL data with an exponential behaviour are best fitted by a function of the form (Mitrovica et al., 2000)

$$RSL(t) = A(e^{-t/\tau} - 1) + c. \tag{4.3}$$

Not only was Andrews, 1970 the first to model the sea level in Hudson Bay as an exponential, he also gave an expression for the decay time as

$$\tau = \frac{2\pi\eta}{\rho g L}, \tag{4.4}$$

where η is the mantle viscosity, ρ is its density, g is the gravitational acceleration, and L is a characteristic length-scale of the deformation caused by the ice sheet. What is notable about this expression is that while the decay time depends explicitly on the viscosity of the Earth, it depends on characteristics of the ice sheet only implicitly through the length-scale L. While Andrews, 1970 did not derive the expression in equation 4.4, instead citing Heiskanen and Vening Meinesz, 1958, such an expression can be derived by considering a simplified scenario of the deformation of a viscous half-space, and indeed this had been done decades earlier by Haskell, 1935, who considered such an argument for postglacial uplift in Fennoscandia to estimate the viscosity of the mantle.

The sensitivity of decay times to ice history was explored by Mitrovica and Peltier, 1993 and Mitrovica and Peltier, 1995, first by comparing Hudson Bay decay times generated from the output of a GIA model with ICE-1 and ICE-3 iterations of the ice histories of Peltier's research group (Peltier and Andrews, 1976; Tushingham and Peltier, 1991), and then with a similar study, except where the ice histories were ICE-3 and a simple ice disk model. In both cases Mitrovica and Peltier concluded that there was no significant sensitivity to the assumed ice history (or at the very least, any sensitivity was below the resolving power of the data). As both ICE-1 and ICE-3 are iterations of the same family of ice histories, it may not be unexpected that they would yield similar decay time predictions, but certainly the ice disk is dissimilar enough from ICE-3 that the ice insensitivity of the decay time data is a significant result. However, an indication that the ice insensitivity was not absolute appeared in Mitrovica, 1996, who once again computed decay times for the ICE-1 history and a simple ice disk, but this time for the Fennoscandian ice sheet. By computing decay times for Ångerman River, Sweden and Oslo, Norway, it was found that while the Ångerman River decay times were insensitive to ice variation, the same could not be said for Oslo. This result demonstrated that the geographic position of the sea level data, relative to the geometry of the ice sheet, is important for determining ice-sensitivity of decay times.

More recently, Nordman et al., 2015 revisited the Ångerman river decay time ice sensitivity by generating model results for tens of reconstructions of the Fennoscandian Ice Sheet (FIS). These reconstructions, in contrast to the ICE-N models of the Peltier group which are hand-tuned to minimize the misfit with RSL data, are the output of a 3D thermomechanically coupled ice sheet model, calibrated against RSL, present-day uplift, and ice margin data (Tarasov, 2013). The results of the Nordman study were that an ice sensitivity was observed, but that it was a low-level sensitivity and so they concluded that the decay times were relatively insensitive to ice history. Within the last year, a study lead by an MSc student in our research group (Hill et al., 2018) that used decay time constraints to determine whether the data could resolve the existence of a low viscosity layer above the mantle transition zone, found an ice sensitivity in both Richmond Gulf and Ångerman River that was large enough to influence which Earth viscosities satisfied the data. Because the prevailing wisdom was that postglacial decay times are insensitive to ice history, this was an interesting development, and it is what inspired the work of this chapter.

Before moving on I think it is instructive to provide a derivation for the exponential form of RSL and, in particular, the decay time τ in equation 4.4. The lack of any explicit dependency of τ on the ice history is striking, and so it is worth understanding exactly what assumptions are made. The argument I present here follows those of Turcotte and Schubert, 2002 and Ranalli, 1995.

We will consider the mantle to be a linear fluid, with an initial deformation profile following deglaciation given by

$$W_m(x) = W_0 \cos\left(\frac{2\pi x}{\lambda}\right), \tag{4.5}$$

where the wavelength of the deformation, λ, is assumed to be much greater than the vertical displacement ($\lambda >> W_m$). The Navier-Stokes equations in 2-dimensions (x horizontal and y vertical) for an incompressible Newtonian fluid can be written as

$$-\frac{\partial P}{\partial x} + \eta\left(\frac{\partial^2 u}{\partial x^2} + \frac{\partial^2 u}{\partial y^2}\right) = 0 \tag{4.6}$$

$$-\frac{\partial P}{\partial y} + \eta\left(\frac{\partial^2 v}{\partial x^2} + \frac{\partial^2 v}{\partial y^2}\right) = 0 \tag{4.7}$$

where P is the pressure generated by fluid flow, which is the total pressure minus the hydrostatic pressure, $P = p - \rho g y$, and u and v are the horizontal and vertical velocities (with the vertical axis defined by having $y = 0$ at the undeformed $r = a$ surface, and increasing with depth). The incompressibility condition is

$$\frac{\partial u}{\partial x} + \frac{\partial v}{\partial y} = 0, \tag{4.8}$$

and this is satisfied if we introduce a new function (the *stream function*) ϕ such that

$$u = -\frac{\partial \phi}{\partial y} \tag{4.9}$$

$$v = \frac{\partial \phi}{\partial x} \tag{4.10}$$

which we can then substitute into the Navier-Stokes equations (equations 4.6 and 4.7). We may then eliminate the fluid pressure by taking $\frac{\partial}{\partial y}$ of 4.6 and $\frac{\partial}{\partial x}$ of 4.7 and combining them. This then gives us the biharmonic equation,

$$\frac{\partial^4 \phi}{\partial x^4} + \frac{\partial^4 \phi}{\partial y^4} + 2\frac{\partial^4 \phi}{\partial^2 x \partial^2 y} = 0. \tag{4.11}$$

Because our initial displacement profile is harmonic with a period of $2\pi/\lambda$, it is reasonable to assume the same for the solution ϕ, and we further assume a separable solution, $\phi(x,y) = \sin\left(\frac{2\pi x}{\lambda}\right)Y(y)$. In fact, a function of this form does satisfy equation 4.11, with possible solutions for Y

$$Y(y) = e^{\pm\frac{2\pi y}{\lambda}}$$
$$Y(y) = ye^{\pm\frac{2\pi y}{\lambda}}.$$

So that the solution remains finite as $y \to \infty$, we choose only the negative exponential solutions, and so our general solution is something of the form

$$\phi(x,y) = \sin\left(\frac{2\pi x}{\lambda}\right)e^{-\frac{2\pi y}{\lambda}}(A + By). \tag{4.12}$$

The stream function allows us to compute the velocities u and v, which are

$$u = -\frac{\partial \phi}{\partial y} = e^{-\frac{2\pi y}{\lambda}} \sin\left(\frac{2\pi x}{\lambda}\right)\left(\frac{2\pi}{\lambda}(A + By) - B\right) \tag{4.13}$$

$$v = \frac{\partial \phi}{\partial x} = \frac{2\pi}{\lambda}e^{-\frac{2\pi y}{\lambda}} \cos\left(\frac{2\pi x}{\lambda}\right)(A + By) \tag{4.14}$$

To determine B, we can apply the no-slip condition at the top of the mantle, $u(y = W) = 0$. Because $W << \lambda$, we can take this condition to be approximately $u(y = 0) = 0$, which gives us the condition that $B = \frac{2\pi A}{\lambda}$. We can determine conditions on A by relating the pressure induced by the topography with the fluid pressure. For a linear fluid, we have

$$\sigma_{yy} = p - 2\eta\dot{\epsilon}_{yy}, \tag{4.15}$$

and because $\dot{\epsilon}_{yy} = \frac{\partial v}{\partial y} = 0$ at the upper surface,we have $p = -\rho g W$. We can also solve for the pressure by substituting ϕ into the Navier Stokes equation 4.6 and integrating, which gives us the pressure at the upper surface

$$p = 2\eta A\left(\frac{2\pi}{\lambda}\right)^2 \cos\left(\frac{2\pi x}{\lambda}\right), \tag{4.16}$$

and therefore we have

$$A = -\frac{\rho g W_0}{2\eta}\left(\frac{2\pi}{\lambda}\right)^{-2}. \tag{4.17}$$

What we are ultimately interested in is the vertical deformation through time, $\dot{W}$. This is of course v at the surface, $y = W$, though we will again use the small displacement approximation to consider instead v at $y = 0$, which is

$$v(x, y = 0) = A\frac{2\pi}{\lambda}\cos\left(\frac{2\pi x}{\lambda}\right). \tag{4.18}$$

Putting equations 4.17 and 4.18 together, we have

$$\dot{W} = -\frac{\rho g W \lambda}{4\pi\eta}, \tag{4.19}$$

with the exponential solution

$$W = W' e^{-\frac{\rho g \lambda t}{4\pi\eta}}. \tag{4.20}$$

We have recaptured the decay time expression in 4.4, associating the deformation lengthscale L with half the wavelength λ. Now that we've repeated the derivation, we are able to see where problems might arise when applying it to ice sheets in the real world. The first thing to note is that, while it was never necessary to choose the centre of the deformation $x = 0$, the deformation profile was assumed to be a cosine function. It is likely that this is a good approximation at the deformation centre, but not at greater distances. It is also noteworthy that at several points in the derivation we used the $W << \lambda$ condition to treat the surface $y = W$ as though it were instead $y = 0$. Realistically, the maximum vertical deformation observed in Hudson Bay or Ångerman River is hundreds of metres, with a corresponding horizontal length scale measured measured in hundreds of kilometres, so that W is on the order of a thousandth λ, which may not be small enough to make this simplifying approximation robust. Another point to note is that we ignored the effects of a lithosphere (except to provide a rigid boundary to apply the no-slip condition), and considered only vertical uplift of the mantle given an initial deformation profile. The final point, which leads into our next section, is that we derived the exponential form of uplift by considering uplift after the removal of an external load. The key point is that exponential uplift applies in the absence of external forces, and we will see that in the real world, such a situation rarely exists.

4.2 Contending With Reality: The Limitations Inherent in Real Data

Let's assume for a moment that the Earth is perfectly described as a laterally homogeneous Maxwell material, and that the analysis in the previous section applies without reservation to the uplift of the Earth in previously glaciated areas. Even in such a world, we run into two key hurdles. The first is the availability and distribution of RSL data, and the second is that RSL data record the history of the changing ocean load, and as a consequence free decay in the absence of external loading can not be measured by RSL data. These aspects lead to two novel data-corrections that we apply in Kuchar et al., 2018b that I will motivate and describe here.

In this section, I will discuss the data available in Hudson Bay in particular, which have been used over the years to infer very different decay times depending on the study and exactly what subsets of data were used, and how they were treated. For example, Peltier, 1996 derived decay times for different locations in Hudson Bay, and obtained decay times with a range from 3.06 ka in Ottawa Island to 7.23 ka in Richmond Gulf. In a subsequent study, Peltier, 1998 combined all the available data (comprising various types of mussels and mixed shells, as well as driftwood and bone samples) across a large spatial area in Hudson Bay to argue for a single decay time of 3.4 ka for the entire region. In Figure 4-2 I show the locations of all the data used by Peltier, 1998, as well as which samples are which material.

It is evident in Figure 4-2 that the full collection of sea level indicators in Hudson Bay has a large spatial extent, and is composed of many different materials. This is important because different sea level indicators have different *indicative meanings*, which is the defined relationship between the indicator and the height of mean sea

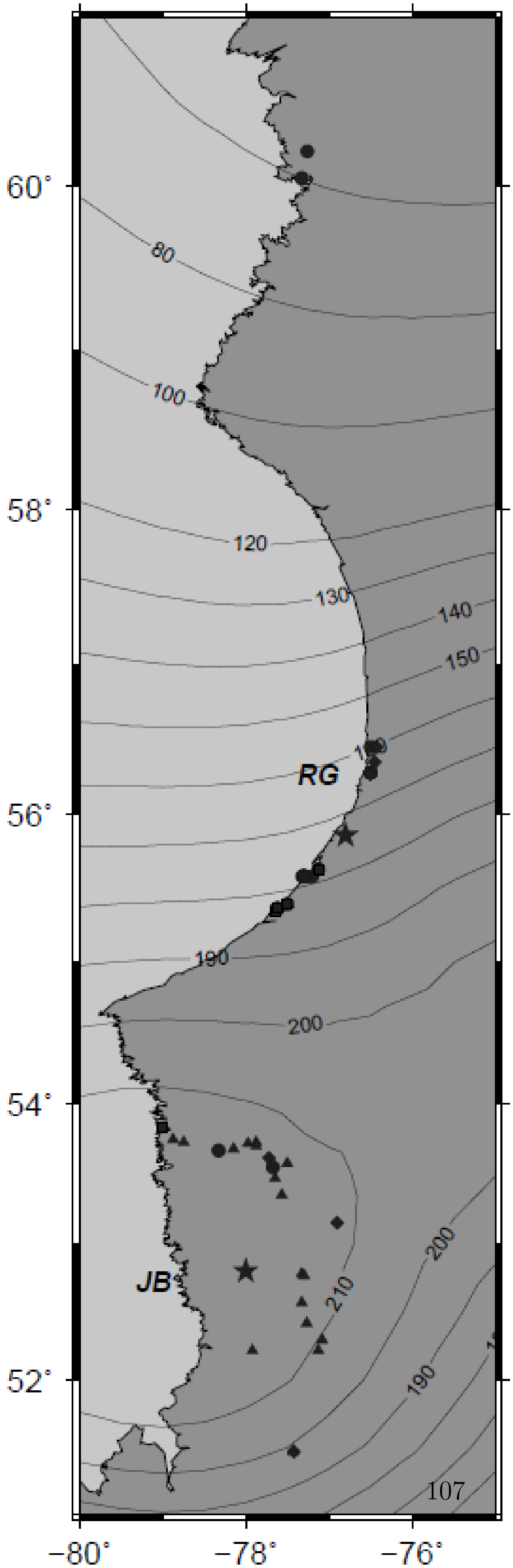

Figure 4-2: The spatial distribution of RSL data used by Peltier, 1998 (provided in their Table 1). Solid black circles indicate *Mytilus edulis* samples, diamonds indicate samples of Hiatella arctica, triangles indicate samples of mixed shells, and squares indicate driftwood samples. With RG and JB I indicate the Richmond gulf and James Bay regions, with stars showing the locations of what I refer to as "aggregate sites" that are used when computing decay times from the data (see text). The contours show an example of calculated sea RSL across Hudson Bay at 7ka BP for an Earth model with a 71km thick lithosphere, a 3×10^{20} Pa s upper mantle viscosity, and a 1×10^{22} Pa s lower mantle viscosity. The ice history assumed is ICE5G.

level at the time it was formed. For example, samples of *Mytilus edulis* (more commonly known as Blue Mussels) indicate their environment was in shallow waters below the intertidal zone within a well-defined depth range (Pendea et al., 2010), while a driftwood sample is what is called *limiting data* as it indicates only that sea level was an unquantifiable depth below the elevation of the driftwood sample at the time of deposition. The large spatial extent of the data is problematic because, as we show with the contours in Figure 4-2, there is a large sea level gradient from the southernmost to northernmost data samples. It is common to place data from nearby locations on to a single RSL-time plot in order to estimate an exponential decay time; however, this will lead to errors when there is a large sea level gradient between the sample sites.

The data presented in Peltier, 1998 was revisited by Mitrovica et al., 2000, who addressed the issues in the preceding paragraph by 1) considering only the samples of *Mytilus edulis*, and 2) considering separate aggregate sites for Richmond Gulf and James Bay, rather than cluster all data samples together. In the analysis of Mitrovica et al., they conclude that the Richmond Gulf decay time is in the range 4 - 6.6 ka, and the James Bay decay time is a significantly lower 2.0 - 2.8 ka. This Richmond Gulf decay time estimate has since been used to constrain Earth viscosity structure by Lau et al., 2016. The lower James Bay decay time is interesting, because if decay times are insensitive to local ice geometry and the structure of the Earth is not expected to vary greatly (as you would expect for Richmond Gulf and James Bay, which are only approximately 500 km apart), you would expect similar decay times. This difference was attributed to be caused either by lateral variations in local Earth structure or flaws in the data. Indeed, the James Bay data was later re-examined by Pendea et al., 2010, who noted that the original James Bay data were presented without uncertainty, and were composed of both *Mytilus edulis* and *Hiatella arctica* samples, the latter of which are a variety of saltwater clam found living at depths of up to 40 m, significantly deeper than the *Mytilus* samples. A new decay time of 2.7 - 4.7 ka for James Bay was estimated by Lau et al., 2016, using the data of Pendea et al., 2010.

Figure 4-2 shows that, even considering only *Mytilus edulis*, and considering only the samples clustered in Richmond Gulf, as was done in Mitrovica et al., 2000, there can be a sizeable RSL gradient across the data locations (tens of metres at 7 ka for the parameters shown). Because it is necessary to have all data from a region placed on the same time series to fit the data and determine a decay time, the spatial variability of the sea level among those data points poses a problem. My method to solve this problem in the attached manuscript was to calculate a correction to the sea level data to shift them to the location of an aggregate site. This was done by computing RSL at the individual location and age of each sea level index point, as well as at the aggregate location (shown by a star in Figure 4-2), and then shifting the recorded RSL of the data by the difference in modelled RSL between the actual data location and the aggregate location, for each set of model parameters (so that the data is corrected for every model run). As a clarifying example, let's consider Figure 4-2. The northernmost datapoint in the Richmond Gulf region is right on the 160 m contour, and the aggregate location is between the 170 and 180 m contours, so let's say $RSL_N = 160$ m and $RSL_A = 175$ m. In this case, the RSL measured by the actual datapoint would be shifted up by the difference, 15 m (assuming in this example that the datapoint corresponds to the time step shown in the figure). We found that applying this spatial correction to the data is important as it affected the model parameter space allowed by some data sets.

The second consideration we need to make is that sea level indicators measure changes in sea level, or equivalently, changes in the thickness of the column of water at that location. This is important because, as the derivation in the previous section illustrated, the exponential uplift of a material with a linear viscosity applies only after the forcing is removed. As the sea level changes, so too does the size of the ocean load, and so the sea level indicators are measuring sea level in response to a fully removed ice load, but also a present and changing ocean load. This issue was explored in detail by Han and Gomez, 2018, who investigated the impact of the ocean load on decay time observations in Hudson Bay, and who found that the ocean load can contaminate the free decay signal by as much as 1.6 ka. In fact, when we first encountered an apparent sensitivity to ice histories in our modelled decay times, I assumed it was due to this ocean loading effect. To correct for this, the sea level code is run and the contribution to RSL due to just the ice load is isolated. This way, $RSL_{\text{full}} - RSL_{\text{ice}}$ gives the contribution to RSL from the ocean load and rotation. The modelled RSL_{ice} at a given location will give the modelled free decay signal that can be used to obtain a model decay time, and the difference $RSL_{\text{full}} - RSL_{\text{ice}}$ is applied to the data, so that the contributions of the ocean load and rotation are removed.

4.3 Research Summary and Conclusions

We tackled the problem of determining the sensitivity of postglacial decay times to ice history by using a suite of ice histories output from glaciological models (Tarasov et al., 2012; Tarasov, 2013), as well as the popular ICE5G (Peltier, 2004) and Australian National University (ANU) (Lambeck et al., 2014) ice models. In total we considered twelve reconstructions of the North American Ice Sheet (NAIS) and 10 reconstructions of the Fennoscandian ice sheet (FIS). For the NAIS we computed model decay times in Richmond Gulf and James Bay, which are separated by approximately 500 km, and Ångerman River for the FIS. Data from all three locations have historically been used to constrain Earth viscosity (Peltier, 1998; Mitrovica et al., 2000; Nordman et al., 2015; Lau et al., 2016).

The results of the paper are split into two sections, the first is a model sensitivity analysis, and the second is a model-data comparison. In the former section the goal is to determine whether there is a significant ice sensitivity to the computed model decay times, and in the latter section it is to determine how this sensitivity impacts the ability of the data to resolve Earth structure. We performed the model sensitivity by computing RSL_{ice} for the three study locations, for all ice histories and a suite of Earth viscosity structures, and fitting the model curves via a least squares routine to determine the best fitting curve of the form

$$RSL(t) = A(e^{-\frac{t}{\tau}} - 1). \tag{4.21}$$

We observed that there is an ice sensitivity to the decay times, particularly in James Bay, where decay times for a given viscosity structure differ by several thousand years for different ice histories. The least sensitivity is seen in Richmond Gulf, but it is not completely absent. Given the relatively high degree of sensitivity in James Bay, we conclude that the James Bay data are not appropriate for constraining Earth structure with their associated decay times. The data-model comparison for Richmond Gulf indicates that, while the model decay time sensitivity is low, the overall poor quality of the data has the result that the ability of the data to constrain earth viscosity is also poor, with a large number of models being accepted by the data constraints. The Ångerman River data-model comparison, however, results in relatively few viscosity models being accepted by all ice histories. If we consider viscosity models accepted by the Ångerman River data for all FIS reconstructions and by the Richmond Gulf data for all NAIS reconstructions, then there are only two viscosity models that satisfy both constraints. Both have an upper mantle viscosity of 0.3×10^{21} Pa s, and they have lower mantle viscosities of 10 and 20×10^{21} Pa s, respectively. These results agree with other recent studies (e.g. Nordman et al., 2015, Lau et al., 2016), but I note that combining the constraints makes the assumption that the viscosity structure of the Earth is laterally homogeneous, and while this is consistent within our modelling framework, it is expected that the real Earth features significant lateral viscosity variations.

4.4 Article 3: On the Usefulness of Relative Sea level Decay Times for Constraining Earth Viscosity Structure

Statement of Contribution

The following manuscript is my own written work performed under the supervision of Dr. Milne. I generated all model results and produced all figures. I also developed the data corrections described in the text. Alexander Hill is an MSc student in our research group, and this project was motivated by results he had generated. Specifically, he was using postglacial decay times to determine whether they could constrain Earth models with low viscosity layers, but observed an ice history dependency to his results. This was not supposed to happen, according to the literature, and so I performed this study to understand and quantify this sensitivity. Lev Tarasov provided the majority of the ice histories we consider.

An investigation into the sensitivity of postglacial decay times to the assumed ice history

Joseph Kuchar[1], Glenn Milne[2], Alexander Hill[2], and Lev Tarasov[3]

1. Department of Physics, University of Ottawa
2. Department of Earth and Environmental Science, University of Ottawa
3. Department of Physics and Physical Oceanography, Memorial University of Newfoundland

Abstract

At the centers of previously glaciated regions such as Hudson Bay and Sweden it has been observed that the sea level history follows an exponential form, and it has been shown that the time constant is relatively insensitive to the changes in the ice load history. We revisit the issue of decay time ice load sensitivity by computing relative sea level histories for Richmond Gulf and James Bay in Hudson Bay and Ångerman River in Sweden for a suite of reconstructions of the North American and Fennoscandian Ice Sheets and Earth viscosity profiles. We find that while some Earth viscosity models do indeed show insensitivity in computed decay times to the ice history, this is not true in all cases. Moreover, we find that the location of the study site relative to the geometry of the ice sheet is an important factor in determining ice sensitivity, and based on our set of ice sheet reconstructions, conclude that the James Bay decay time should not be used to constrain Earth viscosity. We describe novel corrections to the RSL data to remove the effects associated with the spatial distribution of sea level indicators as well as for other signals unrelated to regional ice loading (ocean loading, rotation and global mean sea-level changes) and demonstrate that they can significantly affect the inference of viscosity structure. We performed a forward modelling analysis based on a commonly adopted 2-layer, sub-lithosphere viscosity structure to determine how the solution space of viscosity models changes with the input ice history at the three study sites. While the solution spaces depend on ice history, in both Richmond Gulf and Ångerman River there are regions of parameter space where solutions are common across all or most ice histories, indicating low ice sensitivity for these mantle viscosity parameters. In Richmond Gulf, UMV values of (0.3-0.5)x10^{21} Pa s and LMV values of (5-50)x10^{21} Pa s tend to satisfy the data constraints consistently for most ice histories. Similarly, the Ångerman River solution spaces contain a solution with a UMV value of 0.3x10^{21} Pa s and LMV values of (5-50)x10^{21} Pa s common to 9/10 ice histories considered there.

1. Introduction

The Earth's response to the transportation of mass between the oceans and continents during glacial cycles includes deformation of the solid Earth as well as perturbations to the Earth's gravitational field (associated both with the initial mass flux and with the mass redistribution of the Earth and oceans), and rotation vector. This process is termed glacial isostatic adjustment (GIA), and is the dominant process determining sea level changes on 1-10 ka timescales during the transition from glacial to interglacial conditions.

The key inputs to a model of GIA are a history of ice loading to force the model and an Earth viscosity model to determine how the Earth will deform in response to the applied load. These parameters are generally not well known in advance, and so a typical study will proceed by either *i)* generating output and comparing to observables to constrain Earth rheology given an assumed ice history, *ii)* determining an Earth viscosity model independently and using the data to constrain the ice history, or else *iii)* a joint inversion to determine the combination of ice history and Earth rheology that best fit the data. Studies of the first type proceed by using as input one or more previously determined ice histories and varying Earth model parameters to compare to observables, most commonly RSL (e.g. Peltier *et al.*, 2002; Steffen and Kauffman, 2005; Love *et al.*, 2017) or GPS data (e.g. Sella *et al.*, 2007). Studies of the 2nd type proceed by using observations that are insensitive to variations in the ice history to constrain the Earth viscosity model, before using observations to constrain the ice history. For example the VM1 (Peltier, 1996) and VM2 (Peltier, 2004) radial viscosity models are designed to satisfy postglacial decay time observations (which are the focus of this study and will be discussed in more detail below) and are subsequently further validated by comparing to a broader range of GIA observables. In the final type, optimal Earth and ice model components are jointly determined by, for example, assuming an initial ice history that can be scaled regionally, and searching for combinations of scaling parameters and Earth rheologies that minimise the data misfit (e.g. Lambeck *et al.*, 1998; Lambeck *et al.*, 2017, Caron *et al.*, 2017). In most cases, because RSL data are sensitive to both ice and Earth parameterizations, parameter trade-off makes it difficult to independently determine either parameter, resulting in most inferences of Earth structure based on a GIA analysis being necessarily coupled to the ice history that was used, or vice-versa.

As mentioned above, one method of constraining Earth viscosity structure while minimizing dependence on ice history is through the use of postglacial decay times. In previously glaciated regions such as Hudson Bay or Fennoscandia, it is known that the RSL curve can be approximated by an exponential decay (McConnell, 1968; Andrews, 1970; Cathles, 1975; Mitrovica *et al.*, 2000). It has been shown that, while the amplitude of the exponential curve is directly dependent on ice history, the decay constant is relatively insensitive to changes in the ice history (e.g. McConnell, 1968; Andrews, 1970; Mitrovica and Peltier, 1995; Lau *et al.*, 2016). This feature has made the RSL observations in Hudson Bay and Sweden, and their associated decay times, key constraints on Earth rheology in many GIA studies (e.g. Mitrovica and Peltier, 1993; Mitrovica and Peltier, 1995, Peltier, 2004; Nordman *et al.*, 2015; Roy and Peltier, 2015; Lau *et al.*, 2016; Hill *et al.*, 2018) This paper was primarily motivated by the results of a recent study (Hill *et al.*, 2018), which demonstrates some sensitivity to decay times in Hudson Bay and Ångerman River to the extent that, in some case, the inferred Earth viscosity models depend on the assumed ice history. While the insensitivity of postglacial decay times to ice history is often cited, there have been relatively few studies probing the extent of the insensitivity, and only one attempt at a systematic investigation involving a large variety of both ice histories and Earth rheologies (Nordman *et al.*, 2015, discussed in more detail below). Indeed, it is only relatively recently that the development of glaciological models (e.g. Tarasov *et al.*, 2012; Tarasov, 2013) has resulted in a significant increase in the number of ice histories available to GIA modellers, making the sort of investigation of Nordman *et al*., or this study, possible.

An excellent overview of the use of the postglacial decay time approximation is found in Mitrovica *et al.* (2000), and here we end this section with a brief discussion centered around the conclusion of the insensitivity of this parameter to variations in the regional ice loading history.

For a Maxwell Earth, the Love numbers describing the viscoelastic response to an impulse loading in time and point-like in space contain an immediate elastic component, as well as a sum over modes of weighted exponentials (Peltier, 1974). For example, the Love number that represents radial deformation is defined as,

$$h_l(t) = h_l^E \delta(t) + \sum_{k=1}^{N} e^{-s_k^l t}, \tag{1}$$

where h_l^E is the immediate elastic component of the response at spherical harmonic degree l, and the sum contains the non-elastic component of the response as a sum of decaying exponentials with amplitudes r_k^l and individual decay times $1/s_k^l$. The vertical land motion response to a general loading is given by convolving this loading function over time and space with $h_l(t)$. Based on this normal mode theory, the deformational response is characterised by a sum of weighted exponential functions. Thus, representing this response by a single relaxation time is an approximation; however, it provides the basis for a method to estimate mantle viscosity structure from near-field data while minimising sensitivity to the uncertainty in the ice history.

The sensitivity of postglacial decay times to ice history was investigated in Mitrovica and Peltier (1993) and again in Mitrovica and Peltier (1995). The first study compared decay times inferred from ICE-3G (Tushingham and Peltier, 1991), and ICE-1 (Peltier and Andrews, 1976), and concluded that the resolution of the data was not enough to differentiate between the ice histories. Similarly, Mitrovica and Peltier (1995) investigated the ice history sensitivity of decay times by computing normalised RSL curves for two very different ice histories (one given by ICE-3G and the other a simple ice disk model) at several sites within Hudson Bay and showing that the decay times for the two ice histories were similar for their assumed Earth rheology (see their Figures 6 and 7). A similar test was performed by Mitrovica (1996), where RSL curves were computed in Ångerman River and Oslo for a simple ice disk and for ICE-1, finding that while Ångerman River decay times were insensitive to ice history, the same could not be said for Oslo, demonstrating that the ice sensitivity depended on the choice of study site with respect to the geometry of the ice load. Our goal here is to perform similar sensitivity tests, but with a wider variety of Earth viscosity models and more realistic ice histories. More recently, Nordman *et al.* (2015) computed decay times for a suite of glaciological reconstructions of the Fennoscandian Ice Sheet (FIS) from Tarasov (2013). They found there was some sensitivity to ice history in their computed decay times (see their Figure 5), but concluded that the decay times were still relatively insensitive to this parameter. Our analysis is very similar to that of Nordman *et al.*, and our results are compatible in that we find some sensitivity in the computed decay times to variations in the ice history. Our main goal here is to explore this sensitivity and the possible consequences of it for inferring viscosity structure. It has often been stated that decay times are relatively insensitive to changes in the adopted ice history and so we aim to provide a quantitative assessment of this statement that extends results presented in the studies described above.

Methodology

1.1 The GIA Model

We employ a model of GIA to compute sea level and Earth deformation. The GIA model inputs are a history of ice loading and an Earth rheology to describe the deformation of the Earth in response to a changing load. In total 20 ice histories are implemented: ICE5G (Peltier, 2004), the Australian National University (ANU) ice model Lambeck *et al.*, 2014), 10 reconstructions of the North American Ice Sheet (NAIS) from Tarasov *et al.* (2012) that we patch into a background given by ICE5G, and 8 reconstructions of the Fennoscandian Ice Sheet (FIS) from Tarasov (2013), also patched in to ICE5G. All ice histories are shown at their 20 ka BP configuration in Figures S1 and S2. An ice history is developed with an assumed Earth viscosity model; ICE5G was developed with the VM2 radial viscosity model (Peltier 2004) and the Tarasov glaciological models were developed with the VM5a viscosity profile (Peltier and Drummond, 2008), both of which are constrained by postglacial decay time observations. The ANU ice history, on the other hand, was developed by iteratively inverting for the ice history and Earth rheology simultaneously, without the use of postglacial decay times.

We assume a spherically symmetric Maxwell viscoelastic model of the Earth (Peltier, 1974) where the elastic and density structures are given by PREM (Dziewonski and Anderson, 1981) and the viscosity structure is characterised by a very high viscosity lithosphere, and a sub-lithosphere mantle composed of upper and lower mantle components with a boundary at 670km and with viscosities that are parameters in the modelling. We vary upper mantle viscosity (UMV) from $1x10^{20}$ to $1x10^{21}$ Pa s and the lower mantle viscosity (LMV) from $1x10^{21}$ to $5x10^{22}$ Pa s. We solve the extended sea level equation (Mitrovica and Milne, 2003; Kendall *et al.*, 2005) and so we include the effects of time-varying shorelines; the feedback of GIA-induced changes in Earth rotation is also incorporated (Milne and Mitrovica, 1998; Mitrovica et al., 2005). Because our focus is ultimately with determining the ability of sea level data to constrain sub-lithosphere viscosity independently of ice history, we leave the thickness of the lithosphere at a constant value of 71km in this study. As noted in previous studies (e.g. Mitrovica and Forte, 1997; Lau *et al.*, 2016), variations in this Earth model parameter, compared to changing upper and/or lower mantle viscosity, has the least impact on decay time estimates.

The sea level model we employ is linear in the load response, which means that once the sea level has been determined, we can consider the Earth and sea level response to the ice load separately from the ocean load. An assumption in the accuracy of the exponential form for RSL curves is that the solid Earth is in free decay, that is, there are no locally changing loads. Because the ocean is itself a load that changes over the region and timescale of interest (Han and Gomez, 2018), we computed decay times for RSL curves for the ice response only. In the rest of this paper, whenever we refer to modelled RSL we mean the component that comes from the ice load in particular, unless we explicitly state otherwise. Another motivation for considering only the ice load is that our results will isolate the sensitivity associated with this load and so will be easier to interpret.

1.2 The Data

The RSL data used in this study is a compilation of data presented in Mitrovica *et* al. (2000), Nordman *et al*. (2010) and Pendea *et al.* (2010). The Mitrovica *et al.* study included an assessment of published RSL data for the Hudson Bay region, with data in both the Richmond Gulf and James Bay areas. As the James Bay data discussed in Mitrovica *et al*. is likely flawed (Mitrovica *et al.*, 2000; Pendea *et al.*, 2010) we consider only the Richmond Gulf data, and for consistency and as recommended by Mitrovica *et al.* (2000) only those data determined from samples of *Mitylus Edulis*. The data comprises 28 index points spanning the last 6 thousand years. The published data are presented with their C14 age in Mitrovica *et al.* (2000) and therefore we calibrated the C14 ages before comparing model output to the data. For the calibration we use the Calib software (Stuiver and Reimer, 1993) and the Marine13 curve of Reimer *et al.* (2013) (See Table S1). The three youngest points are discarded as they are too recent for the calibration to be valid. For James Bay we use the data of Pendea *et al.*, which consists of 6 data points covering the past 7 thousand years. The Ångerman River data was compiled by Nordman *et al*. and comprises 23 data points spanning 8 thousand years; the majority of these are based on a varve chronology with others dated via C14 methods. We show the locations of the aggregate sites and data distribution for Richmond Gulf and Ångerman River in Figure 1. The James Bay data of Pendea *et al.* are shown in a map only (their Figure 1) without precise latitude and longitude information published. Therefore all the James Bay data are treated as if they were located at the estimated aggregate site (Figure 1). The aggregate sites for Richmond Gulf and James Bay are visually estimated midpoints of their respective regions, while the Ångerman site is determined by a weighted mean. The aggregate east longitude, latitude pairs for Richmond Gulf, James Bay, and Ångerman River are (-76.8, 55.86), (-78, 52.8), and (17.473, 63.051) degrees, respectively.

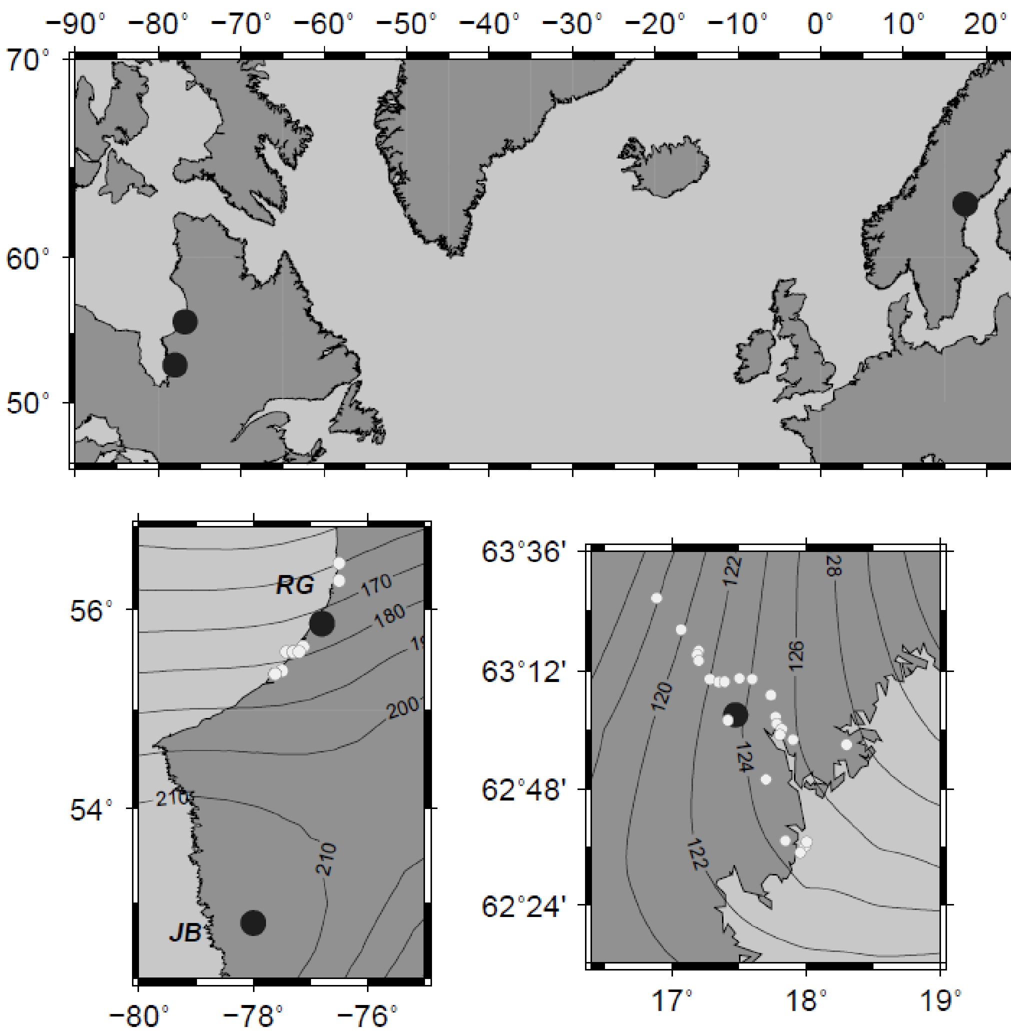

Figure 1 Study areas and locations of sea level index points (white dots) and aggregate sites (large black circles). The aggregate site for James Bay is estimated from Pendea *et al.* (2010). The contours in the lower two figures show a sample calculation of RSL at 7 ka BP for the ICE5G ice history and an Earth model with a 3x10^{20} Pa s UMV and a 1x10^{22} Pa s LMV.

1.3 Curve Fitting and Data Corrections

Model decay times are determined from computed RSL histories using the Scientific Python (SciPy) curvefit routine, which uses least-squares regression to determine fit parameters. The model output is fitted with the equation

$$RSL(t) = A\left(e^{-\frac{t}{\tau}} - 1\right). \tag{2}$$

Decay times are obtained from historical data by fitting a modified form of equation (2) that includes a possible vertical shift (c) to account for systematic error and uncertainty (Mitrovica *et al.*, 2000):

$$RSL(t) = A\left(e^{-\frac{t}{\tau}} - 1\right) + c. \tag{3}$$

These systematic uncertainties may be, for example, displacements related to particularly strong storm surges. The vertical shift was first introduced by Walcott (1980) on the grounds that the sea level data provide a stronger constraint on relative elevation changes between samples than they are on height relative to present-day mean sea level, and therefore should not be forced to go through the origin at present day.

Because the historical data contain uncertainties in both altitude and timing, to fit equation (3) we use SciPy's ODR (Orthogonal Distance Regression) package. Orthogonal distance regression can be considered a generalised least-squares minimization, and the SciPy ODR package is an implementation of the Fortran ODRPACK package (Boggs *et al.*, 1989; Boggs *et al.*, 1992). This package estimates parameters as well as standard error, which we adopt as the 1-σ uncertainty. As a point of comparison, using the Richmond Gulf data and this curve fitting algorithm, we obtain a decay time of 5.5±1.6 ka (see Figure 2) to 2σ uncertainty, which agrees with the published Richmond Gulf decay times of Mitrovica *et al.* (2000), who report a decay time range of 4 to 6.6 ka.

Because the NAIS reconstructions used here are ice free in Hudson Bay by approximately 8 ka BP, to avoid elastic deformation effects we consider the time period from 7 ka BP to present for Hudson Bay. In Fennoscandia, we use an 8 ka window for computing decay times. While Hudson Bay is itself ice free over our study period, some ice persists peripheral to Hudson Bay until approximately 5 ka. We tested the sensitivity of the Hudson Bay sites to ice changes after 7 ka by computing RSL due to those ice changes only and found that the effects were negligible.

A condition for the exponential decay time approximation to be most valid is that the study region is in free decay and is not being influenced by active load changes. One active load is the ice, and this can be dealt with if we consider only a time window after deglaciation. However, sea level indicators are, of course, a measure of sea level, and changes in RSL correspond to changes in the ocean load in the study region. The ocean load is itself a forcing on the Earth that drives sea level change through deformation of the solid Earth and gravitational potential, and this complicates the assumption of free decay. Past studies (Mitrovica *et al.,* 2000; Nordman *et al.*, 2015) applied corrections to the sea level data to remove the eustatic (meltwater) component of sea level, which produces a global rise in RSL that is independent of the local RSL response and impacts the decay time estimate. The influence of the regional ocean loading – a sea-level fall of 100s of metres since the completion of ice melting - has recently been considered by Han and Gomez (2018), who show that the contribution of this load to decay time estimates is both non-negligible and spatially variable across the Hudson Bay region. Because the data is a record of all processes that influence sea level, and not only the isostatic response to the ice load in particular, we removed from the data all of the contributions except that due to the ice loading for every model parameter set considered. This 'correction' (equation (4)) includes the influence of ocean loading, GIA-induced changes in Earth rotation and changes in global mean sea level associated with ice melting (eustasy) and GIA (syphoning; e.g., Mitrovica and Milne, 2002). The model correction applied to the data to account for these effects can be expressed as

$$RSL_{cor} = RSL_{full} - RSL_{ice}, \qquad (4)$$

where RSL_{full} represents model output of RSL that incorporates all processes described above and RSL_{ice} is the component due only to the ice load. Because the correction (RSL_{cor}) is dependent on the input parameters, the decay time determined from the RSL data is different, in general, for each model run. Essentially, if the model output (RSL_{full}) is considered as a sum of an ice loading signal, and an everything-but-the-ice-load signal, then the former is used to determine the model decay time, and the latter (defined by equation (4)) is used as a data correction to determine a data decay time. Figure 2 (frames A & B) illustrate the impact of this model correction on the estimated decay time at Richmond Gulf for a given model parameter set. The parameters ($3x10^{20}$Pa s for UMV and $1x10^{22}$ Pa s for LMV) lead to a decrease in the decay time from 5.5±1.6 ka to 4.6±1.3 ka. For comparison, a model with a more modest viscosity contrast featuring a $1x10^{21}$ Pa s UMV and a $1x10^{22}$ Pa s LMV leads to a corrected decay time of 5.0± 1.4 ka. A second reason to perform this data correction and thus focus on the ice response only is that we are specifically concerned with the sensitivity to this parameter. If the full signal were used to examine decay time variations across ice histories, then the resulting decay times would be influenced not only by the ice variations, but also by the other component signals.

At two of the locations considered (Richmond Gulf and Ångerman River), the data are spread over a large area and so a second model correction was applied to shift the data spatially to their aggregate locations. It is common practice to place data from multiple locations to one for visualization or for curve fitting, but if there is a large gradient in sea level between the actual locations where the data were collected then this can introduce significant error (Nordman *et al.*, 2015; Han and Gomez, 2018). It was shown by Mitrovica *et al.* (2000) that when data from Richmond Gulf and James Bay are combined into a single curve to determine decay times (as was done in Peltier, 1998) it leads to a considerably different decay time than would be found by considering the locations separately. In fact, the RSL difference between the northernmost and southernmost data points in the Richmond Gulf dataset is sufficiently large (up to several tens of metres at 7 ka BP, see lower left frame of Figure 1) that it significantly affects the estimated decay time. Therefore all data points were shifted by the difference in modelled sea level between the aggregate location and the actual data location. For example, if modelled RSL at a given time and sea level index point location is computed to be 200 m of RSL and RSL at the aggregate location is computed to be 150 m at the same time step, then that corresponding data point will be shifted by -50 m before the decay time is estimated. In Figure 2 (frames C & D) we illustrate the impact of this spatial correction on estimating the decay time. In this case the decay time is increased by 0.36 ka when this correction is applied for the chosen viscosity model parameters (see caption). For Ångerman River, using the same Earth model parameters and the FIS model 78311 gives an increase in the computed decay time (after application of the correction defined in equation (4)) of 0.43 ka. A similar spatial correction was performed in Nordman *et al*. (2015), except that their correction was determined by sampling the model parameter space and using the maximum differences to determine a single correction, rather than computing parameter-specific data corrections as we do here. The amplitude and sign of the spatial correction will depend on the spatial distribution of the index points relative to the local RSL gradient as well as the adopted model parameter set. Regarding the latter, we note that thinner lithospheres generally result in larger RSL gradients when all other parameter are fixed, and it is therefore likely that our choice of a relatively thin (71 km) lithosphere will increase the importance of the spatial correction.

The area over which the James Bay data has been collected is significantly smaller (Pendea *et al.*, 2010), and comprises only 6 data points, and so the spatial correction is applied only to the Richmond Gulf and Ångerman River data. The correction defined in equation (4) is applied at all three locations. As a concluding point, it is generally true (but not exclusively, particularly for models featuring low viscosity upper mantles) for the data considered here that the correction defined by equation (4) lowers the estimated decay time and the spatial correction raises it.

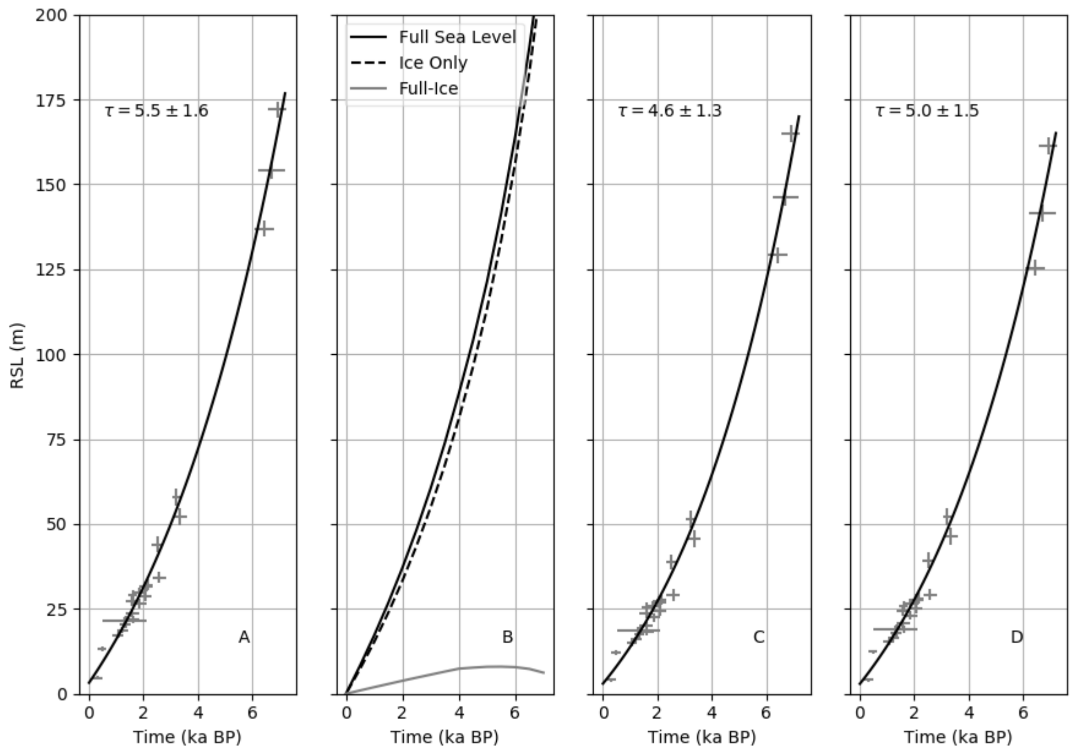

Figure 2 A) The uncorrected Richmond Gulf data and the best-fitting curve of form defined by equation (3). B) The modelled RSL curve including ice, ocean, and rotation contributions (solid black), the ice load contribution isolated (dashed black), and the difference between them (grey), for a model run with the 4247 ice history of Tarasov (2012), a 71 km lithosphere, a $3\text{x}10^{20}$ Pa s upper mantle, and a $1\text{x}10^{22}$ Pa s lower mantle. When we remove the grey curve from the second frame from the Richmond Gulf data, we obtain the data best-fitting curve in (C). D) corrected data of frame (C) with the additional spatial variability correction (see Section 2.3) and the best-fitting curve.

2. Results and Discussion

2.1 Parameter Sensitivity Investigation

We computed RSL for a suite of Earth rheologies and ice histories. In Figure 3 we show computed model decay times for all ice histories for a subset of Earth models. For Richmond Gulf, most decay times are fairly closely clustered together, typically with a difference of around 500 years for the $2x10^{21}$ Pa s LMV (left frame), and around 1 ka when the LMV is increased by an order of magnitude (right frame). Uncertainties are not shown in Figure 3 to avoid cluttering the image, but it should be pointed out that uncertainties typically increase as viscosities and decay times increase. For example, using the 1246 ice history as an example, the $0.5x10^{21}$ Pa s UMV and $2x10^{21}$ Pa s LMV best-fitting decay time is 3.36±0.06 ka, and when the LMV is increased to $2x10^{22}$ Pa s the best-fitting decay time increases to 5.29±0.25 ka. As viscosities increase the modelled curves become more linear, leading to larger parameter uncertainties. For the models shown in Figure 3 the decay time uncertainties are small compared to the spread from the ice models.

In comparison with Richmond Gulf, the spread of decay times at James Bay is large, particularly for the models featuring a higher viscosity lower mantle. There are differences of decay times among ice models of nearly 3 ka. For Richmond Gulf and James Bay ICE5G is an outlier for the higher viscosity UMV values, with a decay time significantly below the majority of the rest for both LMV values shown. The Ångerman River decay times exhibit more spread than those of Richmond Gulf, and especially for the larger LMV value (right-hand frames), but significantly less than James Bay; as for the Richmond Gulf and James Bay results, the spread in modelled decay times significantly increases when the LMV is increased by an order of magnitude. There is a general trend of the spread of decay times being larger for the higher LMV models.

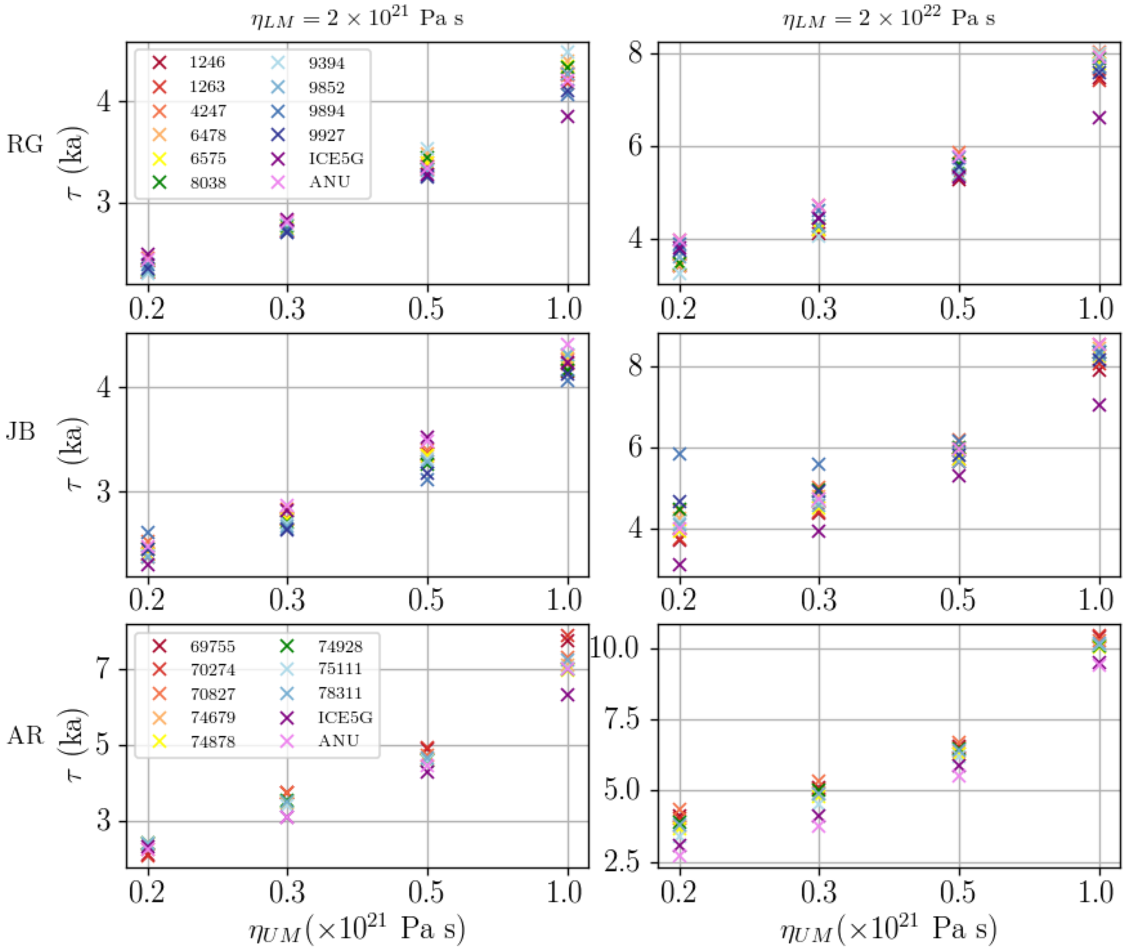

Figure 3 Computed model decay times for all ice histories at Richmond Gulf (top row), James Bay (middle row), and Ångerman River (bottom row). The left column shows results for a LMV of $2x10^{21}$ Pa s while the right column shows output for a LMV of $2x10^{22}$ Pa s. The Richmond Gulf legend also applies to James Bay.

While an increase in the spread of decay times is to be expected as the curve-fitting uncertainties increase, the magnitude of spread relative to the size of the uncertainties (not shown) indicates that the decay time sensitivity to the ice model increases at higher viscosities. This indicates that a stiffer mantle is more sensitive to details in the loading history than a weaker mantle. A possible reason for this is that a stiffer mantle will have a greater memory for past ice changes.

We extend the results in Figure 3 to a broader viscosity space in Figure 4 and show both the mean decay times (where the mean is computed across ice histories) and the spread in decay times across ice histories, which is the difference between the largest and smallest computed decay times. The general structure of the mean (frame A) is similar in each of the three locations considered, with the modelled decay time generally increasing with increasing UMV and LMV, but there are also significant differences. As noted in Figure 3 there is a clear difference in decay times for low UMV and high LMV values between Richmond Gulf and James Bay. The decay time structure of Ångerman is similar to that of Richmond Gulf, except for the region with high UMV values, where the decay times are higher for Ångerman, reflecting a greater sensitivity of the Ångerman location to changes in the UMV (e.g. Lau *et al*., 2016). Also, we do not include the weakest UMV for the Ångerman River results. This is because the Ångerman River RSL curves we have computed are non-exponential for most ice histories for the weakest upper mantle we considered (see Hill *et al.* (2018) for more detail on this point).This is because most of the relaxation occurred before 8 ka as a consequence of the low viscosity values and the relatively early retreat of ice from the region. As it is not reasonable to consider decay times of non-exponential curves, we omit those models from our discussion of the Fennoscandian decay times.

The spread in decay times is shown in frame B) of Figure 4. It is generally true for all three sites that the lower/middle left section of parameter space (corresponding to low UMV and LMV values) shows the smallest spread in decay times, with the spread increasing as both UMV and LMV increase. The spread is typically largest for models with high UMV and LMV (top right section of parameter space), except for James Bay, which also features a large spread for the lowest UMV value. The large spread at high UMV values is in part because the RSL curve becomes more and more linear for higher viscosities, with higher and higher decay times required to fit the modelled behaviour, and so while the differences in decay times are large, the decay times themselves are also large. As the spread shows maximum differences, which may be misleading if there are outlier models, the standard deviation has also been computed, which shows a similar structure to the spread and is provided as Figure S3.

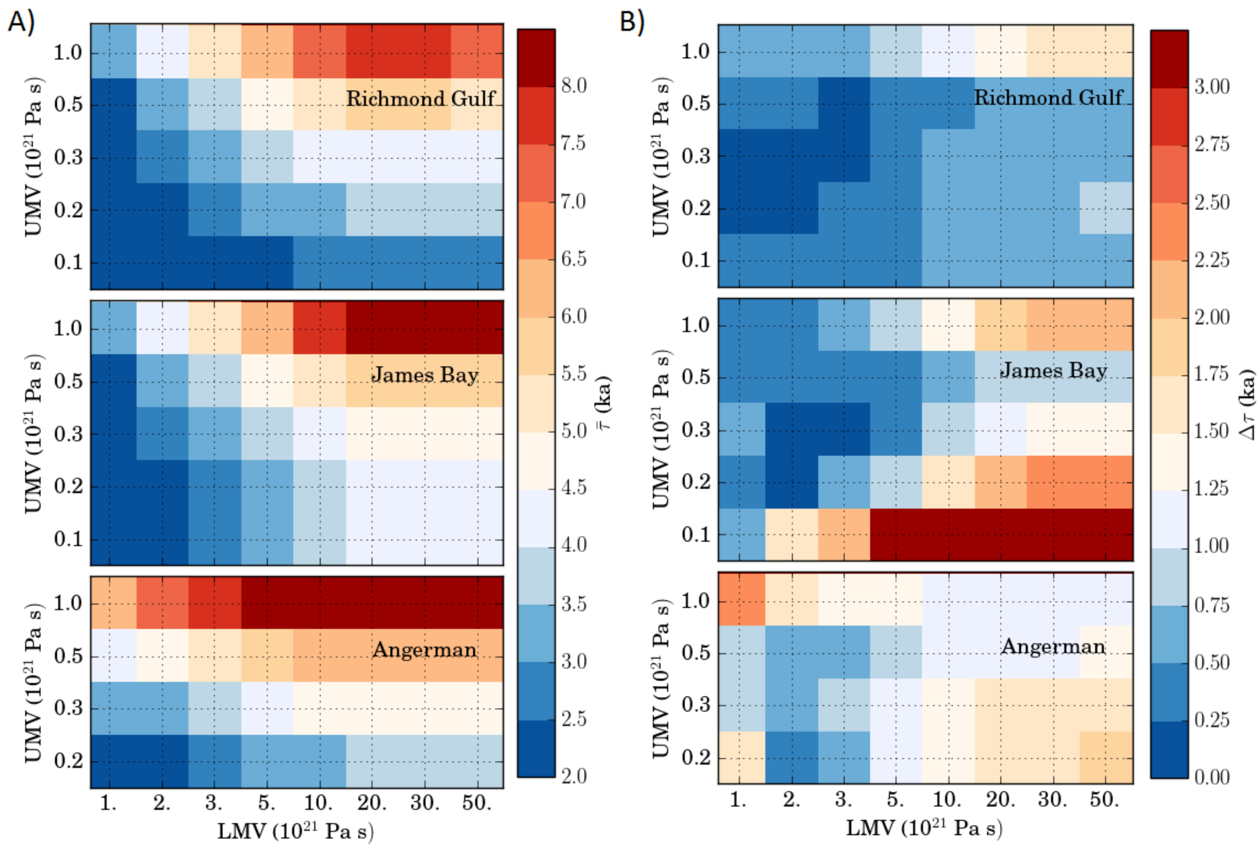

Figure 4 A) Mean decay times (averaged over the number of ice histories) as a function of upper and lower mantle viscosity. B) Spread (that is, difference between the largest and smallest) of computed model decay times. The UMV lower limit is not the same for Ångerman as it is for the Hudson Bay sites as the lowest UMV considered resulted in non-exponential RSL behaviour for many ice histories there.

Richmond Gulf shows a consistently small spread in decay times across the parameter space, except for those models with both high UMV and LMV values. Both James Bay and Ångerman River, however, show considerable spread in decay times, particularly for models with high LMV values. This indicates that Richmond Gulf decay times are relatively insensitive to ice history across most of the considered parameter space, with Ångerman River and James Bay more sensitive. This is particularly interesting for James Bay, as it is close to Richmond Gulf and so would be expected to show generally similar behaviour, but this is not evident in the model results. A partial explanation for the noted difference between these two sites follows.

In Figure 5 we show a spatial plot of RSL at 6 ka BP for all 12 NAIS reconstructions. The first thing to notice is that in almost none of these scenarios can both James Bay and Richmond Gulf be considered to be at the center of the main uplifting region, and often neither can. In fact, for most ice models considered, a center of uplift would be East of Hudson Bay (i.e. Northern Quebec), which Richmond Gulf is nearer to than James Bay. We say *a* center of uplift rather than *the* center of uplift as the Laurentide had several domes and there would therefore be multiple centers of uplift (and in the frame showing the RSL of model 9894 there is a second uplifting center visible in central Hudson Bay). Comparing uplift patterns for the different ice histories at this time step, Richmond Gulf is generally nearer to a major center of depression than James Bay, which features significant variety in the type of uplift it is experiencing depending on ice history. We postulate that this consistency in the case of Richmond Gulf and variability in the case of James Bay is reflected in the spread of decay times seen in Figure 4(B).

2.2 Data Model Comparison

While we have demonstrated that there is a sensitivity of computed decay times to changes in the input ice sheet history, it is important to determine the impact of this sensitivity when inferring Earth viscosity structure. After all, if the viscosity models most sensitive to ice history do not satisfy the data constraints, then we may conclude that the sensitivity is unimportant.

For every ice history we consider whether a particular Earth model is consistent with the data by calculating decay times for the model-generated RSL curves and the model-corrected data (as described in Section 2.3). We then simply determine whether the decay times agree to within the estimated uncertainties determined from the curve fitting routines. We show the results of this exercise for Richmond Gulf, James Bay, and Ångerman River in Figures 6-8, respectively (for both 1σ and 2σ uncertainty estimates). Our purpose in this section is not to perform a rigorous inversion for an Earth viscosity model, as we are not taking into account any kind of depth sensitivity of the different ice history/Earth viscosity combinations (e.g. Mitrovica 1996, Lau *et al.*, 2016). Rather, our goal is simply to determine how the spread in decay times observed in the previous section can manifest in an inversion that assumes a simplistic, but commonly assumed, 2-layer sub-lithosphere mantle viscosity structure. We are primarily interested in how the solution space changes, rather than in the solutions themselves.

What can be seen from these Figures is that while each location has an acceptable region of parameter space with a similar shape, there is still significant variability among ice histories. For example, for the Richmond Gulf data (Figure 6), most ice histories show a band of acceptable models with an UMV of $0.2x10^{21}$ Pa s, but this is absent for the 4247 and 8038 histories. Additionally, half of the ice models show a band of acceptable viscosity models with a $1x10^{21}$ Pa s UMV, which is absent from the rest. Another interesting feature of the results in Figure 6 is that the bottom left corner of parameter space, corresponding to weak UMV and LMV combinations, which was identified in Figure 4as being relatively insensitive to variations in ice history, is also a region that does not fit the Richmond Gulf data. That being said, there is generally agreement among ice histories for UMV values of $(0.3 – 0.5)x10^{21}$ Pa s and higher LMV values satisfying the data, reflecting the low sensitivity seen in the previous section. There is additionally a region with a UMV value of $0.2x10^{21}$ Pa s and LMV values of $(20\text{-}50)x10^{21}$ Pa s, where 10/12 ice histories lead to model-data agreement. This indicates that viscosity inferences in this region of parameter space should not be significantly influenced by ice history. There are also regions of parameter space where only a subset of ice histories lead to model-data agreement, which indicates that there is a sensitivity significant enough to impact a viscosity inversion. For instance, 5/12 ice histories lead to model-data agreement in the region of parameter space with a UMV value of $1x10^{21}$ Pa s and LMV values of $(30\text{-}50)x10^{21}$ Pa s.

The James Bay data (Figure 7) result in similarly shaped acceptability regions as seen for Richmond Gulf, but generally shifted to lower UMV values, and significantly narrower. It may seem counterintuitive that the James Bay model-data agreement space is narrower than for Richmond Gulf, as with only 6 data points we may expect broader parameter estimation uncertainties than is the case for Richmond Gulf, but in fact the opposite is true. While there are relatively few data points in the James Bay dataset, they are typically easily fit with an exponential (such that all points lie on or nearly on the best-fitting curve), while the much larger Richmond Gulf dataset is such that there are always points that are not close to the curve. As a result, the James Bay parameter uncertainties are typically significantly smaller than those determined from the Richmond Gulf dataset (for examples of best-fitting curves for all three sites, see Figure S5). ICE5G and 9894 are outliers, as neither show the bands of acceptable models of (0.1-0.2)x10^{21} Pa s UMV common among the rest. The results for the 9894 ice history are indicative of how much different the behaviour at James Bay is relative to Richmond Gulf; for Richmond Gulf, the model fits lead to an acceptance region that looks very similar to those of 9852 and 9927, but for James Bay there is a large change in the acceptability space, with all LMV values higher than 5x10^{21} Pa s being rejected. As we have seen in Section 3.1, the James Bay model decay times are relatively sensitive to ice history, and this is also reflected in the model-data comparison. Unlike Richmond Gulf, where there are many Earth models that satisfy the data constraints common to all ice histories, in the case of James Bay there are no solutions common across all ice histories, though there are solutions with a UMV of 0.2x10^{21} Pa s and LMV values of (10-50)x10^{21} Pa s common to 7/12 ice histories. Given that there is no consistent data-model agreement for most ice histories, and the location is one where the model output shows ice sensitivity independently of the data, we conclude that these data are not well-suited for using decay times to infer Earth viscosity structure. It is possible that more data in James Bay may improve the ability to constrain Earth model parameters, but given the sensitivity in the model output to ice history, that is probably not the case.

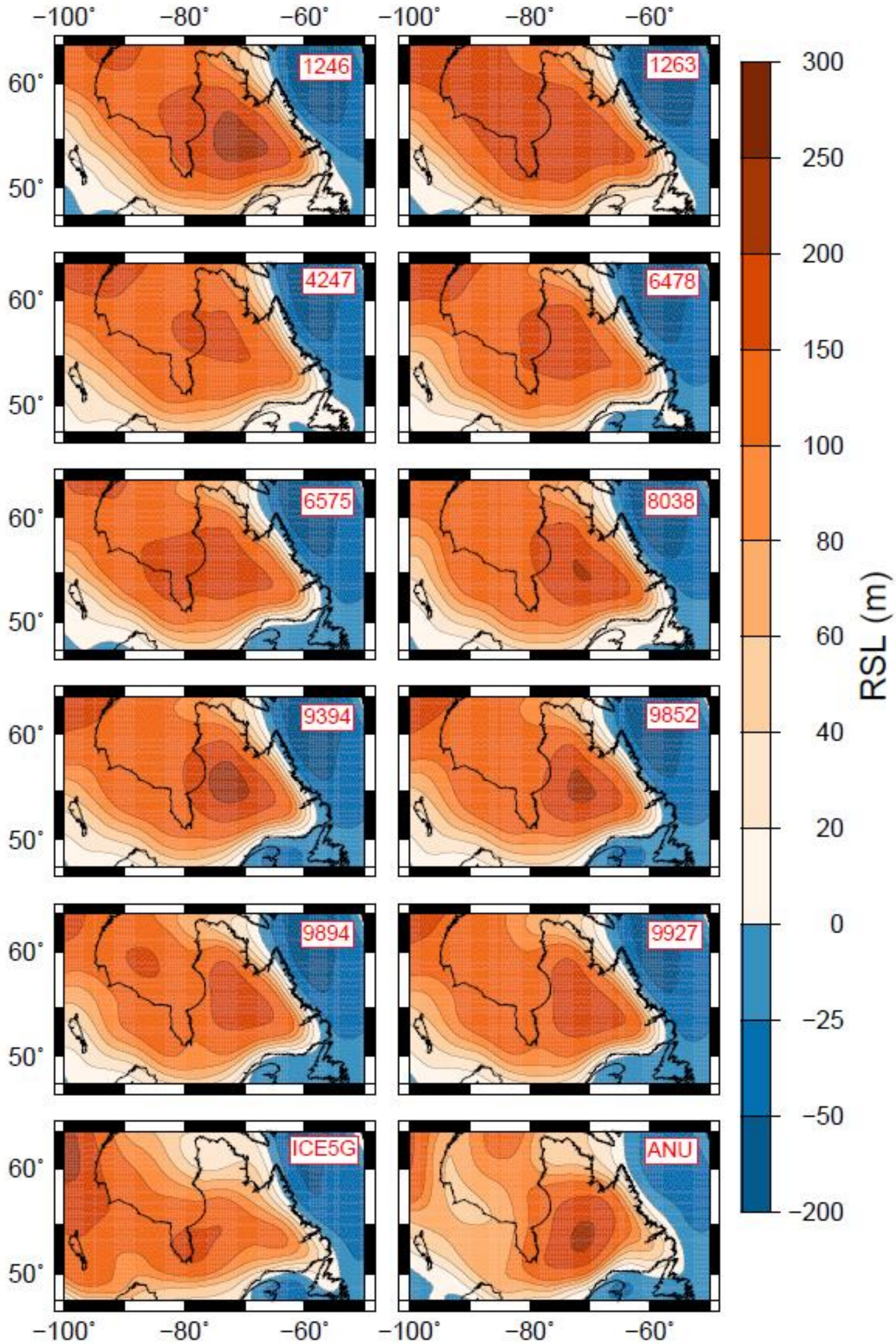

Figure 5 RSL at 6 ka BP for an Earth model with a 71km thick lithosphere, 5x10^{20} Pa s UMV, and a 1x10^{22} Pa s LMV.

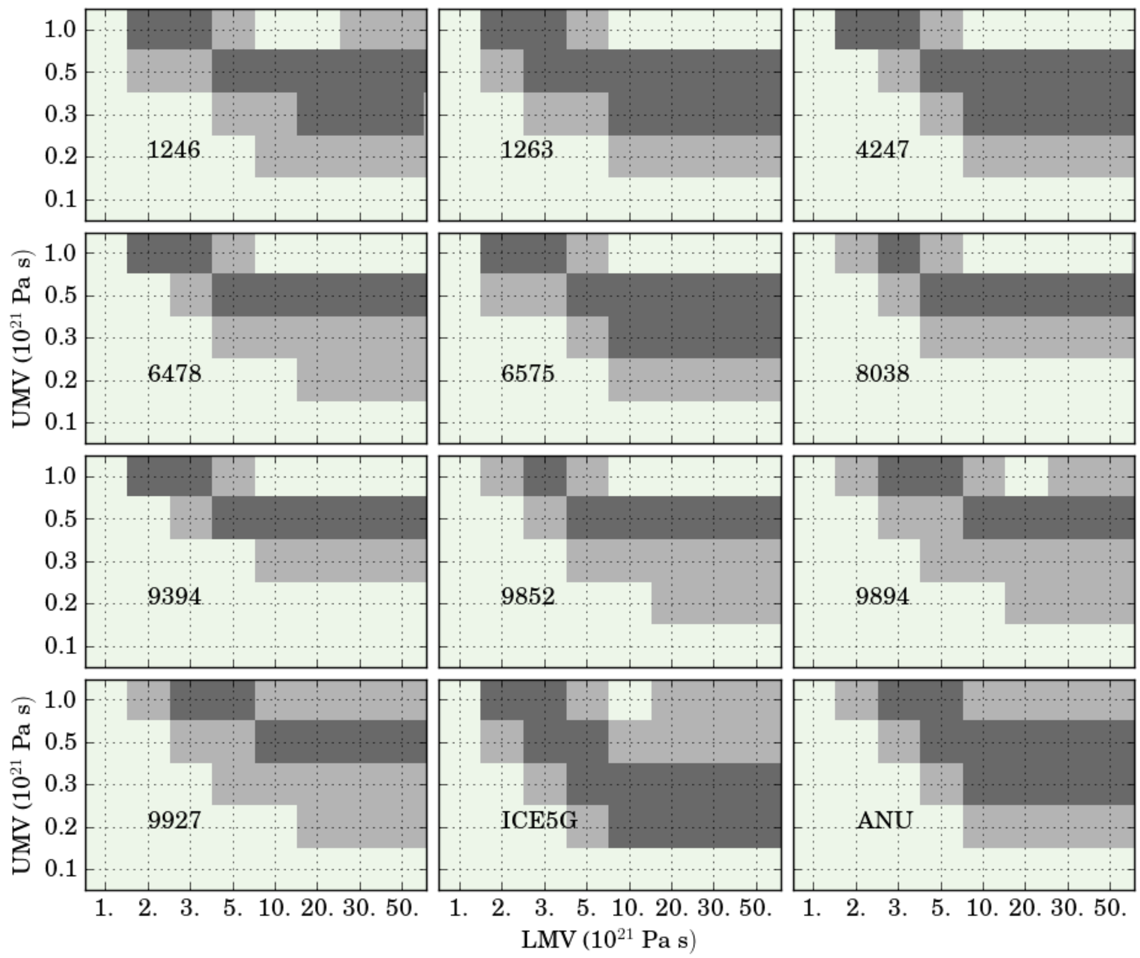

Figure 6 In grey we show the regions of parameter space where the model output decay time agrees with the Richmond Gulf model-corrected data decay time to within uncertainty (1σ in dark grey and 2σ in light grey).

The Ångerman River data fits (Figure 8) give a solution region that is consistent with the Richmond Gulf case, which is largely characterised by a low UMV, with structure that varies with ice history. The scale is different from those of James Bay and Richmond Gulf, with a UMV starting at $0.2x10^{21}$ Pa s. The space of model-data agreement is much smaller than Richmond Gulf, which likely reflects the relatively small age uncertainties of the Ångerman River data (most of which are based on a varve chronology) compared to the larger uncertainties of calibrated C14 ages in the Richmond Gulf dataset. Comparing Figure 8 with Figure 5 of Nordman *et al.* (2015), who used the same dataset but a different suite of ice histories to compute decay times, we see consistent results in that there is general model-data agreement for a $0.3x10^{21}$ Pa s UMV for high LMV values. There is also some ice history variability in the decay times in the Nordman *et al.* figure, but their choice of scales (for instance, using a single colour for the range 0-4.2 ka) makes variability in those ranges impossible to determine. Such a choice is justifiable on the basis that variability in decay time ranges that are not supported by the data are not important.

For Ångerman River (Figure 8) we also see that most ice histories lead to a band of acceptable Earth models with a UMV of $0.3x10^{21}$ Pa s, but ICE5G also accepts a lower value of $0.2x10^{21}$ Pa s. All ice histories (9/10) except for 70827 lead to acceptable Earth models with a UMV of $0.3x10^{21}$ Pa s and a LMV from $(5\text{-}50)x10^{21}$ Pa s, similar to one of the classes of solutions of the Richmond Gulf data. However, when the 70827 ice history is included, then the range of acceptable LMV values shrinks to $(5\text{-}20)x10^{21}$ Pa s. This demonstrates a low ice sensitivity in this region of parameter space, particularly for LMV values in the range of $(5\text{-}20)x10^{21}$ Pa s. There is also a solution of a UMV value of $0.5x10^{21}$ Pa s and LMV value of $2x10^{21}$ Pa s common to all 10 ice histories. Given that the numbered ice models were developed with only a single earth viscosity profile (VM5a), a key future step will be the joint calibration of the ice histories and viscosity models.

Overall, our results are compatible with those of Hill *et al.* (2018), who explored ice model sensitivity as part of an investigation to determining whether postglacial decay times in Richmond Gulf and Ångerman River could constrain Earth models featuring a thin low viscosity layer above the mantle transition zone. The Hill *et al.* study considered a much reduced spread of ice histories relative to the present study, but did still find evidence of ice history sensitivity. Importantly, the Earth models which could be considered to have satisfied the data constraints were dependent on the assumed ice history (for example, see their Figures 3, S2, and S3). This is consistent with our own Figures 6-8, and demonstrates that for a practical application, the often-invoked insensitivity of decay times to the input ice model should not be universally assumed. Moreover, here we have considered only a fairly simple class of Earth models featuring a two layer sub-lithosphere viscosity structure, and Hill *et al.* observe that the ice sensitivity also exists for more complex three layer models. That being said, our results also demonstrate that for a significant region of the viscosity parameter space, data from both Richmond Gulf and Ångerman River can be satisfied with a wide variety of ice histories, demonstrating low ice sensitivity for these viscosity structures.

The primary advantage of the decay time approach is to constrain Earth model parameters independently of ice history, but if it becomes necessary to test ice sensitivity as well (as we do here, and as was done in Hill *et al.*), then the primary advantage of using decay times over raw RSL data is reduced. Of our three study sites, the least sensitivity of computed decay times to ice history is in Richmond Gulf. For this location, there are large regions of parameter space common to all ice models considered that satisfy the data. This can be considered either a positive or a negative result: On the one hand, this supports an interpretation of low functional ice sensitivity there, but on the other, the very large acceptable region of parameter space may make the Richmond Gulf decay time a weak constraint on viscosity structure. Of course, a rigorous inversion for viscosity structure should include more than the decay time from a single region, and so Richmond Gulf would rarely be the only considered constraint.

If we consider regions of parameter space that show low ice sensitivity (e.g., consistency across ice models) that also satisfy the data in both Richmond Gulf and Ångerman River, then we find that models with a UMV of $0.3x10^{21}$ Pa s and an LMV of either $10x10^{21}$or $20x10^{21}$ Pa s are consistent to both. This is broadly consistent with other inversions (e.g. Mitrovica and Forte, 2004; Lau *et al.*, 2016; Nakada *et al.*,2016), and indicates that while there are regions of parameter space that are more sensitive to the input ice history than others, this sensitivity does not seem to extend to the regions of parameter space most favoured by the data. However, the Richmond Gulf and Ångerman River decay times are reflective of their own local viscosity structure, and while it is consistent in our modelling framework to combine these constraints for a 1D spherically symmetric Earth, it may not reflect the real Earth where viscosity structure exhibits significant lateral variation that can significantly affect decay time calculations. For example, Paulson *et al.* (2005) compare computed Hudson Bay decay times from a 3D GIA model with those of 1D models with viscous structure corresponding to global and regional averages of that of the 3D model, and find nearly a 30% misfit when comparing the 3D model to its corresponding global average 1D model, and a reduced but still significant 10% misfit when comparing to the Hudson Bay regional average model.

3.2.1 Effects of Data Corrections

To conclude this section, we briefly discuss the impacts of the applied data corrections (Section 2.3).We have produced versions of Figure 6 and Figure 8 in the Supplemental material where i) we apply no corrections, the uncorrected data at are fit alongside the full modelled sea level (model curve generated at the aggregate location shown in Fig. 1; Figures S6 and S7); ii) only the correction defined in equation (4) is applied to the data, which is then fit alongside the modelled ice component of the RSL (Figures S8 and S9), and; iii) only the spatial variability correction is applied to the data, which is then fit alongside the full RSL output (Figures S10 and S11). This analysis is performed only for Richmond Gulf and Ångerman River and not James Bay in part because the spatial correction was never applied to James Bay, and in part because it has already been discounted as a location that is well-suited to a decay time analysis.

When no corrections are applied to the Richmond Gulf data, the accepted regions on viscosity space are similar but there are also significant differences. The greatest changes, compared to the fully corrected case, are for the 8038 and 9852 ice histories. It is notable, however, that the same Earth models with a UMV of $(0.3\text{-}0.5)\text{x}10^{21}$ Pa s are common to all ice models in both the uncorrected and fully-corrected cases. The uncorrected Ångerman River data lead to many of the models having the acceptable space of UMV values lowered from 0.3 to $0.2\text{x}10^{21}$ Pa s. The decreased sensitivity of Richmond Gulf relative to Ångerman River to the data corrections is likely due to the larger time uncertainties on the calibrated Richmond Gulf data leading to larger parameter uncertainties that dominate over the influence of biases in the uncorrected data. There are no viscosity models that are accepted universally by both the uncorrected Richmond Gulf and Ångerman River data.

When the correction defined in equation (4) is applied, the acceptable model space for Richmond Gulf is, again, broadly similar to that for the fully corrected case.   For Ångerman River the effect of this correction relative to the uncorrected case is broaden the region of accepted parameters at lower UMV values. This suggests that the contribution from ocean loading can impact the viscosity inference at this location.

Finally, when only the spatial corrections are applied, there is a significant reduction in the size of the acceptance space in Richmond Gulf relative to the uncorrected case. The acceptable models common to all ice histories still contain a UMV of $0.3\text{x}10^{21}$ Pa s and a LMV of at least $10\text{x}10^{21}$ Pa s, or a UMV of $0.5\text{x}10^{21}$ Pa s and a LMV of at least $3\text{x}10^{21}$ Pa s. For Ångerman River this correction has a less significant effect than in Richmond Gulf (though it does still change the solution space). This may be due to the amplitude of the spatial correction being larger at Richmond Gulf (see Figure 1).

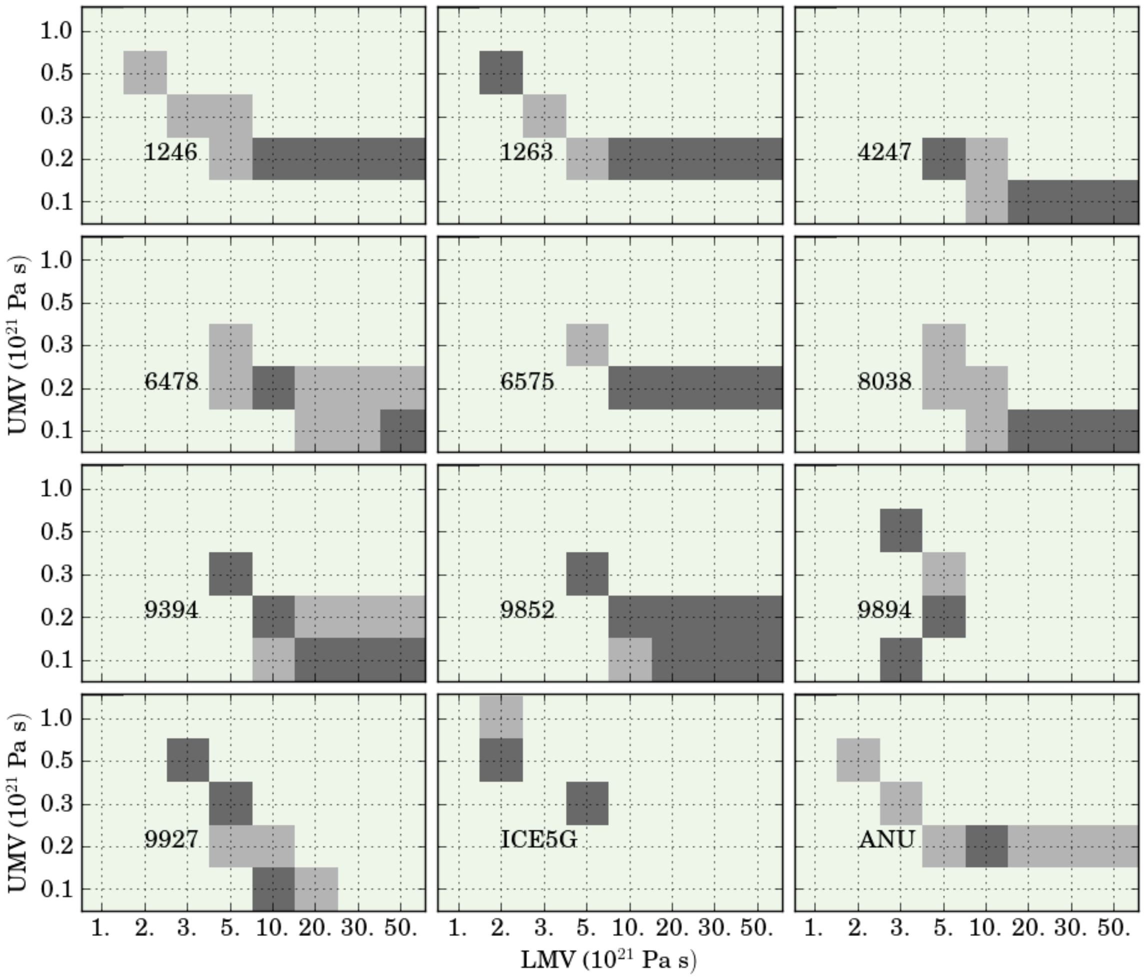

Figure 7 As in Figure 6 but for the James Bay data.

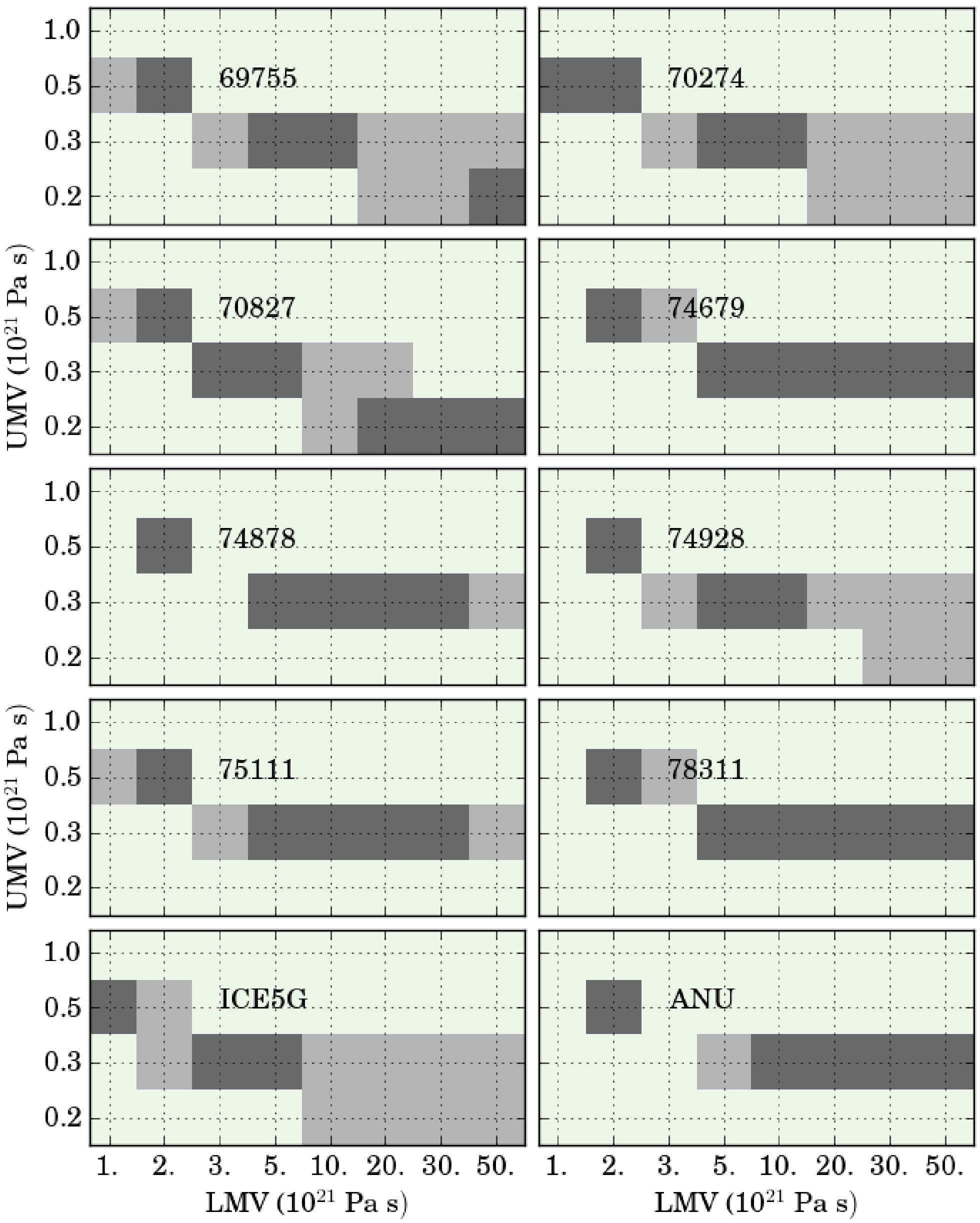

Figure 8 As in Figure 6 but for the Ångerman River data.

3. Conclusions

While RSL data are generally sensitive to both the Earth's viscosity structure and to the assumed ice history, postglacial decay times have been shown to reduce the sensitivity to the ice history. This makes decay times a useful parameterization for determining Earth viscosity. In this study we have investigated the extent of the sensitivity to the ice input by computing RSL histories and their corresponding exponential decay times for a suite of Earth viscosity profiles and ice histories. We have found that the exponential decay time characteristic to an RSL history is not generally independent of the ice history used to generate it. Moreover, the significant difference in decay times in James Bay and Richmond Gulf for identical Earth viscosity profiles suggests that the decay times computed at a given location may be more sensitive to position relative to the geometry of the ice sheet than has been suggested in the past. Our sensitivity analysis shows that Richmond Gulf decay times are relatively insensitive to ice history, confirming that data from this location are well-suited to a decay time analysis. In contrast, RSL data from James Bay are less well-suited because of the relatively large sensitivity of computed decay times to the input ice model at this location.

We have applied data corrections to account for the spatial distribution of RSL data over the study regions, as well as for the effects of the ocean load, rotation and changes in global mean sea level (associated with meltwater input and syphoning), so that only the local ‘free decay’ related to the removal of the ice load is considered in the decay time analysis. These corrections generally produce a greater effect on the estimated decay times in Ångerman River than in Richmond Gulf due, in part, to the lower temporal resolution of the RSL data in Richmond Gulf. However, the spatial correction has a stronger effect on the Richmond Gulf solution space owing to the relatively large area over which the data are distributed and the relatively large RSL gradient. While the load correction was applied in part to make the ice sensitivity easier to observe, and is therefore likely not necessary in general, we do recommend the spatial correction for instances where RSL data is spread over a region with a significant RSL gradient.

We performed a forward modelling analysis to infer the viscosity in two sub-lithosphere layers (boundary at 670 km depth) that satisfies the decay time data. In general, the inferred range of Earth viscosity values that satisfy the RSL data constraints are ice history dependent to some extent. This analysis yielded regions of parameter space where solutions were common to all or most ice histories, indicating low ice sensitivity, as well as only subsets of ice histories, indicating relatively high sensitivity to the ice input. For example, in Richmond Gulf, UMV values of $(0.3\text{-}0.5)\text{x}10^{21}$ Pa s and LMV values of $(5\text{-}50)\text{x}10^{21}$ Pa s tend to satisfy the data constraints consistently for most ice histories. By contrast, only 5/12 ice histories demonstrate data-model agreement in the region defined by a UMV value of $1\text{x}10^{21}$ Pa s and LMV values of $(30\text{-}50)\text{x}10^{21}$ Pa s. In James Bay there is only a small region of parameter space that satisfies the data, and only for 7/12 ice histories considered. The Ångerman River solution spaces are generally narrower than those of Richmond Gulf, and all ice histories considered lead to solutions with a UMV value of $0.5\text{x}10^{21}$ Pa s and LMV value of $2\text{x}10^{21}$ Pa s. There is an additional solution with a UMV value of $0.3\text{x}10^{21}$ Pa s and LMV values of $(5\text{-}50)\text{x}10^{21}$ Pa s common to 9/10 ice histories. An important caveat is that our analysis has not checked the self-consistency of the ice model and earth model sets under all the other geodetic and RSL constraints that went into their original development. This study therefore points to the importance of joint calibration of ice sheet and earth viscosity models for deglacial (or longer) contexts.

References

Andrews, J.T., 1970. A Geomorphological Study of Postglacial Uplift with Particular Reference to Arctic Canada, *Oxford University Press*, New York.

Boggs, P.T., Donaldson, J.R., Byrd, R.H., ad Schnabel, R.B., 1989. ALGORITHM 676 ODRPACK: Software for Weighted Orthogonal Distance Regression. *ACM Transactions on Mathematical Software*, **15**, 348-364.

Boggs, P.T., Byrd, R.H., Rogers, J.E. & Schnabel, R.B, 1992. User's Reference Guide for ODRPACK version 2.01: Software for Weighted Orthogonal Distance Regression. *Center for Computing and Applied Mathematics, U.S. Department of Commerce*, Gaithersburg, MD.

Caron, L., Métivier, L., Greff-Lefftz, M., Fleitout, L., & Rouby, H., 2017. Inverting Glacial Isostatic Adjustment signal using Bayesian framework and two linearly relaxing rheologies, *Geophys. J. Int.*, **209**, 1126-1147.

Cathles, L.M., 1975. The Viscosity of the Earth's Mantle. *Princeton University Press*, Princeton, NJ.

Dziewonski, A.M. & Anderson, D.L., 1981. Preliminary reference Earth model, *Phys. Earth Planet. Inter.*, **25**(4), 297-356.

Han, H.K. & Gomez, N., 2018. The impact of water loading on postglacial decay times in Hudson Bay, *Earth Planet. Sci. Lett.*, **489**, 1-10, doi:10.1016/j.epsl.2018.02.043.

Hill, A.M., Milne, G.A., Kuchar, J., & Ranalli, G., 2018. Sensitivity of Glacial Isostatic Adjustment to a Partially Molten Layer at 410 km Depth. *Geophys. J. Int. IN REVIEW*

Kendall, R.A., Mitrovica, J.X. & Milne, G.A., 2005. On post-glacial sea level - II. Numerical formulation and comparative results on spherically symmetric models, *Geophys. J. Int.*, **161**(3), 679-706.

Lambeck, K., Smither, C., & Johnston, P., 1998. Sea-level change, glacial rebound and mantle viscosity for northern Europe, *Geophys. J. Int.*, **134**, 102-144.

Lambeck, K., Rouby, H, Purcell, A, Sun, Y. & Sambridge, M., 2014. Sea level and global ice volumes from the Last Glacial Maximum to the Holocene, *Proc. Nat. Acad. Sci.*, **111**(43), 15296-15303.

Lambeck, K., Purcell, A. & Zhao, S., 2017. The North American Late Wisconsin ice sheet and mantle viscosity from glacial rebound analyses, *Quat. Sci. Rev.*, 158, 172-210.

Lau, H.C.P., Mitrovica, J.X., Austermann, J., Al-Attar, D., Crawford, O. & Latychev, K., 2016. Inferences of mantle viscosity based on ice age data sets: Radial structure, *J. Geophys. Res. Solid Earth*, **121**(10), 6991-7012, doi:10.1002/2016JB013043.

Love, R., Milne, G. A., Tarasov, L., Engelhart, S. E., Hijma, M. P., Latychev, K., Horton, B.P., & Törnqvist, T. E. (2016). The contribution of glacial isostatic adjustment to projections of sea-level change along the Atlantic and gulf coasts of North America. *Earth's Future*, **4**(10), 440–464. https://doi.org/10.1002/2016EF000363

McConnell, R.K., 1968. Viscosity of the mantle from relaxation spectra of isostatic adjustment, *J. Geophys. Res.*, **73**, 7089-7105.

Milne, G.A. & Mitrovica, J.X., 1998. Postglacial sea-level change on a rotating Earth, *Geophys. J. Int.*, **133**(1), 1-19.

Mitrovica, J.X., 1996. Haskell [1935] revisited, *J. Geophys. Res.*, **101**(B1), 555-569.

Mitrovica, J.X. & Forte, A.M., 1997. Radial profile of mantle viscosity: Results from the joint inversion of convection and postglacial rebound observables, *J. Geophys. Res.*, **102**(B2), 2751-2769.

Mitrovica, J.X. & Forte, A.M., 2004. A new inference of mantle viscosity based upon joint inversion of convection and glacial isostatic adjustment data, *Earth Planet. Sci. Lett.*, **225**, 177-189.

Mitrovica, J.X., Forte, A.M. & Simons, M., 2000. A reappraisal of postglacial decay times from Richmond Gulf and James Bay, Canada, *Geophys. J. Int.*, **142**(3), 783-800.

Mitrovica, J.X. & Milne, G.A., 2003. On post-glacial sea level: I. General theory, *Geophys. J. Int.*, **154**(2), 253-267.

Mitrovica, J.X. & Peltier, W.R., 1993. A new formalism for inferring mantle viscosity based on estimates of post glacial decay times: application to RSL variations in N.E. Hudson Bay, *Geophys. Res. Lett.*, **20**, 2183-2186.

Mitrovica, J.X. & Peltier, W.R., 1995. Constraints on mantle viscosity based upon the inversion of post-glacial uplift data from the Hudson Bay region, *Geophys. J. Int.*, **122**(2), 353-377.

Nakada, M., Okuno, J., & Yokoyama, Y., 2016. Total meltwater volume since the Last Glacial Maximum and viscosity structure of Earth's mantle inferred from relative sea level changes at Barbados and Bonaparte Gulf and GIA-induced $\dot{J}_2$, *Geophys. J. Int.*, **204**, 1237-1253.

Nordman, M., Milne, G. & Tarasov, L., 2015. Reappraisal of the Ångerman River decay time estimate and its application to determine uncertainty in Earth viscosity structure, *Geophys. J. Int.*, **201**(2), 811-822.

Paulson, A., Zhong, S., & Wahr, J., 2005. Modelling post-glacial rebound with lateral viscosity variations, *Geophys. J. Int.*, **163**, 357-371.

Peltier, W.R., 1974. The impulse response of a Maxwell Earth, *Rev. Geophys.*, **12**(4), 649-669.

Peltier, W.R., 1996. Mantle Viscosity and Ice-Age Ice Sheet Topography, *Science*, **273**, 1359-1364.

Peltier, W.R., 1998. Postglacial variations in the level of the sea: Implications for climate dynamics and solid-earth geophysics, *Rev. Geophys.*, **36**(4), 603-689.

Peltier, W.R., 2004. Global glacial isostasy and the surface of the ice-age Earth: the ICE-5G (VM2) model and GRACE, *Ann. Rev. Earth Planet. Sci.*, **32**, 111-149.

Peltier, W.R., & Drummond, R., 2008. Rheological stratification of the lithosphere: A direct inference based on the geodetically observed pattern of the glacial isostatic adjustment of the North American continent, *Geophys. Res. Lett.*, **35**, doi:10.1029/2008GL034586.

Peltier, W.R., Shennan, I., Drummond, R., & Horton, 2002. On the postglacial isostatic adjustment of the British Isles and the shallow viscoelastic structure of the Earth, *Geophys. J. Int.*, **148**, 443-475.

Pendea, I.F., Costopoulos, A., Nielsen, C. & Chmura, G.L., 2010. A new shoreline displacement model for the last 7 ka from eastern James Bay, Canada, *Quaternary Research*, **73**(3), 474-484.

Reimer, P.J. *et al.*, 2013. IntCal13 and Marine13 radiocarbon age calibration curves 0–50 000 years cal BP, *Radiocarbon*, **55**(4), 1869–1887.

Roy, K., & Peltier, W.R., 2015. Glacial isostatic adjustment, relative sea level history, and mantle viscosity: reconciling relative sea level model predictions for the U.S. East coast with geological constraints, *Geophys. J. Int.*, **201**, 1156-1181.

Sella, G.F., Stein, S., Dixon, T.H., Craymer, M., James, T.S., Mazzotti, S., & Dokka, R.K., 2007. Observation of glacial isostatic adjustment in “stable” North America with GPS, *Geophys. Res. Lett.*, **34**, doi:10.1029/2006GL027081

Steffen, H., & Kaufmann, G., 2205. Glacial isostatic adjustment of Scandinavia and northwestern Europe and the radial viscosity structure of the Earth’s mantle, *Geophys. J. Int.*, **163**, 801-812.

Stuiver, M., and Reimer, P.J., 1993. Extended C14 Data Base and Revised Calib 3.0 C14 Age Calibration Program, *Radiocarbon*, **35**, 215-230.

Tarasov, L., 2013. GLAC-1b: A new data-constrained global deglacial ice sheet reconstruction from glaciological modelling and the challenge of missing ice, *European Geophysical Union General Assembly 2013, Abstracts*, **15**, EGU2013-12342.

Tarasov, L., Dyke, A.S., Neal, R.M. & Peltier, W., 2012. A data-calibrated distribution of deglacial chronologies for the North American ice complex from glaciological modeling, *Earth Planet. Sci. Lett.*, **315–316**, 30–40.

Walcott, R.I., 1980. Rheological models and observational data of glacio-isostatic rebound, *Earth Rheology, Isostasy, and Eustasy*, pp.3-10, ed. Morner, N.-A., John Wiley, New York.

Supplementary

Joseph Kuchar[1], Glenn Milne[2], Alexander Hill[2], and Lev Tarasov[3]

1. Department of Physics, University of Ottawa
2. Department of Earth and Environmental Science, University of Ottawa
3. Department of Physics and Physical Oceanography, Memorial University of Newfoundland

Table S1: The RSL data used for Richmond Gulf, with C14 ages from Mitrovica *et al.* (2000) calibrated using the marine calibration curve of Reimer *et al.* (2013) and the Calib software (Stuiver and Reimer, 1993). All ages given in thousands of years BP.

Latitude	Longitude	C14 Age (ka)	C14 Age Error (ka)	Calibrated Age (ka)	Calibrated Age Error (ka)	Height (m)	Height Error (m)
56.28	-76.5	-6.43	0.15	-6.9085	0.3435	172	2.5
56.45	-76.5	-6.23	0.22	-6.7135	0.4845	154	2.5
56.28	-76.5	-6	0.16	-6.427	0.367	137	2.5
55.63	-77.13	-3.48	0.1	-3.352	0.254	52.3	2.5
55.58	-77.32	-3.36	0.06	-3.2075	0.1615	58	2.5
55.63	-77.13	-2.86	0.1	-2.575	0.237	34.3	1.715
55.58	-77.3	-2.76	0.08	-2.506	0.194	44	2.2
55.63	-77.13	-2.51	0.08	-2.1515	0.1915	32	1.6
55.36	-77.62	-2.47	0.1	-2.1065	0.2335	31.7	1.585
55.36	-77.62	-2.43	0.1	-2.0785	0.2355	28.9	1.445
55.63	-77.13	-2.41	0.09	-2.069	0.222	31.5	1.575
55.36	-77.62	-2.26	0.1	-1.8645	0.2505	26.6	1.33
55.36	-77.62	-2.23	0.1	-1.8345	0.2495	29.9	1.495
55.36	-77.62	-2.05	0.1	-1.621	0.236	21.9	1.095
55.58	-77.3	-2.03	0.06	-1.599	0.163	29	1.45
55.36	-77.62	-2.026	0.1	-1.592	0.235	27.3	1.365
55.36	-77.62	-2.02	0.1	-1.586	0.234	23.7	1.185
55.58	-77.3	-1.79	0.05	-1.3585	0.1105	22	1.1
55.36	-77.62	-1.76	0.09	-1.327	0.192	20.4	1.02
55.36	-77.62	-1.68	0.09	-1.217	0.197	18.8	0.94
55.39	-77.5	-1.68	0.39	-1.3085	0.7995	21.4	1.07
55.36	-77.62	-1.49	0.09	-1.0615	0.1905	17.3	0.865
55.58	-77.3	-0.89	0.1	-0.4815	0.1695	13.3	0.665
55.63	-77.13	-0.67	0.08	-0.3015	0.1775	4.7	0.5

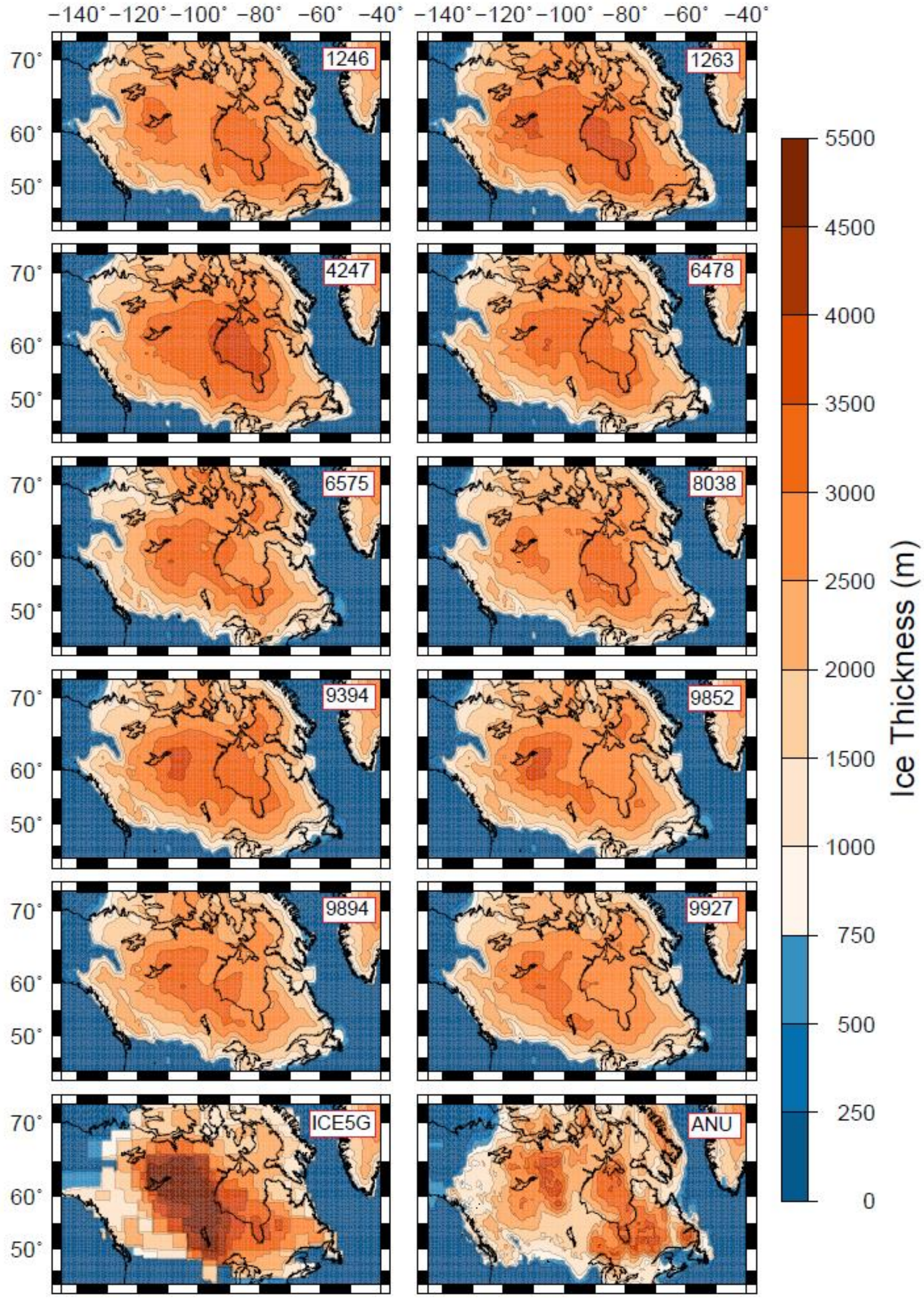

Figure S1: The reconstructions of the North American Ice Sheet (NAIS) used in this study shown at 20ka BP (See main text for details). The first ten shown are reconstructions from Tarasov *et al.* (2012).

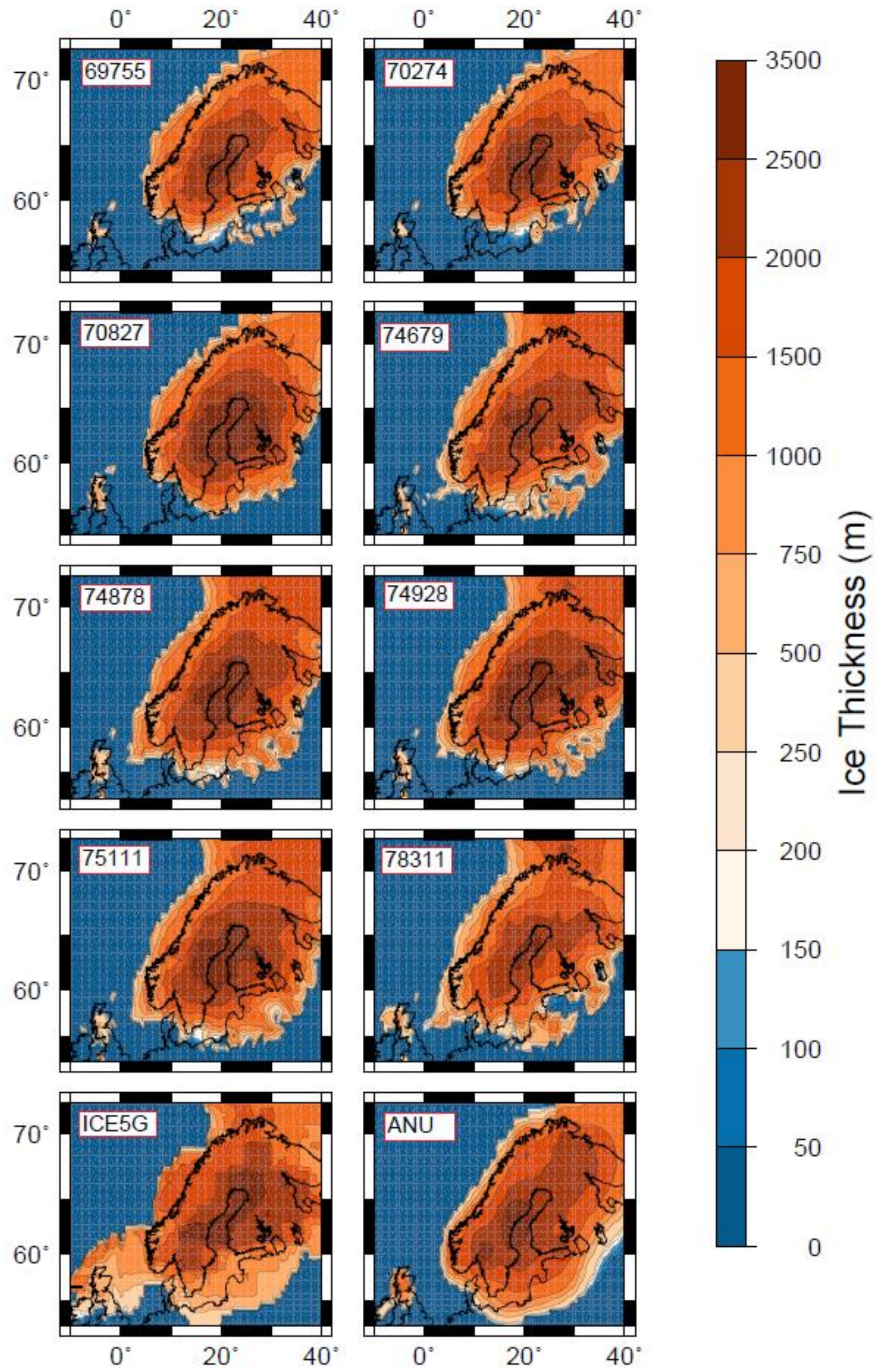

Figure S2: As in Figure S1, but for the Fennoscandian Ice Sheet. The first eight shown are reconstructions from Tarasov (2013).

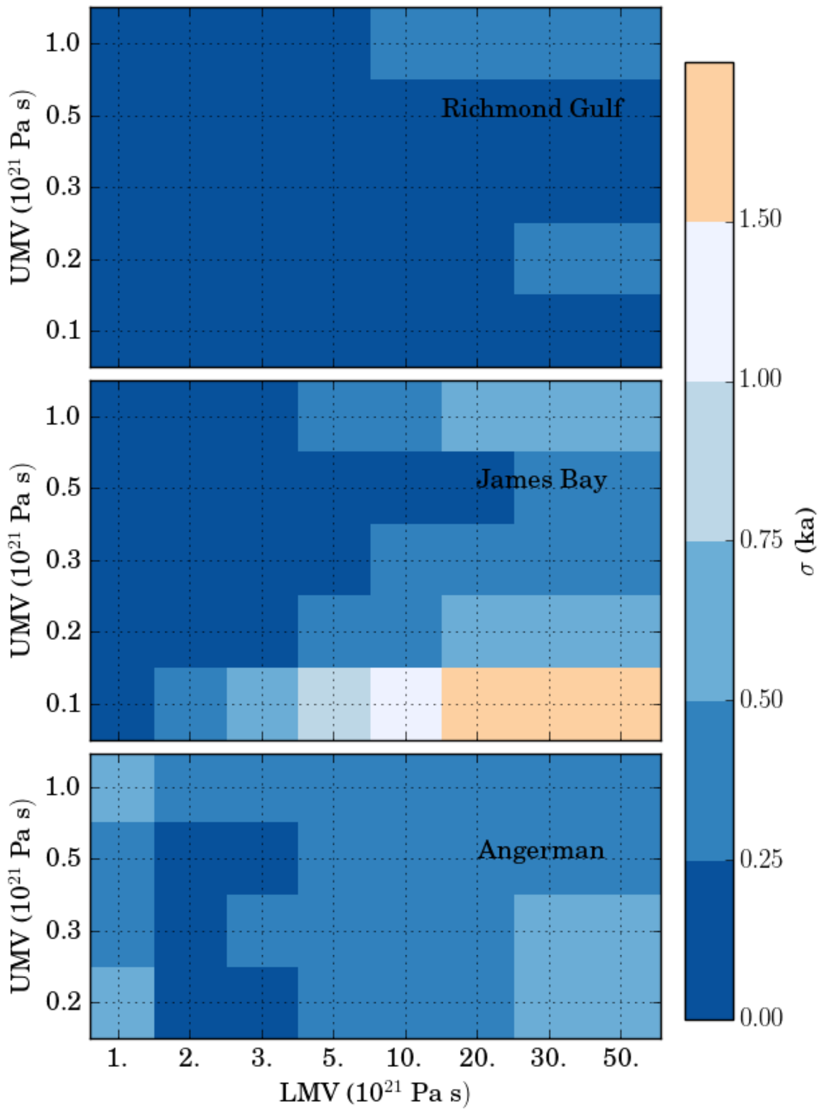

Figure S3: The standard deviation of decay times among ice histories for each study site. The structure is similar to the spread in decay time values (main text, Figure 5), with Richmond Gulf showing the least amount of ice sensitivity.

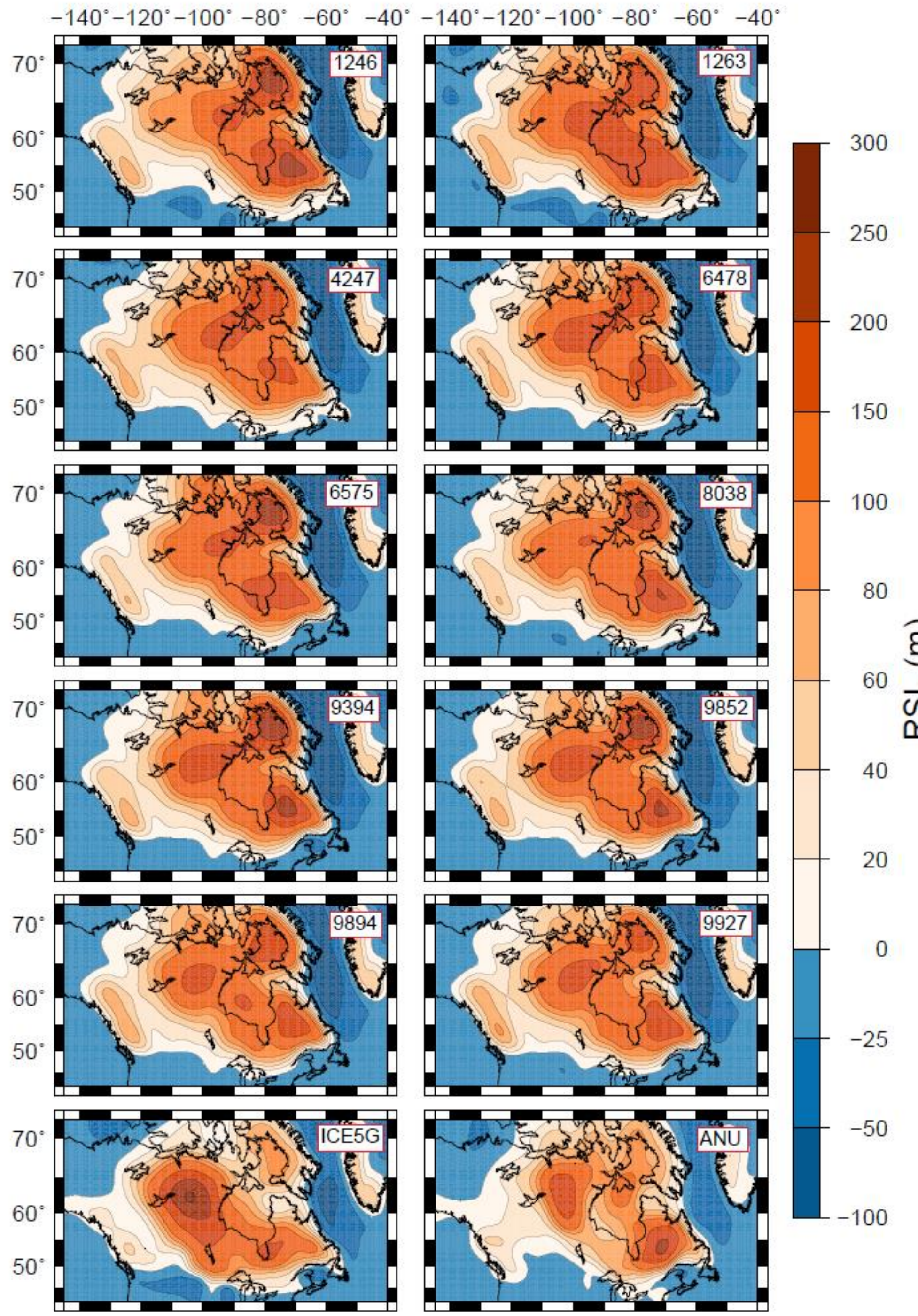

Figure S4 Expanded version of Figure 6 from main text, showing RSL in North America at 7ka, for an Earth model with a 0.5×10^{21} Pa s UMV and a 1×10^{22} Pa s LMV.

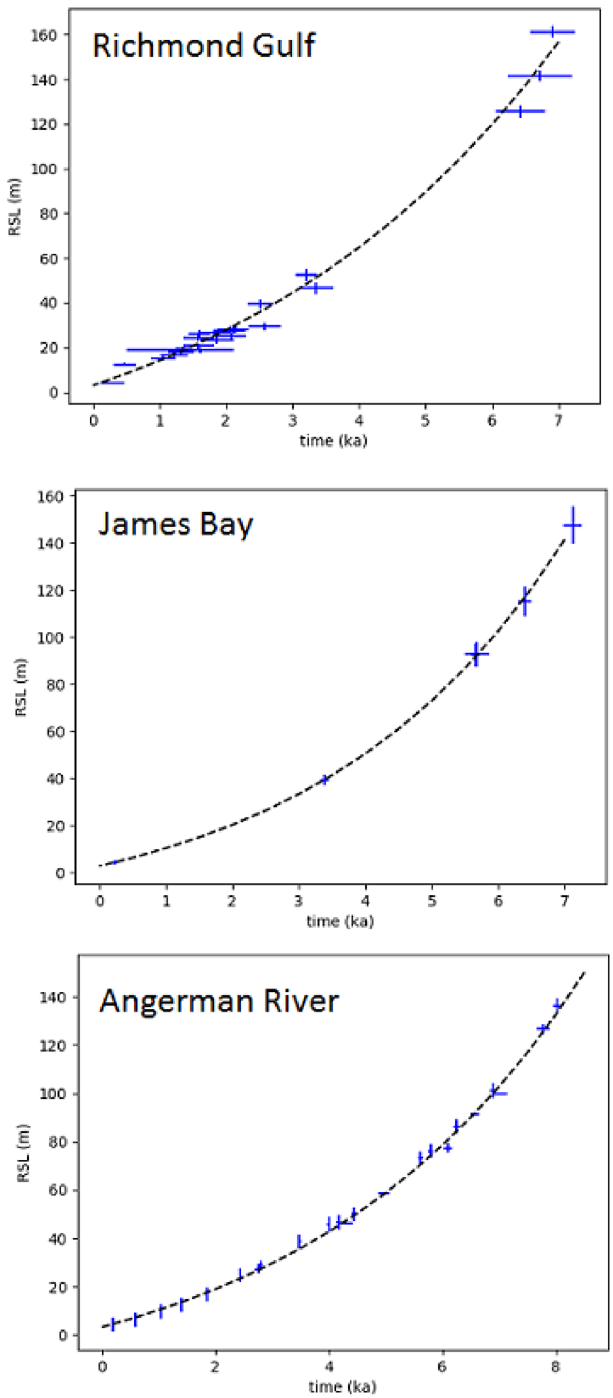

Figure S5 Samples of corrected RSL data for Richmond Gulf (top) and James Bay (middle) and Ångerman River (bottom) with their associated best fit curves, for an Earth model with a 3x10^{20} Pa s UMV and 1x10^{22} Pa s LMV and the 4247 ice history of

Tarasov *et al.* (2012) for the Hudson Bay sites and the 70274 ice history of Tarasov (2013) for Ångerman River. The estimated decay times are 5.0±1.5 ka for Richmond Gulf, 3.67±0.17 ka for James Bay, and 4.52±0.71 ka for Ångerman River.

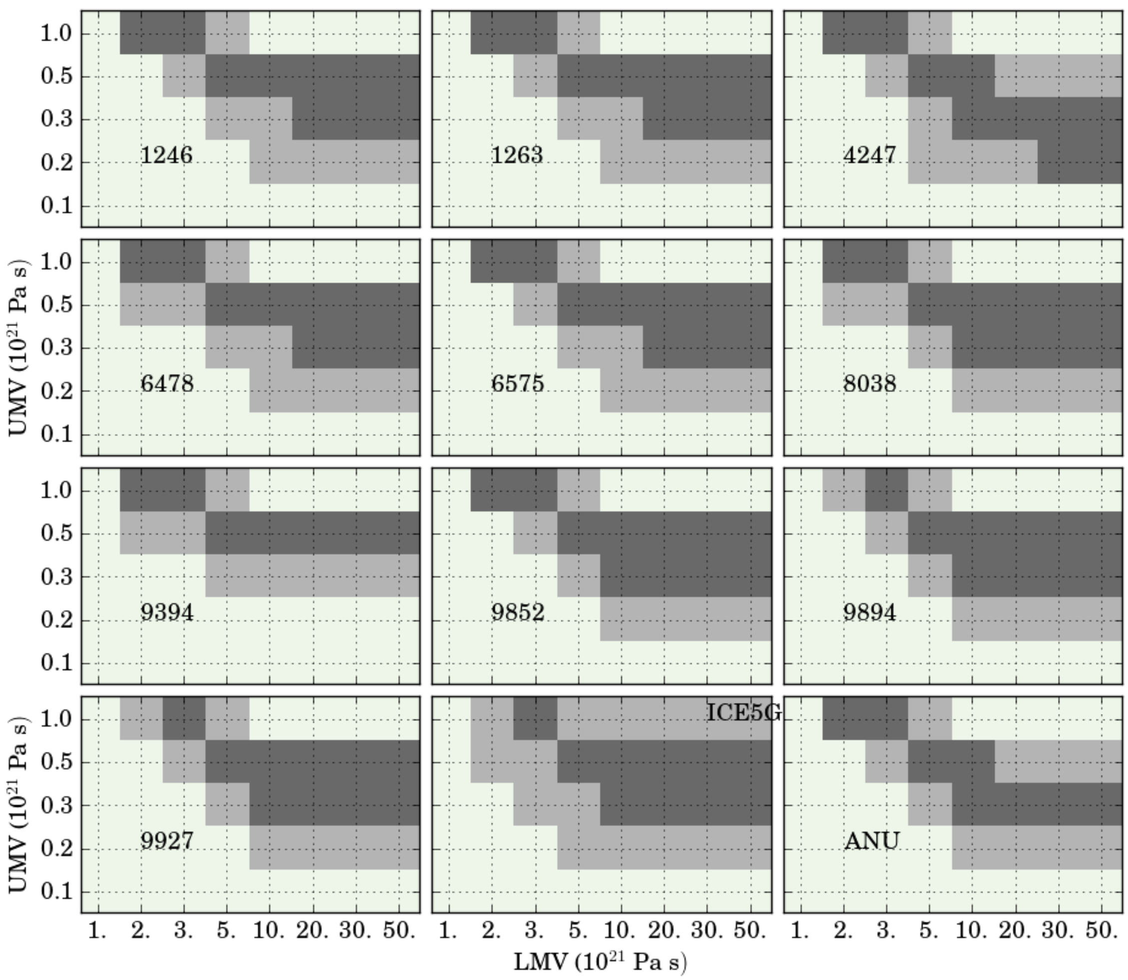

Figure S6 Model-data agreement map for Richmond Gulf but with no corrections applied to the data and the full RSL model output used (i.e. RSL_{full} in equation (4)).

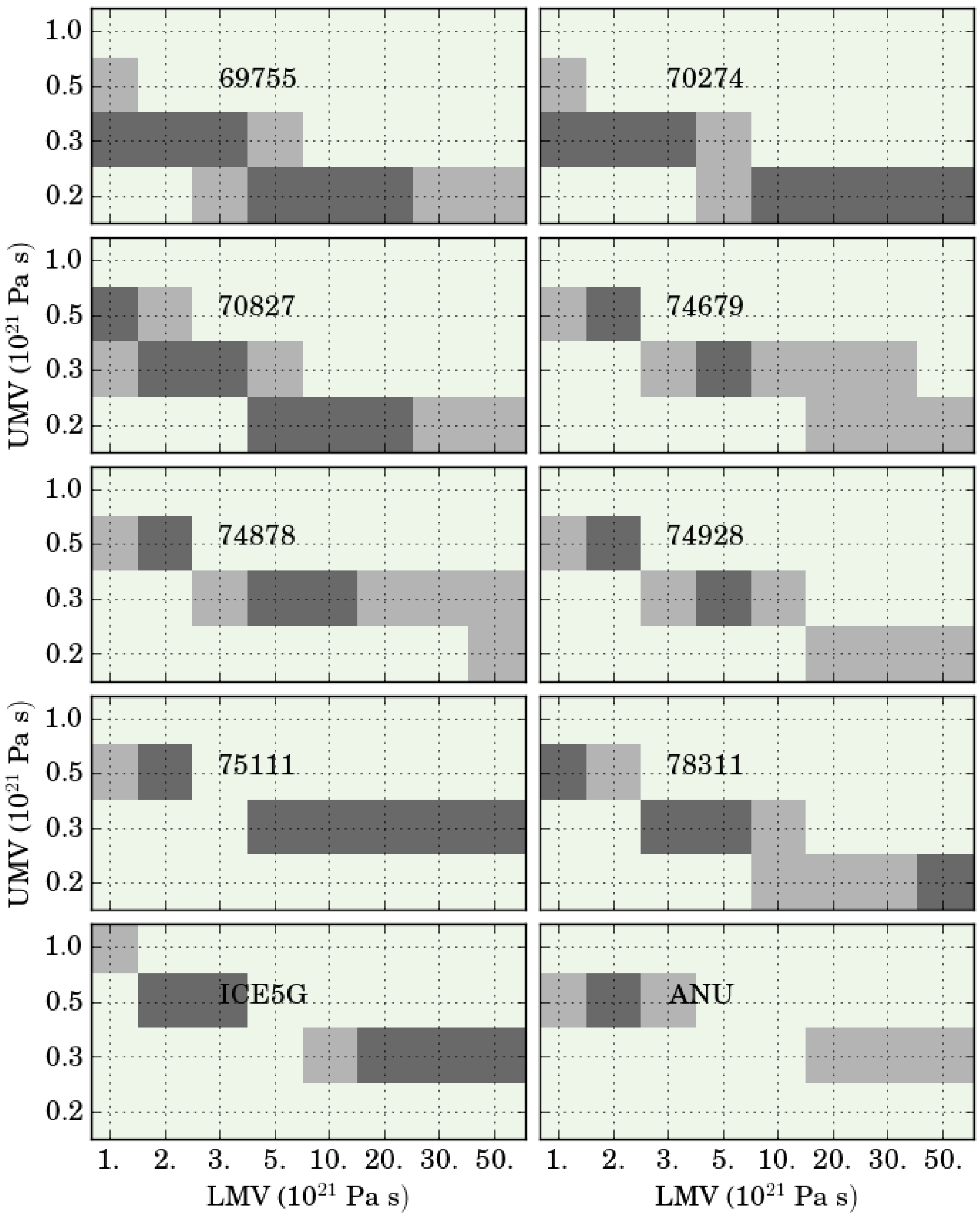

Figure S7 As in Figure S6, but for Angerman River.

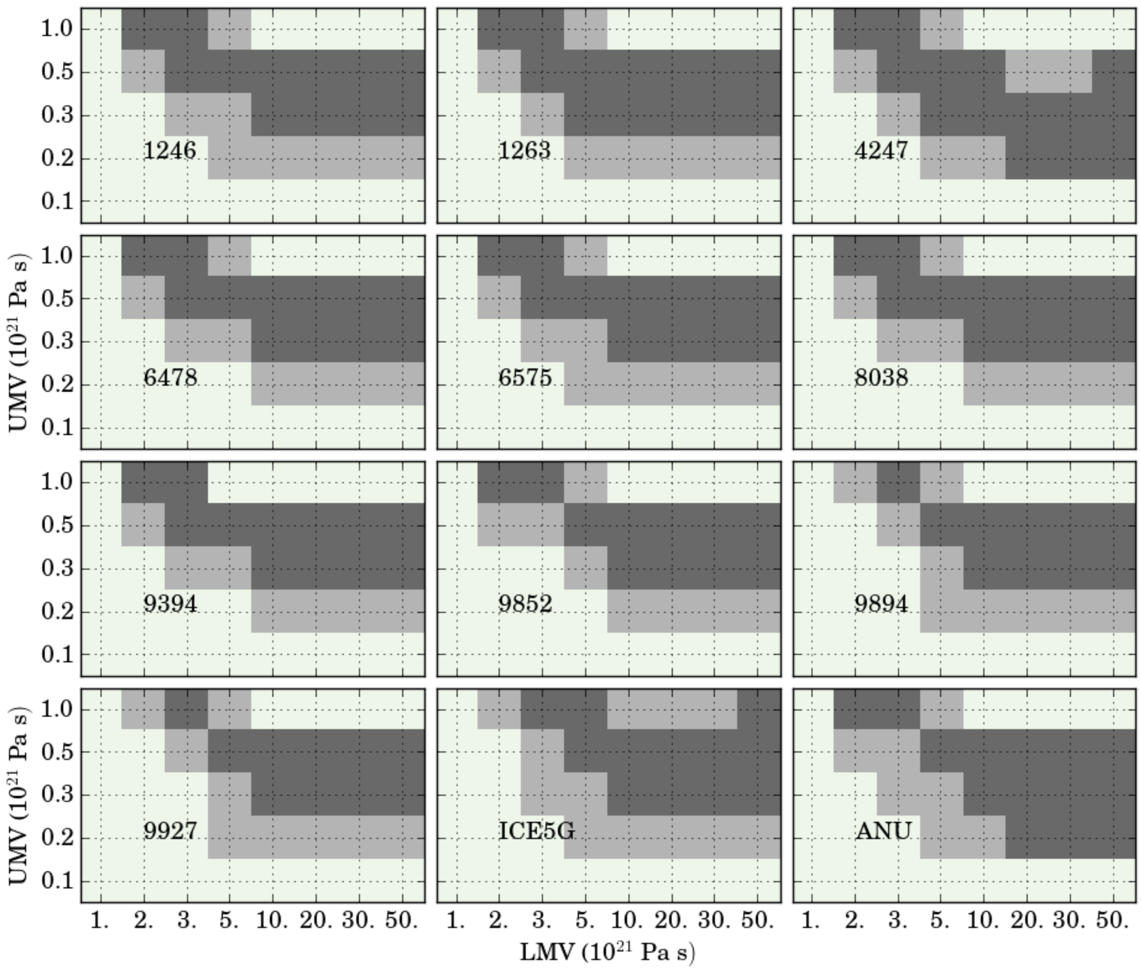

Figure S8 As in Figure S6, but with the correction defined by Equation 4 applied to the data, and only the modelled ice component of RSL considered (i.e. RSL_{ice} in equation (5)).

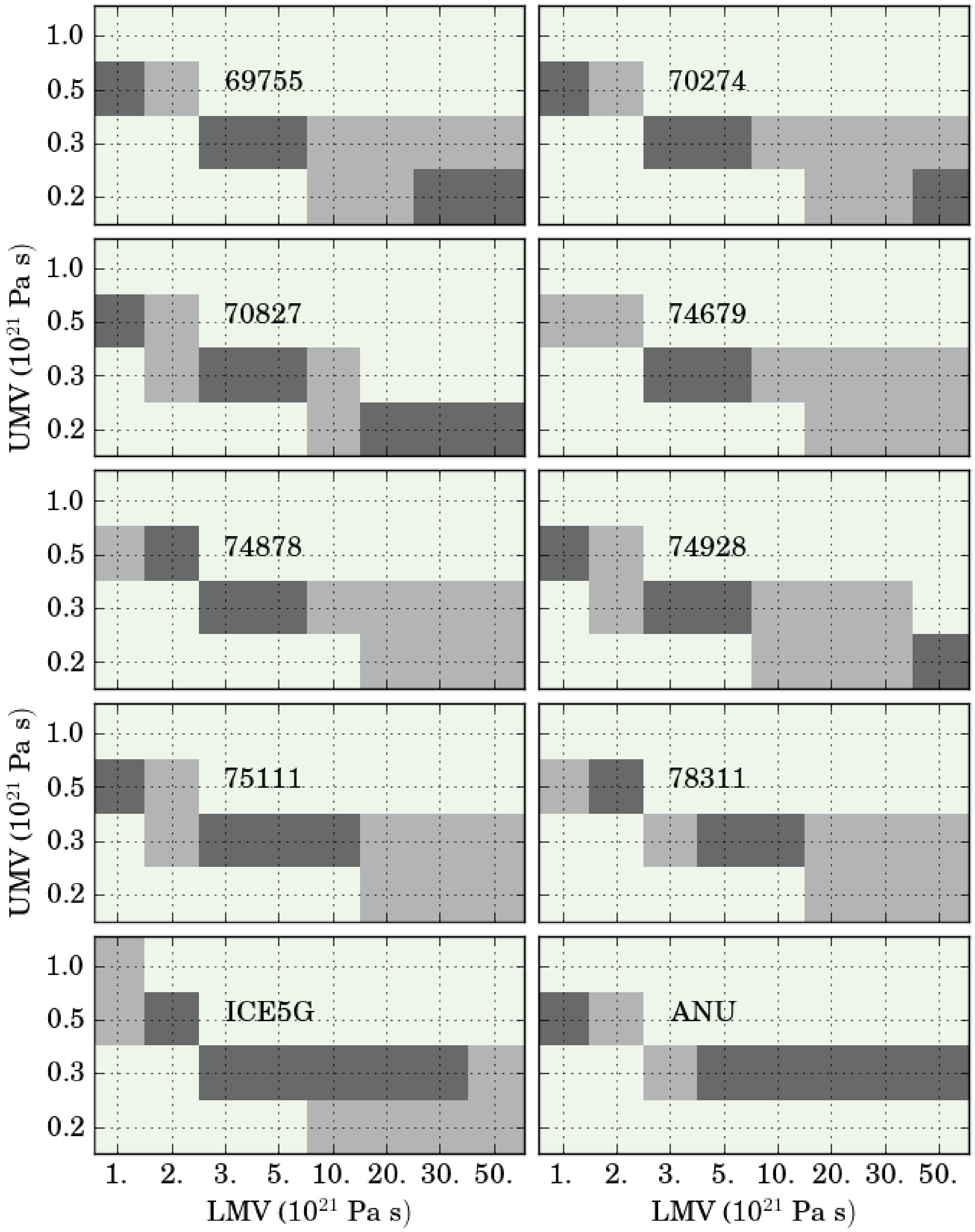

Figure S9 As In Figure S8, but for Angerman River.

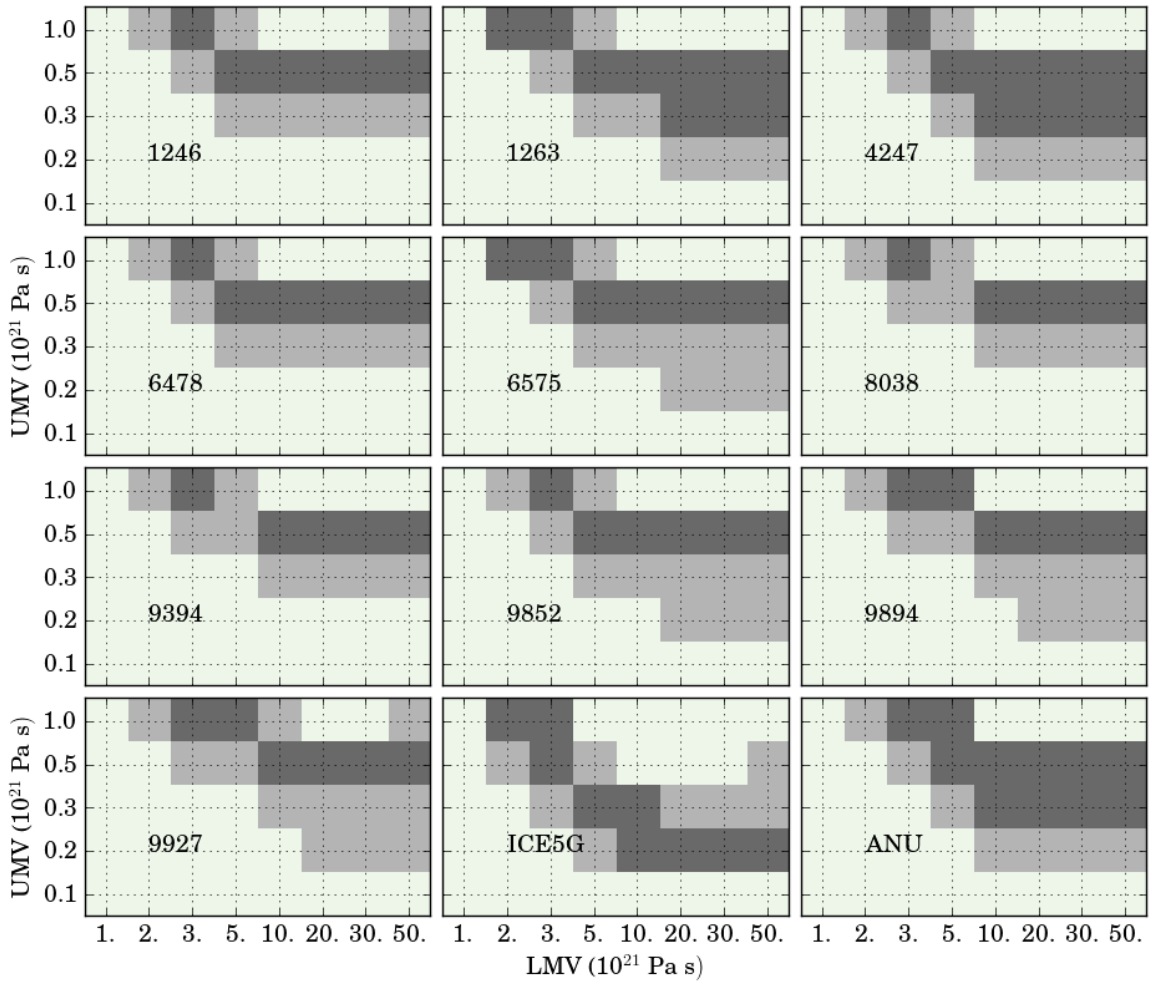

Figure S10 As in Figure S6, but with only the correction for spatial variability applied to the data, and compared to the full modelled RSL (i.e. RSL_{full} in Equation 5).

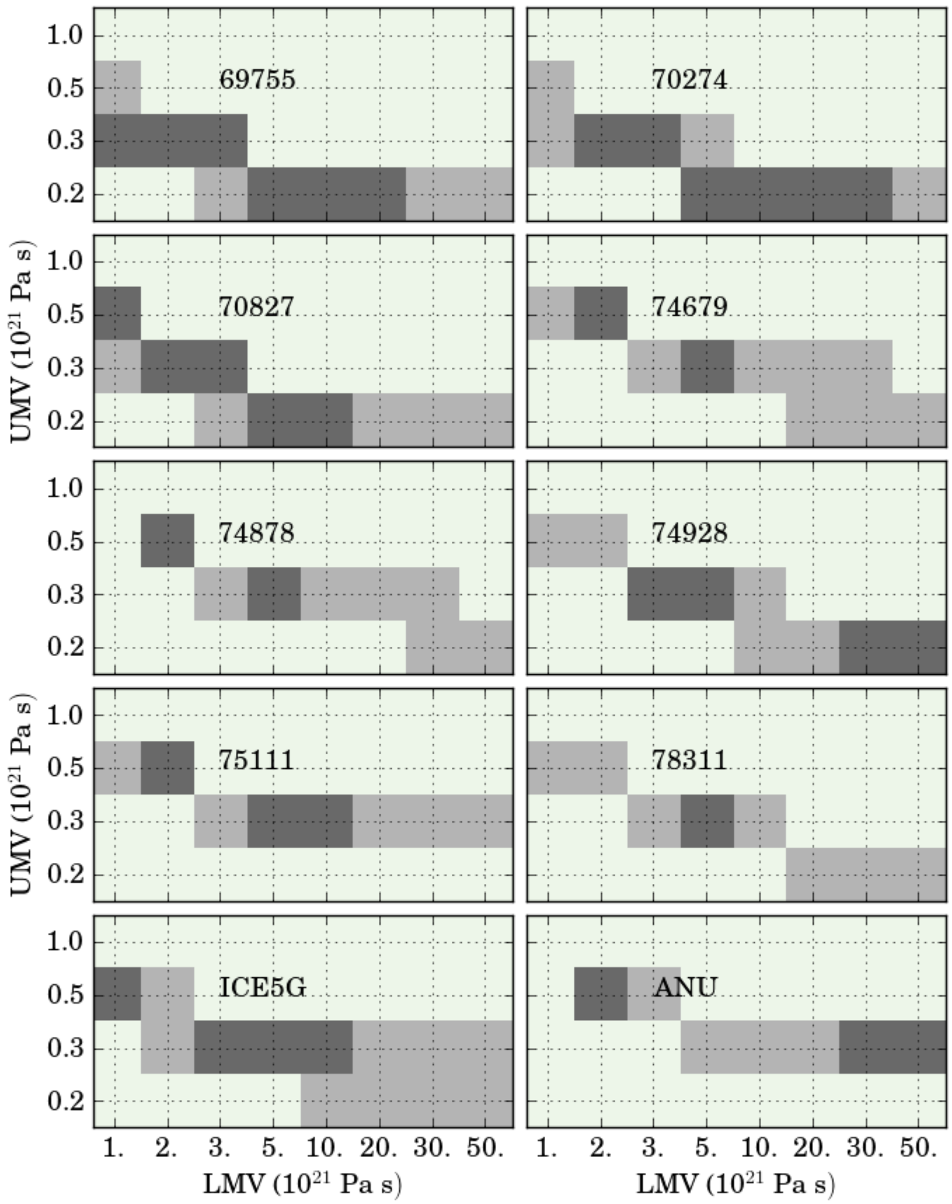

Figure S11 As in Figure S10, but for Angerman River.

As a second approach to study the influence of lateral viscosity variations, we constructed a realistic 3-D viscosity model from seismic tomography models... PGR (post glacial rebound) observations tend to depend on the viscosity structure beneath the ice load, whether or not the observation is made there. ...For local PGR observations away from the loading (sea levels along the North American east coast) none of our 1-D models could reproduce well the results of the calculation with 3-D viscosity. In this case, PGR is sensitive to both the local viscosity structure and the substantially different structure beneath the loaded regions. The nature of this problem is essentially 3-D, so we cannot expect similar deformation from any 1-D viscosity model.

Paulson et al., 2005

5

An Investigation Into the Viscosity Structure Underneath Eastern North America

In the last two Chapters, I have described two research projects where we have investigated GIA in North America (in the Gulf of Mexico and Hudson Bay, respectively), and in both studies we determined what Earth viscosity structures were consistent with the data. In Chapter 3 we investigated the effects of sediment isostatic adjustment on land motion and RSL along the US Gulf coast, and the result of that analysis was that high viscosity Earth models were favoured among all the ice histories considered. Specifically, the lowest model misfit was one with a 5×10^{21} Pa s upper mantle viscosity (UMV) and a 5×10^{22} Pa s lower mantle viscosity (LMV). By contrast, in

Chapter 4, we compared model and data decay times in Hudson Bay for a variety of ice histories, and in Richmond Gulf the viscosity structure that could satisfy the constraints had a UMV of $(0.3 - 0.5) \times 10^{21}$ Pa s and an LMV of at least 10^{21} Pa s. Therefore, we have found that the Gulf coast RSL data requires a significantly higher viscosity upper mantle than is required in Hudson Bay. This is not necessarily surprising, as the viscosity in the real Earth can be expected to vary substantially due to variations in the quantities that determine viscosity (such as temperature and water content). However, this is an issue for a model with spherical symmetry, as it means we can not satisfy both datasets simultaneously. Moreover, the results we obtained for the Gulf coast RSL data is consistent with the recent results of Love et al., 2016, who performed a similar analysis using RSL data for both the Atlantic and Gulf coasts of North America. They found the Atlantic coast data are satisfied by a UMV of 3×10^{21} and a LMV of 3×10^{22}, and the same viscosity structure for the Gulf coast data as we found in Kuchar et al., 2018a . This level of agreement, while comforting, is not surprising: both studies used the North American Ice reconstructions of Tarasov et al., 2012 and tested model predictions against the same Gulf coast RSL database (and while Love et al. did not include SIA explicitly in their model, they did correct the Gulf coast data for an estimated SIA contribution).

Indeed, we are not the first to note difficulties with this dataset. In Engelhart et al., 2011, GIA-driven RSL was computed assuming two ice histories (ICE5G and ICE6G), as well as two Earth viscosity structures (VM5a and VM5b), and compared to a revised sea-level database (Engelhart and Horton, 2012). They found that, for both ice histories, reducing the UMV from 0.5×10^{21} Pa s in VM5a to 0.25×10^{21} Pa s in VM5b results in an improved fit for mid-latitude sites (approximately New York to Virginia), but not for the data in the Carolinas. The authors interpreted the inability to simultaneously fit the data all along the coast as evidence for lateral variability in the viscosity of the upper mantle.

This analysis was extended in Roy and Peltier, 2015, who revisited the Engelhart and Horton database with the updated ICE6G_C (Peltier et al., 2015) ice history. The authors note that the VM5b viscosity profile improves the fit to certain subsets of the Atlantic coast data, but they reject it as it does not satisfy Fennoscandian relaxation time constraints. Interestingly, the authors acknowledge that the viscosity of the actual Earth is expected to exhibit significant lateral variability, but their focus is strictly in determining a single 1-D model that can capture as many phenomena as possible. Ultimately, the Atlantic coast data is used to develop the VM6 viscosity profile, which features a reduction in the viscosity of most of the lower mantle relative to VM5a.

Going back to Love et al., 2016, this study expanded both the number of ice histories considered and the number of viscosity structures, and explicitly considered the effects of lateral viscous structure, and in some ways accounted for its effects. They also extended the database of Engelhart and Horton, 2012, to include data in the US Gulf of Mexico and Atlantic Canada. They demonstrated sensitivity to lateral structure by generating RSL curves with a 3-D model and computing differences in RSL between the 3-D and 1-D models at a selection of sites along the Atlantic and Gulf coasts. This test demonstrated a significant sensitivity to lateral structure, particularly for sites very near to the ice sheet, but also for sites along the southern coast. I'll note that they did not attempt to use the 3-D model to fit observations, only to demonstrate differences relative to 1-D models. While the model parameter inferences and RSL projections performed in Love et al. are done with a 1-D model, they separated the database into Canadian, U.S. Atlantic coast, and Gulf coast components, and determined optimal parameter sets for each component individually. This approach allows for the local viscosity structure and ice history to be determined for each component, but it is problematic when we remember that there was only one ice sheet, and only one Earth, and therefore that sort of approach is not physically consistent. There is an interesting contrast between the approaches of Love et al. and Roy and Peltier, where in the former case there is an attempt made to capture the physics (of lateral viscous structure) at the cost of model consistency, and in the latter the emphasis is on model consistency at the cost of realism. This motivates us, in the present study, to apply a 3-D GIA model to determine whether applying a consistent and realistic model of lateral structure can actually allow us to better fit the RSL data.

The research described in this chapter is an investigation to determine, first of all, why the Atlantic and Gulf coast RSL data require such high viscosities to be fit, and second of all, is this simply a limitation of the 1-D model? Ultimately we answer this question with a combination of 1-D and 3-D GIA modelling: the former to understand why the RSL observations require such high viscosity values, and the latter to determine if high quality fits can be achieved when lateral structure is incorporated into a model in which the global average depth-dependent viscosity structure is compatible with recent inferences of this structure. Before presenting the research, I will present some background on the state of 3-D GIA modelling.

5.1 3-D GIA Modelling

The earliest study, that I am aware of, to examine the effects of lateral viscous structure on GIA predictions of Maxwell Earth models was performed by Sabadini et al., 1986. They investigated the effects of lateral structure in the upper mantle, and their motivation was partly that the RSL data along the US Atlantic coast, used to constrain 1-D Earth model parameters, would be expected to feature significant lateral variability associated with the continental margin. Their method to implement lateral structure was to divide their study region into continental and oceanic regions with different viscous structure. Whereas continental regions featured a thick lithosphere overlying a uniform viscosity upper mantle, oceanic regions were assigned a thinner lithosphere, and a low viscosity aesthenosphere was placed between the lithosphere and upper mantle. Their results indicated that while the lateral structure they imposed had no effect on data within the previously glaciated region, data on the ice margins and in the far-field were much more sensitive to the lateral structure.

While there were other similar studies that employed simplified ice disks and flat Earth approximations, it was not until the 2000's that lateral structure began to be investigated within the context of a spherical Earth model and more realistic ice histories (e.g. Wu et al., 2005; Paulson et al., 2005; Latychev et al., 2005). Some of these, such as Wu et al., 2005, were concerned with determining the ability of RSL observables to constrain lateral structure, and so used simple lateral structure parameterizations, while others (such as Latychev et al., 2005) were instead concerned with computing GIA observables using realistic lateral structure. The model of Wu et al., 2005, used a coupled Laplace-Finite Element method to compute RSL observables such as RSL and geoid rates and horizontal and tangential surface velocities to determine which observables, and at what distances relative to the ice sheet, could resolve lateral structure at different depths. Their implementation of lateral structure was relatively simple, and in fact fairly similar to that of Sabadini et al., 1986, where one viscous structure was assumed beneath the ice sheet, and another in the region beyond the ice sheet. In both cases the sub-lithosphere mantle was divided into a 5-layer discretization. They found that, while tangential velocities were sensitive to both shallow and deep lateral structure both in the near-field and the far-field, the radial velocities and geoid rates could only resolve structure within the ice margins. This sensitivity analysis was made more robust in Wu, 2006, in which the general approach was similar but where this time sensitivity kernels were computed for both laterally homogeneous and laterally heterogeneous Earth models (where they computed, in the former case, sensitivity to changes in viscosity with depth, and in the latter case, sensitivity to changes in viscosity both with depth and laterally). Instead of only having structure defined by one under the ice sheet, and another beyond it, the mantle was instead divided into four depth regions and nine angular distance regions. This test demonstrated that while a given RSL observation is most sensitive to local lateral structure, it will also be influenced by deep lateral structure in neighbouring regions.

An application of the model with a realistic ice history and viscosity structure was performed in Wang and Wu, 2006, where a seismic velocity model was scaled to obtain density perturbations, which were then scaled to obtain temperature perturbations, and finally viscosity perturbations (assuming variations in viscosity are dependent only on temperature). The study investigated the effects of this lateral viscous structure on present-day land motion rates, and found that the lateral structure did not greatly affect the pattern of vertical rates, but it did affect the magnitude (to a degree measurable by GPS). The tangential rates were found to be highly sensitive both in direction and magnitude.

The transformation from seismic velocity models to viscosity variations, as in Wang and Wu, 2006, is how realistic lateral structure is generally obtained in 3D GIA modelling, and is also employed (with variations) in Paulson et al., 2005 and Latychev et al., 2005. The 3-D model I use in this Chapter is that of Latychev et al., 2005, and so I will describe how lateral structure is determined within that model in particular. Lateral variations in viscosity are determined with respect to a reference 1-D viscosity structure $\eta_0(r)$, where the perturbations to the reference are determined by seismic velocity models through equations 5.1 to 5.3:

$$\delta \ln \rho(r, \theta, \phi) = \frac{\partial \ln \rho}{\partial \ln v_s}(r) \delta \ln v_s(r, \theta, \phi) \tag{5.1}$$

$$\delta T(r, \theta, \phi) = -\frac{1}{\alpha(r)} \delta \ln \rho(r, \theta, \phi) \tag{5.2}$$

$$\eta(r, \theta, \phi) = \eta_0(r) e^{-\epsilon \delta T(r, \theta, \phi)} \tag{5.3}$$

In the above, variations in shear-wave velocity, $v_s(r, \theta, \phi)$ are used to scale a reference 1-D density profile, $\rho(r)$, to obtain the (log of) the perturbed density field, $\delta \ln \rho(r, \theta, \phi)$. The perturbed density field is used to calculate a perturbed temperature field $\delta T(r, \theta, \phi)$, assuming a radially-varying thermal expansion coefficient $\alpha(r)$. The temperature perturbation is then used to scale the reference 1-D viscosity profile, $\eta_0(r)$ to obtain the 3-D viscosity profile $\eta(r, \theta, \phi)$, by assuming an exponential relationship between temperature and viscosity, and a scaling parameter ϵ that is assumed constant. The general approach of scaling shear wave velocities to density perturbations to temperature perturbations and finally to viscosity is common, though there are variations within it. For example, in Paulson et al., 2005, a temperature profile is used to generate viscosity by

$$\eta(r) = A_0 \exp\left(\gamma \frac{T_m(r)}{T(r)}\right), \tag{5.4}$$

where T_m is the melting temperature, and γ and A_0 are parameters. The 3-D model is then compared to 1-D models run with Earth structure obtained by weighted averages of the 3-D lateral structure. This is in contrast to the approach of Latychev et al., 2005, where instead a reference 1-D viscosity structure is scaled with temperature to obtain the 3-D lateral structure. What is particularly interesting about the Paulson et al. study, or at least particularly relevant to our focus on the Atlantic coast, is that they compared three GIA observables (Hudson Bay decay times, Atlantic coast RSL, and the James Bay free-air gravity anomaly) for the 3-D model with those of a 1-D model with a viscosity structure corresponding either to the global average viscosity of the 3-D Earth, an average of the structure beneath Hudson Bay, or an average over the East coast. While the Hudson Bay average 1-D model achieved only a 10% misfit with the full 3-D model for computed decay times (compared to >25% for the East coast average and 35% for the global average), the fit to the RSL data was not significantly improved with the East coast average 1D model, and in fact, the misfit between the 3-D model results and the 1-D model results for the East coast RSL was the greatest for the East coast average model, and the misfit was >30% for all three 1-D models. This demonstrates that 1-D models can not capture the 3-D model results for these data, and also suggests that these results are sensitive to non-local lateral structure.

The Latychev et al., 2005 study presented a finite volume formulation for 3-D GIA modelling, and performed benchmark tests by using the 3-D model to compute GIA observables for a spherically symmetric model and comparing to the output of a standard 1-D model. They also presented results where lateral structure was scaled from a seismic velocity model, and demonstrated that while the lateral structure has relatively little impact on present-day radial surface velocities, it has a significant effect on the tangential velocities (which is also what was found by Wang and Wu, 2006). It is worth noting that in this first study, the model did not solve the sea-level equation, and instead only the GIA response to a known ice load and complementary eustatic ocean load.

In recent years, the main application of 3-D models has been in regional analyses, largely to determine whether lateral structure needs to be accounted for when modelling GIA in those regions (or, to determine the consequences of ignoring lateral structure in 1-D studies). For example, Austermann et al., 2013 use the Latychev et al., 2005 model, but updated to solve the extended sea-level equation (Kendall et al., 2005) to model RSL in Barbados. The Barbados record of RSL (which was shown in Figure 4-1 in Chapter 4) is often used as a measure of the eustatic sea-level during the deglaciation (e.g., Peltier and Fairbanks, 2006 use it to conclude that eustatic sea-level at LGM was 120 m below present). However, there are local strong viscosity contrasts associated with the subducting South American Plate and Austermann et al., 2013, show that, when this complex structure is taken into account, then fitting the Barbados data requires an additional 10 m eustatic meltwater equivalent of ice added to the model.

An important focus for 3-D modelling has been in Antarctica (e.g. A et al., 2013, van der Wal et al., 2015; Gomez et al., 2018; Nield et al., 2018), where it is necessary to properly model the GIA in the region both for reconstructing the ice sheet in the past, and for estimating its mass loss in the present. For example, A et al., 2013, consider the effects of a 3-D model and 1-D models based on global or local averages (as in Paulson et al., 2005), and find that even with a 1-D model that is derived from the local structure of Antarctica, there is still up to nearly a 50% mismatch in predicted vertical rates at GPS stations in West Antarctica. The study of van der Wal et al., 2015 actually incorporates a composite rheology into a 3-D Earth model, so that different regions in the mantle may exhibit either linear or power-law creep. They investigated the effects of this lateral structure in determining corrections to GRACE data to determine present-day mass loss of the ice sheet, and found that the 3-D effects were significant, with estimates outside the bounds of what had been found previously using 1-D modelling. Finally, Nield et al., 2018 investigate the effects of lateral lithosphere structure in Antarctica, and consider both a variable thickness elastic lithosphere, and a lithosphere with a power-law rheology (similar to Chapter 2, except that our profile was 1-D and the GIA model was Maxwell). Their focus was on modelling present-day uplift rates in particular, and demonstrated that both the elastic and ductile lithosphere with lateral structure resulted in significant uplift rate gradients relative to 1-D models with an average thickness, and suggest that neglecting this lateral structure may be why previous 1-D modelling attempts were not able to fit the GPS observations.

5.2 Research Summary and Conclusions

To goal of this research is, first of all, to determine why the Atlantic and Gulf coast RSL data require the high viscosities found in Chapter 3 and in Love et al., 2016, and secondly to determine whether a model with a depth-average viscosity structure more in line with previous global analyses and the Hudson Bay decay times (as in Chapter 4), but that incorporates lateral viscous structure, can also satisfy the RSL data. To do this, we use both a 1-D and 3-D model. In the first part of the analysis, we generate RSL curves and Earth vertical displacement contour plots for different 1-D viscosity structures. By decomposing the total RSL signal into components that come from the ice, ocean, and sediment load, we demonstrate that the largest change among the models is in the response to the ice load (and in particular, the response of the solid Earth to the ice load). This suggests that the RSL data are primarily constraining the geometry of the peripheral bulge of the ice sheet. With the relative displacement contour plots, we show that the effect of increasing the viscosity in the model is to effectively reduce the overall peak magnitude and rate of deformation of the peripheral bulge. Following this, we once again create RSL curves and vertical displacement figures, but for a 3-D GIA model, where we consider lateral structure constructed from three different seismic shear wave velocity profiles, as well as three different reference 1-D Earth models. We show that, when lateral structure is incorporated into a model with 1-D structure that satisfies the Hudson Bay and global constraints, the fit to the Gulf coast data is significantly improved, as is the fit to most of the Atlantic coast data. We also show that it is consistently the case that incorporating lateral structure tends to suppress the magnitude of the peripheral bulge, consistent with an increase in viscosity in the region. We do therefore show, as has been inferred in previous studies (but not demonstrated), that lateral structure can be used to improve the GIA model along the Atlantic and Gulf coasts. However, there are also considerable differences among the model predictions for the three different shear wave profiles used, which is an indication of the uncertainty in this model input.

5.3 Article 4: The Impact of Lateral Viscous Structure on GIA Predictions for the US Atlantic and Gulf Coasts

Statement of Contribution

The following manuscript is my own written work, carried out under the supervision of Dr. Milne. I ran the 1-D models, and was provided the output from the 3-D model for that part of the analysis. I produced all figures, and performed the majority of the analysis. The 3-D GIA code was developed by Konstantin Latychev.

The importance of lateral Earth structure for North American Glacial Isostatic Adjustment

Joseph Kuchar[1,*], Glenn Milne[2], Konstantin Latychev[3]

1. Department of Physics, University of Ottawa
2. Department of Earth and Environmental Science, University of Ottawa
3. Department of Earth and Planetary Science, Harvard

* Corresponding author, joseph.kuchar@gmail.com

Abstract

The isostatic response of the Earth to past mass exchange between ice sheets and oceans, so-called glacial isostatic adjustment (GIA), is a dominant geodynamic process in North America. Modelling GIA observables provides one of the few direct methods for estimating deep Earth viscosity structure. We investigate here the requirement for anomalously high mantle viscosities to fit the relative sea level (RSL) data along the Atlantic and Gulf coasts of North America found in recent GIA studies. We demonstrate that this requirement is a constraint primarily on the geometry and evolution of the peripheral bulge of the Laurentide ice sheet. We show that a 3D Earth model with a global average viscosity in the upper mantle of 0.3×10^{21} Pa s and 3×10^{22} Pa s in the lower mantle, which is consistent with both the Richmond Gulf (Hudson Bay) relaxation time and several recent global analyses, is able to produce a much improved fit to the Gulf and Atlantic coast RSL data relative to the 1D Earth model results when no lateral structure is applied. These are the first results to demonstrate that realistic realisations of lateral structure can explain the different viscosity inferences obtained using 1D GIA models and data from different regions of North America. A necessary caveat is that there are significant differences among the computed RSL curves corresponding to the three different realisations of lateral structure considered here, demonstrating significant uncertainty associated with this model input.

1. Introduction

The growth and ablation of continental ice sheets over the late Pleistocene resulted in large volumes of water transported between land and ocean, as well as large scale deformation of the solid Earth. The redistribution of mass within the Earth in response to this climate-induced forcing is termed glacial isostatic adjustment (GIA). Models of GIA require a description of the viscoelastic structure of the Earth, as well as a prescribed ice loading history, both of which involve some degree of uncertainty. The output from models of GIA is used in many applications, for example, correcting tide gauge records for isostatic effects (Davis and Mitrovica, 1996; King *et al.*, 2012), correcting gravity data from GRACE to estimate present-day mass exchanges between the oceans and ice sheets (Wu *et* al., 2010; Velicogna and Wahr, 2013), and making regional sea level predictions for the future (Slangen *et al*., 2012; Love *et al.*, 2016), and so it is important to be able to accurately constrain the model inputs. The rheological properties of the Earth are often found by comparing model output to historical sea level records (e.g. Lambeck *et al., 1998;* Peltier *et al.*, 2002; Milne and Peros, 2013; Lambeck *et al.*, 2014; Roy and Peltier, 2015; Love *et al.*, 2016; Caron *et al.*, 2017), but the inferred parameters often depend on the assumed ice history and the quality and distribution of the data, as well as errors associated with fundamental model limitations. The impact of the ice sheet uncertainty can be minimized in certain situations: for example, regions formerly at the centre of glaciated regions are known to have an exponential-type decay to their uplift response with a decay constant governed primarily by the Earth rheology (Mitrovica and Forte, 1997; Mitrovica *et al.*, 2000); pairs of sites geographically near each other but far from previously glaciated areas will also record differential sea level that will be more sensitive to Earth structure than to changes in the global ice history (Nakada and Lambeck, 1989).

The vast majority of GIA studies to date have been conducted assuming the Earth is a spherically symmetric Maxwell body, so that its viscosity structure varies only with depth. However, depending on the study area and the assumed ice geometry, very different inferences of the viscosity of the mantle have been obtained. Our focus here is on the North American continent and in particular the Eastern part of the continent. In a recent study investigating the effects of sediment isostatic adjustment in the Gulf of Mexico (Kuchar *et al.*, 2018), the authors determined that relatively high viscosities were required to fit the relative sea-level (RSL) data in the region, with a best-fitting model defined by an upper mantle viscosity (UMV) of 5×10^{21} Pa s and a lower mantle viscosity (LMV) of 5×10^{22} Pa s. This is consistent with the work of Love *et al.* (2016), who computed RSL for a large suite of reconstructions of the North American Ice Sheet (NAIS) to provide future sea-level predictions for the US Gulf coast and the Atlantic coast of North America. In particular, Love *et al.* found that the Atlantic coast data preferred an upper mantle viscosity of 3×10^{21} Pa s and a lower mantle viscosity of 3×10^{22} Pa s, and determined that the Gulf coast data preferred the same viscous structure as was found in Kuchar *et al.* (2018). In both of these studies, the preference of the RSL data for high viscosity values was evident regardless of the ice history applied (4 were used in Kuchar *et al*. (2018) and 35 in Love *et al*. (2016)). In a recent analysis of mid-Atlantic coast RSL data from Marine Isotope Stage 3 and older, Pico *et al*. (2017) considered several viscosity models and found that the data they considered is consistent with a range of values, including relatively high viscosities that are compatible with those inferred by Kuchar *et al.* and Love *et al.* (see Supplementary Figure 5 in Pico *et al.*, 2017).

These viscosity inferences along the Atlantic and Gulf coasts are in contrast with what has been typically found to satisfy near-field RSL data, Canadian postglacial decay times, or even global average viscosity models, which have required lower viscosities. For example, a recent publication by Lambeck *et al.* (2017), detailing the development of the North American component to the ANU global ice history, describes a joint inversion for ice history and Earth rheology (lithosphere thickness and mantle viscosities), where they found that their optimal model included a UMV of $(3.5 – 7.5) \times 10^{20}$ Pa s and an LMV of $(0.8 – 2.8) \times 10^{22}$ Pa s. In the study of Lau *et al.* (2015), postglacial decay times from Hudson Bay and Scandinavia were used, along with other GIA observables, to constrain the radial viscosity structure of a 1D average Earth. They determined a mean value of 0.3×10^{21} Pa s for the UMV, and found that the viscosity in the top 1500 km of the mantle is constrained to be around 10^{21} Pa s, which requires that the shallow lower mantle must be more viscous than the upper mantle to obtain the required average, and finally that the viscosity in the deep mantle must increase to the range of $10^{22} – 10^{23}$ Pa s.

Other recent estimates for global average viscosity values for a 1D Maxwell Earth have been obtained by Lambeck *et al.* (2014), and Caron *et al.* (2017), both of whom performed a joint inversion for a global ice history and Earth viscosity parameterization by seeking to minimize the misfit with global RSL data. Lambeck *et al.* constrain the UMV to $(0.1 - 0.2)x10^{21}$ Pa s, and the LMV to two possible solutions, a low viscosity solution of $(0.7 – 4.0)x10^{21}$ Pa s and a high viscosity solution of $(0.1 – 2.0)x10^{23}$ Pa s. Caron *et al.* performed their inversions by applying scaling parameters to the major ice sheets starting from the ICE5G or ANU (Lambeck *et al.* 2014) global ice histories, and obtained different global viscosity solutions in each case. When using the ANU starting ice history, their solution is for a UMV of $(0.3 – 1.7)x10^{21}$ Pa s and a LMV of $(0.24 – 57)x10^{22}$ Pa s. With the ICE5G starting ice history, their solution for a UMV was similar with $(0.3 – 3.6)x10^{21}$ Pa s, and the LMV was not well constrained, with a given range of $(7.3x10^{20} – 4.6x10^{23})$ Pa s. Considering the studies of Lau *et al*., Lambeck *et al*., and Caron *et al.*, it is likely that the average viscosity of the upper mantle is on the order of 10^{20} Pa s, and the viscosity of the lower mantle is not at all well constrained, except that it is likely considerably more viscous than the upper mantle. Notably, these viscosities (of the upper mantle in particular) are in sharp contrast to the Kuchar *et al.* and Love *et al*. values found for the Atlantic and Gulf coast RSL data.

Difficulties in fitting the Atlantic coast data with 1D spherically symmetric GIA models were also noted by Engelhart *et al.* (2011), who suggested this was evidence for lateral viscosity variations impacting GIA along the Atlantic Coast. This issue was revisited in Roy and Peltier (2015), where several 1D viscosity models were tested along with the ICE6G_C ice history. They concluded that, while the VM6 viscosity model they employed was an improvement over the previous iterations employed in the Engelhart *et al*. (2011) study, that persistent misfits still existed (for example, along the Northern US Atlantic coast), which the authors attributed to potential influence of lateral viscous structure. In the previously mentioned study of Love *et al.*, a test with a 3D model was conducted, and they determined that considerable differences between 3D and 1D model predictions exist, particularly for the northern Atlantic coast sites, and thus divided their study area into three regions to account for this in their 1D analysis.

A number of studies have demonstrated the importance of lateral viscosity structure in North America on GIA (e.g. Paulson *et al*., 2005, 2007; Davis *et al.*, 2008; Wang *et al.*, 2008; Wu *et al.*, 2013). Paulson *et* *al*. (2005) showed that while a 1D average Earth model could reasonably well reproduce the results of a 3D model for computing Hudson Bay decay times, the same was not true for the Atlantic coast RSL, with all three 1D models considered (constructed with weighted averages of the 3D viscosity structure) producing a misfit of at least 30% with the 3D model predictions. A key aspect of any 3D analysis is the method used to define lateral structure within the GIA model. In the majority of 3D studies, the lateral viscosity perturbations are based on seismic inferences of velocity variations. The conversion of velocity structure to viscosity structure is non-trivial and prone to significant uncertainty (e.g. Ivins and Sammis, 1995; Wu *et al*., 2013). One important source of uncertainty is that associated with the input seismic velocity model (e.g. Milne *et al*., 2018). Another is the relative influence of temperature versus compositional and structural influences on viscosity. Previous studies have attempted to quantify the relative importance of these effects in different regions of the mantle based on modelling GIA observables (Wang *et al*., 2008; Wu *et al*., 2013; Li *et al*., 2018).

The majority of previous 3D GIA modelling studies have focused on sensitivity tests to quantify the significance of lateral structure for modelling-based inferences of viscosity structure or ice history. There has been a lack of analyses aimed at determining whether the additional of lateral structure can explain regional variability in viscosity inferred from 1D GIA modelling. One recent paper with this focus (Li *et al*., 2018), searched for a 3D model that could best satisfy global RSL data as well as rates of change of gravity and vertical uplift in Laurentia and Fennoscandia. Their global ice history was given by ICE6G_C (Peltier *et al*., 2015), and lateral structure obtained by scaling background 1D viscosity models with a given seismic velocity model to obtain viscosity variations. As noted above, they also considered a scaling constant β that reflects the relative importance of temperature versus compositional and structural controls on lateral viscosity variations. While they were not able to find a model that could satisfy the Fennoscandian gravity and uplift rate observations, they were able to satisfy those in Laurentia with a background UMV of around 0.3×10^{21} Pa s.

Our goal here is to investigate why the RSL data along the Atlantic and Gulf coasts require such high viscosity values, and whether it is an indication that lateral structure is required to accurately model GIA along these coasts. To do this, we first consider output from a 1D GIA model, and decompose predicted RSL curves at a selection of sites into components from the ice and ocean loads to determine which component dominates and the sensitivity of each to viscosity structure. Additionally, we compute vertical land motion and show that the RSL data ultimately constrain the evolution of the peripheral bulge and it is this feature that requires the high viscosity values. Finally, we use the 3D GIA model developed by Latychev *et al.* (2005) to compute Earth deformation and RSL on the Atlantic and Gulf coasts for different lateral viscosity profiles to determine whether different estimates of lateral structure can accommodate the RSL observations without the need for high depth-average viscosities (as is required by the 1D GIA models). Indeed, the availability of high quality RSL data and the existing evidence for lateral structure in this region makes it an ideal testing ground for 3D GIA models.

2. Methodology

A GIA model has three components: a specified ice surface loading history to force the model; an Earth model to compute surface deformation and perturbation to the geopotential; and a sea level model that solves the sea level equation to determine how sea level will change in response to a change in the ice load history. We apply both a 1-dimensional and 3-dimensional Earth model in this study.

We use the same input ice history for both the 1D and 3D model, which has a background global history given by ICE5G (Peltier, 2004) and a North American component given by model 9894 from the reconstructions of Tarasov *et al.* (2012). This particular reconstruction which was found by Love *et al.* (2016) to give the best fit (among the reconstructions of Tarasov *et al.*) to the Atlantic coast sea level data.

The 1D Earth model is a spherically symmetric Maxwell model with an elastic and density structure given by PREM (Dziewonski and Anderson, 1981). Its viscosity structure is parameterised by a very high viscosity lithosphere (so that it behaves functionally as elastic), an upper mantle that extends from the base of the lithosphere to the 670 km seismic discontinuity, and a lower mantle that extends from 670 km depth to the core-mantle boundary. We solve the generalised sea level equation (Kendall *et al.*, 2005; Mitrovica and Milne, 2003), which accounts for time-varying shorelines and perturbations to the Earth's rotation vector.

The 3D model we apply was originally presented in Latychev *et al.* (2005), and it computes GIA for a 3D Maxwell viscoelastic Earth that is elastically compressible and self-gravitating. It includes rotation and solves the generalised sea level equation. The 3D model results are compared with those of a 1D reference model to gauge the impact of including lateral structure.

The viscosity structure is significantly more complex than in the 1D models, as the viscosity will vary both with depth and laterally. The viscosity structure is scaled from a reference 1D model by a shear wave velocity profile (Latychev et al., 2005; Austermann et al., 2013), as described in equations (1) to (3).

$$\delta \ln \rho(r,\theta,\varphi) = \frac{\partial \ln \rho}{\partial \ln v_s}(r)\delta \ln v_s(r,\theta,\varphi) \tag{1}$$

$$\delta \mathrm{T}(r,\theta,\varphi) = -\frac{1}{\alpha(r)}\delta \ln \rho(r,\theta,\varphi) \tag{2}$$

$$\delta \ln \eta(r,\theta,\varphi) = \eta_0(r)e^{-\epsilon\delta \mathrm{T}(r,\theta,\varphi)} \tag{3}$$

In the equations above, a seismic shear wave velocity model $\delta \ln v_s$ is scaled by a density-to-shear wave velocity profile with depth, $\frac{\partial \ln \rho}{\partial \ln v_s}(r)$, to obtain 3-D variations in density. We adopt the profile of Forte and Woodward (1997) for the density-to-shear wave velocity scaling which accounts for both anharmonic and elastic effects (Karato, 1993). The computed density variations are then scaled by variations with depth in the coefficient of thermal expansion, $\alpha(r)$, to obtain variations in temperature (equation (2)). We use the profile of Chopelas and Boehler (1992) for $\alpha(r)$. The variations in temperature are then used to compute variations in viscosity from a 1D reference viscosity profile, η_0, by assuming an exponential scaling between temperature and viscosity, with a scaling constant $\epsilon=0.04\ °C^{-1}$. This value for the scaling parameter gives viscosity variations of ~5 orders of magnitude over our study area (Figure 1) at most depths. A further requirement is that the global mean value of the viscosity at any depth will be equal to the reference viscosity at that depth.

A key input to a given 3D viscosity profile is the spatial variation in shear wave velocity. We apply three seismic tomography models to add lateral viscosity structure to a given reference 1D viscosity model using the above equations. These seismic velocity models are S40RTS (Ritsema *et al.,* 2011), SEMUCB-WM1 (French and Romanowicz, 2014), and Savani (Auer *et al.*, 2014). These models represent results of different modelling approaches as well as constraints from different sets of seismic data. These same models were recently applied by Milne *et al.* (2018), and so we refer the reader there and to the original articles for further details. By considering three seismic models instead of only one we probe the effects of different plausible viscosity scenarios and their effects on GIA model output.

In Figure 1 we show viscosity variations at 200 km, 600 km, and 1000 km depth (corresponding to shallow upper mantle, deep upper mantle, and shallow lower mantle) for our three chosen seismic velocity models. With these seismic models the viscosity in the shallow upper mantle is consistently close (less than an order of magnitude greater, in general) to the reference viscosity along the Atlantic coast, with a significant increase in viscosity in the northern part of the interior of the continent underlaying the formerly glaciated region. In comparison, the deep upper mantle has considerably greater spatial variability (for each model and among the models), but it is generally true that at this depth the viscosity in the north under the ice sheet is typically lower than the reference viscosity, significantly so in the case of Savani and moderately in the case of S40RTS and SEMUCB. At this depth there is also generally a reduction in viscosity along the Atlantic coast, with the Gulf Coast showing a gradient from west to east in viscosity from more viscous to less viscous. In the shallow lower mantle much of the Atlantic coast is generally at higher viscosities than the background reference model, though underneath the ice sheet there is significant variability and regions of both higher and lower viscosities. It does seem that much of the region between the centre of the load and the RSL data sites is at relatively high viscosities, however, which is important in governing the evolution of a peripheral bulge. Sensitivity of modelled uplift rates to lateral viscosity perturbations at different depths and angular distances was investigated by Paulson *et al*. (2005), where it was shown that while for large angular distances (around 40 to 50 degrees) the uplift rates were mainly sensitive to the structure beneath the load and in the observation region, for more moderate angular distances of 10 to 30 degrees (which is the range for our observational data), the uplift was also sensitive to structure in the region between the load and observation point. This is also shown in Wu (2006), who computed sensitivity kernels of RSL observables for laterally heterogenous Earth models and showed that RSL and present-day radial velocities are sensitive to the structure between the load and observation point.

In addition to mantle structure, the 3D model also has laterally varying lithosphere thickness. We incorporate the global elastic lithosphere thickness model of Zhong *et al.* (2003).

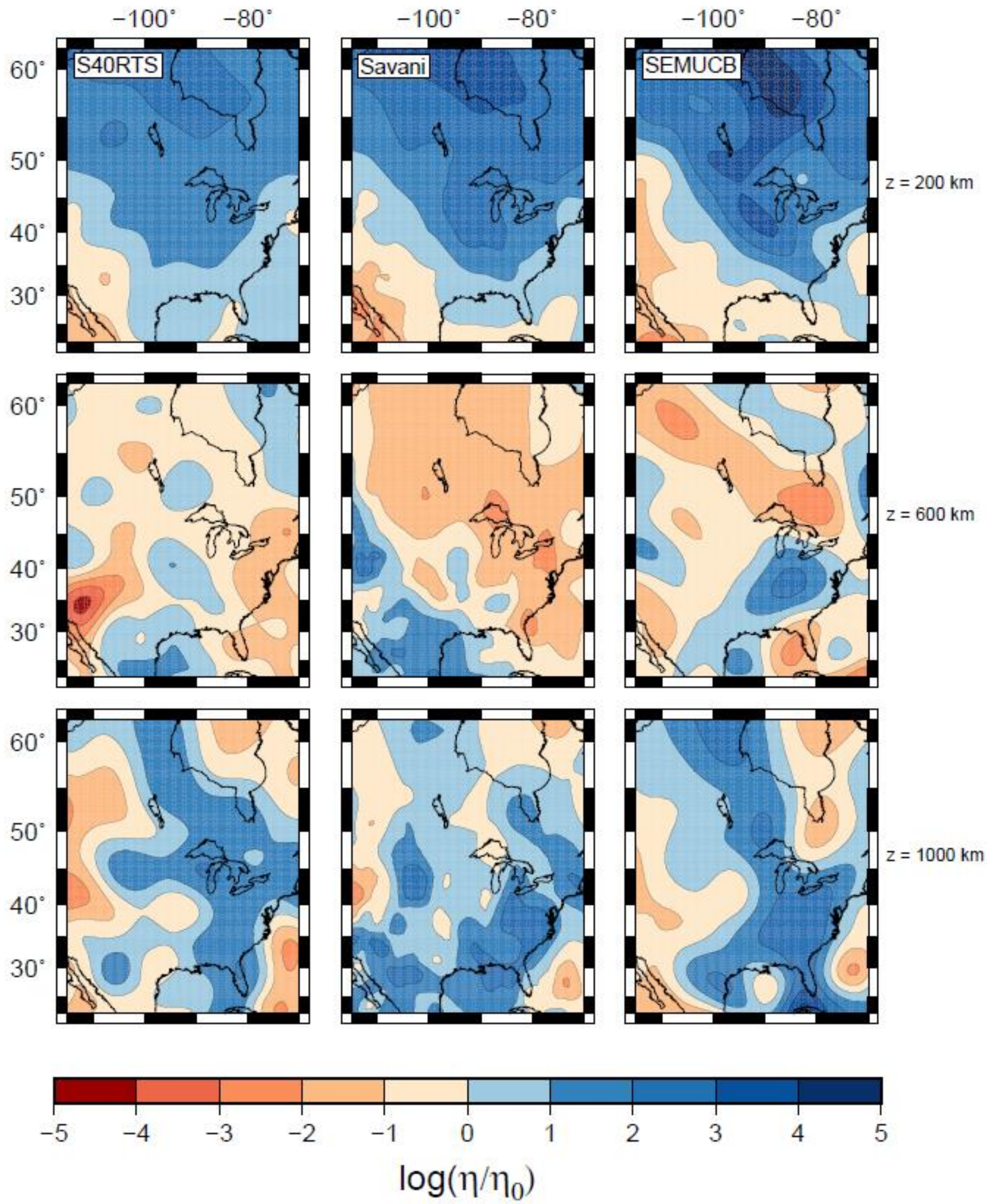
S40RTS
Savani
SEMUCB
−100°
−80°
60°
50°
40°
30°
z = 200 km
z = 600 km
z = 1000 km
−5
−4
−3
−2
−1
0
1
2
3
4
5
log(η/η0)

Figure 1: Viscosity variations with respect to a 1D reference model at a depth of 200 km (top row), 600 km (middle row), and 1000 km (bottom row) for the S40RTS (left column), Savani (middle column), and SEMUCB-WM1 (right column) seismic velocity models.

3. **Results and Discussion**

3.1 1-D Earth Model

In Figure 2 we show our chosen selection of RSL data sites along the US Gulf and Atlantic coasts which is a subset of those featured in Kuchar *et al.* (2018) and Love *et al*. (2016). These were chosen to sample the RSL response along these coasts while also staying a comfortable distance from the ice margin.

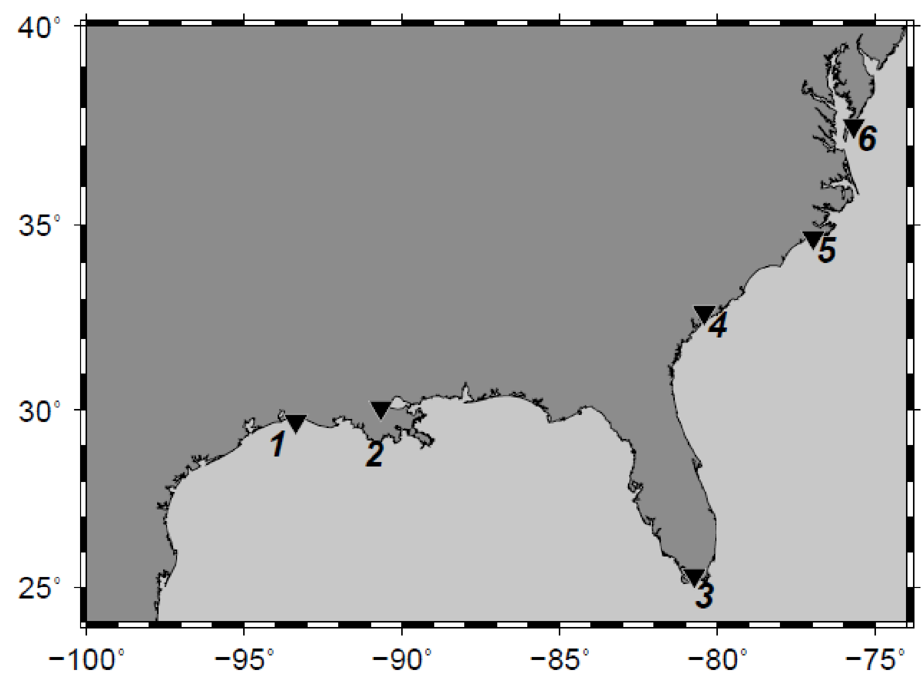

Figure 2: Chosen locations to compute RSL: 1. West Louisiana, 2. East Mississippi Delta, 3. South Florida, 4. South South Carolina, 5. South North Carolina, 6. East Shore.

In Figure 3 we show RSL as computed using a 1D Earth model as well as the contributions from the individual loading components (that is, the ice and ocean loads). Note that the contributions shown do not include the eustatic sea level component nor rotation, and so the sum of the component curves will not give the total RSL curve also shown in the figures. All results shown in this section include a 71 km lithosphere, and we denote UMV, LMV pairs in brackets with reference to a standard viscosity of 10^{21} Pa s, so that for example (0.5, 10) refers to a model with a UMV of $0.5x10^{21}$ Pa s and an LMV of $1x10^{22}$ Pa s. In Figure 3 we show the RSL for an Earth model with a (5, 50) viscosity structure (which was found in Kuchar *et al.* (2018) to be a good fit to the US Gulf coast data) with solid curves, and the (0.5, 10) viscosity structure with dashed curves. For the (5, 50) structure, the total RSL signal at all sites is dominated by the eustatic component in the early Holocene. The contribution from the ocean load is consistently positive and decreasing, while that from the ice load transitions from positive and decreasing in the early Holocene to negative and increasing towards the late Holocene. This behaviour is consistent with first the development of a peripheral bulge, which has the effect of positive vertical land motion and a sea-level fall, and then subsequent collapse of the bulge, leading to a sea level rise. We note that, after around 6 ka, the total RSL is very close to that of the ice response, indicating that it is the ice load that dominates during this time frame.

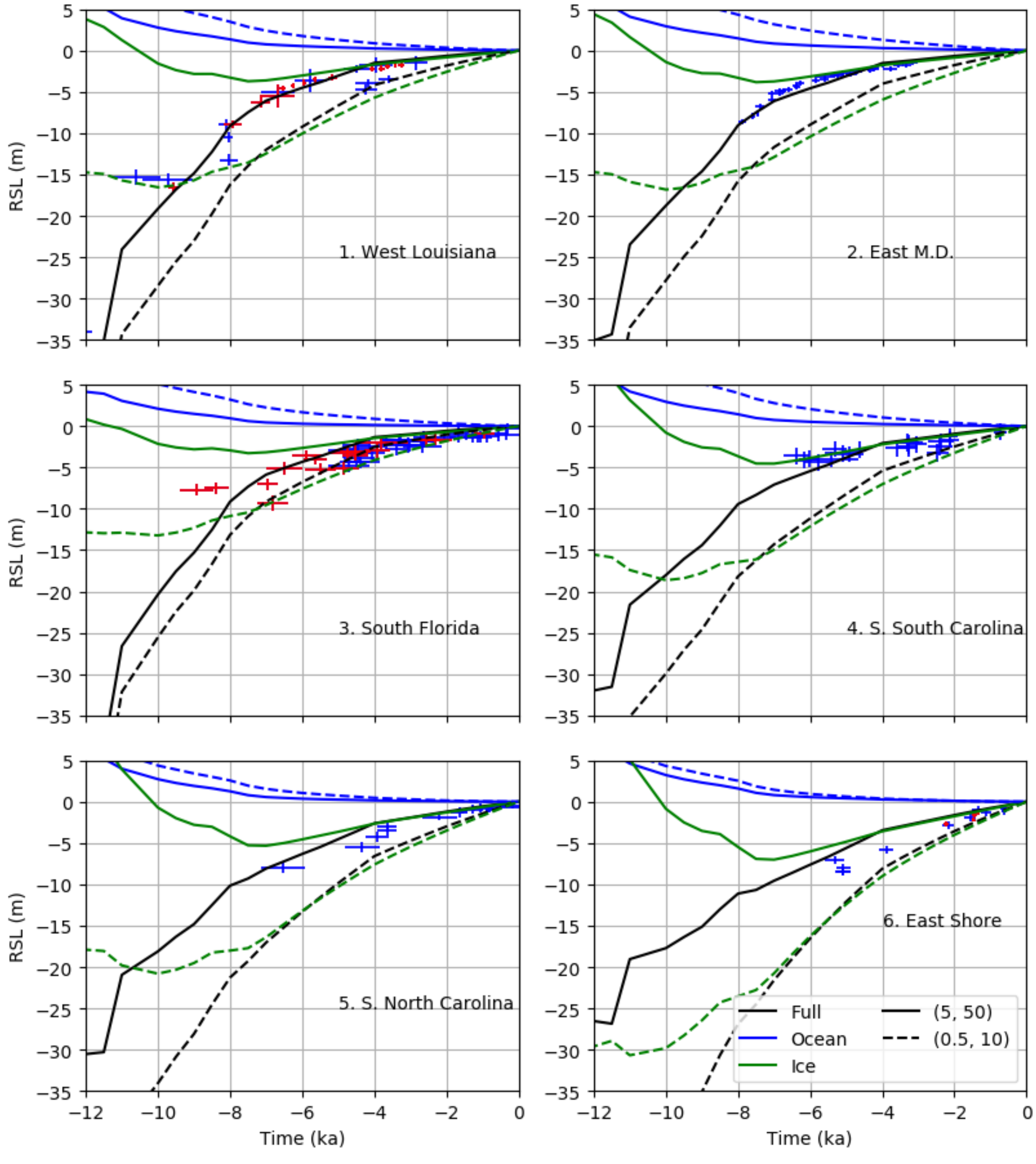

Figure 3. RSL at selected sites for a 71km lithosphere, and the (5, 50) (solid) and (0.5, 10) (dashed) mantle viscosity structures. The black curve is the full computed RSL signal including rotation and

eustatic effects, and the blue and green curves are contributions from the ocean and ice loads. Data that are compaction-free are shown in blue. Since these model results do not include sediment isostatic adjustment, we have corrected the RSL data from West Louisiana and East Mississippi Delta for this effect (Love et al, 2017; Kuchar et al., 2018).

When the UMV and LMV values are reduced to (0.5, 10), the largest sensitivity to the applied change in Earth viscosity structure comes from the ice load response. The ice load response is consistently negative and increasing over the Holocene, indicating that with this lower viscosity the peripheral bulge reached it its maximum height and began its subsequent collapse sooner. The response to the ocean load is fairly similar to that of the (5, 50) model, though the RSL fall is steeper, indicating more displacement of the solid surface due to the ocean load for lower viscosities. Since the largest difference between the RSL curves of the two viscosity models considered is due to the ice load, we conclude that it is this response component and its influence on the peripheral bulge that is most constrained by the data. We considered other viscosity models and found that this conclusion remained valid in all cases where there is significant difference between UMV and LMV values.

The RSL response to the ice load can be separated into two components: its direct gravitational effect on the geopotential surface governing sea-surface height changes and the induced solid Earth deformation which affects RSL through vertical motion of the ocean floor and perturbing the geopotential via mass distribution of the solid Earth. Because the ice history has not changed, the direct gravitational effect of the ice will be the same. This means that the sensitivity to the ice load shown in Fig. 3 is due to the induced Earth deformation. Effectively, the RSL data are constraining the geometry of the peripheral bulge (relative to its present-day geometry).

To determine bulge geometry, we plot computed relative vertical height of the solid Earth surface over our study area in Figure 4. We show the relative height of this surface from 10 ka relative to present, so that areas with positive values will subside over time to reach the present-day geometry, and areas with negative values will uplift. The higher viscosity (5, 50) model in Figure 4 shows that from 10ka to present most sites in our study area will subside 0-10m, leading to a subsidence rate of order 0-1 m/ka. The lower viscosity (0.5, 10) model, on the other hand, shows relative displacements from 20 to 50+ metres, leading to subsidence rates exceeding 5 m/ka. In Figure S1 we show the computed total vertical displacement (since the initiation of the model run at 120 ka) at 10 ka to illustrate the spatial extent and amplitude of the modelled peripheral bulge. While this is not relevant to RSL since these data are referenced to present time, it provides some insight regarding the influence of viscosity structure on bulge geometry and amplitude. The results in Figure S1 show that the lower viscosity models result in a bulge with greater amplitude but also considerably broader extent in directions away from the ice loading. Thus, increasing viscosity values acts to both suppress deformation rates and reduce the overall extent of the peripheral bulge. In addition to determining the magnitude of the bulge, the pattern of the uplift is also sensitive to the viscosity structure. As the UMV increases, the hingeline of the bulge is pushed further south, and when the UMV is increased from (0.5, 10) to (5, 10), a gradient of increasing relative displacements from North to South develops, which is in contrast to the transition from (0.5, 10) to (0.5, 50), which instead results in an enhanced decrease in the relative uplift from North to South. As indicated above, the RSL data prefer high viscosity values, and Figures 5 and S1 demonstrate that this is due to a preference for diminished peripheral bulge effects. The question we address in the following section is whether a similar effect can be produced by the addition of lateral structure to a 1D viscosity profile that is consistent with past inferences.

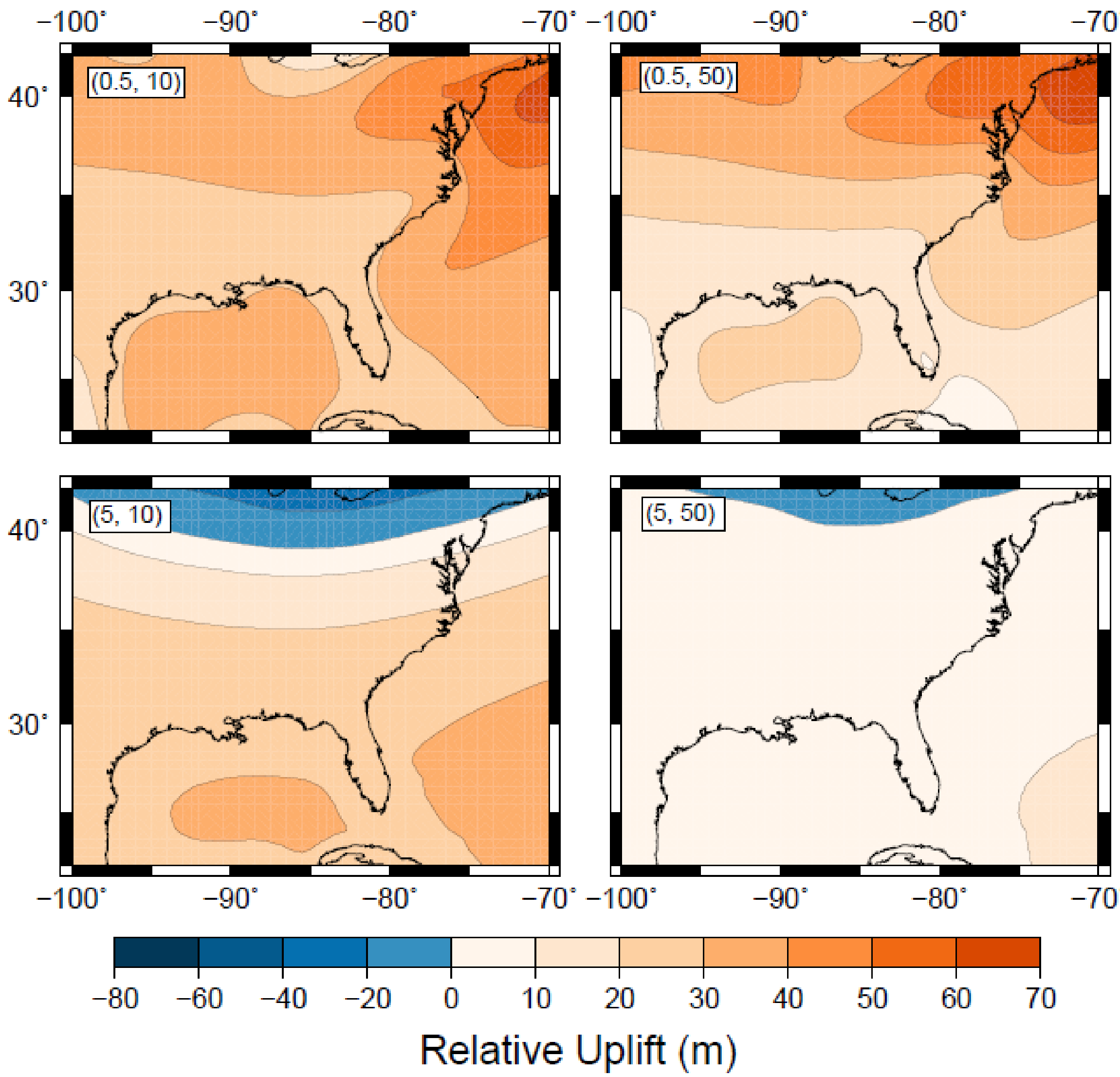

Figure 4: Modelled height of the solid Earth at 10ka relative to that at present. The number pairs in each frame define the UMV and LMV values (UMV, LMV). The lithosphere thickness is 71 km in all cases. The upper mantle viscosity increases from the first row to the second row, while the LMV increases from the left column to the right.

3.2 3D Earth Model Results

To investigate the effects of lateral structure on the dynamics of the peripheral bulge we have computed RSL and relative uplift for 3D Earth models with viscosity structure generated from three 1D reference viscosity models and three different seismic velocity models (see section 2.2). The three reference 1-D Earth models all have a 71km lithosphere, and (0.3, 30), (0.3, 3), and (1, 30) sub-lithosphere mantle viscosity structures. In the main text we will show only the (0.3, 30) model results, as this is a 1D viscosity structure consistent with the Hudson Bay decay time constraints (Lau *et al*., 2016) and the viscosity constraints for a 1D average Earth determined by Lau *et al.* (2016). It is also broadly compatible with the North American near-field viscosity inference of Lambeck *et al*. (2017) and the global analyses described in the Introduction (Lambeck *et al*., 2014; Caron *et al.*, 2017). This UMV value is also consistent with what was found by Li *et al.* (2018) to satisfy gravity and uplift rates in Laurentia as a background viscosity to their 3D model, though their LMV is that of VM5a (Peltier and Drummond, 2008) and so is an order of magnitude lower. We present the results for the other models in the supplementary material (though they will also be discussed here). In fact, before we discuss the impact lateral structure has on the Atlantic coast, it is appropriate to determine whether the Richmond Gulf decay time constraint (the RSL data at this location provide the most precise decay time in Hudson Bay) is satisfied when lateral structure is included. Mitrovica *et al*. (2000) report that the Richmond Gulf decay time (corrected for eustatic meltwater changes) is in the range 4 – 6.6 ka. We have computed RSL curves at Richmond Gulf for these models, and fit them to an exponential of the form

$$RSL(t) = A\left(e^{\frac{t}{\tau}} - 1\right),$$

using the Scientific Python *curvefit* routine (Jones *et al.*, 2001-). The estimated decay times are shown in Table 1. Of the three realisations of lateral structure considered, two of them (Savani and SEMUCB) satisfy the Richmond Gulf constraint. In all cases, adding lateral structure increases the computed decay time. This reflects the lateral structure imposed beneath Hudson Bay which is generally an increase in viscosity at most depths (Figure 1). We now go on to consider whether these realisations of lateral structure can fit RSL data along the US Atlantic and Gulf coasts.

Model	Decay Time (ka)
S40RTS	7.1
Savani	5.1
SEMUCB	6.3
Reference (1D)	5.1

Table 1: Computed decay times for models run with a (0.3, 30) reference viscosity and lateral structure derived from the three seismic models considered. The decay time range accepted by the Richmond Gulf data is 4 – 6.6 ka (Mitrovica et al., 2000).

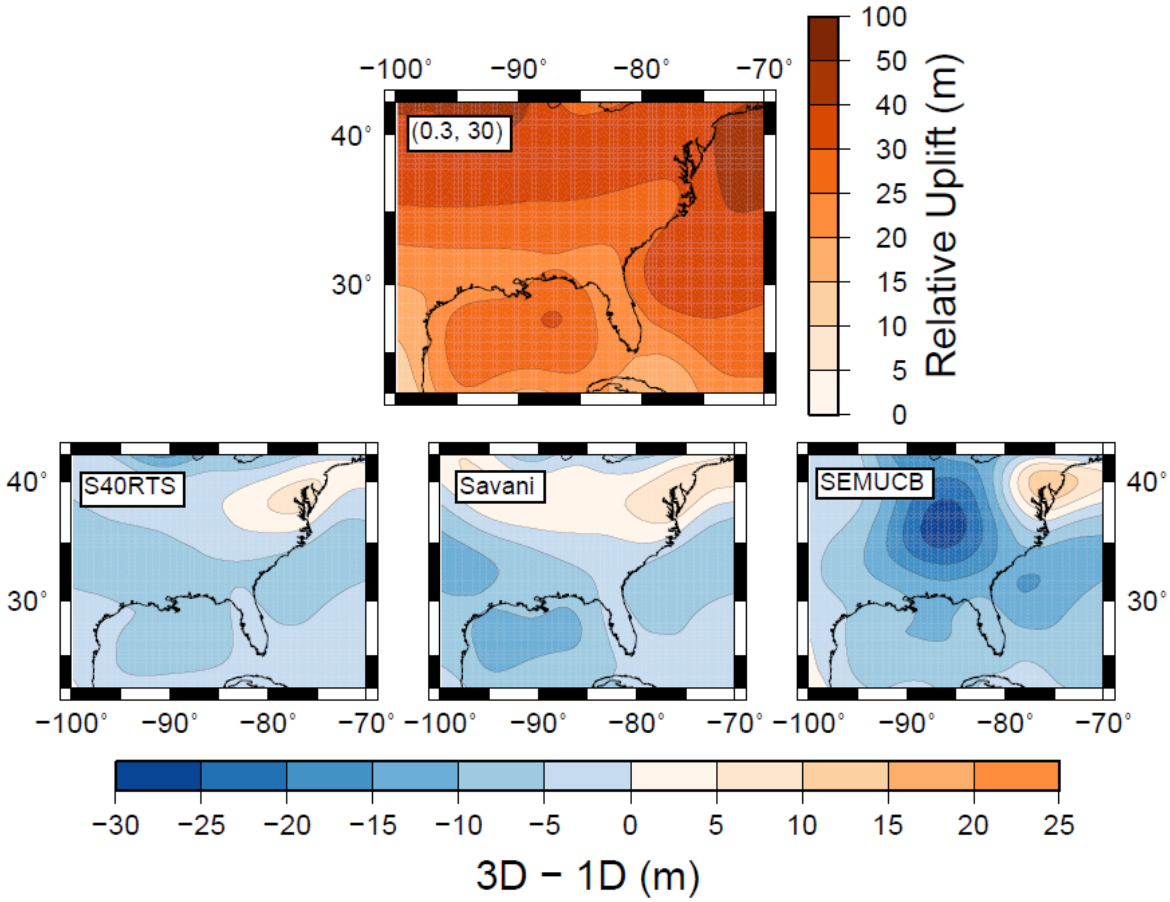

Figure 5: Relative vertical displacement for the (0.3, 30) 1D reference viscosity model (top), and differences in this displacement field (3D-1D) when lateral structure is added (bottom).

In Figure 5 we show the height of the solid surface at 10ka relative to present for the (0.3, 30) reference model and the deviations to this output due to the addition of lateral structure (that is, 3D model results minus the 1D results). In this section, all reference model results are computed with the same 3D GIA model as the Earth models that contain lateral structure. The reference model is characterised by high relative displacements (>30m) along the Northern part of the Atlantic Coast, and 20-30m along the southern coast. Since the 3D model results show differences with respect to the reference, negative values indicate that the relative displacement of the 3D model is less than that of the reference model. For all three of the seismic velocity models shown we see that the 3D structure leads to suppression of the deformation relative to the reference model (though not enough to reproduce the low deformation of the high viscosity 1D model in Figure 4), particularly along the Gulf Coast. In fact, along the northern Atlantic coast all three seismic models lead to an increase in the uplift relative to the reference model. The pattern of the deformation is clearly sensitive to the assigned lateral viscous structure, as the three seismic models lead to very different deformation patterns. The greatest amount of bulge suppression is for the SEMUCB model, which features a reduction of the relative uplift by nearly 30 metres in the interior of the continent. Referring to the viscosity slices in Figure 5, it is evident that this region of reduced bulge displacement coincides with a region of consistently high viscosity through all three depth slices. Similarly, the Savani results show a region of large negative values corresponding to reduced relative displacement along the west coast of the Gulf of Mexico, which is consistent with high viscosities for this seismic model in that region.

To determine the relative importance of lateral structure in the upper versus lower mantle on the results in Figure 5, in Figure S2 we show relative displacement differences for the same (0.3, 30) reference model with the S40RTS lateral structure, but where lateral structure is confined to only the upper mantle or only the lower mantle. What is evident from this test is that when the 3D structure is restricted to the upper mantle only, the computed deformation is fairly similar to the model results featuring full lateral structure (that is, ‘S40RTS’ in Figure 5). In contrast, when the lateral structure is confined to the lower mantle only, the deformation is more similar to that of the reference case. Thus giving the counter-intuitive result for this particular loading history and reference viscosity model, that upper mantle structure has the dominant role in suppressing bulge dynamics. This is consistent with the analysis of the Atlantic coast RSL data of Engelhart *et al.* (2011), who concluded the sensitivity of the data to the UMV suggested evidence for the importance of lateral structure at that depth. The particular reference model we are using also features a strong viscosity gradient from the upper to lower mantle, which has the effect of focusing deformation in the upper mantle.

In Figure 6 we show RSL curves for the (0.3, 30) reference case and its associated 3D models. For all sites except the most northern one (East Shore), including lateral viscous structure has the effect of pushing the RSL curve to higher (less negative) values, which is what we would expect for higher viscosities based on our 1D results (e.g., Figures 3 and 4). All three seismic models lead to a remarkably improved fit for the Mississippi Delta sites in particular (West Louisiana and East Mississippi Delta). This supports the hypothesis that the discrepancy between inferred Earth viscosity parameters for the Hudson Bay data and the Gulf coast data can be addressed by incorporating lateral viscous structure. The data-model comparisons for South Florida are interesting, as the 3D models improve the fit to the two oldest data points, at the expense of a worse fit (particularly for the SEMUCB model) for the younger data. However, we note that the large vertical scatter in these data indicate a low precision compared to data at other locations, with some evidence of a sizeable compaction effect (e.g. index points dating to ~7 ka). All three seismic models improve the model-data fit in the Carolinas, and significantly so in the case of SEMUCB. In fact, incorporating lateral viscous structure with this particular reference model produces an improved data-fit to the majority of the sites considered, with the exception of East Shore, where both the Savani and SEMUCB models predict a more negative RSL curve relative to the reference model, and South Florida, where the 1D reference actually fits the data fairly well. As East Shore is the most northern of our study sites, this is consistent with the relative deformation differences shown in Figure 5, where the northern coast featured an enhanced bulge effect relative to the reference model. The improved fit to the RSL data for the Gulf coast sites and the Carolinas is striking, as it has been suggested in past works that difficulties satisfying these data (along the Atlantic coast in particular) with 1D models suggests the presence of lateral Earth structure. Our results support this suggestion and demonstrate that, with realistic lateral structure, it is possible to simultaneously satisfy these data as well as the Richmond Gulf decay time constraint with a single model. Finally, we note that the spread among the models is large, up to approximately 15m at 10ka. This demonstrates that the differences between the assumed seismic velocity models used here has a significant impact on the RSL predictions.

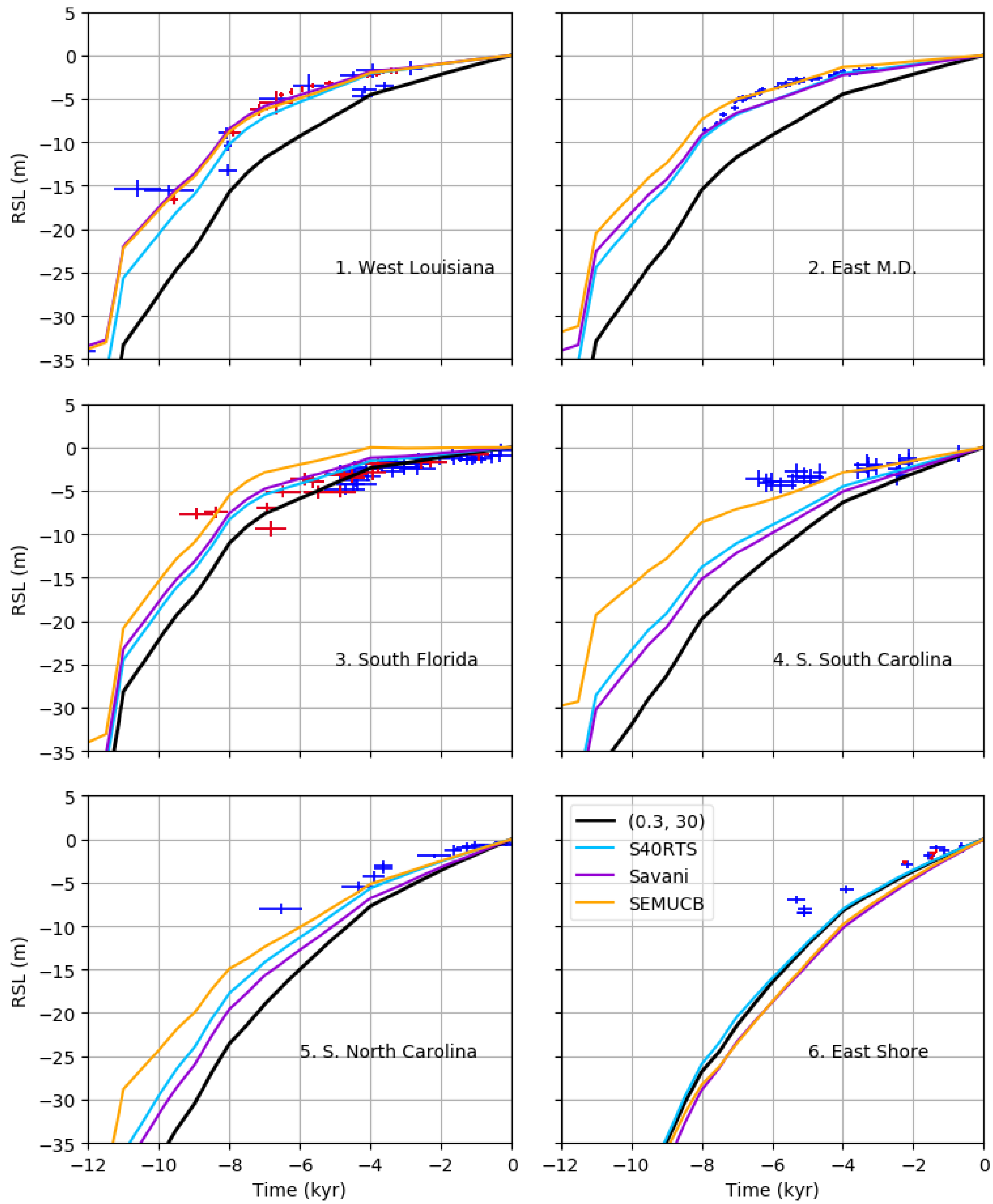

1. West Louisiana
2. East M.D.
3. South Florida
4. S. South Carolina
5. S. North Carolina
6. East Shore
(0.3, 30)
S40RTS
Savani
SEMUCB
RSL (m)
Time (kyr)

381

Figure 6: RSL curves for the (0.3, 30) 1D reference model (black), and for its associated 3D models. Since these model results do not include sediment isostatic adjustment, we have corrected the RSL data from West Louisiana and East Mississippi Delta for this effect (Love et al, 2017; Kuchar et al., 2018).

We have seen that for the (0.3, 30) reference Earth viscosity model, including lateral structure leads to suppression of the peripheral bulge at most Atlantic and Gulf coast locations, and thus an improved fit with the majority of the RSL data. To determine whether this behaviour is a general feature of including lateral structure, or specific to the assumed reference model, we have re-produced Figures 5 and 6 for the other two 1D reference models (0.3, 3) and (1, 30) in Supplementary Figures S3 – S6.

We have computed the relative height differences for the (0.3, 3) and (1, 30) reference models in Figures S3 and S4. Both are consistent with the results shown for the (0.3, 30) reference model in Figure 5, where the reference model shows large relative deformation, and lateral structure leads to a reduction in the uplift (and thus a suppression of the peripheral bulge) in the study area for all three seismic models at 10 ka. The low viscosity reference model, (0.3, 3), features the largest relative deformation, but also the corresponding largest suppression effects, where the lateral structure reduces the deformation by the greatest amount. In the case of the SEMUCB model, the difference is greater than 30 metres, and is off of our chosen colour scale. For all three reference models, the effect of lateral structure determined by the three seismic models is consistent with a general increase in viscosity in the study area.

We show the computed RSL (as in Figure 6) for the (0.3, 3) and (1, 30) models in Figures S5 and S6. Interestingly, for the lower viscosity (0.3, 3) reference model, it is no longer the case that the RSL curves for the Gulf coast sites are uniformly higher than the reference, and instead they actually intersect the reference curve around 5ka so that RSL is shifted higher for older times but lower for times younger than ~5 ka. It remains true that the presence of lateral structure for this reference model does tend to improve the data-model fit, but not as significantly as for the (0.3, 30) reference model. The (1, 30) model results show greater similarity to those of the (0.3, 30) reference model, as the RSL curves are shifted to higher values relative to the reference for all times. However, in this case it does not typically improve the data-model fit, as the reference model parameters already satisfy the data reasonably well. An exception is East Shore, where the higher viscosity reference leads to the model results with lateral structure being shifted higher (and not lower as was seen for the (0.3, 30) reference model), resulting in an improved fit there. This is consistent with the relative height differences seen in Figure S4, where the higher viscosity model does not feature the enhanced bulge effect on the north Atlantic coast as seen for the other two models.

4. **Conclusions**

We have computed RSL and vertical land motion for both 1D and 3D GIA models in order to determine why RSL data from the US Atlantic and Gulf coasts have a strong preference for high mantle viscosity values and whether incorporating lateral viscous structure is able to satisfy these data while adopting a global (1D) reference structure that is in-line with recent estimates. By considering the individual components of the 1D RSL curves we conclude that the preference of the RSL data for high viscosity values reflects the fact that they do not support a large peripheral bulge signal. By computing uplift with the 3D model we were able to show that bulge suppression may also be achieved by incorporating lateral structure within a model with reference 1D viscosity structure that is compatible with recent estimates (i.e. UMV of 3×10^{20} Pas and LMV of 3×10^{22} Pas). All three seismic models we considered (S40RTS, Savani, and SEMUCB) lead to a reduction in bulge subsidence from 10 ka to present. Thus we have shown that for a reference 1D model that satisfies the Hudson Bay constraints and is in agreement with recent 1D average Earth viscosity estimates, but not the Atlantic and Gulf coast RSL data, the model fits to these data can be significantly improved by incorporating lateral structure. This is especially true along the Gulf coast. Moreover, two of the three of the lateral structure variations we considered satisfied the Hudson Bay constraint. This is the first set of results that demonstrates the ability of lateral structure to accommodate spatial variability inferred in 1D modelling studies by satisfying constraints in Hudson Bay as well as RSL data along the US Atlantic and Gulf coasts.

An important caveat is that the 3D models we consider, corresponding to three different seismic velocity models, resulted in significantly different RSL predictions over the early Holocene, demonstrating that the uncertainty associated with this model input is significant. Moreover, in our analysis, we did not consider plausible variations in parameters used to infer viscosity variation from seismic velocity variations (equations 1 to 3) and we assumed that seismic velocities are directly related to viscosity through temperature, thus ignoring the possible influence of compositional and structural variations. While our results indicate that lateral viscous structure has a significant effect on RSL predictions along the Atlantic coast of North America, further work to better quantify uncertainty in estimating this lateral structure is warranted.

Acknowledgements

JK and GM acknowledge the National Science and Engineering Research Council and the University of Ottawa. KL acknowledges his other affiliated institutions, Boston College and Columbia University.

References

Auer, L., Boschi, L., Becker, T.W., Nissen-Meyer, T. & Giardini, D. (2014), *Savani*: A variable resolution whole-mantle model of anisotropic shear velocity variations based on multiple data sets, *J. Geophys. Res. Solid Earth*, **119**, 3006–3034.

Austermann, J., Mitrovica, J.X., Konstantin, L., Milne, G. (2013), Barbados-based estimate of ice volume at Last Glacial Maximum affected by subducted plate, *Nature Geoscience*, **6**, 553-557.

Caron, L., Métivier, L., Greff-Lefftz, M., Fleitout, L., and Rouby, H. (2017), Inverting Glacial Isostatic Adjustment signal using Bayesian framework and two linearly relaxing rheologies, *Geophys. J. Int.*, **209**, 1126-1147.

Chopelas, A. & Boehler, R. (1992), Thermal expansivity in the lower mantle, *Geophys. Res. Lett*, **19**, 1983-1986.

Davis, J.L., and Mitrovica, J.X. (1996), Glacial isostatic adjustment and the anomalous tide gauge record of eastern North America, *Nature*, **379**, 331-333.

Davis, J. E., Latychev, K., Mitrovica, J.X., Kendall, R., & Tamisiea M.E. (2008), Glacial isostatic adjustment in 3-D earth models: implications for the analysis of tide gauge records along the U.S. east coast, *J. Geodyn.*, **46**(35), doi:10.1016/j.jog.2008.04.007

Dziewonski, A., and D. Anderson (1981), Preliminary reference Earth model, *Phys. Earth Planet. Inter*., **25**, 297-356.

Engelhart, S.E., Peltier, W.R., and Horton, B.P. (2011), Holocene relative sea-level changes and glacial isostatic adjustment of the U.S. Atlantic coast, *Geology*, **39**, 751-754.

French, S. and Romanowicz, B. (2014), Whole-mantle radially anisotropic shear-velocity structure from spectral-element waveform tomography, *Geophys. J. Int*., **199**, 1303-1327.

Forte, A.M. and Woodward, R.L. (1997), Seismic-geodynamic constraints on three-dimensonal structure, vertical flow, and heat transfer in the mantle, *J. Geophys. Res.*, **102**.

Ivins, E. R., and Sammis, C.G. (1995), On lateral viscosity contrast in the mantle and the rheology of low frequency geodynamics, *Geophys. J. Int.*, **123**, 305–322.

Jones, E., Oliphant, E., Peterson, P., *et al.* (2001-), SciPy: Open Source Scientific Tools for Python, http://www.scipy.org/ [Online; accessed 2018-10-01].

Karato, S-I. (1993), Importance of anelasticity in the interpretation of seismic tomography, *Geophys. Res. Lett*, **20**.

Kendall, R., Mitrovica, J., and Milne, G. (2005), On post-glacial sea level – II. Numerical formulation and comparative results on spherically symmetric models. *Geophys. J. Int.*, **161**(3), 679-706.

King, M.A., Keshin, M., Whitehouse, P.L., Thomas, I.D., Milne, G, and Riva, R.E.M. (2012), Regional biases in absolute sea-level estimates from tide gauge data due to residual unmodeled vertical land movement, *Geophys. Res. Lett.*, **39**.

Kuchar, J., Milne, G., Wolstencroft, M., Love, R., Tarasov, L., and Hijma, M. (2018), The Influence of Sediment Isostatic Adjustment on Sea Level Change and Land Motion Along the U.S. Gulf Coast, *Journal of Geophysical Research: Solid Earth*, **122**.

Lambeck, K., Smither, C., and Johnston, P (1998), Sea-level change, glacial rebound and mantle viscosity for northern Europe, *Geophys. J. Int.*, **134**, 102-144.

Lambeck, K., Purcell, A., and Zhao, S. (2017), The North American Late Wisconsin ice sheet and mantle viscosity from glacial rebound analyses, *Quat. Sci. Rev.*, **158**, 172-210.

Lambeck, K., Rouby, R., Purcell, A., Sun, Y., and Sambridge, M. (2014), Sea level and global ice volumes from the Last Glacial Maximum to the Holocene, *Proc. Natl. Acad. Sci. U.S.A.*, **111**, 15296-15303.

Latychev, K., Mitrovica, J., Tromp, J., Tamisiea, M., Komatitsch, D., and C. Christara (2005), Glacial isostatic adjustment on 3-D earth models: a finite-volume formulation, *Geophys. J. Int.*, **161**(2), 421–444, doi:10.1111/j.1365-246X.2005.02536.x.

Lau, H.C.P., Mitrovica, J.X., Austermann, J., Al-Attar, D., Crawford, O. & Latychev, K. (2016), Inferences of mantle viscosity based on ice age data sets: Radial structure, *J. Geophys. Res. Solid Earth*, **121**(10), 6991-7012.

Li, T., Wu, P., Steffen, H., Wang, H.S. (2018), In search of laterally heterogeneous viscosity models of Glacial Isostatic Adjustment with the ICE-6G_C global ice history model, *Geophys. J. Int.*, **214**, 1191-1205 doi: 10.1093/gji/ggy181

Love, R., Milne, G.A., Tarasov, L., Engelhart, S.E., Hijma, M.P., Latychev, K., Horton, B.P., and T.E. Törnqvist (2016), The contribution of glacial isostatic adjustment to projections of sea-level change along the Atlantic and Gulf coasts of North America, *Earth's Future*, **4**, 440–464.

Milne, G.A. and Peros, M. (2013), Data-Model comparison of Holocene sea-level change in the circum-Caribbean region, *Global and Planetary Change*, **107**, 119-131.

Milne, G.A., Latychev, K., Schaeffer, A., Crowley, J.W., Lecavalier, B.S., and Audette, A. (2018), The influence of lateral Earth structure on glacial isostatic adjustment in Greenland, *Geophys. J. Int.*, **214**, 1252-1266.

Mitrovica, J.X., Forte, A.M. (1997), Radial profile of mantle viscosity: Results from the joint inversion of convection and postglacial rebound observables. *J. Geophys. Res.*, **102**, 2751-2769.

Mitrovica, J.X., Forte, A.M. & Simons, M. (2000), A reappraisal of postglacial decay times from Richmond Gulf and James Bay, Canada, *Geophys. J. Int.*, **142**(3), 783-800.

Mitrovica J, Milne G (2003), On post-glacial sea level: I. general theory, *Geophys. J. Int.*, **154**, 253–267.

Nakada, M., and Lambeck, K. (1989), Late Pleistocene and Holocene sea-level change in the Australian region and mantle rheology, *Geophysical Journal*, **96**, 497-517.

Paulson, A., Zhong, S., and Wahr, J. (2005), Modelling post-glacial rebound with lateral viscosity variations, *Geophys. J. Int.*, **163**, 357-371.

Paulson, A., Zhong, S. & Wahr, J. (2007), Inference of mantle viscosity from GRACE and relative sea level data, *Geophys. J. Int*., **171**, 497–508.

Peltier, W.R. (2004), Global glacial isostasy and the surface of the ice-age earth: the ICE-5G (VM2) model and GRACE, *Annu. Rev. Earth Planet. Sci.*, **32**(1), 111–149.

Peltier, W.R., Argus, D., and Drummond, R. (2015), Space geodesy constrains ice age terminal deglaciation: the global ICE-6G_C (VM5a) model, *J. Geophys. Res.*, **120**(1), 450-487.

Peltier, W.R. and Drummond, R. (2008), Rheological stratification of the lithosphere: A direct inference based on the geodetically observed pattern of the glacial isostatic adjustment of the North American continent. *Geophys. Res. Lett.*, **35**.

Peltier, W.R., Shennan, I., Drummond, R., and Horton, B. (2002), On the Postglacial Isostatic Adjustment of the British Isles and the Shallow Viscoelastic Structure of the Earth, *Geophys. J. Int.*, **148**, 443-475.

Pico, T., Creveling, J.R., and Mitrovica, J.X. (2017), Sea-level records from the U.S. mid-Atlantic constrain Laurentide Ice Sheet extent during Marine Isotope Stage 3, *Nature Communications*, **8**, 15612.

Ritsema J., Deuss A., van Heijst H.J., and Woodhouse J.H. (2011), S40RTS: a degree-40 shear-velocity model for the mantle from new Rayleigh wave dispersion, teleseismic traveltime and normal-mode splitting function measurements, *Geophys. J. Int.*, **184(3)**, 1223–1236.

Roy, K., and Peltier, W.R. (2015), Glacial isostatic adjustment, relative sea level history and mantle viscosity: reconciling relative sea level model predictions for the U.S. East coast with geological constraints, *Geophys. J. Int.*, **201**, 1156-1181.

Slangen, A.B.A., Katsman, C.A., van der Wal, R.S.W., Vermeersen, L.L.A., and Riva, R.E.M. (2012), Towards regional projections of twenty-first century sea-level change based on IPCC SRES scenarios, *Clim. Dyn.*, **38**, 1191-1209

Tarasov, L., Dyke, A., Neal, R., and W.R. Peltier (2012), A data-calibrated distribution of deglacial chronologies for the North American ice complex from glaciological modeling, *Earth Planet. Sci. Lett.*, **315–316**, 30–40.

Velicogna, I., and Wahr, J. (2013), Time-variable gravity observations of ice sheet mass balance: Precision and limitations of the GRACE satellite data, *Geophys. Res. Lett.*, **40**, 3055-3063.

Wang, H., Wu, P., and Van der Wal, W. (2008), Using postglacial sea level, crustal velocities and gravity-rate-of-change to constrain the influence of thermal effects on mantle lateral heterogeneities, *J. Geodyn.*, **46**(3-5), 104–117.

Wu, P. (2006), Sensitivity of relative sea levels and crustal velocities in Laurentide to radial and lateral viscosity variations in the mantle. *Geophys. J. Int.*, **165**, 401-413.

Wu, X., Heflin, M.B., Schotman, H. Vermeersen, B.L.A., Dong, D., Gross, R.S., Ivins, E.K., Moore, A.W., and Owen, S.E. (2010), Simultaneous estimation of global present-day water transport and glacial isostatic adjustment, *Nature Geoscience*, **3**, 642-646.

Wu, P., Wang, H., and Steffen, H. (2013), The role of thermal effect on mantle seismic anomalies under Laurentia and Fennoscandia from observations of Glacial Isostatic Adjustment, *Geophys. J. Int.*, **192**, 7–17

Zhong, S.J., Paulson, A. & Wahr, J. (2003), Three-dimensional finite element modelling of Earth's viscoelastic deformation: Effects of lateral variations in lithospheric thickness. *Geophys. J. Int.*, **155**, 679-695.

Supporting Information

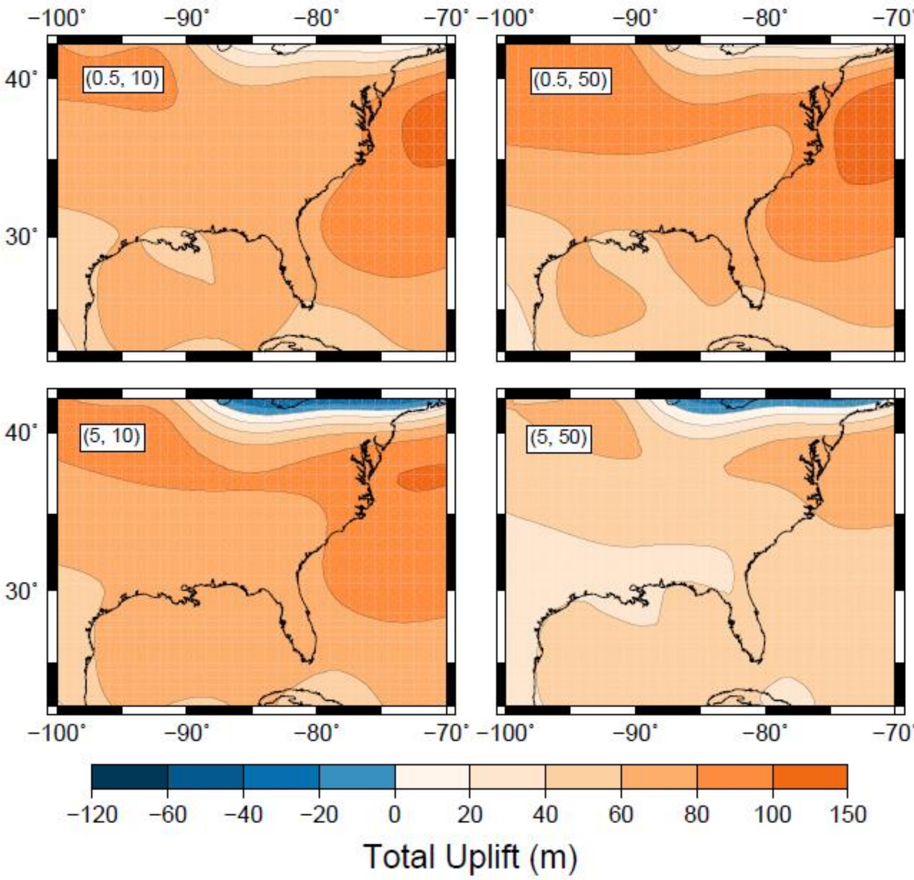

Figure S1: As in Figure 4, but showing total vertical deformation at 10 ka (relative to the start of the model run).

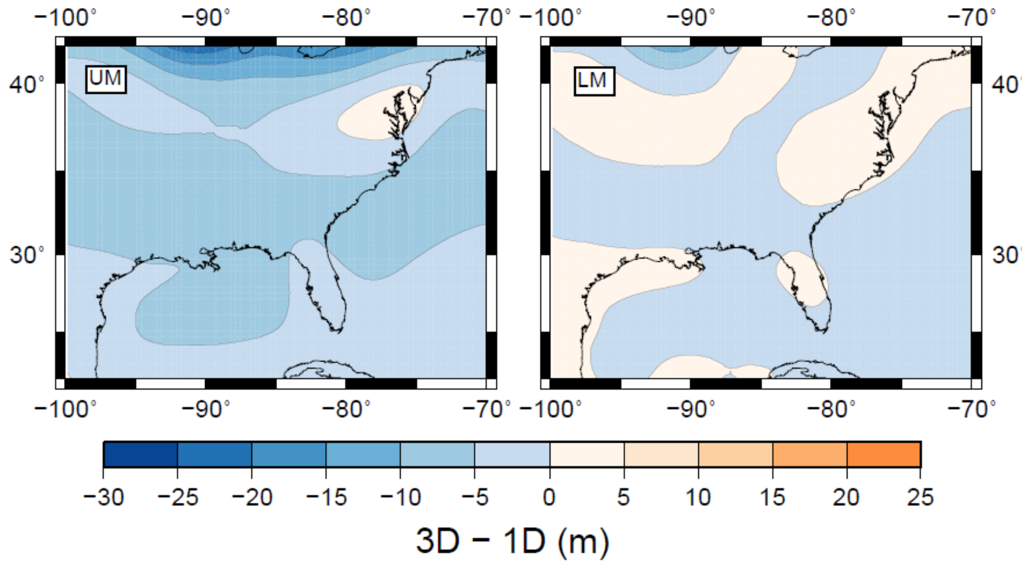

Figure S2: As in Figure 6, but for the S40RTS seismic model and with lateral structure confined to only the upper mantle (left), and only the lower mantle (right).

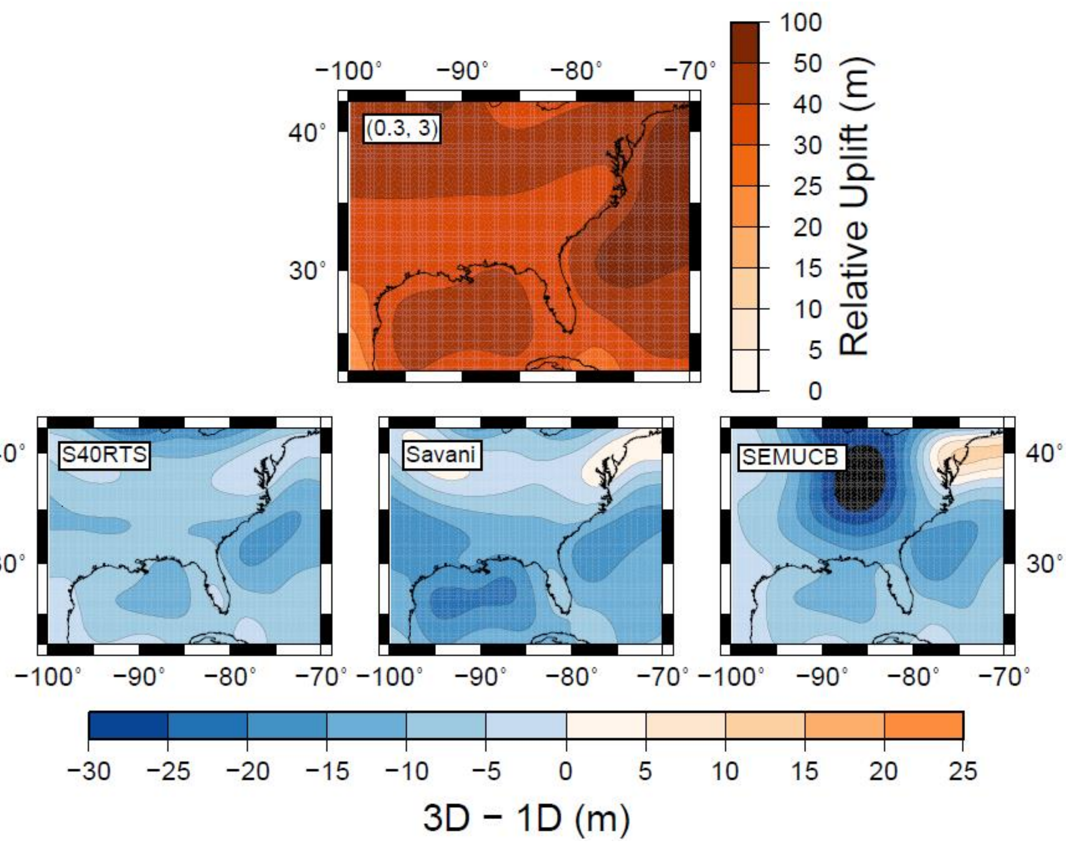

Figure S3: As in Figure 6, but for the (0.3, 3) reference 1D viscosity model.

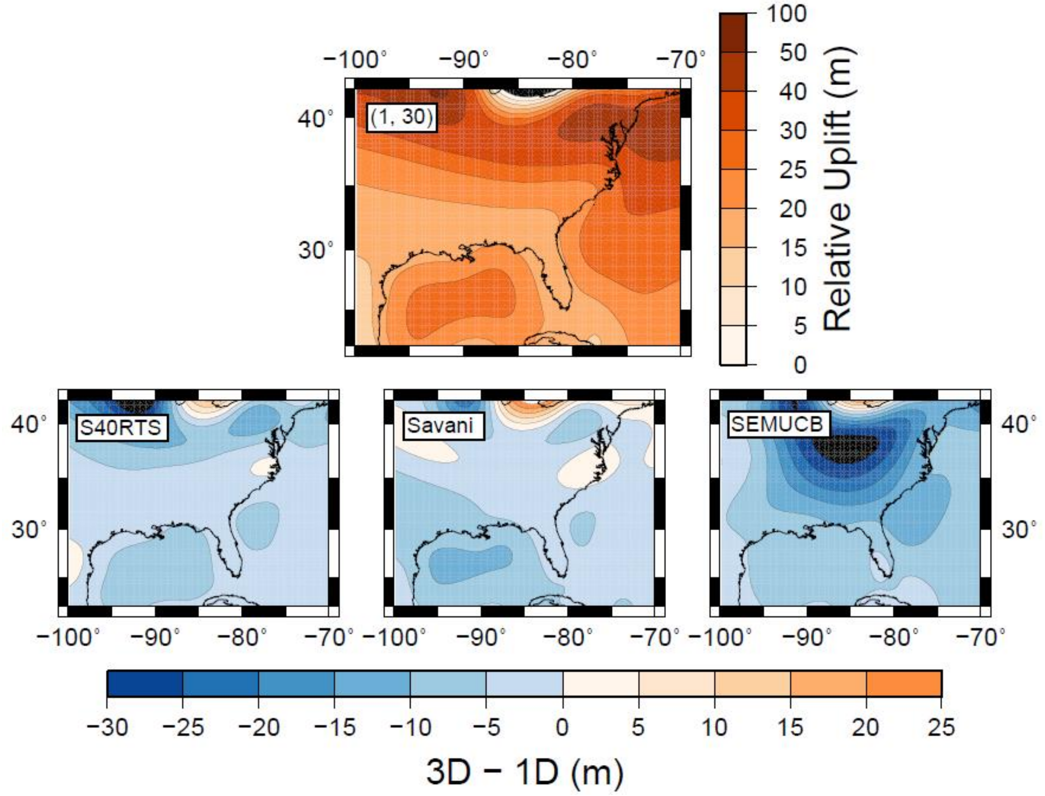

Figure S4: As in Figure 6, but for the (1, 30) reference 1D viscosity model.

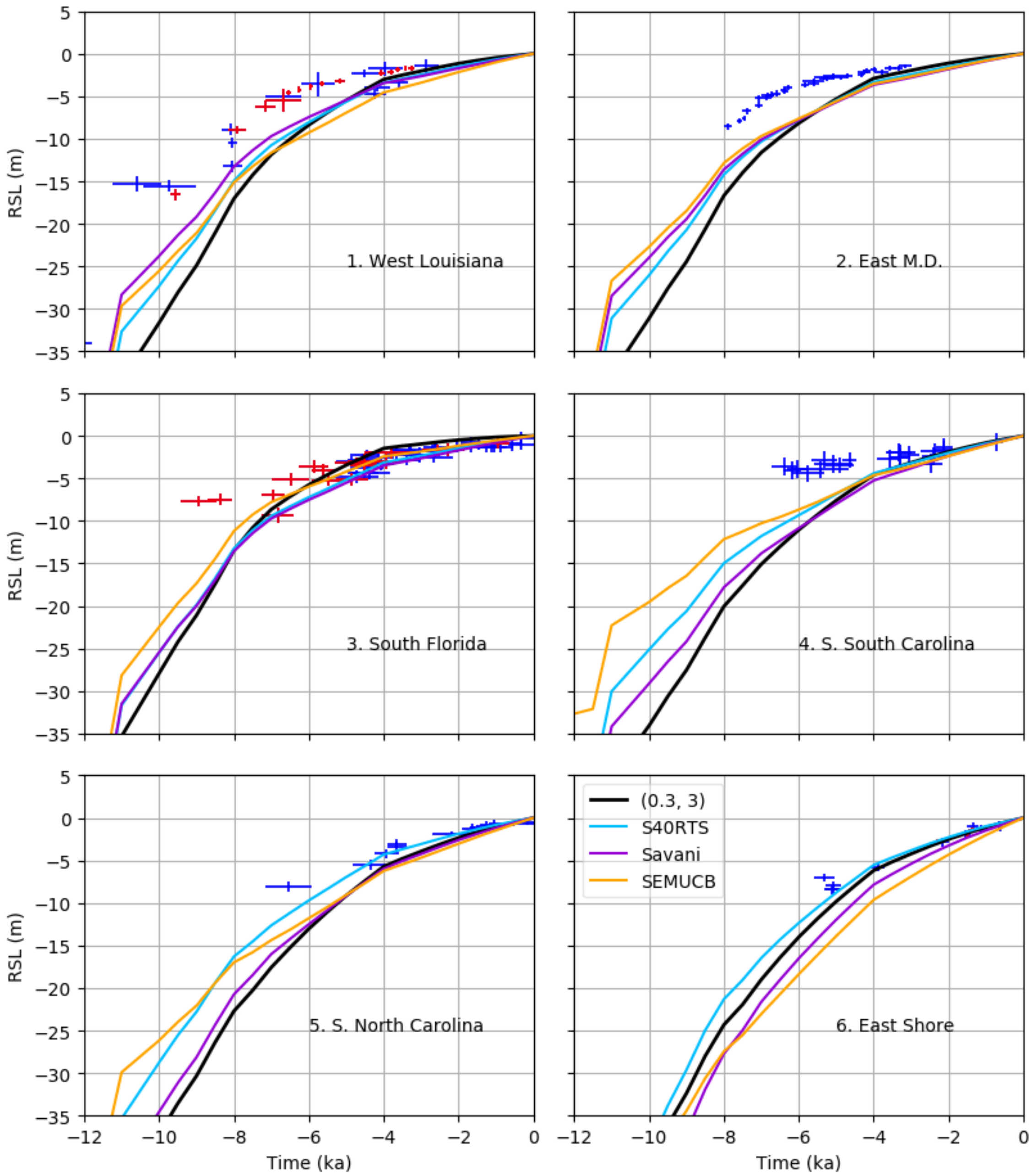

Figure S5: As in Figure 7, but for the (0.3, 3) reference 1D viscosity model.

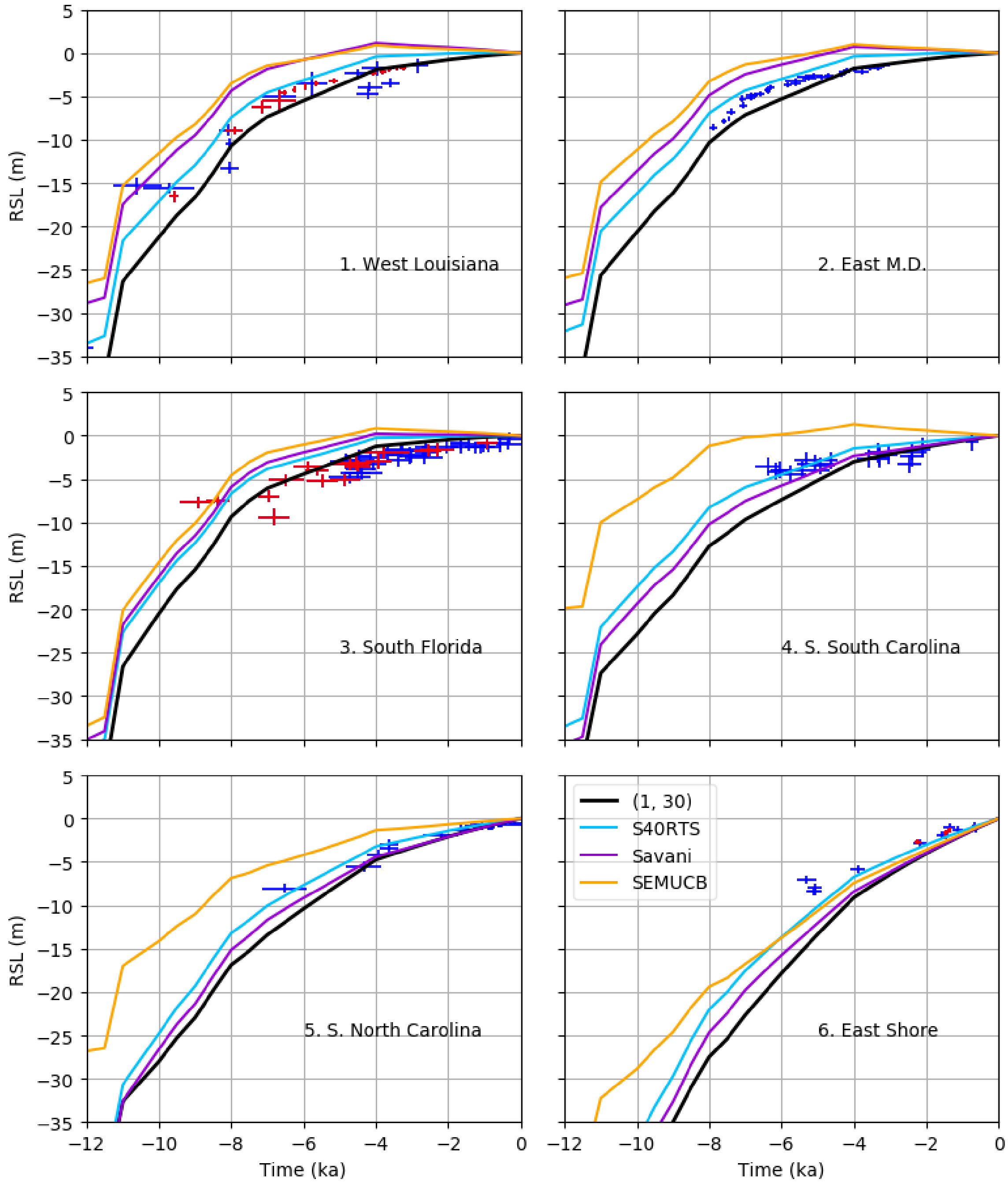

Figure S6: As in Figure 7, but for the (1, 30) reference 1D viscosity model.

6
Conclusion

I have presented four research projects in this thesis. Here we summarise the main conclusions of each project, and present a more broad discussion in the Reflections chapter that follows.

In Chapter 2, we incorporated realistic viscosity structure into the lithosphere component of a GIA model by determining viscosity through temperature profiles and creep laws instead of treating the lithosphere as an elastic layer. We found that the RSL predictions of a given ductile structure lithosphere model are generally most similar to those of a significantly thinner elastic lithosphere, suggesting that GIA analyses that treat the lithosphere as an elastic layer likely underestimate the actual thickness of the lithosphere. We found that while the response of a given ductile model was similar to that of an equivalently thick elastic model on short time scales (~ 2 kyr), the ductile model effectively thins on a time scale of ~ 10 kyr.

In Chapter 3, we used a gravitationally self-consistent treatment of sea level to account for sediment isostatic adjustment (SIA) and a realistic reconstruction of the Mississippi Delta sediment loading history to compute GIA and SIA along the U.S. Gulf coast. By considering a large parameter space of four ice histories and hundreds of Earth viscosity models, and determining model-data misfits with RSL data free from sediment compaction, we demonstrate that the misfit is minimized for Earth viscosity models with high values in the upper and lower mantle. We found that the contribution of SIA within the Delta region is on the order of a few metres during the Holocene, and that its contribution to present-day sea-level rates is on the order of a tenth of a millimetre per year. By comparing model predictions of present-day surface uplift caused by GIA and SIA with GPS records, we conclude that the large discrepancies between the GPS records in the Delta region and the model output indicates that most subsidence is from non-isostatic processes such as sediment compaction.

In Chapter 4 we computed RSL histories and their corresponding decay times for a suite of Earth viscosity models and 20 ice histories for Richmond Gulf and James Bay in Hudson Bay, and for Ångerman River in Sweden. By isolating the response to the ice load from the ocean and rotation signals, we demonstrate that the decay times generated for a given Earth viscosity structure are in general not independent of the ice history used. In particular, we found that there is a relatively high degree of sensitivity (indicated by the variability in computed decay times across ice histories) in James Bay, and relatively low sensitivity in Richmond Gulf. This indicates that the James Bay data are not suitable for a decay time analysis to determine Earth structure. Ångerman River demonstrated less sensitivity to ice history than James Bay but more than Richmond Gulf, and so there may be unaccounted for uncertainty in viscosity inversions from this location owing to ice input uncertainty. We also developed corrections to the RSL data to account for spatial variability of sea level and for the effects of the ocean load and rotation signal in order to compare model decay times to data decay times. The result of this comparison is that, while Richmond Gulf as a location is relatively insensitive to ice history variations, the low temporal resolution of the available data leads to fairly large allowed regions of parameter space, indicating that it is not a strong constraint on Earth viscosity structure.

In Chapter 5 we used a combination of 3-D and 1-D GIA modelling to determine why the Atlantic and Gulf coast RSL data require high (1-D) viscosities to satisfy, and whether incorporating realistic lateral viscous structure can satisfy these data while also satisfying viscosity inferences from global GIA studies and Hudson Bay decay time constraints. From our 1-D modelling we determined that the effect of the high viscosity upper and lower mantle was to suppress the amplitude of the peripheral bulge and its rate of collapse, suggesting that the RSL data to not support a large and dynamic peripheral bulge. We demonstrated that the peripheral bulge could also be suppressed in a 3-D model by incorporating lateral viscous structure (determined by scaling seismic velocity models) into a model with an average global viscosity structure in broad agreement with previous inferences. Moreover, we showed that the fit to the RSL data along the Gulf and Atlantic coast of the U.S. is significantly improved when lateral structure is included (relative to the 1-D reference that satisfies global constraints but not Atlantic and Gulf coast RSL data). An important caveat is that there are significant uncertainties in the lateral structure realisation, demonstrating a need to better constrain this model input in the future.

In general, our aim has been to improve our understanding of the GIA process by either including more realism into the model (as in Chapters 2, 3, and 5) or by re-appraising certain long-held assumptions (as in Chapter 4). All of these projects have implications for how we infer the viscous structure of the Earth, which is an important component of the Earth system for predicting future sea level, or for inferring how past ice sheets responded to climactic forcings. The versatility of the 1-D GIA model with an elastic lithosphere layer stems from having a parameter space that is easy to explore and computationally inexpensive to run. An important avenue of future work is to explore the parameter space of ductile lithosphere models, and 3-D models, to the extent that optimal models and model uncertainties can be reliably estimated.

7

Reflections

In this thesis I have presented four research projects that we have conducted during my PhD, each different enough from the rest to warrant a separate introduction to each Chapter. The purpose of this chapter, then, is both to relate these projects as well as to place them appropriately into a larger context. I discuss each Chapter in turn, and include suggestions for future research as part of the discussion. As discussed at the start of this thesis, the fundamental problem with the Earth sciences is that there is only one Earth and that it does not fit in a laboratory. Fortunately, the Earth's history of sea-level changes, captured in various biological and geological indicators, reveals a surprising amount about the viscous interior and deformation of the Earth, along with the history of the ice sheets and glaciers that are responsible for deforming it. In the research I've presented here, we have improved our understanding of the viscous structure underneath eastern North America, in particular, and have pushed forward GIA models by incorporating additional processes and physics. We have also mainly used ice histories developed by glaciological modelling, which I believe is an important direction for the field to ensure the key model inputs actually reflect our understanding of the underlying physical processes.

In Chapter 2, we developed a ductile lithosphere component to a 1-D Maxwell Earth model by computing lithosphere temperature profiles and assuming a power law relationship between stress and strain rate and an exponential relationship with temperature. When this more realistic lithosphere structure is incorporated, the lithosphere is effectively thinned (relative to an elastic analogue), and a time-dependency to its behaviour is introduced. This work straddles the line between studies that incorporate power-law rheologies and those that use the standard Maxwell rheology, as we assumed a power-law to derive our viscosity profile, but then used it within a Maxwell model. The time-dependence of the behaviour is interesting, because it is a potential explanation for the difficulty of certain models to satisfy different datasets simultaneously. For example, Wolstencroft et al., 2014 found that a thin lithosphere was favoured by the Mississippi River long profile (a record of its displacement history over the past 80 thousand years), and a thicker lithosphere favoured by the RSL observations over the past few thousand years. This may reflect the lithosphere effectively thinning through ductile flow on the longer timescale associated with the long profile deformation. Recently, a power-law rheology in the lithosphere has been applied by Nield et al., 2018 to model present-day uplift rates in Antarctica. Significant differences exist between the results of the power-law and elastic lithosphere models, and therefore it may be an important model component for determining present-day mass loss. In my mind, the work of this Chapter was an important first step in determining first of all, what a realistic lithosphere viscosity profile might look like, and second of all, what effects it would have. However, there is significant work to be done in exploring the parameter space of these models in a systematic way.

It was the observation of Wolstencroft et al., 2014 (who is a former post-doctoral researcher in the group) that lead to the research of Chapter 3. After developing the ductile lithosphere models, it was natural to consider ideal testing grounds for them, which are systems that would include observations relating processes with different time scales, and thus loads with different chronologies. The Mississippi Delta region is a perfect example, because the RSL data and the deformation history of the Mississippi River measure responses over different (an order of magnitude or so) timescales, and the region is sensitive both to the growth and collapse of the Laurentide ice sheet, as well as to local and regional sediment loading. However, before applying these new Earth models, we decided it was necessary to address an inconsistency in the method of Wolstencroft et al., 2014, which was to compute sea level change in response to a given ice history and vertical motion in response to the sediment load, and to add them together. This neglects the feedback the sediment load has on sea level, as well as the effect of water displacement in areas of marine sedimentation. We therefore chose to incorporate the theory of Dalca et al., 2013 into the sea-level solver, and the length of the resulting manuscript (and a preference to not include too many novel interactions in one manuscript) lead to the ductile lithosphere models not having a place in Chapter 3. By instead considering a simpler parametrization of the Earth, we were able to provide modelled estimates (with uncertainty) for future sea-level and present-day uplift rates. This was a valuable contribution, because we were able to demonstrate that the present-day uplift rates predicted by the model, combining both glacial and sediment isostatic adjustment, are not enough to reproduce the high rates recorded by GPS stations. This shows that most ongoing subsidence in the region is from non-isostatic processes such as sediment compaction and fluid extraction. Moreover, as the modelled contribution of SIA for the future is small, other modellers may now safely conclude that they may simply correct the RSL data for an estimated SIA signal (as was done in Love et al., 2016) rather than model it directly, or else ignore the SIA contribution entirely if they deem its estimated contribution is less than some threshold. Fortunately, an application of the ductile lithosphere models to the Mississippi Delta region is under way by an MSc student in the group. Another interesting test case for the model would be in the British Isles, where an extensive and high quality RSL database exists, and where the RSL is more sensitive to the structure of the lithosphere due to the relatively small British-Irish Ice Sheet.

In Chapter 4 we investigated the extent of the ice load insensitivity of postglacial decay times by considering a suite of realistic ice histories and corrections to RSL data that we developed to make sure that the model-data comparisons being made were apple-to-apple comparisons. We found that there is a pronounced sensitivity among the ice histories considered to the James Bay location, suggesting that it is not an appropriate location for a decay time analysis. On the other hand, we also determined that Richmond Gulf is relatively (though not entirely) insensitive to the ice history. We also provided an estimate for Earth viscosity structures that satisfy the Richmond Gulf and Ångerman River decay times, both separately and together, though given what we know about lateral viscous structure and with Chapter 5 in mind, I would not personally recommend combining the constraints. In fact, research for Chapter 5 began before Chapter 4, because it was immediately clear that the viscosity models preferred by the Gulf coast data were in contrast to those models known to satisfy the Hudson Bay decay time constraints. However, around this same time a member of our group, Alexander Hill, observed an apparent sensitivity to the ice history input in a paper he was working on. Early on in my PhD I had looked into the Hudson Bay decay times (and concluded at the time that the Richmond Gulf and James Bay data could not be reconciled), and so I took this opportunity to revisit the problem. My initial belief was that the sensitivity was likely to reflect the different ocean loads associated with the ice histories, and that if the ice response were to be isolated then the classic result of ice insensitivity would be regained. Instead, we found that while the ocean load does play a role (as shown by Han and Gomez, 2018), this was ultimately not the case, and is an example of the (perhaps apocryphal) Isaac Asimov quote, "The most exciting phrase to hear in science, the one that heralds new discoveries, is not 'Eureka!', but 'That's funny...' ".

And finally, in Chapter 5 we investigated the cause of the discrepancy in viscosity values found for the Gulf coast RSL data in Chapter 3 and the Richmond Gulf decay times in Chapter 4. To do this we applied both 1-D and 3-D GIA models to compute vertical displacement of the solid Earth as well as RSL. We found that the effect of a high viscosity mantle is to suppress the dynamics of the peripheral bulge, and that the RSL data's preference for high viscosities is a reflection of the fact that they do not record a strong bulge signal. We then demonstrated that a 3-D model with realistic lateral structure and a depth-average viscosity consistent with various 1-D studies can markedly improve the modelled fit to the RSL data along the Gulf and Atlantic coast. This study answers one question, which is whether the available data be satisfied if realistic lateral structure is used, but highlights several more that so far remain unanswered. In particular, the uncertainty associated with the seismic velocity models needs to be investigated: is one seismic velocity model more appropriate for our purposes than another? What is the systematic uncertainty associated with the scaling method to obtain the viscosity structure from the input seismic velocity model (and how does it compare to the uncertainty of the seismic velocity input)? This has been investigated to an extent, e.g. by Wang et al., 2008, where a weighting factor β was applied to the temperature-to-viscosity scaling (so that $\beta = 1$ corresponds to lateral structure determined fully by temperature variations, and $\beta = 0$ corresponds to no lateral structure), however, this scaling adjustment simply reduces the effect temperature has on producing lateral structure, and therefore does not account for variations due to compositional differences. The approach of Nield et al., 2018 and van der Wal et al., 2015 is to determine viscosity structure through calculated temperature profiles and laboratory-determined properties of mantle rocks (similar to how we derived the lithosphere viscosity profiles in Chapter 2), which is perhaps a more satisfying procedure than to simply assign viscosity as a parameter and vary it, as instead the viscosity is determined by other physical parameters. However, it effectively shifts the uncertainty from the input viscosity to the material parameters (extrapolated from laboratory conditions to mantle conditions) and a temperature profile, likely derived from a seismic velocity model. The difficulty with determining the model uncertainties for 3-D models is both that the parameter space is much larger than those of 1-D models, and also that the computational time is much greater. For example, in the study of Chapter 3, computing SIA and GIA in the Mississippi Delta region, to explore the parameter space I performed 3200 model runs, which represents several days worth of computational time. Several days is also how much time it takes to run the 3-D model a single time. This is an issue, because recent research indicates that lateral structure is a necessary accommodation for increasingly many study areas. The failure of 1-D models to satisfy GPS records in West Antarctica has been established (Wolstencroft et al., 2015), and we may conclude that it is also necessary to accurately model GIA in eastern North America.

Bibliography

A, Geruo, John Wahr, and Shije Zhong (2013). “Computations of the viscoelastic response of a 3-D compressible Earth to surface loading: an application to Glacial Isostatic Adjustment in Antarctica and Canada”. In: *Geophysical Journal International* 192.

Amante, C. and B. W. Eakins (Mar. 2009). “ETOPO1 1 Arc-Minute Global Relief Model: Procedures, Data Sources and Analysis.” In: *NOAA Technical Memorandum NESDIS NGDC* 24, pp. 19+.

Andrews, J.T. (1970). *A Geomorphological Study of Postglacial Uplift with Particular Reference to Arctic Canada*. Oxford University Press.

Austermann, Jacqueline et al. (2013). “Barbados-based estimate of ice volume at Last Glacial Maximum affected by subducted plate”. In: *Nature Geoscience* 6.

Blum, Michael D. and Harry H. Roberts (2012). “The Mississippi Delta Region: Past, Present, and Future”. In: *Annual Review of Earth and Planetary Sciences* 40.1, pp. 655–683.

Bürgmann, Roland and Georg Dresen (2008). “Rheology of the Lower Crust and Upper Mantle: Evidence from Rock Mechanics, Geodesy, and Field Observations”. In: *Annual Review of Earth and Planetary Sciences* 36.1, pp. 531–567.

Caron, L. et al. (2017). “Inverting Glacial Isostatic Adjustment signal using Bayesian framework and two linearly relaxing rheologies”. In: *Geophysical Journal International* 209.2, pp. 1126–1147.

Church, J.A. et al. (2004). “Estimates of the Regional Distribution of Sea Level Rise over the 1950-2000 Period”. In: *Journal of Climate* 17.

Church, J.A. et al. (2013). “Sea Level Change”. In: *Climate Change 2013: The Physical Science Basis. Contribution of Working Group I to the Fifth Assessment Report of the Intergovernmental Panel on Climate Change*. Ed. by T.F. Stocker et al. Cambridge, United Kingdom and New York, NY, USA: Cambridge University Press. Chap. 13, pp. 1137–1216.

Couvillion, B.R. et al. (2017). *Land area change in coastal Louisiana 1932 to 2016: U.S. Geological Survey Scientific Investigations Map 3381, 16 p. pamphlet.*

Dalca, A. V. et al. (2013). “On postglacial sea level—III. Incorporating sediment redistribution”. In: *Geophysical Journal International* 194.1, pp. 45–60.

Day, John W. et al. (2007). “Restoration of the Mississippi Delta: Lessons from Hurricanes Katrina and Rita”. In: 315.5819, pp. 1679–1684.

DiDonato, G. et al. (2000). “The influence of a ductile crustal zone on glacial isostatic adjustment: Geodetic observables along the U.S. East Coast”. In: *Geophysical Research Letters* 27.18, pp. 3017–3020.

Dziewonski, A.M. and D.L. Anderson (1981). “Preliminary reference Earth model”. In: *Physics of the Earth and Planetary Interiors* 25.

Engelhart, S.E., W.R. Peltier, and B.P. Horton (2011). “Holocene relative sea-level changes and glacial isostatic adjustment of the U.S. Atlantic coast”. In: *Geology* 39, pp. 751–754.

Engelhart, Simon E. and Benjamin P. Horton (2012). “Holocene sea level database for the Atlantic coast of the United States”. In: *Quaternary Science Reviews* 54, pp. 12–25.

Farrell, W. E. and J. A. Clark (1976). “On Postglacial Sea Level”. In: *Geophysical Journal of the Royal Astronomical Society* 46.3, pp. 647–667.

Fei, Hongzhan et al. (2016). “New constraints on upper mantle creep mechanism inferred from silicon grain-boundary diffusion rates”. In: *Earth and Planetary Science Letters* 433, pp. 350–359.

Ferrier, Ken L. et al. (2015). “Sea-level responses to erosion and deposition of sediment in the Indus River basin and the Arabian Sea”. In: *Earth and Planetary Science Letters* 416, pp. 12–20.

Fisk, H.N. (1939). “Depositional terrace slopes in Louisiana”. In: *Journal of Geomorphology* 2.

Fleming, Kevin et al. (1998). “Refining the eustatic sea-level curve since the Last Glacial Maximum using far- and intermediate-field sites”. In: *Earth and Planetary Science Letters* 163.1, pp. 327–342.

Furlong, K.P. and D.S. Chapman (2013). “Heat Flow, Heat Generation, and the Thermal State of the Lithosphere”. In: *Annual Review of Earth and Planetary Sciences*.

Gomez, Natalya, Konstantin Latychev, and David Pollard (2018). “A coupled ice sheet-sea level model incorporating 3D Earth structure: Variations in Antarctica during the last deglacial retreat”. In: *Journal of Climate* 31.

Gomez, Natalya et al. (2012). “Evolution of a coupled marine ice sheet-sea level model”. In: *Journal of Geophysical Research: Earth Surface* 117.

Han, Holly Kyeore and Natalya Gomez (2018). “The impact of water loading on postglacial decay times in Hudson Bay”. In: *Earth and Planetary Science Letters* 489, pp. 156–165.

Haskell, N.A. (1935). “The Motion of a Viscous Fluid Under a Surface Load”. In: *Journal of Applied Physics* 6.

Heiskanen, W.A. and F.A. Vening Meinesz (1958). *The earth and its gravity field*. McGraw-Hill Book Company Inc.

Hill, Alexander et al. (2018). “Sensitivity of glacial isostatic adjustment to a partially molten layer at 410 km depth”. In: *Geophysical Journal International*.

Hubbard, Alun et al. (2009). “Dynamic cycles, ice streams and their impact on the extent, chronology, and deglaciation of the British-Irish ice sheet”. In: *Quaternary Science Reviews* 28.

Ivins, E.R., R.K. Dokka, and R.G. Blom (2007). “Post-glacial sediment load and subsidence in coastal Louisiana”. In: *Geophysical Research Letters* 34.

Jankowski, K.L., T.E. Törnqvist, and A.M. Fernandes (2017). “Vulnerability of Louisiana’s coastal wetlands to present-day rates of relative sea-level rise”. In: *Nature Communications*.

Jones, C.E. et al. (2016). “Anthropogenic and geologic influences on subsidence in the vicinity of New Orleans, Louisiana”. In: *Journal of Geophysical Research: Solid Earth* 121.5, pp. 3867–3887.

Jurkowski, G., J. Ni, and L. Brown (1984). “Modern Uparching of the Gulf Coastal Plain”. In: *Journal of Geophysical Research* 89.

Karato, Shun-Ichiro and Patrick Wu (1993). “Rheology of the Upper Mantle: A Synthesis”. In: *Science*.

Karegar, Makan A., Timothy H. Dixon, and Rocco Malservisi (2015). “A three-dimensional surface velocity field for the Mississippi Delta: Implications for coastal restoration and flood potential”. In: *Geology* 43.6, p. 519.

Kendall, R., J.X. Mitrovica, and R. Sabadini (2003). “Lithospheric thickness inferred from Australian post-glacial sea-level change: The influence of a ductile crustal zone”. In: *Geophysical Research Letters* 30.9.

Kendall, Roblyn A., Jerry X. Mitrovica, and Glenn A. Milne (2005). “On post-glacial sea level – II. Numerical formulation and comparative results on spherically symmetric models”. In: *Geophysical Journal International* 161.3.

King, M.A. et al. (2012a). “Lower satellite-gravimetry estimates of Antarctic sea-level contribution”. In: *Nature* 491, pp. 586–589.

King, Matt A. et al. (2012b). “Regional biases in absolute sea-level estimates from tide gauge data due to residual unmodeled vertical land movement”. In: *Geophysical Research Letters* 39.14, n/a–n/a.

Klemann, V. and D. Wolf (1998). “Modelling of stresses in the Fennoscandian lithosphere induced by Pleistocene glaciations”. In: *Tectonophysics* 294, pp. 291–303.

— (1999). “Implications of a ductile crustal layer for the deformation caused by the Fennoscandian ice sheet”. In: *Geophysical Journal International* 139, pp. 216–226.

Kuchar, Joseph and Glenn A. Milne (2015). “The influence of viscosity structure in the lithosphere on predictions from models of glacial isostatic adjustment”. In: *Journal of Geodynamics* 86.

Kuchar, Joseph et al. (2012). “Evaluation of a numerical model of the British–Irish ice sheet using relative sea-level data: implications for the interpretation of trimline observations”. In: *Journal of Quaternary Science* 27.6, pp. 597–605.

Kuchar, Joseph et al. (2018a). “The Influence of Sediment Isostatic Adjustment on Sea Level Change and Land Motion Along the U.S. Gulf Coast”. In: *Journal of Geophysical Research: Solid Earth* 123.1, pp. 780–796.

Kuchar, Joseph et al. (2018b). “On the usefulness of relative sea level decay times for constraining Earth viscosity structure”. In: *Geophysical Journal International*.

Lambeck, Kurt et al. (2014). “Sea level and global ice volumes from the Last Glacial Maximum to the Holocene”. In: *Proceedings of the National Academy of Sciences* 111.43, pp. 15296–15303.

Latychev, Konstantin et al. (2005). “Glacial isostatic adjustment on 3-D Earth models: a finite-volume formulation”. In: *Geophysical Journal International* 161.

Lau, Harriet et al. (2016). “Inferences of mantle viscosity based on ice age data sets: Radial structure”. In: *Journal of Geophysical Research: Solid Earth* 121.10, pp. 6991–7012.

Longman, I.M. (1963). “A Green’s function for determining the deformation of the Earth under surface mass loads,2, computations and numerical results”. In: *Journal of Geophysical Research* 68.

Love, Ryan et al. (2016). “The contribution of glacial isostatic adjustment to projections of sea-level change along the Atlantic and Gulf coasts of North America”. In: *Earth’s Future* 4.10.

Meade, R.H. and J.A. Moody (2010). “Causes for the decline of suspended-sediment discharge in the Mississippi River system, 1940-2007”. In: *Hydrological Processes* 25.

Milne, Glenn (1998). “Refining models of the glacial isostatic adjustment process”. PhD thesis. Toronto, Canada: University of Toronto.

Milne, Glenn A. and Jerry X. Mitrovica (1998). "Postglacial sea-level change on a rotating Earth". In: *Geophysical Journal International* 133.1, pp. 1–19.

— (2008). "Searching for eustasy in deglacial sea-level histories". In: *Quaternary Science Reviews* 27.25, pp. 2292–2302.

Mitrovica, J. X., A. M. Forte, and M. Simons (2000). "A reappraisal of postglacial decay times from Richmond Gulf and James Bay, Canada". In: *Geophysical Journal International* 142.3, pp. 783–800.

Mitrovica, J. X. and W. R. Peltier (1995). "Constraints on mantle viscosity based upon the inversion of post-glacial uplift data from the Hudson Bay region". In: *Geophysical Journal International* 122.2, pp. 353–377.

Mitrovica, J.X. (1996). "Haskell [1935] revisited". In: *Journal of Geophysical Research: Solid Earth* 101.B1, pp. 555–569.

Mitrovica, J.X. and W.R. Peltier (1992). "A comparison of methods for the inversion of viscoelastic relaxation spectra". In: *Geophysical Journal International* 108.

— (1993). "A new formalism for inferring mantle viscosity based on estimates of post glacial decay times: application to RSL variations in N.E. Hudson Bay". In: *Geophysical Research Letters* 20.

Mitrovica, Jerry X. and Glenn A. Milne (2003). "On post-glacial sea level: I. General theory". In: *Geophysical Journal International* 154.2, pp. 253–267.

Morelli, Andrea and Stefania Denesi (2004). "Seismological imaging of the Antarctic continental lithosphere: a review". In: *Global and Planetary Change* 42.

Morton, R.A., J.C. Bernier, and J.A. Barras (2006). "Evidence of regional subsidence and associated interior wetland loss induced by hydrocarbon production, Gulf Coast region, USA". In: *Environmental Geology*.

Nakada, Masao and Kurt Lambeck (1989). "Late Pleistocene and Holocene sea-level change in the Australian region and mantle rheology". In: *Geophysical Journal* 96.

Nield, Grace A. et al. (2018). "The impact of lateral variations in lithospheric thickness on glacial isostatic adustment in West Antarctica". In: *Geophysical Journal International* 214.

Nordman, Maaria, Glenn Milne, and Lev Tarasov (2015). “Reappraisal of the Ångerman River decay time estimate and its application to determine uncertainty in Earth viscosity structure”. In: *Geophysical Journal International* 201.2, pp. 811–822.

Paulson, Archie, Shije Zhong, and John Wahr (2005). “Modelling post-glacial rebound with lateral viscosity variations”. In: *Geophysical Journal International* 163.

Peltier, W. R. (1974). “The impulse response of a Maxwell Earth”. In: *Reviews of Geophysics* 12.4, pp. 649–669.

Peltier, W. R. and J. T. Andrews (1976). “Glacial-Isostatic Adjustment I. The Forward Problem”. In: *Geophysical Journal of the Royal Astronomical Society* 46.3, pp. 605–646.

Peltier, W. R., D. F. Argus, and R. Drummond (2015). “Space geodesy constrains ice age terminal deglaciation: The global ICE-6G_C (VM5a) model”. In: *Journal of Geophysical Research: Solid Earth* 120.1, pp. 450–487.

Peltier, W. R. and Rosemarie Drummond (2008). “Rheological stratification of the lithosphere: A direct inference based upon the geodetically observed pattern of the glacial isostatic adjustment of the North American continent”. In: *Geophysical Research Letters* 35.16.

Peltier, W.R. (1985). “The LAGEOS Constraint on Deep Mantle Viscosity: Results From a New Normal Mode Method for the Inversion of Viscoelastic Relaxation Spectra”. In: *Journal of Geophysical Research* 90.

— (1994). “Ice Age Paleotopography”. In: *Science* 265.

— (1996). “Mantle viscosity and Ice-Age Ice Sheet Topography”. In: *Science* 273.

— (1998). “Postglacial variations in the level of the sea: Implications for climate dynamics and solid-earth geophysics”. In: *Reviews of Geophysics*.

— (2004). “GLOBAL GLACIAL ISOSTASY AND THE SURFACE OF THE ICE-AGE EARTH: The ICE-5G (VM2) Model and GRACE”. In: *Annual Review of Earth and Planetary Sciences* 32.1, pp. 111–149.

Peltier, W.R. and R.G. Fairbanks (2006). "Global glacial ice volume and Last Glacial Maximum duration from an extended Barbados sea level record". In: *Quaternary Science Reviews* 25.23. Critical Quaternary Stratigraphy, pp. 3322–3337.

Peltier, W.R. and A.M. Tushingham (1991). "Influence of glacial isostatic Adjustment on Tide Gauge Measurements of Secular Sea level Change". In: *Journal of Geophysical Research* 96.

Pendea, I.F. et al. (2010). "A new shoreline displacement model for the last 7 ka from eastern James Bay, Canada". In: *Quaternary Research* 73.

Pollard, David, Natalya Gomez, and Robert M. Deconto (2017). "Variations of the Antarctic Ice Sheet in a Coupled Ice Sheet-Earth-Sea Level Model: Sensitivity to Viscoelastic Earth Properties". In: *Journal of Geophysical Research: Earth Surface* 122.

Ranalli, G. (1995). *Rheology of the Earth*. 2nd. Chapman and Hall.

Ranalli, G. and B. Fischer (1984). "Diffusion Creep, Dislocation Creep, and mantle Rheology". In: *Physics of the Earth and Planetary Interiors* 34.

Rannalli, G. and D. Murphy (1987). "Rheological stratification of the lithosphere". In: *Tectonophysics* 132.

Roy, K. and W.R. Peltier (2015). "Glacial isostatic adjustment, relative sea level history and mantle viscosity: reconciling relative sea level model predictions for the U.S. East coast with geological constraints". In: *Geophysical Journal International* 201.2, pp. 1156–1181.

Sabadini, Roberto, David A. Yuen, and Mark Portney (1986). "The effects of upper-mantle lateral heterogeneities on postglacial rebound". In: *Geophysical Research Letters* 13.

Schoof, Christian (2007). "Ice sheet grounding line dynamics: Steady states, stability, and hysteresis". In: *Journal of Geophysical Research* 112.

Shennan, Ian et al. (2006). "Relative sea-level changes, glacial isostatic modelling and ice-sheet reconstructions from the British Isles since the Last Glacial Maximum". In: *Journal of Quaternary Science* 21.6, pp. 585–599.

Tarasov, Lev (2013). "GLAC-1b: A new data-constrained global deglacial ice sheet reconstruction from glaciological modelling and the challenge of missing ice".

Tarasov, Lev et al. (2012). "A data-calibrated distribution of deglacial chronologies for the North American ice complex from glaciological modeling". In: *Earth and Planetary Science Letters* 315-316. Sea Level and Ice Sheet Evolution: A PALSEA Special Edition, pp. 30–40.

Tesauro, M., M.K. Kaban, and S. Cloetingh (2009). "A new thermal and rheological model of the European lithosphere". In: *Tectonophysics* 476.

Törnqvist, T.E. et al. (2008). "Mississippi Delta subsidence primarily caused by compaction of Holocene strata". In: *Nature Geoscience* 1.

Turcotte, D.L. and G. Schubert (2002). *Geodynamics*. Cambridge University Press.

Tushingham, A.M. and W.R. Peltier (1991). "ICE-3G: A New Global model of Late Pleistocene Deglaciation Based Upon Geophysical Predictions Of Post-Glacial Relative Sea Level Change". In: *Journal of Geophysical Research* 96.

van der Wal, Wouter and Thijs IJpelaar (2017). "The effect of sediment loading in Fennoscandia and the Barents Sea during the last glacial cycle on glacial isostatic adjustment observations". In: *Solid Earth* 8.

van der Wal, Wouter, Pippa L. Whitehouse, and Ernst J.O. Schrama (2015). "Effect of GIA models with 3D composite mantle viscosity on GRACE mass balance estimates for Antarctica". In: *Earth and Planetary Science Letters* 414.

van der Wal, Wouter et al. (2010). "Sea levels and uplift rate from composite rheology in glacial isostatic adjustment modeling". In: *Journal of Geodynamics* 50.1, pp. 38–48.

Walcott, R.I. (1980). "Rheological models of the earth from glacio-isostatic rebound". In: *Earth Rheology, Isostasy, and Eustasy*. Ed. by Morner. John Wiley.

Wang, Hangsheng and Patrick Wu (2006). "Effects of lateral variations in lithospheric thickness and mantle viscosity on glacially induced surface motion on a spherical, self-gravitating Maxwell Earth". In: *Earth and Planetary Science Letters* 244.

Wang, Hangsheng, Patrick Wu, and Wouter van der Wal (2008). In: *Journal of Geodynamics* 46.

Watson, Christopher S. et al. (2015). "Unabated global mean sea-level rise over the satellite altimeter era". In: *Nature Climate Change* 5.

Whitehouse, Pippa and Sarah Bradley (2013). "Eustatic sea level changes since the last glacial maximum". In: *Encyclopedia of Quaternary Science*. Ed. by Scott Elias.

Wolstencroft, M. et al. (2014). "Understanding subsidence in the Mississippi Delta region due to sediment, ice, and ocean loading: Insights from geophysical modeling". In: *Journal of Geophysical Research: Solid Earth*.

Wolstencroft, Martin et al. (2015). "Uplift rates from a new high-density GPS network in Palmer Land indicate a significant late Holocene ice loss in the southwestern Weddell Sea". In: *Geophysical Journal International* 203.

Woodward, R.S. (1888). "On the Form and Position of the Sea-Level as dependent on Superficial Masses Symmetrically Disposed with Respect to a Radius of the Earth's Surface". In: *Annals of Mathematics* 2.

Wu, P. (1997). "Effect of viscosity structure on fault potential and stress orientations in eastern Canada". In: *Geophysical Journal International* 130, pp. 365–382.

Wu, P. and W.R. Peltier (1982). "Viscous gravitational relaxation". In: *Geophysical Journal of the Royal Astronomical Society* 70.

Wu, Patrick (1995). "Can observations of postglacial rebound tell whether the rheology of the mantle is linear or nonlinear?" In: *Geophysical Research Letters* 22.

— (2002). "Effects of mantle flow law stress exponent on postglacial induced surface motion and gravity in Laurentia". In: *Geophysical Journal International* 148.

— (2006). "Sensitivity of relative sea levels and crustal velocities in Laurentide to radial and lateral viscosity variations in the mantle". In: *Geophysical Journal International* 165.

Wu, Patrick and W. R. Peltier (1983). "Glacial isostatic adjustment and the free air gravity anomaly as a constraint on deep mantle viscosity". In: *Geophysical Journal of the Royal Astronomical Society* 74.2, pp. 377–449.

Wu, Patrick and Hangsheng Wang (2008). "Postglacial isostatic adjustment in a self-gravitating spherical earth with power-law rheology". In: *Journal of Geodynamics*.

Wu, Patrick, Hangsheng Wang, and Hugo Schotman (2005). "Postglacial induced surface motions, sea-levels, and geoid rates on a spherical, self-gravitating laterally heterogeneous earth". In: *Journal of Geodynamics* 39.

Yu, S-Y, T.E. Törnqvist, and P. Hu (2012). "Quantifying Holocene lithospheric subsidence rates underneath the Mississippi Delta". In: *Earth and Planetary Science Letters*.

Zharikov, A.V. et al. (2003). "Permeability of the rocks from the Kola superdeep borehole at high temperature and pressure: implication to fluid dynamics in the continental crust". In: *Tectonophysics* 370.1, pp. 177–191.